INTENSIVE DRYING AND THE RELATED MICROSTRUCTURE FEATURES IN AGGLOMERATE SPHERES

by

Rostyslav Kudlyk

A thesis
presented to the University of Waterloo
in fulfillment of the
thesis requirement for the degree of
Doctor of Philosophy
in
Chemical Engineering

Waterloo, Ontario, Canada, 1999

© Rostyslav Kudlyk, 1999

National Library of Canada
Acquisitions and Bibliographic Services
395 Wellington Street
Ottawa ON K1A 0N4
Canada

Bibliothèque nationale du Canada
Acquisitions et services bibliographiques
395, rue Wellington
Ottawa ON K1A 0N4
Canada

Your file Votre référence

Our file Notre référence

The author has granted a non-exclusive licence allowing the National Library of Canada to reproduce, loan, distribute or sell copies of this thesis in microform, paper or electronic formats.

L'auteur a accordé une licence non exclusive permettant à la Bibliothèque nationale du Canada de reproduire, prêter, distribuer ou vendre des copies de cette thèse sous la forme de microfiche/film, de reproduction sur papier ou sur format électronique.

The author retains ownership of the copyright in this thesis. Neither the thesis nor substantial extracts from it may be printed or otherwise reproduced without the author's permission.

L'auteur conserve la propriété du droit d'auteur qui protège cette thèse. Ni la thèse ni des extraits substantiels de celle-ci ne doivent être imprimés ou autrement reproduits sans son autorisation.

0-612-38249-4

Canada

The University of Waterloo requires the signatures of all persons using or photocopying this thesis. Please sign below, and give address and date.

ABSTRACT

Most metal ore concentrates are fine particulates with a wide particle-size distribution. Industrially they are pelletized by tumbling in balling discs or drums into spheres, an operation which requires the addition of typically up to 10% by weight of water. Further processing of these agglomerates involves first drying and then induration by heating up to 1250^{0}C.

The main objective of this thesis was the study of the interrelationship between the microstructure of the agglomerates with, on the one hand, the mechanical and physical properties of the pellets and their behaviour during intensive drying, on the other.

The previously developed model of the drying process identified the loss of capillarity, resulting from the vapour lock, to be a critical component of the mechanism of intense as opposed to 'classical' drying. It was shown that the absence of the constant-rate drying period is a natural consequence of this effect.

Several significant shortcomings of the previous model have been identified. This model treats the period of transition between surface- and shrinking-core drying as an instantaneous event. The new extended model, which overcomes the original model limitations, was developed in this project. In its formalism, the new model includes the pore-size distribution and thus simulates a gradual surface/shrinking-core transition.

It was shown that the nature of the transition between the surface- and shrinking-core drying regimes during intensive drying is fundamentally different from that of classical drying, i.e.

carried out at mild temperatures. In the latter case, liquid is being delivered to the surface through the network of interconnected small pores reaching the surface. The transition occurs when the larger pores, also reaching the surface, are being drained. On the other hand, under intense-drying conditions, the rate-limiting factor is the vapour lock. The latter phenomenon will occur in the smaller pores first, as they have smaller liquid pressure. Hence, they will be the first to become dry, while surface drying continues through the system of interconnected larger pores reaching the surface.

Experimental research to be described validates the extended model for the drying of agglomerates that have a wide range of particle size and have been dried under wide range of drying conditions.

New insights have been gained by applying this new drying model. Critical aspects of microstructure of agglomerates were investigated more specifically in the light of these new insights. They include pore-matrix expansion during drying due to the engulfment of fine particles into the contacts between the larger, structure-creating ones. Experimental results validate the matrix-expansion hypothesis developed in this study.

Although this study focused on a specific industrial process, the pelletizing of iron-ore concentrates, the interrelationship between microstructure and drying behaviour has important implications in understanding the nature of soils, rocks, ceramics and processed foods.

ACKNOWLEDGEMENTS

I would like to take this opportunity to thank Dr. J.R.Wynnyckyj for his help, valuable guidance and encouragement in this project. I would also like to thank Donna Lisieczko (nee Bodnar) and Joseph Slusarczyk, whose original experimental results are incorporated in this study. Technicians and staff of the Chemical Engineering Department are thanked for their help.

I owe the most thanks, however, to my wife Roxana; her encouragement and emotional support made it possible for me to finish this work.

Dedicated to the memory of my father, Dr. Bohdan Kudlyk

TABLE OF CONTENTS

ABSTRACT iv

ACKNOWLEDGMENTS vi

DEDICATION vii

TABLE OF CONTENTS viii

LIST OF TABLES xi

LIST OF FIGURES xii

Chapter 1

PROBLEM DEFINITION, PROJECT SCOPE AND OBJECTIVES 1.1

1.1. Extension of the Drying Model 1.1

1.2. Microstructural Aspects of Drying 1.3

1.3. Drying-Rate and Temperature-Profile Experiments 1.3

1.4. Tumbling and Drying 1.4

1.5. Commentary 1.5

Chapter 2

LITERATURE REVIEW AND THEORETICAL BACKGROUND 2.1

2.1. Forces of Adhesion between Particles 2.1

2.2. Microstructure of Particle Packings 2.5

2.2.1. Packing Characteristics of Single-Size Particles 2.5

2.2.2. Packings of Particles with a Size Distribution 2.8

2.2.3. Microstructure of Agglomerates Produced by Tumbling 2.12

2.2.3.1. Significance for Present Research 2.16

2.3. Drying Phenomenology 2.18

2.3.1. The "Classical" Drying Curve 2.18

2.3.2. Intense Drying and the Vapour Lock 2.24

2.4 The Zaharchuk Drying Model 2.27
2.4.1. Surface Drying Regime 2.27
2.4.2. Shrinking Core Drying Regime 2.33
2.4.3. Calculation of Matrix Stresses 2.38
2.4.3.1 Thermal Stresses 2.38
2.4.3.2 Pressure Stresses. 2.41
2.4.4. Sample Results of Zaharchuk Model 2.42
2.5. Mechanical Properties of Iron-Ore Agglomerates 2.48
2.5.1. Agglomerate Strength 2.48
2.5.2. Resistance to Spalling during Drying 2.54

Chapter 3
CONTRIBUTION TO THEORY 3.1
3.1. Limitations of the Zaharchuk Model 3.1
3.2. Extended Drying Model 3.7
3.2.1. Program Algorithm 3.13
3.2.2. Modelling the Shrinking-Core Drying Period 3.19
3.3. Effect of Bentonite on Drying Behaviour 3.20
3.4. Matrix Expansion and a Hypothesis of its Cause 3.22

Chapter 4
RESULTS OF MODELLING INVESTIGATIONS 4.1
4.1. Conditions for the Occurrence of the Vapour Lock 4.1
4.2. Modelling of Drying Behaviour 4.6
4.3.The Concepts of Mild and Intense Drying and Transition Between them 4.16
4.4. Tumbling-and-Drying Investigations 4.23
4.4.1 Existing Experimental Data Base 4.23
4.4.2. Modelling the Drying Behaviour of Tumbled-and-Dried Pellets .. 4.25
4.4.3. Modelling of the Spalling Resistance during Intense Drying 4.29
4.5. Modelling of the Effect of Bentonite on Spalling Resistance 4.31

Chapter 5.
EXPERIMENTAL MATERIALS AND PROCEDURES 5.1
5.1. Experimental Materials 5.3
5.2. Drying Apparatus 5.5
5.3 Direct Measurement of Pellet-Centre Temperature 5.9
5.4 Scanning Electron Microscopy 5.9
5.5 Porosity and Dry Strength Measurement 5.11

Chapter 6.
EXPERIMENTAL RESULTS AND MODEL VALIDATION 6.1
6.1 Drying Experiments to Validate the Model 6.1

6.1.1 Drying of Coarser-Particle-Size Pellets 6.1
6.1.2. Center-Temperature Measurement 6.10
6.2. Matrix Expansion Studies 6.21
6.2.1. Porosity Measurements 6.23
6.2.1.1. Griffith Iron Ore Agglomerates 6.23
6.2.1.2. Porosity Measurement throughout a Drying Run 6.24
6.2.2. Repetitive Drying 6.26
6.3. Dry Strength Measurement 6.35
6.4. Binder-Additive Behaviour 6.38
6.4.1 Microstructural Investigation of Bentonite Precipitation 6.38
6.4.2. Porosity and Dry Strength Measurements 6.49
6.4.3. Drying Experiments and Modelling 6.51
6.4.3.1. Drying of Fine-Particle-Size Pellets with Bentonite 6.51
6.4.3.2. Drying of Coarser-Particle-Size Pellets with Bentonite .. 6.58
6.4.3.3. Center-Temperature Measurement 6.75

Chapter 7.
SUMMARIZING DISCUSSION 7.1
7.1. Drying Investigations 7.1
7.2. Microstructural Investigations. 7.4
7.3. Binder Additive Behaviour 7.7

Chapter 8.
CONCLUSIONS 8.1

Chapter 9
LITERATURE 9.1

Chapter 10
NOMENCLATURE 10.1

Appendix A
DERIVATION AND NUMERICAL SOLUTION OF THE HEAT BALANCE EQUATION A.1

LIST OF TABLES

2.2.1.1. Results of the Packing Density Measurements 2.7

2.4.4.1. "Typical" Pellet Parameters and Drying Conditions [1] 2.46

2.5.2.1. Experimental Results of Tigerschiold and Ilmoni [103] 2.55

2.5.2.2. Experimental Results of Roorda et al. [94] 2.58

3.4.1. Volume Increase of Iron Ore Pellets upon Drying [50] 3.23

4.4.1.1 Results of Tumbling-and-Drying Experiment [92] 4.24

4.4.2.1. Parameters of Tumbled-and-Dried Pellets [52] 4.26

6.1.1.1. Guide to the Results of Drying Experiments 6.9

6.1.2.1. Guide to the Results of Center-Temperature Measurements 6.20

6.2.1.1.1 Porosity Measurements of Iron Ore Pellets upon Drying 6.23

6.2.2.1. Guide to the Results of Repetitive Drying Experiments: Griffith Concentrate 6.30

6.3.1. Results from Dry Strength Measurements 6.37

6.4.1.1 Results of Elemental Analysis of Bentonite Deposits on Nickel-Beads Pellets with Particle Size 5 -10μm 6.42

6.4.2.1. Porosity and Dry Strength Measurements of Pellets with Bentonite 6.50

6.4.3.1.1. Guide to the Results of Drying Pellets with Bentonite (d_p=*7.1μm*) 6.53

6.4.3.2.1. Guide to the Results of Drying Pellets with Bentonite (d_p=*18.6μm and 19.9μm*) 6.74

6.4.3.3.1. Guide to the Results of Center-Temperature Measurements 6.76

LIST OF FIGURES

2.2.1.1. Effect of Small Particles on the Porosity of Agglomerate [30] 2.9

2.2.2.1 Schematic Arrangement of a Densest Packing of Fractions of Monosized Spherical Particles [9] 2.10

2.2.3.1. a) – Microstructure of a Typical Iron-ore Agglomerate with a Wide Particle-size Distribution [10]; b) -- Photomicrograph of an Iron-ore Pellet Interior Featuring a Trapped Air Bubble 2.14

2.2.3.2 a) – Sample Cumulative Pore-size Distribution Curve - Lab Pellet; Griffith Concentrate (0.0% bentonite) [47];
b) – Mercury Porosimetry; Intrusion and Drainage Curves - Lab. Pellets; Griffith Concentrate (0.8% bentonite) [47] 2.17

2.3.1.1. Drying Rate vs. Moisture Content Curve [36] 2.19

2.3.1.2 Simplified Pore Structure Showing Moisture Migration for the Mild Drying Conditions [38] 2.22

2.3.2.1 Experimental Drying-rate Curves at Temperatures: (1) - 100^{0}C; (2) - 200^{0}C; (3) - 300^{0}C [42] 2.25

2.4.4.1 Saturation Profile for 'Typical' Pellet and Conditions [1] 2.43

2.4.4.2 Drying Rate: 'Typical' Pellet Drying Rate versus Time [1] 2.44

2.4.4.3 Surface, Centre, and Interface Temperature for a 'Typical' Pellet and Drying Conditions [1] 2.45

2.4.4.4 Stress Distribution within Pellet: (a) Thermal Circumferential; (b) Thermal Radial; (c) Pressure Circumferential; (d) Pressure Radial [1] 2.49

2.4.4.5 Total Stress Distribution within Pellet; (a) Circumferential Stresses; (b) Radial Stresses [1] 2.50

2.4.4.6 Distribution of Stresses at the Interface [1] 2.51

2.5.2.1. Spalling Behaviour; Experimental Results of Schultz et al. [93]: a) -- Drying Furnace; b) -- Decrepitation Resistance as a Function of Particle Size; c) -- Effect of Bentonite Additions on Decrepitation Resistance; d) -- Effect of Stach additions on Decrepitation Resistance. 2.57

3.1.1 Model Predictions of: Drying Rate, Liquid Pressure and Vapour Pressure vs. Pellet Saturation (particle size 7.1μm) 3.2

3.1.2 Model Predictions of: Drying Rate, Liquid Pressure and Vapour Pressure vs. Pellet Saturation (particle size 17μm) 3.3

3.1.3 Drying-rate Curve (1); Temperature at the Surface (2) and at the Interface (3) 3.5

3.2.1 Simplified Pore Structure Showing Moisture Migration for the Intense Drying Conditions 3.8

3.2.2 Simplified Physical Picture of the Intense Drying During the Transitional Period 3.10

3.2.1.1 Program Algorithm Flow Chart 3.15

3.4.1 Schematic Representation of Pore-expansion Hypothesis 3.24

4.1.1 Dependence of Critical Pore Radius and Related Particle Diameter on Surface Temperature and Saturation: a) over Temperature Range 0-80 deg.C; b) over Temperature Range 0 -94 deg.C. 4.4

4.2.1 Drying Curve Predicted by: (a) - Zaharchuk Model; (b) - by Extended Model: Particle Diameter 7.1μm 4.7

4.2.2 Drying Rate vs. Time Curve Predicted by: (a) - Zaharchuk Model; (b) - by Extended Model: Particle Diameter 7.1μm 4.8

4.2.3 (a) - Surface-, Interface- and Center Temperature vs. Time Curves Predicted by Zaharchuk Model; (b) - Surface- and Interface Curves Predicted by Extended Model: Particle Diameter 7.1μm 4.9

4.2.4 Drying Curve Predicted by: (a) - Zaharchuk Model; (b) - by Extended Model: Particle Diameter 20μm 4.12

4.2.5 Drying Rate vs. Time Curve Predicted by: (a) - Zaharchuk Model; (b) - by Extended Model: Particle Diameter 20μm 4.13

4.2.6 (a) - Surface-, Interface- and Center Temperature vs. Time Curves Predicted by Zaharchuk Model; (b) - Surface- and Interface Curves Predicted by Extended Model: Particle Diameter 20μm 4.14

4.3.1. Maximum Surface-Drying Rates and Absolute Maximum Drying Rates Predicted by the Zaharchuk Model for a 'Typical Pellet' Parameters with Variable Particle Size. 4.18

4.3.2. Dependence of Model-predicted Maximum Drying Rates on Particle Diameter and Drying Temperature. Maximum Surface-Drying Rates are Shown with Dotted Lines; Solid Lines are the Absolute Maximum Drying Rates.. ..... 4.20

4.3.3 Dependence of Model-predicted Maximum Drying Rates on Porosity and Drying Temperature. Maximum Surface-Drying Rates are Shown with Dotted Lines; Solid Lines are the Absolute Maximum Drying Rates.. ..... 4.22

4.4.1.1 Experimental Results of Dependence of Dry Strength on Porosity In Tumbled-and-dried Pellets 4.25

4.4.2.1 Model Drying-rate Curves of Pellets Produced by Tumbling-and-drying 4.27

4.4.2.2 Total Circumferential Stresses at Interface during Drying at 400 deg.C of the Tumbled-and-dried Pellets 4.25

4.5.1 Results of Modelling of the Shock Temperature as a Function of Bentonite Content 4.32

4.5.2 Modelling of the Dependence of Total Circumferential Stresses at Interface and Dry Strength as a Function of Bentonite Content 4.33

5.1.1 Particle Size Analysis of the Griffith Concentrate by CANMET [51] 5.2

5.2.1 Schematic Representation of Drying Apparatus 5.4

5.2.2 Drying Zone Temperature Calibration Chart 5.7

5.2.3 Drying Apparatus 5.8

5.5.1 Cutting Tools Used to Shape Pellets into Spheres [47, 51] 5.13

6.1.1.1. Drying Rate Curves of a Sample Pellet without Bentonite Plotted versus: Drying Time (a); Percent Moisture (b) [2]. 6.2

6.1.1.2-6.1.1.6 Model Predictions of Experimental Drying-Rate Curve: a) - Zaharchuk Model; b) - Extended Model.. ..... 6.4 - 6.7

6.1.2.1 (a-d) Model Predictions of: (a) - Experimental Drying-Rate Curve; (b) - Temperature at the Pellet's Center.. ..... 6.11 - 6.14

6.1.2.2 (a-e) Extended-Model Predictions of: (a) - Experimental Drying-Rate Curve; (b) - Temperature at the Pellet's Center and Surface ... . 6.15 - 6.19

6.2.1.2.1 Results of Porosity Measurement throughout Drying Run 6.25

6.2.2.1 (a-c) Comparison of Drying Rate Curve of a Fresh Pellet without Bentonite Dried at 400°C to that of the Rewetted Pellet Originally Dried at 150°C, then Rewetted and Re-Dried at 400°C. ..... 6.27 - 6.29

6.2.2.2 Comparison of Drying Rate Curve of a Pellet without Bentonite Dried at 400°C then Rewetted and Re-Dried at the Same Temperature. 6.31

6.2.2.3 Comparison of Drying Rate Curve of a Pellet without Bentonite Dried at 150°C then Rewetted and Re-Dried at the Same Temperature. 6.32

6.2.2.4 Comparison of Drying Rate Curve of a Fresh Pellet without Bentonite Dried at 150°C to that of the Rewetted Pellet Originally Dried at 400°C, then Rewetted and Re-Dried at 150°C. 6.33

6.2.2.5 Drying-rate Curve Predicted by the Model for Two Different Porosities: 0.32 and 0.35 ..... 6.36

6.4.1.1 Experimental Drying-rate Curve of a Sample Nickel-beads Pellet Dried under Mild Conditions 6.40

6.4.1.2 Experimental Drying-rate Curve of a Sample Nickel-beads Pellet Dried under Intense Conditions 6.41

6.4.1.3 Photomicrographs of a Glass-beads Pellet with the Particle Size 200μm and 1.0% Bentonite Dried at 400^{0}C: (a, b) - Pellet Interior (c, d) - Near-the-Surface 6.43

6.4.1.4 Photomicrographs of a Nickel-beads Pellet with the Particle Diameter 7.5 um and 1.0% bentonite Dried at 100 Degrees C:(a-c) - Pellet Interior; (d) - Near the Surface Area 6.44

6.4.1.5 Photomicrographs of a Nickel-beads Pellet with the Particle Diameter 7.5 um and 1.0% bentonite Dried at 400 Degrees C:(a, b) - Pellet Interior; (c, d) - Near the Surface Area 6.45

6.4.1.6 Distribution of Bentonite Inside Nickel-beads Pellets Dried at: (a) - 100 deg.C; (b) - 400 deg.C 6.48

6.4.3.1.1. Drying Rate Curves of a Sample Pellet with 0.8% Bentonite Plotted versus: (a) - Drying Time; (b) - Percent Moisture [2]. 6.52

6.4.3.1.2 - 6.4.3.1.5
Drying Rate Curves of a Pellet with 0.8% Bentonite (avg. part. size 7.1um) Plotted versus:(a) - Drying Time ; (b) -Percent Moisture..... 6.54 - 6.57

6.4.3.2.1. Model/experiment Correlation for a Drying-rate Curve of a Pellet with 0.6% Bentonite 6.59

6.4.3.2.2 - 6.4.3.2.8
Model Predictions of Experimental Drying-Rate Curve for a Pellet with 0.6% Bentonite: (a) - Zaharchuk Model; (b) - Extended Model ..... 6.60 - 6.66

6.4.3.2.9 - 6.4.3.2.15
Model Predictions of Experimental Drying-Rate Curve for a Pellet with 1.2% Bentonite: (a) - Zaharchuk Model; (b) - Extended Model ..... 6.67 - 6.73

6.4.3.3.1 (a - d) Model Predictions of: (a) - Experimental Drying-Rate Curve; (b) - Temperature at the Pellet's Center. ..... 6.77 - 6.80

6.4.3.3.2 (a-g) Extended-Model Predictions of: (a) - Experimental Drying-Rate Curve; (b) - Temperature at the Pellet's Center and Surface ..... 6.81 - 6.87

6.4.3.3.3 (a-h) Extended-Model Predictions of: (a) - Experimental Drying-Rate Curve; (b) - Temperature at the Pellet's Center and Surface ..... 6.88 - 6.95

Chapter 1

PROBLEM DEFINITION, PROJECT SCOPE AND OBJECTIVES

The main concern of this project was the study of the microstructure of porous agglomerates as it determines their mechanical and physical properties, and as it is affected by and reflected in their drying behaviour. One of the important challenges was to observe and interpret drying phenomenology as a practical method of investigation of the microstructure of the porous agglomerates.

1.1. Extension of the Drying Model

The model of the drying process, developed by my predecessor D.J. Zaharchuk [1], proved to be a highly effective tool to predict the drying behaviour under intense drying conditions. It has been experimentally validated by the author [2]. One of the very significant contributions was the identification of the loss of capillarity, resulting from the vapour lock, as a critical component of the mechanism of intense, as opposed to 'classical', drying. The absence of the constant rate drying period was shown to be a natural consequence of this effect.

At the same time, some shortcomings of the model have been identified. The Zaharchuk model treats the transition between the surface and the shrinking core drying as an instantaneous event. It is known, however, that this transition occurs over a finite period of time. Some of the

experiments, described in the author's M.A.Sc. Thesis [2], showed that the model assumption of an instantaneous surface/shrinking core transition, while being valid during drying of the fine agglomerates (avg. particle size 7.1 μm), causes the model to fail to predict the experimental results when coarser agglomerates (avg. particle size >15 μm) are being dried. One of the objectives of this project, therefore, was to extend the model to incorporate a surface/shrinking-core transition which is still caused by the vapour lock but is gradual, rather than instantaneous.

Another objective of the model improvements was to elucidate the nature of the transition between the surface and shrinking-core drying regimes during intensive drying, and to show that it is fundamentally different from that during drying at mild temperatures. The latter is a well-studied phenomenon that occurs during the 'first falling-rate period'. During such "normal" drying, liquid is being delivered to the surface through the small pores which are interconnected and reach the surface. This process drains the larger pores within the body, which may also be interconnected.

On the other hand, as mentioned above, the mechanistic cause of the transition between surface-drying to the shrinking-core drying regimes under rapid drying conditions is the vapour lock, or loss of capillarity. The latter phenomenon occurs in the smaller pores first. It is the latter pores that have the lower liquid pressure and, hence, they will be the first to become dry. Yet surface drying may continue through the interconnected system of the larger pores reaching the surface. More extensive modelling and experimental work have been undertaken in this thesis to quantify and validate this mechanism.

1.2. Microstructural Aspects of Drying

The following aspects of microstructure of agglomerate were investigated more specifically in the light of questions raised and the insights gained by the Zaharchuk model:

-*pore size distribution*. The pore size distribution (rather than only a single average pore size in the Zaharchuk model) was included in the model algorithm. The calculations emphasized the drying rate during the surface/shrinking-core transition period.

-*density changes during drying*. Experimental results obtained in earlier studies in our research group have shown that drying of the iron ore agglomerates causes a definite pore volume increase. (Note that this is not a generally acknowledged effect. Agglomerate shrinkage is the more common phenomenon [37, 45, 86]. The starting assumption of our study, later confirmed, attributes such an increase to particle migration, or engulfment [46], caused by the receding water-gas-solid interface within the agglomerate pore structure. Relevant experimental and theoretical studies were carried out in this project. Their objective was to establish the stage of drying at which this pore expansion occurs, by what mechanism, and, finally, how the porosity evolution correlates with the drying rate.

1.3. Drying-Rate and Temperature-Profile Experiments

The *experimental* investigation of the drying rates of pellets of various types, as well as their wet-core temperature variations during drying, was one of the tasks of this project. The primary objective of these studies was to provide two independent and mutually-complementary

sets of experimental data to validate the drying model. In addition to the investigation of drying in its own right, a further objective was also to characterize the pellet microstructure.

The experimental apparatus, originally designed by D. Zaharchuk [1], is capable of measuring the dependence of the weight loss on drying time. A significant modification to the experimental setup was the introduction of an extra thermocouple immersed into the wet-core interior of the pellet. This provided a new and powerful tool to obtain data on the temperatures of the wet core during drying simultaneously with the drying-rate curve. Such data enables us to validate *directly* the model-calculated temperature profiles.

1.4. Tumbling and Drying

Tumbling-and-drying of the iron ore pellets is potentially an attractive modification of the industrial process for the production of pellets. This operation densifies the green pellets while decreasing their water content. The result is an increase of dry strength of the pellets. Both effects are important in industrial drying and induration.

At the same time, the mechanistic aspects of the densification process are of direct interest and dovetailed with the other parts of this study. Of interest in its own right is how the pore structure evolves during such densification.

Addressed in this project was the effect of the tumbling-and-drying operation on the decrease in porosity of the pellets and, consequently, higher dry strength, resulting in an increase in their resistance to spalling during high-temperature-drying.

1.5. Commentary

The scope of the work outlined above appears to be rather broad and multifaceted. As the titles of sections within this chapter indicate, these are drying of porous materials (sections 1.1 and 1.3), the study of pore microstructure of agglomerates (section 1.2) and, finally, the study of practical pellet manufacturing operations (section 1.4). Thus, in addition to comprising both experimental and theoretical work (including mathematical modelling), this thesis brings together as integral parts of a single thesis program several ostensibly diverse and quasi-unrelated but well-established areas of engineering science.

In the opinion of the author, however, there is a strong unifying theme forming a basis for the present thesis. Microstructure of agglomerates is the key property in understanding the practical aspects of dry and fired strength of iron ore pellets. It is one of the keys to successful drying and induration of agglomerates. In addition, microstructural development in agglomerates has important implications on understanding the nature of, for example, soils, rocks, ceramics, catalyst pellets and processed foods.

Previous work in our group has established that pore microstructure of agglomerates evolves during drying. Conversely, it was shown that measuring and defining characteristics of behaviour during drying can be an important means for studying pore microstructure and its origin.

Such an interrelationship between agglomerate microstructure, significant pellet properties and the behaviour of pellets during drying, it is asserted, creates a subject unity. The objective of this thesis work was to study these interrelationships quantitatively and to document them.

Chapter 2

LITERATURE REVIEW AND THEORETICAL BACKGROUND

In this Chapter, the literature and theoretical background relevant to the present project are reviewed. In the first sections, the forces of adhesion between agglomerated particles and resulting microstructural characteristics of the agglomerates are documented (Sections 2.1 and 2.2).

Next, the phenomenology of drying porous agglomerates and the established 'laws' of drying are reviewed (Section 2.3). This is followed by documenting the Zaharchuk drying model [1], which has served as a theoretical basis, and a subject for further improvements, in the present thesis (Section 2.4).

The final section is devoted to reviewing mechanical properties of iron-ore agglomerates produced by tumbling, and how these properties are affected by drying (Section 2.5).

2.1. Forces of Adhesion between Particles

Agglomeration is the unit operation where particles are combined to form larger entities. Distinct ways of doing this, in addition to tumbling, are operations of tableting and nodulizing [26].

Adhesion forces or interparticle bond strengths affect the packing processes as well as growth kinetics and the resulting physical properties of the agglomerate. A classification of attractive forces and bonding mechanisms has been originally proposed by Rumpf [29]. The

mechanisms, relevant to our study, are reviewed below. They may be divided into three major groups [9]:

I. ***Attraction forces between solid particles***

1. *Intermolecular forces.* Hammaker [62] showed that the adhesion of small particles to one another is due to Van der Waals forces. These forces arise from the atomic structure of the material and become important when the interparticle distances are a <100 nm.

For the sphere/sphere model, Hammaker postulated that the adhesion force A_v equals:

$$A_v = \frac{H}{24 \cdot a^2} \cdot x \qquad (2.1.1)$$

where x is the sphere diameter and H - the Hammaker's constant which depends on the material characteristics, and has values in the order of 10^{-20} to 10^{-19} J. As is evident from this equation, the inverse dependence of the adhesion force on the squared interparticle distance suggests that the adhesion diminishes quickly with increasing distance. Since the roughness peaks of smaller particles are, from an absolute point of view, smaller than those of larger ones, the adhesion probability is much higher for fine powders. Such particles approach each other with larger surface areas to smaller distances whereby high adhesion forces are obtained.

Another point to be made with regard to small particles is that, according to eqn. 2.1.1, the interparticle adhesion is proportional to the particle diameter x. This implies that it is easier to overcome the adhesion of smaller particles upon subjecting them to vibration or tapping. However, it should be noted, that the vibrational impact forces acting on individual particles are themselves a function of particle weight. The latter, in turn, is proportional to the volume of the

particle and (assuming its sphericity) - to the particle diameter *cubed.* This argument suggests that, if vibration is applied to a smaller and a larger particle both attached to the same surface, it will affect the latter one to a greater degree, causing it to separate from the surface, even though the Van der Waals adhesion of this larger particle is stronger.

The arguments above suggest an explanation of why the presence of smaller particles causes a particle mass of disperse sizes to pack less closely than the larger ones, as will be discussed in Sections 2.2.1 and 2.2.2. Small particles are the major contributors to bridging and arching within the bulk [30]. For this reason, particles with a wide size distribution (which includes particles <10μm) are less susceptible to densification by vibration or tapping.

2. *Electrostatic and magnetic forces.* Rumpf [63] showed that electrostatic forces were an order of magnitude weaker than the Van der Waals forces. This was confirmed by Turner and Balasubramanian [64]. The influence of magnetic and electrostatic forces is less well understood, largely because the former depends on grain orientation, and the latter is dependent on prefatory factors [47].

II. ***Interfacial forces and capillary pressure at freely movable liquid surfaces***

1. Liquid bridges. The role of movable liquid bridges as a source of binding strength between particles was first developed by Haines [59, 60] and subsequently by Newitt and Conway-Jones [61] in their classical work on agglomeration.

At low moisture levels (about 20% saturation), water is held between particulates as discrete lens-shaped rings: this is known as the pendular state [36]. As the moisture content increases the water forms a continuous network within the agglomerate pores and is interdispersed with the gas phase: this is known as the funicular state. When almost fully saturated

with liquid, the agglomerate is in the capillary state, so named for the multitude of capillaries at the surface, and the fully-established continuity of the liquid phase within the pore structure.

2. *Capillary forces at the surface of aggregates filled with liquid.* When the volume between the particles is completely filled with liquid and concave menisci form at the pore ends on the surface of the agglomerate, a negative pressure develops in the interior, causing a net inward force responsible for holding the agglomerate together [61].

Additional moisture will encapsulate the entire agglomerate in a liquid sphere. This is called the saturated state. At this point, the liquid surface becomes flat or even convex and the capillary pressure forces are lost. In this condition, the agglomerate frequently flattens out and/or "liquefies".

III. ***Adhesion in not-freely movable binders***

1. *Highly viscous binders, adhesives.* Highly viscous liquids, such as glues, have a low liquid mobility and thus the liquid surface does not readily respond to external forces. The adhesional forces of the liquid-solid bond and the cohesional forces within the liquid are therefore exploited to a greater degree as the stresses on these bonds are not reduced via liquid mobility. In addition, viscous liquids are frequently used as binding agents because they may create solid bridges upon hardening.

2. *Adsorption layers* (thickness <3-5 nm). The absorption of water is caused by molecular attraction between the polar water molecule and the unsatisfied bonds of the solid surface molecules. If the adsorbed water between particles has a radius or thickness >5 nm, it will create a liquid meniscus and act as a mobile liquid (see above). If the layer's thickness is smaller than 3nm, the entire force of the molecular attraction causing adsorption may bind two particles

together when they share a common adsorption layer [58].

2.2. Microstructure of Particle Packings

In this Section, the microstructural characteristics of particle packings are reviewed. Microstructural features of agglomerates produced by tumbling are of particular significance to the present work. The relevant literature review is in Section 2.2.3. To set the stage for this review further elaborations regarding characteristics of elementary packings of spherical particles (both single-size and multi-size) are documented (Sections 2.2.1 and 2.2.2).

2.2.1. Packing Characteristics of Single-Size Particles

The random-packing concept, in which the positions of the particles are randomly distributed, has been reviewed widely [5-8] and is part of text books [4, 9, 12]. In practice, the nearest approach to the formation of a random array occurs when the particles approach the packing from random directions and remain in position as soon as they come into contact with the packing.

During deposition particles form a bed under the influence of several constraining forces including gravity. They take up positions of minimum potential energy. Their positions are related to the packing formed at that stage and to the behaviour of other depositing particles. This real packing, which sometimes may be ordered, is also referred to as haphazard packing [4]. It has been shown experimentally [8] that monosize particles will pack to 40% porosity on pouring and with the addition of a slight vibration or tapping will further consolidate to 36.4% porosity. The latter porosity is typical of what is commonly referred to as a random packing.

Based on extensive experimental investigations, McGeary [5] proposed that three regular local particle arrangements should be considered in describing random packings:

a) Orthorhombic, porosity $\varepsilon = 0.3954$;

b) Tetragonal spheroidal or double nested, $\varepsilon = 0.3019$;

c) Rhombohedral or hexagonal close packed, $\varepsilon = 0.2595$.

He also found that the most commonly occurring ordered arrangement in a random packing of spheres was case (a). Case (b) occurred in approximately 20% of all random packings, while case (c) did not occur *at all.*

Other studies [6, 7] analysed the properties associated with a given packing arrangement. When spherical particulate material is poured into a container, the particles settle within the confines of the container walls in a random configuration which is generally of stable character. The closer the packing of the particles and smaller the voids, the more stable the packing obtained. Thus, for loose packed assemblies ($\varepsilon \approx 0.400$) there exists a means by which the loose assembly can be transformed into a random close packed one ($\varepsilon \approx 0.363$) by introducing small energy increments by tapping or vibration. As mentioned above, this random close packing is thought to be made up of ortho-rhombic and tetragonal packing arrays within a loose packed geometrical network [5].

The practice of compaction of granular beds after deposition by subjecting them to some vibratory or tapping treatment is widespread and has been studied extensively [5, 16-18]. It involves the supply of increments of energy to the bed of particles at a selected frequency for a selected time. The initial structure of the bed after deposition is such that, upon vibration, it can deform sufficiently. This allows the particles to slip into new positions with minimum potential

energies, comprising a compact and mechanically stable structure.

The effect of compaction of granular beds by vibration is shown in Table 2.2.1.1, in which results obtained in different studies have been summarized.

Table 2.2.1.1. Results of the Packing Density Measurements

Case	Example	Average Porosity	Mean Coordination Number	Reference
Ultra loose random packing	Flocculation	0.8 - 0.9	2 - 4	Orr [14]
Very loose random packing	Fluidization	0.52 - 0.54	6	Ergun [15]
Loose random packing	Individual particle pouring	0.40 - 0.41	7	Macrae and Gray [16]
Poured random packing	Poured heaps	0.38 - 0.39	7.5	Debbas and Rumpf [17]
Dense random packing	Vibrated	0.36 - 0.38	8.5	Bernal [18]

Another important factor in particle packings is *absolute particle size*. Richards [28] observed that very small particles pack less closely than larger ones. Also, small particles were found to be major contributors to bridging and arching within the bulks. It has been found [28] that particles with diameters ≤ 25 μm, when subjected to a tapping action, form agglomerates within the bulk of the packing. At this particle size range, interparticle van der Waals forces become dominant (see argument in Section 2.1). In many such cases, the material tends to be very cohesive.

Berg et al. [30] studied the influence of particle size on the compaction of fine powders

by tapping. Their results show that the relatively fine particles (<100 μm) fail to be compacted in a manner common to larger ones. A plot of their results showing the relationship between particle diameter and porosity of the agglomerate is shown in Figure 2.2.1.1. The failure to compact and decrease porosity is said to be due to bridging of the interstices between the particles.

2.2.2. Packings of Particles with a Size Distribution

Much has been written concerning how smaller particles may fill the void space between the larger particles. The densest packing is obtained with the so-called 'Fuller distribution' [19]. Theoretically it consists of several monosized fractions of spherical particles, the sizes and amounts of which are just sufficient to fill the voids between close packed particles of the next larger fraction. Figure 2.2.2.1, taken from Pietsch [9], depicts an applicable two-dimensional model of one such void. While the space filling and packing of such type is conceivable only theoretically, experimental observations found [10] that the densest packing from size distributions of spherical particles is obtained if their polydisperse mixture can be described by a geometric series:

$$dM = q \cdot M \cdot dx/x \qquad (2.2.2.1)$$

where dM/M is a relative change in the particulate amount featuring size x, dx/x is the relative change of the particle size x, and q is a constant. Equation (2.2.2.2) represents the exponential distribution:

$$M = \left(x / x_{max} \right)^q \qquad (2.2.2.2)$$

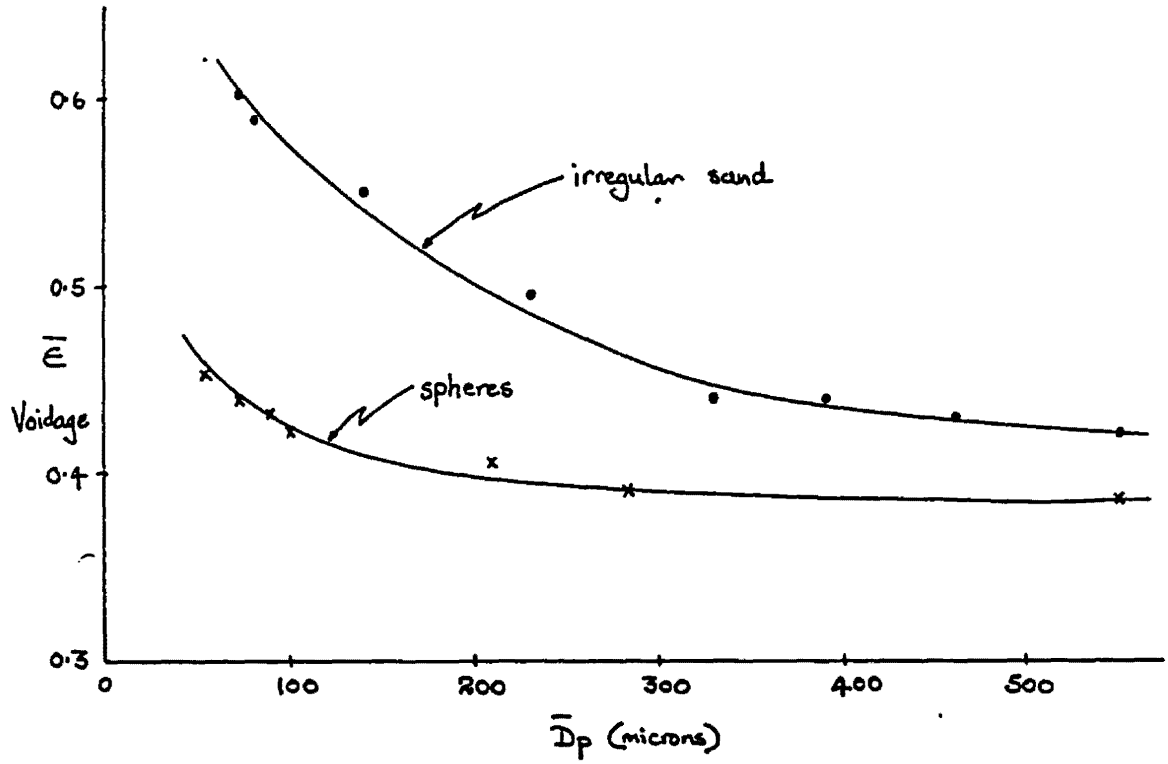


Figure 2.2.1.1. Effect of small particles on the porosity of agglomerate [30].

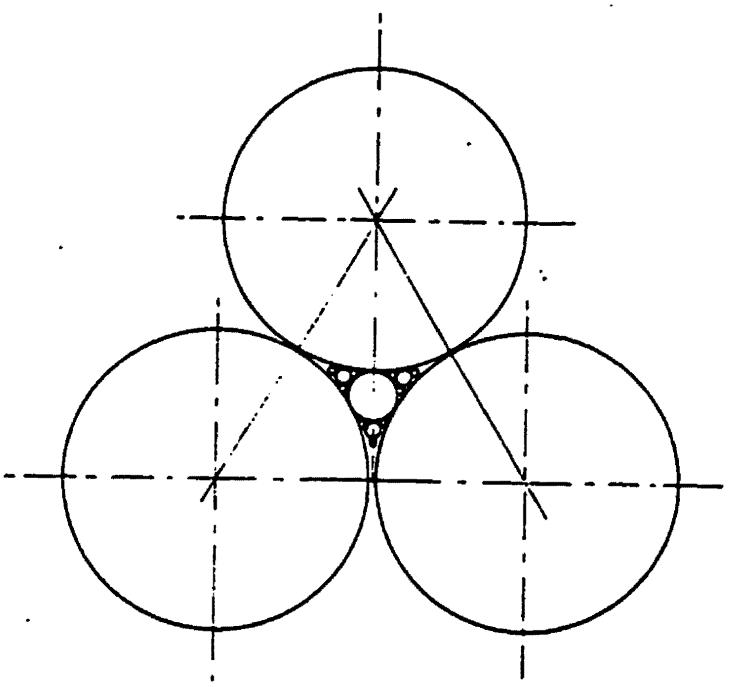


Figure 2.2.2.1 Schematic arrangement of a densest packing of fractions of monosized spherical particles [9].

According to Fuller [11], the value of q must be between 1/3 and 2/3 to obtain the densest packing. It has been found useful to define a packing efficiency. For example, as mentioned previously, the random-packing porosity for a one component system is 36.44%. This makes the packing efficiency equal to 0.6366 by volume.

For a two-component (binary) system [7], assuming the finer component will pack randomly and unhindered into the pore space left by the first coarse component, the packing efficiency is

$$\Phi_{bin} = \eta_1 + (1 - \eta_1)\eta_2 \qquad (2.2.2.3)$$

Here η_1 and η_2 are the values of packing efficiency for coarse and fine components respectively. Using η_1=0.6366 and η_2=0.6366, i.e both sizes packing to the normal randomly achieved limit, then the optimal packing efficiency Φ_{bin} = 0.8680.

Also, for maximum packing efficiency, the mass fractions of each component in a multi-component mixture can be calculated using the expression from Sherrington and Oliver [12]:

$$W_r^{(n)} = \frac{\eta_1(1-\eta_1)^{r-1}}{1-(1-\eta_1)^n} \qquad (2.2.2.4)$$

where

η_1 is the normally expected random packing density;

n is total number of components;

r is the component under investigation.

Thus, for a binary system with a maximum packing efficiency (0.868) fractions of coarse

and fine components will be 0.7335 and 0.2665 respectively.

Batterham and Oliver [13] measured the maximum packing efficiency achievable by tapping for dry four- and five-component systems. They found that packing efficiencies of these systems were in the range 0.75-0.90, but often proved difficult to reproduce or maintain. At the same time, the measured packing efficiencies of simple binary systems were in the range 0.75-0.80 and were easy to reproduce.

Åberg [45] suggested a division of agglomerated granular materials into two types:

Type A - where all the grains are fixed in their positions because each grain has a sufficiently large number of contacts with adjacent grains. All grains form the skeleton of the granular material, and all the grains take part in the transmission of forces through the material.

Type B - where only some of the grains (usually the larger ones) are immovably fixed in their positions and constitute the skeleton of the material. The smaller grains, called loose, have such a small number of contacts with adjacent grains that they can move to a certain extent within the voids of the skeleton. The type *B* structure normally occurs [45] in the materials with a wide particle size distribution and with a significant amount of fine particles.

2.2.3. Microstructure of Agglomerates Produced by Tumbling

This is the agglomeration method of prime concern presently and is known by the term pelletizing. The tumbling is done in pelletizing discs or drums and the product is spherical pellets, and hence the name. To be pelletized in such equipment and to produce pellets of the industrially required wet (also called green) and dry strengths, the particulate must be relatively fine-sized and have a broad size distribution. This means, typically, 100% minus

100 mesh or 150 μm, and containing a significant fraction less than 4 μm. Note that the latter size is well in the range where major increases in agglomerate porosity with decreasing particle size are typical, as shown in Figure2.2.1.1. The Griffiths concentrate, used for most of the measurements in the present project, consists of this size (see Section 5.1 of this thesis).

The microstructure of pellets produced by tumbling has been investigated extensively over the years [4, 9, 12, 34, 85]. More recent studies in our group, partly reported by Wynnyckyj [34], have contributed to a reasonably complete and satisfactory definition of the microstructural features, as well as to understanding their mechanistic causes.

The key features of these microstructures are as follows:

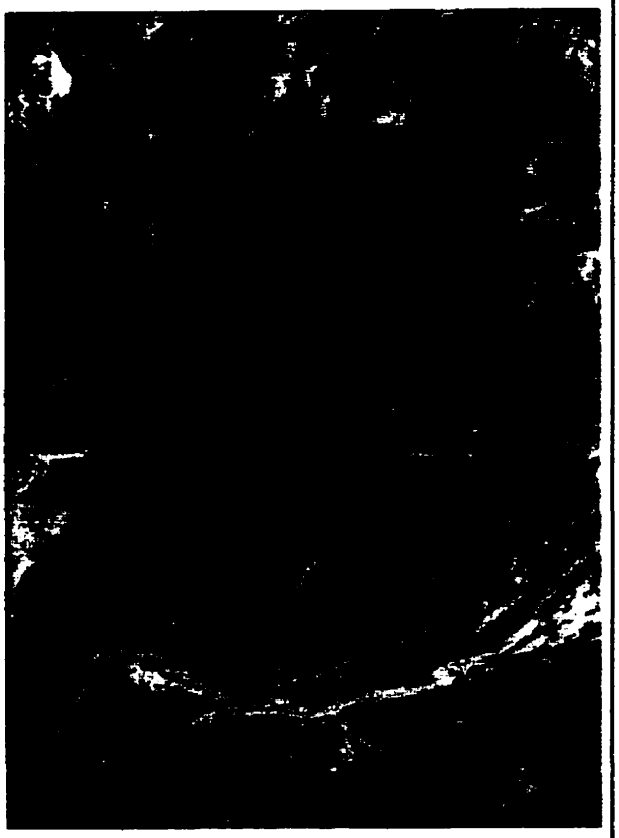
(1) Most significant presently is the presence of large pores, of the order of the average particle size, i.e. much larger than the particles in the finer fraction of the size distribution. Thus there is extensive failure of the fine-fraction particles in filling the pores created by the contact of the larger ones, in accordance with Figure 2.2.3.1 (a) [109] (see regions *A* in the Figure).

(2) The large pores, as per (1) above, result from the existence of a "skeletal network" formed by the largest and mid-sized particles coordinating each other. An additional and frequent feature, however, is that particles belonging to the smallest fraction, locate at the contacts between the larger ones thus being part of the skeletal network (see regions *B* in Figure 2.2.3.1 (a)).

(3) Part of the volume of the pores formed by the skeletal network is filled by the finer-fraction particles. They are, however, not part of the skeleton and are, therefore,



a)



b)

Figure 2.2.3.1 a) -- Microstructure of a Typical Iron Ore Agglomerate with a Wide Particle Size Distribution [10]; b) -- Photomicrograph of an Iron-ore Pellet Interior Featuring a Trapped Air Bubble [10].

loosely packed (see Figure 2.2.3.1 (a)).

Another property of the microstructure relevant presently is the 'ink-bottle' effect [34]. The large pores referred to above are interconnected with each other by much smaller pores. This feature is partly evident upon careful inspection of photomicrographs, but a more quantitative measure of it is provided by mercury porosimetry measurements.

Mercury porosimetry is widely used to determine the pore size distribution of porous media [92, 104-107]. Here mercury is made to penetrate into a previously evacuated sample and the amount intruded at a given pressure is plotted as a function of the pressure. A given penetration pressure is uniquely related to the pore size by the Young-Laplace equation:

$$p_c = p_T - p_l = \frac{2\gamma}{r_c}\cos\theta \qquad (2.2.3.1)$$

An alternative plot, therefore, is the volume penetrated as a function of pore radius. In equation 2.2.3.1 r_c is the radius of the cylindrical pore, θ -- the contact angle, and γ-- the surface tension of mercury. Since $\theta_{Hg} > 90^0$ for mercury on most solids, a positive pressure is required to force it into the pores. Conversely, once mercury has been made to penetrate a porous medium and the pressure is subsequently released, mercury withdraws or drains out from some of the pores and to the surface. The drainage would be complete for fully interconnected pores of gradually decreasing size, i.e. the curve of the volume of drainage versus pressure would be identical to the volume penetrated curve.

If the ink bottle effect is present, however, such complete drainage will not occur. As just noted, a positive pressure is required to force mercury through a pore. Following pressure

release, there is no driving force for the mercury trapped in a large pore to drain through a smaller, an ink-bottle type, pore. The drainage versus pressure curve, therefore, will differ from the intrusion versus pressure curve, in that some of the intruded mercury will fail to drain. The degree of difference will be a measure of the ink-bottle effect.

Many mercury porosimetry studies of iron ore pellets have been carried out in our group [47, 85]. A typical cumulative pore size distribution curve, obtained by D. Zaharchuk [47], is reproduced in Figure2.2.3.2 (a). A characteristic feature of the curve is the steep slope in the region of the mode value of the pore size, about 0.8 μm. The range around this mode value, for 90 percent of the pores, is between about 0.3 and 2.0 μm, i.e. surprisingly narrow, given the evidence regarding the pore size distributions evident from microscopy.

Figure 2.2.3.2 (b) shows two sets of results [47] (typical of many others) of the measurement of both the mercury intrusion and drainage behaviour. It is evident that the drainage is limited to only about 10 % of the mercury intruded during the pressurization stage. The significant element of these results for the present is that they show that the ink bottle type pores account for as much as 90 to 95 percent of the total pore volume in iron ore pellets.

2.2.3.1. Significance for present research

It is evident from the above that iron ore pellets belong to the Type B structure as defined by Åberg and referred to in Section 2.2.2. Also, as shown in Chapter 2.2.3, one of the important features of this microstructure is the existence of large and mid-sized particles in contact with each other and relatively large pores between them. Fine particles are mostly

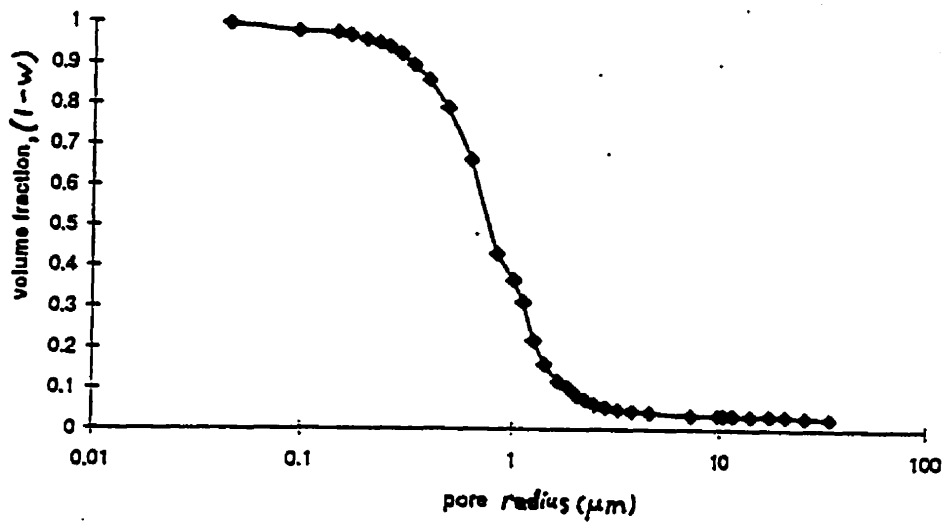


Figure 2.2.3.2 a. Sample cumulative pore size distribution curve - lab pellet; Griffith concentrate (0.0% bentonite [47].

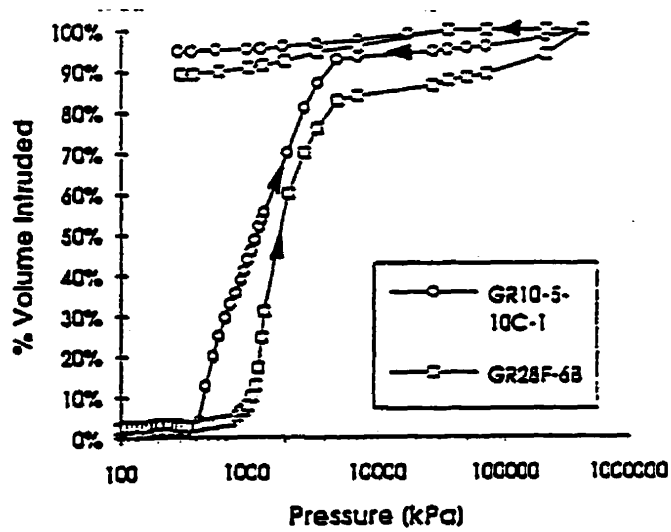


Figure 2.2.3.2 b. Mercury porosimetry; intrusion and drainage curves - lab. pellets; Griffith conc. (0.8% bentonite) [47].

located in the contacts of the skeletal network (see Figure 2.2.3.1 (a)).

The latter effect is better seen in Figure 2.2.3.1 (b) [108], which represents a microstructure of an air bubble trapped within the pellet interior. Evidently, the pellet structure consists of large particles, that constitute the skeletal network. Fine particles are completely withdrawn into the contact areas between the larger ones.

It has been suggested by Omenyi, Smith and Neumann [46] that the reason for such withdrawal of fines into the skeletal-network contacts is the engulfment phenomenon. During the latter processes, the liquid/solid/gas interface recedes, dragging along the fine loose particles.

Further investigations of this particle-migration phenomenon and its effect on the resulting microstructural and physical characteristics of the dried pellets became part of the present research and are included in Section 3.3 of the thesis. It is shown that the engulfment effect is an important feature of mild drying. The smaller particles are dragged into the pendular bridges at the contacts between the skeletal-network particles.

2.3. Drying Phenomenology

2.3.1. The "Classical" Drying Curve

There are two ways to represent the drying process graphically. One form is a plot of the weight loss vs. time [36]. The other is the slope of the former (or first derivative) plot versus drying time *or* moisture content. The latter is known as a drying-rate curve. This type of curve has long served as the basis for describing the drying behaviour, identifying drying periods and the associated rate controlling factors [37-39, 40, 42]. An example of the second type of plot, taken from Treybal [36], is shown in Figure 2.3.1.1.

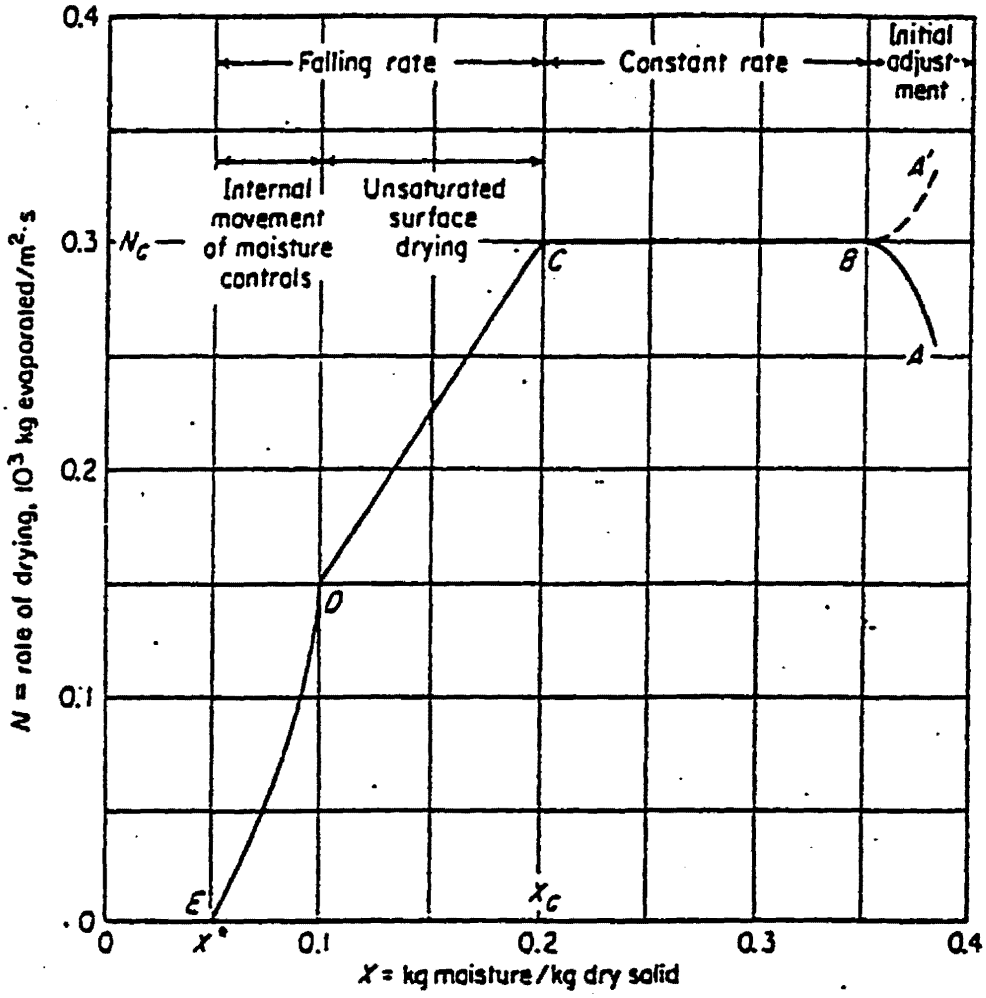


Figure 2.3.1.1.Drying rate vs. moisture content curve [36].

According to Figure 2.3.1.1, the drying of unconsolidated porous agglomerates proceeds in four distinct "periods". The four periods encompass two distinct mechanisms or stages; surface drying and shrinking-core drying.

The drying periods are:

-*The initiation period* (portion *A-B* of the graph). Two possibilities are shown: a decreasing (*A'B*) and increasing (*AB*) drying rate. Conditions of rapid drying are of interest presently; here the surface temperature and drying rate rises, as in case *AB*.

As long as drying is at the surface, the water vapour pressure at the surface is the equilibrium vapour pressure. The drying rate is controlled by heat and mass transfer across the boundary layer. The initiation period continues until a certain temperature is reached (point *B*) at which the incoming heat flux is consumed by the thermal requirements to evaporate the water supplied to the surface.

Starting at point *B* the drying period known as *the constant-rate period*, and shown as portion *B-C* at the graph, sets in. During this period drying continues at the surface. Liquid is transported from the interior of the porous body to the surface by Darcy flow relatively rapidly; driven by capillary action.

The surface maintains itself at a constant temperature, known as the wet-bulb temperature. All heat reaching the surface is consumed by vaporizing the water there. The drying rate is *constant* and, as in case *A-B*, is still controlled by the heat and mass transfer across the boundary layer [37]. The key part of the mechanism is the ability of the porous system to deliver the water to the surface rapidly, so that the rate of delivery is *not* rate limiting. The driving force for the water flow to the surface is capillarity.

A critical moisture content is reached at point *C* where the rate of the delivery of liquid to the surface by capillary action becomes less than the ability of the liquid to be vaporized and the vapour to be removed from there. As a result, the liquid flow to the surface becomes the rate-limiting factor. Starting at this point unsaturated surface drying [36], otherwise known as *the first falling-rate period* [37], sets in (portion *C-D* on the graph). Evaporation continues at the pellet surface, but the equilibrium vapour pressure is no longer sustained uniformly at all pores connected to the surface. A simplified picture of this process, taken from [38], is shown in Figure 2.3.1.2. Water is being delivered to the surface through the small pores reaching the surface (pore *B* in the Figure). This is because these small pores have the lower liquid pressure (a higher capillary rise) (see eqn. 2.2.3.1). But water delivery to the surface through the small pores can proceed only by the larger pores (pore *A* in Figure 2.3.1.2) being drained. Drying at the surface continues as long as the capillarity-driven Darcy flow through the interconnected small (type *B*) pores is able to supply enough water to balance the heat supply across the boundary layer. The overall rate is limited simultaneously by both the boundary layer transport *and* the water supply.

According to Treybal [36], one of the distinctive features of the first falling-rate period is the appearance of dry patches as more and more large pores in the overall particle size distribution are being drained. Although this picture makes it easier to visualize the transitional nature of this drying period, the concept of dry patches may be misleading. While seeming reasonable at the micro scale of the individual pores, the existence and growth of *macro* dry patches leads to the conclusion that there should be the adjacent populations of large and small pores at the pellet surface. The latter conclusion seems unreasonable, given the

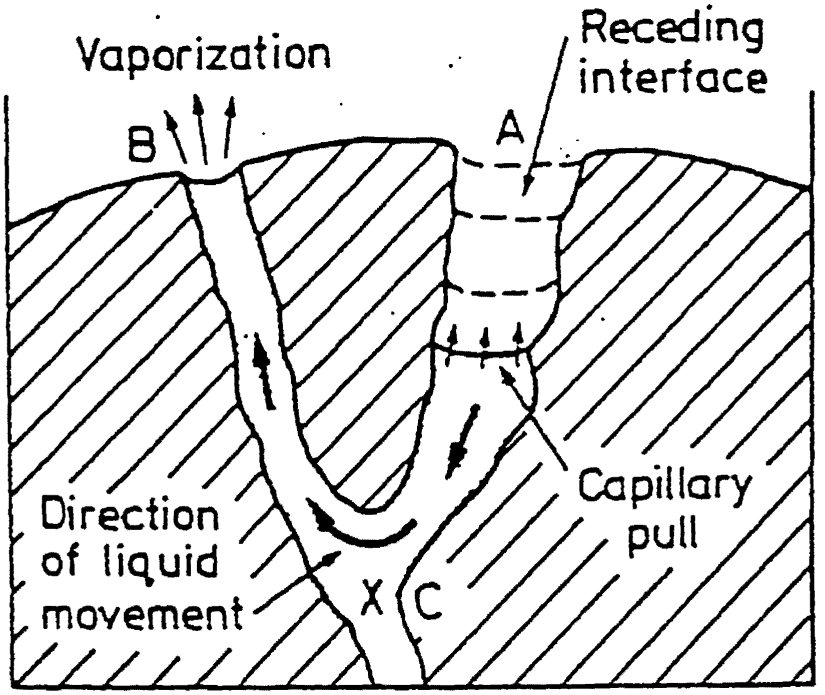


Figure 2.3.1.2 Simplified pore structure showing moisture migration for the mild drying conditions [38].

probability of the random pore size distribution in the pellets' microstructure (see Section 2.2.3).

At point *D* in Figure 2.3.1.1, where the heat supply exceeds the heat demand for evaporating the water transported to the surface, a change in mechanism occurs. Starting at this point *the second falling-rate period* sets in (portion *D-E* on the graph). During this period water evaporates in the interior. A wet/dry interface is set up which recedes from the surface to the internal regions of the porous body. The product vapour must now be transported through the dry porous shell to the pellet surface. This latter factor contributes to the control of the drying rate during the second falling rate period.

Point *D* also marks the transition between the surface- and shrinking core drying regimes as the wet/dry interface at this point moves entirely from the surface to the interior. Important here is that in 'conventional' or mild drying this occurs at the late stage, when the moisture content had dropped almost to the pendular level (saturation level ~20%), where the water phase becomes discontinuous.

In practice such a drying pattern prevails only under conditions of mild drying (~100°C) of relatively coarse granular materials (particle size >100 μm). The surface/shrinking-core transition, caused by the liquid phase discontinuity at low saturations, has been considered the dominant factor in most previous drying models [39, 40].

Another condition which could cause water delivery to the surface to be interrupted is when viscosity of the liquid phase increases during drying, e.g. when the liquid contains dissolved polymers. Then the capillarity-induced flow to the surface may not be rapid enough to consume the heat supplied to the surface [41, 1]. Research results to be described in

Sections 3.2 and 6.4 show that this condition may apply in the case of drying of iron ore pellets when they contain bentonite.

2.3.2. Intense Drying and the Vapour Lock

It is known in the literature [38, 42, 43] that if drying conditions become intense, typically at drying gas temperatures of 200^{0}C and above, significant deviations from the 'classical' drying rate pattern may occur. This phenomenon is illustrated in Figure 2.3.2.1 [42], which shows the drying rate vs. time curves of 14 mm-diameter iron ore pellets dried at 100^{0}C, 200^{0}C and 300^{0}C (curves *1*. *2* and *3* respectively). The most significant difference between curves *2* and *3*, as opposed to curve *1*,is the complete absence of the horizontal portion, i.e of the constant rate drying period, and the sharp minima.

Our search of the literature indicates that there is no quantitatively backed physical explanation in the open literature of why and how this phenomenon happens. The Zaharchuk model[1] [1], not yet published in the open literature, seems to be the first to offer an explanation.

Generally, the interruption of fluid flow due to gas phase nucleation within the liquid continuum is a recognized phenomenon [61, 62]. It occurs when the liquid pressure is less than the equilibrium vapour pressure for a given temperature:

---

[1] Zaharchuk drying model [1] will be discussed in Section 2.4.

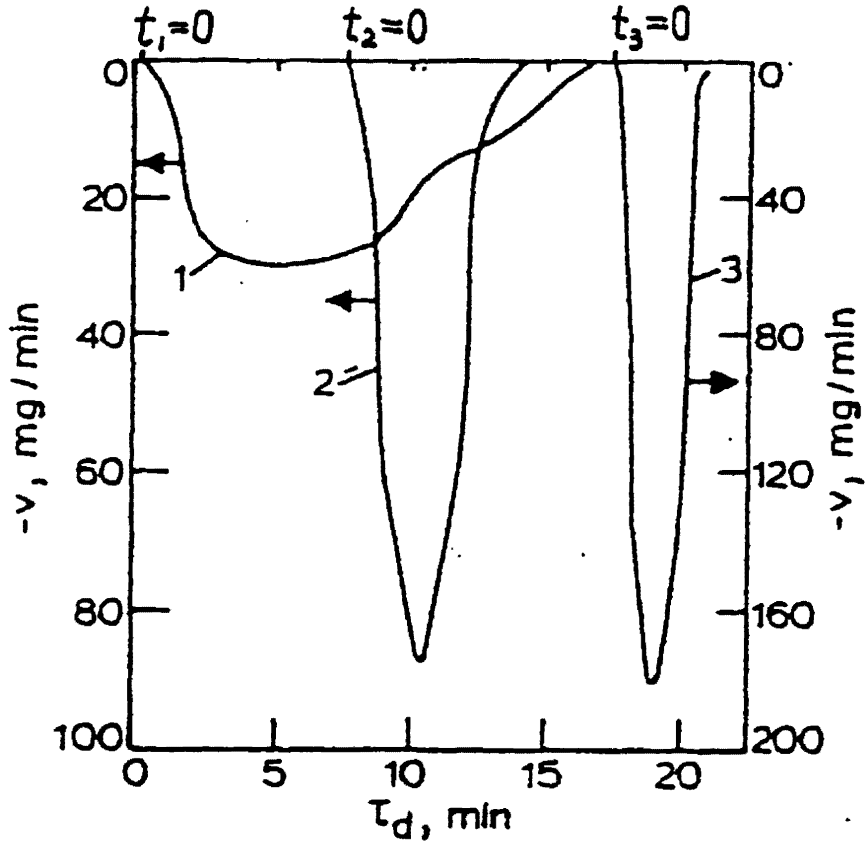


Figure 2.3.2.1 Experimental drying rate curves at temperatures: (1) - 100°C; (2) - 200°C; (3) - 300°C. [42].

$$p_l = p_v^o \qquad (2.3.2.1)$$

In the automotive industry this phenomenon is known to cause interruptions of fuel flow to an engine due to blockage of passages in the fuel system by fuel vapour and it is termed a *vapour lock* [62, 63]. Another term for this physical phenomenon, which is widely encountered with in hydraulic machines such as turbines, pumps, propellers etc., is *cavitation* [62].

The loss of capillarity due to the interruption of liquid flow to the surface was tentatively suggested by Oliver and Newitt [59] as an explanation for the early termination, or complete absence, of the constant rate drying period.

From the results of the Zaharchuk model calculations [1] and the author's corroborating experiments [2] it follows that the reason for the absence of the constant-rate drying period during rapid drying of fine agglomerated spheres is that the transition to the shrinking core drying regime shifts into what has hitherto been defined as the initiation period. This happens because the wet-bulb temperature, required for the constant-rate drying period, cannot be established at the surface.

The cause of the early interruption of the Darcy flow to the surface is the vapour lock or cavitation. It occurs when p_v^o, the equilibrium vapour pressure near the surface (see eqn. 2.3.2.1) becomes equal to or higher than the liquid pressure p_l, generated under the water menisci in the capillaries reaching the pellet surface. As a result, the gas phase nucleates under these menisci and the capillary effect becomes inoperative, causing the interruption of Darcy flow to the surface. When the driving force for liquid delivery to the surface disappears, the gas/water interface moves into pellet interior and the shrinking core drying regime sets in.

2.4. The Zaharchuk Drying Model

Extensive research has been conducted in our group concerning the drying behaviour of iron-ore pellets. It resulted in the development of a comprehensive mathematical drying model [1]. The feature of this model is that it describes the drying process rigorously in terms of the fundamental laws of heat, mass and momentum transfer. All property parameters are defined mathematically, and experimentally measured values are used. There are no adjustable parameters in the model.

The model algorithm is divided into two sections. The first section corresponds to drying on the surface, and the second -- to the shrinking core drying regime.

2.4.1. Surface Drying Regime

For the surface drying conditions the heat balance is described in the model by the transient heat conduction equation [1][1]:

$$\frac{\partial T}{\partial t} = \frac{\alpha_{wet}}{r^2}\left[\frac{\partial}{\partial r}\left(r^2 \frac{\partial T}{\partial r}\right)\right] - \left(\frac{\Delta H \cdot G}{\rho_{wet} C_{P_{wet}} V}\right)_{r=R_p} - \left(\frac{\rho_l C_{P_l}}{\rho_{wet} C_{P_{wet}}}\right)\frac{v_l \partial T}{\partial r} \qquad (2.4.1)$$

The first term of right hand side represents the Second Fourier law, while the second represents heat expenditure on water evaporation at the surface. The last term -- the expenditure on heating the water moving towards the surface.

One boundary condition, reflecting symmetry at the sphere centre, is :

---

[1] A derivation of the heat balance equation and a key aspect of its numerical solution are presented in Appendix A.

:

$$\left.\frac{dT}{dr}\right|_{r=0} = 0 \qquad (2.4.2)$$

The second boundary condition represents heat balance at the surface:

$$k_{eff_{wet}} \left.\frac{dT}{dr}\right|_{r=R_p} = h(T_\infty - T|_{r=R_p}) + \sigma_{SB}\varepsilon_R(T_\infty^4 - T^4|_{r=R_p}) - \left(\frac{\Delta H_v \cdot G}{4\pi R_p^2}\right) - \left(\frac{G \cdot C_{P_l}}{R_p}\right)\left.\frac{dT}{dr}\right|_{r=R_p} \qquad (2.4.3)$$

The heat conducted inward from the surface is equated to the four terms on the right hand side. The latter represent respectively heat delivery by convection and radiation minus heat consumed by water evaporation at the surface and minus that consumed by heating of the water travelling towards the surface.

Volume-averaged parameters [64] are used to characterize the pellet matrix. Thus:

$$\alpha_{wet} = \frac{k_{wet}}{C_{P_{wet}} \cdot \rho_{wet}} \qquad (2.4.4)$$

where

$$C_{P_{wet}} = (1-\varepsilon)C_{P_{solid}} + \varepsilon S C_{P_{H_2O}} \qquad (2.4.5)$$

For the surface drying conditions the model calculates the drying rate using the boundary-layer transfer equation [36]:

$$G_{BL} = \frac{h_m 4\pi R_p^2}{R_o T_f}(p_v^o - p_{v_\infty}) \qquad (2.4.6)$$

where T_f represents the boundary film temperature, taken as the average between surface and ambient gas temperature. The pressure terms in brackets represent the vapour pressure difference across the boundary layer. It is this pressure difference that controls the rate of surface drying. The equilibrium vapour pressure p^0_v is calculated in the model using the standard data [43]:

$$p^0_v = exp(60.448\text{-}6834.27/T\text{-}5.17\ lnT) \tag{2.4.7}$$

The heat and mass transfer coefficients, h and h_m are calculated in the model using the Ranz and Marshall correlations [65, 66]:

$$Nu(1+B) = \left(\frac{2hR_p}{k_f}\right) = 2.0 + 0.6 \cdot \mathrm{Re}^{0.5} \cdot \mathrm{Pr}^{0.333} \tag{2.4.8}$$

$$Sh = \left(\frac{2R_p h_m}{D_{AB}}\right) = 2.0 + 0.6 \cdot \mathrm{Re}^{0.5} \cdot Sc^{0.333} \tag{2.4.9}$$

where B is the dimensionless Spalding number used to adjust the heat transfer correlation [67]:

$$B = \frac{C_{psteam} \cdot (T_{r=R_p} - T_\infty)}{\Delta H} \tag{2.4.10}$$

The mass balance for the liquid water in the pellet is [39]:

$$\frac{\partial S}{\partial t} = \frac{k_p k_r}{\varepsilon \mu r^2} \frac{\partial}{\partial r}\left(r^2 \frac{\partial p_l}{\partial S} \frac{\partial S}{\partial r}\right) \tag{2.4.11}$$

where S represents fraction saturation and μ represents liquid viscosity. Boundary conditions are:

$$\left.\frac{\partial S}{\partial r}\right|_{r=0} = 0 \tag{2.4.12}$$

again reflecting symmetry at the centre. The initial condition is:

$$S(r)=1.0 \qquad 0 \le r \le R_p \tag{2.4.13}$$

The rate of water delivery to the surface by the capillarity-induced Darcy flow is [39]:

$$G_{DF} = 4\pi R_p^2 \frac{k_p k_r}{\mu} \left.\frac{\partial p_l}{\partial r}\right|_{r=R_p} \tag{2.4.14}$$

Matrix permeability k_p is given by the first term of the Ergun equation [15]:

$$k_p = \frac{d_p^2 \varepsilon^3}{150(1-\varepsilon)^2} \tag{2.4.15}$$

where d_p is the "characteristic" particle size.

Relative permeability k_r is given by [39]:

$$k_r = \left(\frac{S - S_p}{1 - S_p}\right)^3 \tag{2.4.16}$$

where S is the degree of saturation and S_p -- that in the pendular state.

The critical variable in equation (2.4.14) is p_l, the liquid pressure. The latter is set by the capillary effect. It is defined by the Young-Laplace equation:

$$p_T - p_l = \frac{2\gamma_{lv}}{r_c} \tag{2.4.17}$$

This is the same formulation as equation 2.2.3.1, except that here it is assumed that $\theta = 0^0$, so the term $cos\theta$ disappears. The assumption is consistent with experiment: the contact angle between water and the solids studied presently is indeed zero.

In turn, the value of r_c in equation 2.4.17 is given by [44]:

$$r_c = \sqrt{\frac{8k_p}{\varepsilon}} \tag{2.4.18}$$

The critical dependence of p_l, therefore, is on the capillary radius of the characteristic pores in the porous agglomerate of particles, forming the pellet microstructure. In the model this is calculated by the following equation:

$$p_T - p_l = B_1(1 - e^{B_2(1-S)}) + B_3(1-S)^{B_4} + \frac{B_5(1-S)}{(S-(S_p-0.015))^{B_6}} \quad S_p \le S \le 1.0 \tag{2.4.19}$$

Zaharchuk constructed this equation on the basis of the suction potential versus degree of saturation curves, extending ideas of Chen and Whitaker [39]. The values for the parameters B are selected empirically to fit suction potential versus degree of saturation curves for porous

media of interest to us. The parameter B_l in equation (2.4.19) is defined by the Young-Laplace equation (eqn. 2.4.17). Critical here is the inverse dependance of p_l of the capillary radius r_c.

The critical condition limiting capillarity-driven transport is $p_l = p_v^0$. The moment this condition is reached, it is assumed that the supply of water to the surface is interrupted and thus at that instant the drying front recedes into the pellet interior. Model calculations applicable to the shrinking core drying period are set in action at that instant (see the following Section). The original Zaharchuk model ignores the existence of any gradual surface/shrinking-core transition period. Extension to the model to overcome this model limitation was a part of this project. It is presented in Chapter 3 of this thesis.

2.4.2. Shrinking Core Drying Regime

During this period, water evaporates at a receding interface between wet core and dry shell. Heat conducted through the shell is spent on heating up both the dry and the wet regions of the pellet, on evaporating the water at the receding interface and, finally, on heating up the vapour while it escapes through the dry porous shell.

Existence of wet and dry regions during shrinking core drying requires simultaneous solving of two heat balance equations:

- for the dry shell region:

$$\frac{\partial T}{\partial t} = \frac{\alpha_{dry}}{r^2}\left[\frac{\partial}{\partial r}\left(r^2\frac{\partial T}{\partial r}\right)\right] - \left(\frac{\Delta H_v \cdot G}{\rho_{dry} \cdot C_{pdry} \cdot V}\right)\Big|_{r=\Pi} - \left(\frac{G \cdot C_{P_{steam}}}{r^2 \rho_{dry} C_{P_{dry}}}\right)\frac{\partial T}{\partial r} \qquad (2.4.20)$$

where $\Pi(t)$ represents radius of interface, and the last two terms on the right hand side represent heat losses due to evaporation and heating of the escaping vapour, respectively,

- for the wet core region:

$$\frac{\partial T}{\partial t} = \frac{\alpha_{wet}}{r^2}\left[\frac{\partial}{\partial r}\left(r^2\frac{\partial T}{\partial r}\right)\right] - \left(\frac{\rho_l \cdot C_{P_l}}{\rho_{wet} C_{P_{wet}}}\right)\frac{v_l \partial T}{\partial r} \qquad (2.4.21)$$

Boundary conditions for this problem are:

- at the surface:

$$k_{eff_{dry}} \left.\frac{dT}{dr}\right|_{r=R_p} = h(T_\infty - T_{r=R_p}) + \sigma_{SB}\varepsilon_R(T^4{}_\infty - T^4{}_{r=R_p}) - \left(\frac{G \cdot C_{P_{steam}}}{r}\right)\left.\frac{\partial T}{\partial r}\right|_{r=R_p} \quad (2.4.22)$$

-at the interface:

$$k_{effdry}\left.\frac{dT}{dr}\right|_{\Pi^+} - k_{effwet}\left.\frac{dT}{dr}\right|_{\Pi^-} = \frac{G \cdot \Delta H_v}{4\pi\Pi^2} - \left(\frac{G \cdot C_{P_l}}{\Pi}\right)\left.\frac{dT}{dr}\right|_{\Pi^-} \quad (2.4.23)$$

- at the centre:

$$\left.\frac{dT}{dr}\right|_{r=0} = 0 \quad (2.4.24)$$

In the solution of the heat balances the thermal conductivities $k_{eff\ dry}$ and $k_{eff\ wet}$ are required. To obtain their numerical values, the correlations of Krupiczka [68] were used in a modified form [69] to accommodate both Knudsen and mixed gas effects in the pores.

The thermal conductivity for the pellet matrix was calculated by [68]:

$$k^o_{eff} = k_{fluid}\left(\frac{k_s}{k_{fluid}}\right)^{0.280-0.757\log\varepsilon-0.057\log\left(\frac{k_s}{k_{fluid}}\right)} \quad (2.4.25)$$

where k_s represents the conductivity of the native solid and k_{fluid} represents the conductivity of water in the wet core or the gas mixture in the dry shell. In the model, correlations from data in

standard handbooks [70, 71] were used to calculate the thermal conductivities of air, liquid water and steam.

Knudsen effects were included in the model by calculating an equivalent gas conductivity when gas motion is Knudsen-dominated [69]:

$$k_K = \frac{25}{12} D_K \frac{P_g}{R} C_v \tag{2.4.26}$$

for monoatomic gases and

$$k_K = \frac{25}{12} D_K \frac{P_g}{R}\left(\frac{2}{5} C_v + 0.9R\right) \tag{2.4.27}$$

for polyatomic gases.

The model uses eqn. 2.4.27 to calculate the Knudsen diffusion coefficient for both air and water vapour. The conductivity of a multi-component gas is given by [72]:

$$k_{mix} = \sum_{i=1}^{n} \frac{y_i k_i (MW_i)^{1/3}}{y_i (MW_i)^{1/3}} \tag{2.4.28}$$

Once this is known, it is combined with the Knudsen conductivity of each gaseous species to give an overall gas conductivity:

$$\frac{1}{k_{gas}} = \frac{1}{k_{mix}} + \left[\sum_{i=1}^{n} k_{K_i}\right]^{-1} \tag{2.4.29}$$

The model also accounts for the fact that during drying the gas is not stagnant (as in Krupiczka's formalism), but is moving against the direction of heat flow [73]. The equation is:

$$k_{flow} = 0.5\,\mathrm{Re}\cdot\mathrm{Pr} \tag{2.4.30}$$

Finally, the radiation effect is included into the model by [73]:

$$k_{rad} = k_{gas}\,0.707\,Nu_r^{\,0.96}\left(\frac{k_{gas}}{k_s}\right) \tag{2.4.31}$$

The radiative Nussult number is given by [73]:

$$Nu_r = \frac{h_r d_p}{k_s} \tag{2.4.32}$$

where radiative heat transfer coefficient is calculated by:

$$h_r = \frac{0.2268}{\left(\frac{2}{\varepsilon_R - 1}\right)}\left(\frac{T}{100}\right)^3 \tag{2.4.33}$$

Adding all factors gives:

$$k_{eff} = k_{eff}^0 + k_{flow} + k_{rad} \tag{2.4.34}$$

Water evaporation rate at the interface is defined by the vapour pressure there, which is

equal to the equilibrium vapour pressure at specific temperature of the interface. At the same time, this pressure is the driving force for vapour diffusion through the dry shell. Equations from Hadley [74] were used in the model to describe both total and partial vapour pressure gradients across the dry porous region:

$$\frac{dP_T}{dr} = -\frac{J}{\left(\frac{D_{K-eff_{H_2O}}}{R_m T} + \frac{k_p}{\mu}\left(\rho_v^o + \frac{D_{K-eff_{H_2O}}}{D_{K-eff_{air}}}\rho_a^o\right)\right)} \tag{2.4.35}$$

and

$$\frac{dP_v}{dr} = -J\left(\frac{R_m T}{D_{K-eff_{H_2O}}} + \frac{R_m \rho_a^o T}{\rho^o D_{K-eff_{H_2O}}}\right) - \frac{R_m T k_p \rho_v^o}{D_{K-eff_{H_2O}}\mu}\frac{dP_T}{dr} \tag{2.4.36}$$

where J represents the molar flux of water vapour. These two equations incorporate all Knudsen, molecular diffusion and Darcy flow effects. The effective vapour diffusivity is given by [75]:

$$D_{eff} = \frac{D_{H_2O-air}\,\varepsilon}{\tau} \tag{2.4.37}$$

The molecular diffusion coefficient, $D_{H2O-air}$, is given by an equation taken from [76]:

$$D_{H_2O-air} = 1.2 \cdot 10^{-9} \cdot T^{1.75} \tag{2.4.38}$$

The Knudsen diffusion coefficient is given by [77]:

$$D_K = \frac{2}{3} r_c \left(\frac{8 R_m \cdot 10^{-3} T}{\pi M W} \right)^{0.5} \tag{2.4.39}$$

where r_c is calculated according to equation (2.4.18).

The model starts calculations for the shrinking core drying regime when

$$\Pi(t) = 0.9995 \cdot R_p \tag{2.4.40}$$

is satisfied, and continues until the receding interface reaches the location of 0.1 R_p.

2.4.3. Calculation of Matrix Stresses

The model [1] includes calculations of the effective stresses that are generated in the pellet throughout the drying process. These include thermal stresses that result from temperature gradients arising during the shrinking-core drying period and the internal pressure stresses induced by the steam formation.

The total maximum stresses arising at the wet/dry interface during drying are then compared to the values of dry strength, also calculated by the model (see Section 2.5.1). In the process, the pellet susceptibility to spalling is determined.

2.4.3.1. Thermal Stresses

Model calculations show [1] that during the shrinking core drying period the wet core is

essentially at a uniform temperature . There are, therefore, no thermal stresses therein. The dry shell, on the other hand, is subject to high temperature gradients and, consequently, will expand on the pellet surface differently than at the interface. Continuum considerations suggest that circumferential stresses will be compressive at the surface and will change linearly with pellet radius to become highly tensile at the interface. The radial stresses will be tensile throughout the shell as there are no obstacles for radial expansion of the shell.

The model uses equations from Burgreen [29] for radial temperature gradients, to calculate circumferential (σ_C) and radial (σ_R) stresses within the dry shell:

$$\sigma_{Cs}^{T} = \frac{2E_s\alpha_s}{1-\nu_s}\left(\frac{r^3-\Pi^3}{r^3\left(R_p^3-\Pi^3\right)}\int_{\Pi}^{R_p}\Delta T(r)r^2dr - \int_{\Pi}^{r}\Delta T(r)r^2dr\right) \qquad (2.4.41)$$

$$\sigma_{Rs}^{T} = \frac{2E_s\alpha_s}{1-\nu_s}\left(\frac{2r^3+\Pi^3}{r^3\left(R_p^3-\Pi^3\right)}\int_{\Pi}^{R_p}\Delta T(r)r^2dr + \int_{\Pi}^{R_p}\Delta T(r)r^2dr - \Delta T(r)\right) \qquad (2.4.42)$$

The modulus of elasticity E is calculated in the model as a function of bentonite content, based on the experimental data gathered in the diametral compression study [52]:

$$E = 29.663\cdot 10^6 + 68.8446\cdot B \qquad (2.4.43)$$

The model treats the wet core and the dry shell regions of the pellet as two separate systems. To account for the continuity of the pellet the concept of interference pressure p^i is introduced. The latter enables calculation of the impact of dry-shell expansion on the deformation of the wet core and vice versa. The interference pressure around the wet core is distributed uniformly, acting in a manner similar to a hydrostatic stress and pulling the core towards the shell. Within the dry shell the interference pressure acts in the opposite direction, i.e. pulling it towards the wet core. Interference pressure is distributed throughout the shell according to:

$$\sigma_{Rs}^{T} = -\frac{\Pi^3 p^i}{R_p^3 - \Pi^3}\left(1 - \frac{R_p^3}{r^3}\right) \tag{2.4.44}$$

and

$$\sigma_{Cs}^{T} = -\frac{\Pi^3 p^i}{R_p^3 - \Pi^3}\left(1 - \frac{R_p^3}{2r^3}\right) \tag{2.4.45}$$

The total stress level caused by thermal effects is calculated in the model by adding the stresses within the wet core and dry shell (as if they were two separate bodies) to the respective interference pressures, accounting for interaction of two regions.

It should be mentioned here that all the relations used in the model have originally been derived for homogeneous elastic solids. To make them relevant to porous agglomerates (where particulates will partially expand into the pore space) the volume average approach suggested by Touloukian et al. [26] was used in the model:

$$\alpha_{ts} = (1-\varepsilon)\alpha_t \tag{2.4.46}$$

where α_t represents the thermal expansion coefficient for solid magnetite. This formalism was designed originally for loose granular packings where thermal expansion was negligible. Since iron ore agglomerates are rather on the dense side of the 'porosity spectrum', this approximation will possibly overpredict thermal stresses.

2.4.3.2. Pressure Stresses

The 'thermal analogy' proposed by Lubinski [58] to calculate internal vapour pressures within a porous agglomerate is used in the model. It considers the analogy between thermal and pressure expansion effects on the behaviour of a packing. Temperature gradients, which are the reason for uneven thermal expansion of the body have the same impact on its deformation as pressure gradients. The usefulness of this analogy is that the same assumptions and formalisms used for thermal stresses can be applied for vapour pressures. The effective pressure stresses in the dry shell (which is of prime interest because of the higher stress level) are stated below:

$$\sigma_{Cs}^{P} = (1-\beta)\frac{2(1-2\nu_s)}{1-\nu_s}\left(\frac{r^3-\Pi^3}{r^3(R_p^3-\Pi^3)}\int_{\Pi}^{R_p} P\cdot r^2 dr - \frac{1}{r^3}\int_{\Pi}^{r} P\cdot r^2 dr\right) + P \tag{2.4.47}$$

$$\sigma_{Rs}^{P} = (1-\beta)\frac{2(1-2\nu_s)}{1-\nu_s}\left(\frac{2r^3+\Pi^3}{r^3(R_p^3-\Pi^3)}\int_{\Pi}^{R_p} P\cdot r^2 dr + \frac{1}{r^3}\int_{\Pi}^{r} P\cdot r^2 dr - P\right) + P \tag{2.4.48}$$

where β represents the ratio of the compressibility of the porous material over the compressibility of native material and is defined as follows:

$$\beta = \frac{E_s / (1 - 2\nu_s)}{E_o / (1 - 2\nu_o)} \tag{2.4.49}$$

where subscript *o* refers to magnetite. Interference pressures are distributed throughout the wet core and dry shell in the same manner as they are for thermal stresses.

2.4.4. Sample Results of Zaharchuk Model

In this Section selected results of the Zaharchuk model [1] are reproduced. Two groups of modelling results are included, both for a 'model pellet'-- those predicting the drying behaviour and those calculating the matrix-stress buildup during drying.

Figures 2.4.4.1. to 2.4.4.3 [1] present the Zaharchuk model results for what will henceforth be referred to as 'typical pellet' properties and drying conditions. These parameters have been used by Zaharchuk [1] in many model calculations. Their values correspond to typical pellet properties and drying conditions in the shaft furnaces at the Griffith-Mine plants, Red Lake, Ontario. Even though this mine is no longer functioning, much of the work done in this and previous studies by our group have used the Griffith concentrate. The values of the pellet parameters and drying conditions used in the model simulations have been fully justified in Zaharchuk's PhD Thesis [1]. They are itemized in Table 2.4.4.1.

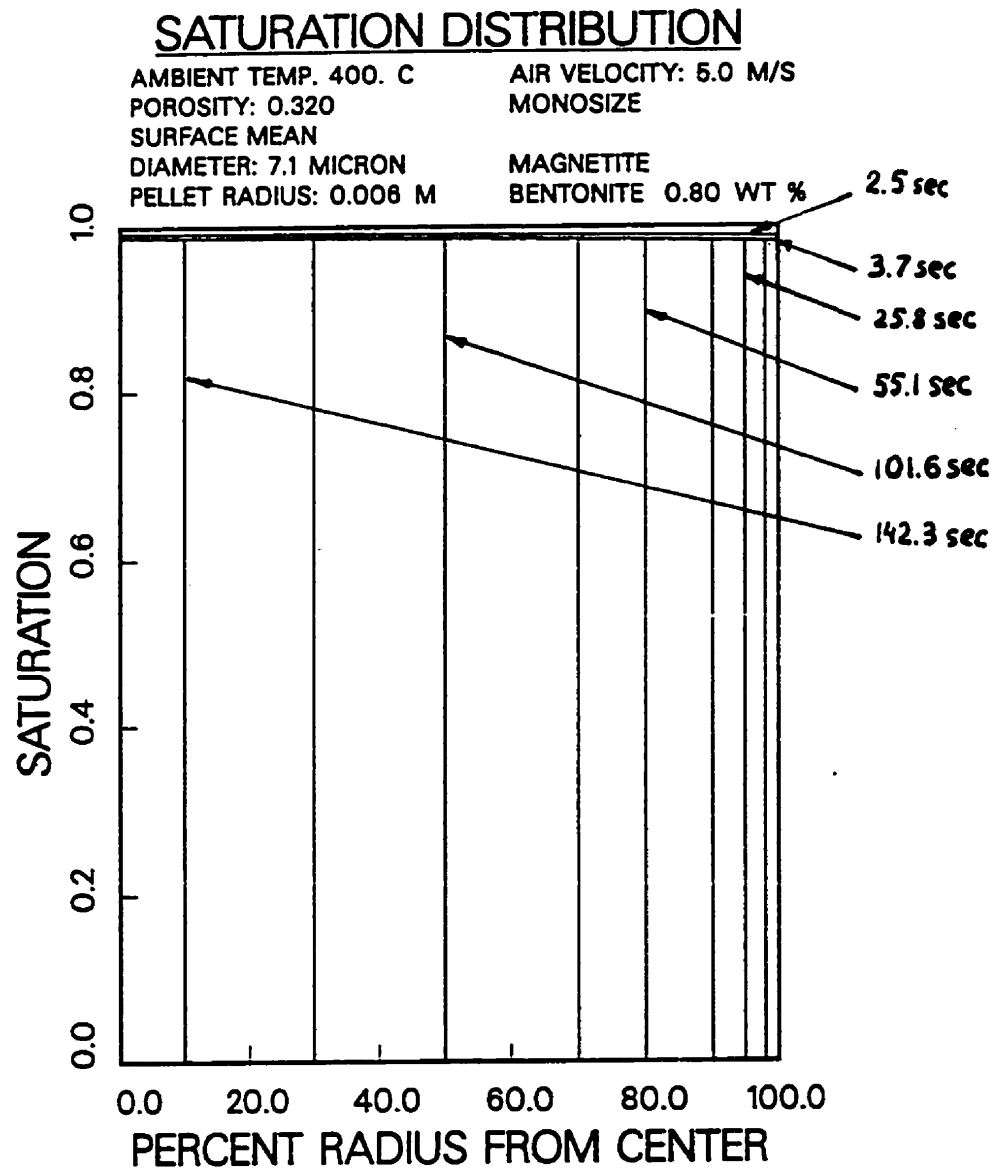


Figure 2.44.1. Saturation Profile for Typical Pellet and Conditions [17].

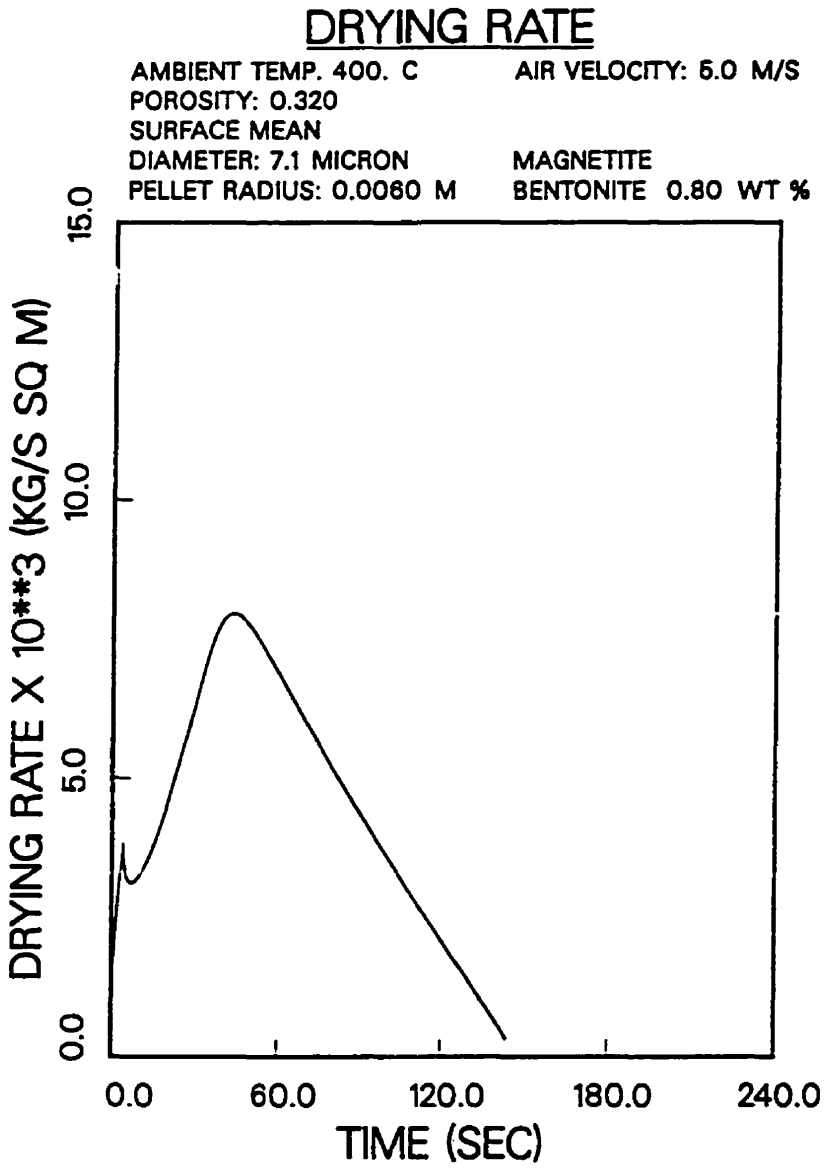


Figure 2.4.2 Drying Rate: Typical Pellet Drying Rate versus Time [1].

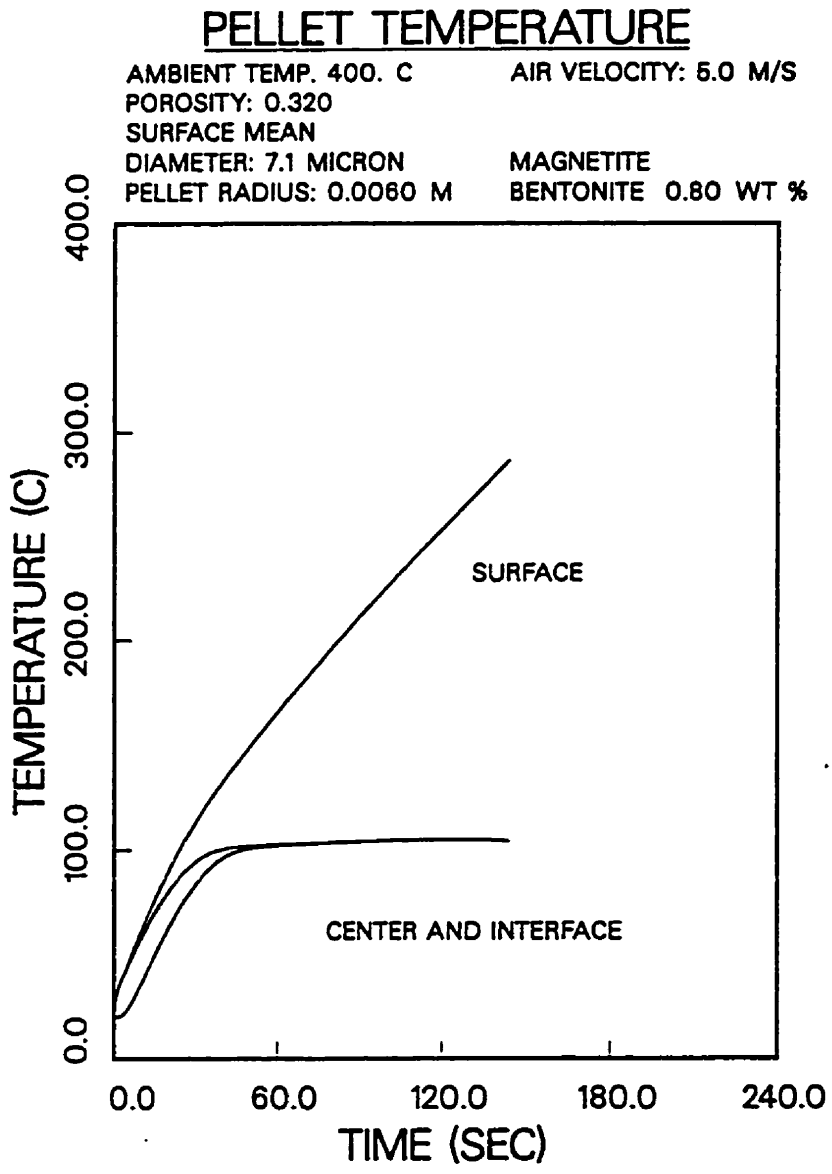


Figure 2.13 Surface, Center, and Interface Temperature for Typical Pellet and Drying Conditions [1].

Table 2.4.4.1. "Typical" Pellet Parameters and Drying Conditions [1]

Pellet Radius	R_p	0.006 m
Porosity	ε	0.32
Particle Diameter	d_p	7.1 μm
Magnetite Conductivity	k_s	7.0 W/mK
Critical Saturation	S_c	0.20
Tortuosity	τ	3.9
Emissivity	ε_R	0.85
Magnetite Density	ρ_S	4910.3 kg/m^3
Parameters B_n in eqn. 2.3.19		
	$-B_2$	40.000
	$-B_3$	11 000 Pa
	$-B_4$	1.001
	$-B_5$	150 Pa
	$-B_6$	1.150
Initial Pellet Temperature	T_i	25.0^{0}C
Drying Temperature	T	400^{0}C
Drying Gas Velocity	T_∞	5.0 m/s

Figure 2.4.4.1. represents a series of model curves of saturation distribution within the pellet calculated at different times during the surface- and shrinking core drying periods. During the first 3.7 sec of the drying process water evaporates on the surface and the saturation distribution is uniform over the pellet radius. The surface drying regime, however, is interrupted early in the drying process (saturation ~98% in the Figure), and the shrinking-core drying period sets in. Starting at this point (t=3.7 sec) drying proceeds at a sharp receding interface (vertical lines in the Figure), while saturation distribution of the wet core remains uniform.

Figure 2.4.4.2 is a model drying rate curve plotted versus time. There is an initialization period where the drying rate increases to a sharp local maximum. This period lasts approximately ten seconds. But, unlike in the 'classic' drying rate curve (see Section 2.3.1), the constant-rate period is not established. Instead, the shrinking core drying regime sets in early in the drying

process (see also Figure 2.4.4.1). The drying-rate curve is seen to continue rising following the onset of the shrinking-core regime, i.e. beyond the local maximum. The reason is as follows: the drying rate is at this time controlled by mass transfer across the boundary layer. At the same time the rate of heat transfer across this boundary layer is greater than the rate of consumption by the vapourization of water at the surface (the latter amount being limited by mass transfer). As a result, the pellet temperature, and thus the water-vapour pressure continues to rise. Since the latter controls the transport of water through the boundary layer, the rate continues to rise.

Figure 2.4.4.3 depicts the temperatures at the pellet surface, interface and centre plotted against time. As noted above, the model predicts a rising surface temperature during the entire drying process. The interior temperatures, however, are different. When the shrinking core period sets in (see point of separation between surface- and interface temperature curves in Figure 2.4.4.3, which, in time, corresponds to the sharp local maximum in Figure 2.4.4.2) the surface temperature is approximately 42^{0}C. The pellet centre temperature is ~21^{0}C. As the shrinking core period continues the pellet centre and interface temperature both increase until they reach 100^{0}C. When the wet core has reached this temperature, which is 55 seconds into the drying, it stays at or close to 100^{0}C.

Thus, the drying-characteristics curves, calculated by the Zaharchuk model, follow a pattern that can be explained physically. Further model simulations, aimed at explaining and justifying the drying patterns predicted by the Zaharchuk model, were carried out in this project. They are reported in Section 3.1.

Figure 2.4.4.4 depicts a series of model predictions of both thermal and pressure stress

distributions in both circumferential and radial directions. The individual curves correspond to the same times as in Figure 2.4.4.1. First, it is to be noted that pressure stresses are at least one order of magnitude smaller than the thermal stresses. They, can, therefore, be considered a minor contributor to the overall stress level. Nevertheless, they are not disregarded in the subsequent calculations but are added to the thermal stresses. The resulting total stress distributions in the circumferential and radial directions, as predicted by the model, are shown in Figure 2.4.4.5.

The graphs in both Figures show that stresses are the highest in the vicinity of the wet/dry interface. Also, circumferential stresses (Figure 2.4.4.5 (a)) are about an order of magnitude higher than the respective radial ones (Figure 2.4.4.5 (b)). The maximum total stresses that arise at the wet/dry interface in circumferential direction are summarized graphically in Figure 2.4.4.6 by plotting the tips of the curves in Figure 2.4.4.5 (a). Also plotted on the same graph is the total radial stress level at the interface, obtained similarly from Figure 2.4.4.5 (b).

2.5. Mechanical Properties of Iron-Ore Agglomerates

2.5.1. Agglomerate Strength

The two important issues addressed in this Section are: firstly, how is an agglomerate strength measured experimentally, and, secondly, how are the interparticle bonds resolved into an agglomerate strength.

The overall strength of an agglomerate is dependent on the bond strength between particles. The generally accepted treatment of agglomerate strength is that of Rumpf [97]. For an agglomerate of particles which are held together by an average bond force F, given a particle diameter d_p, porosity ε, coordination number k^0, the agglomerate strength is given by:

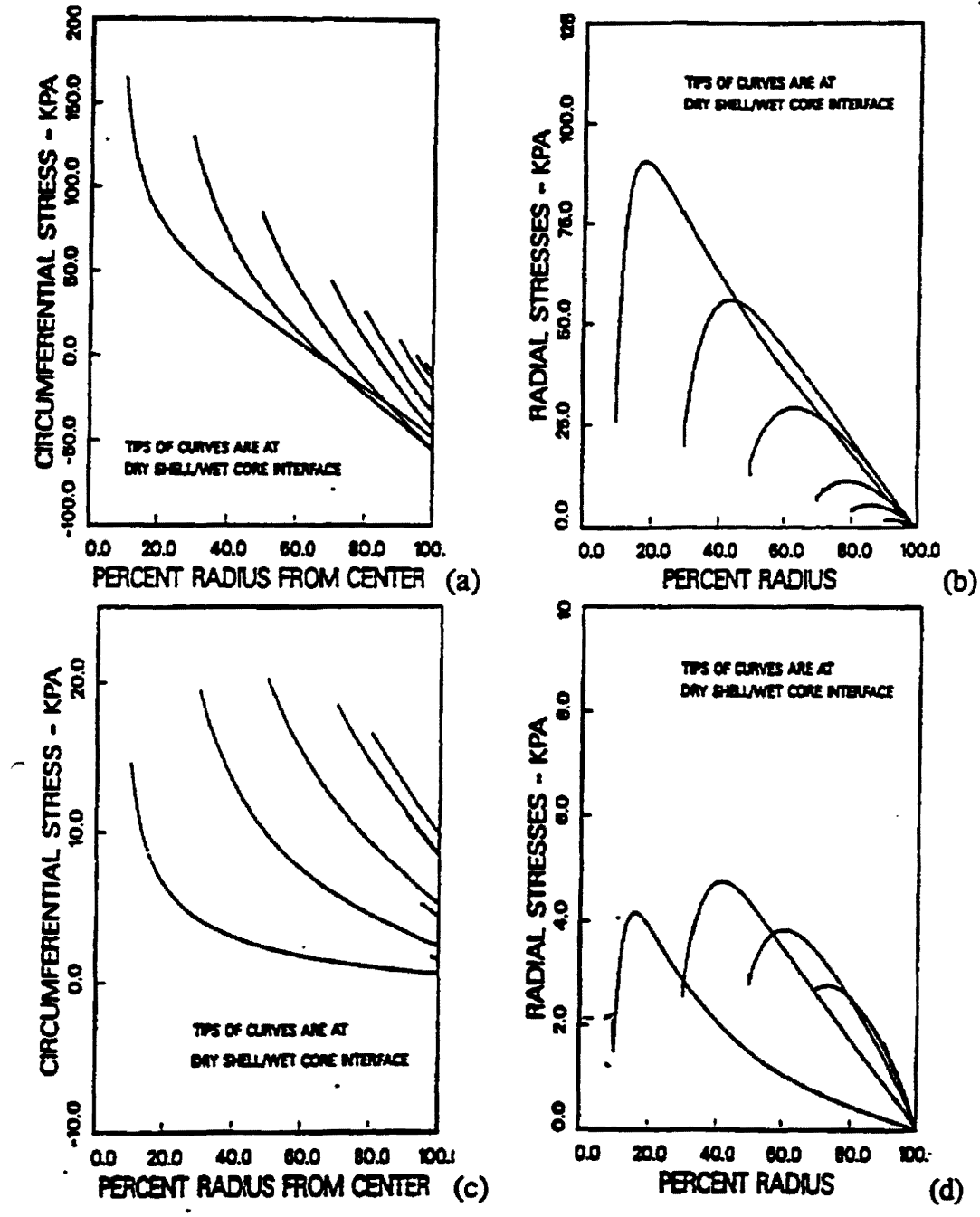


Figure 2.4.4.4. Stress Distribution within Pellet: (a) Thermal Circumferential; (b) Thermal Radial; (c) Pressure circumferential; (d) Pressure Radial.[1].

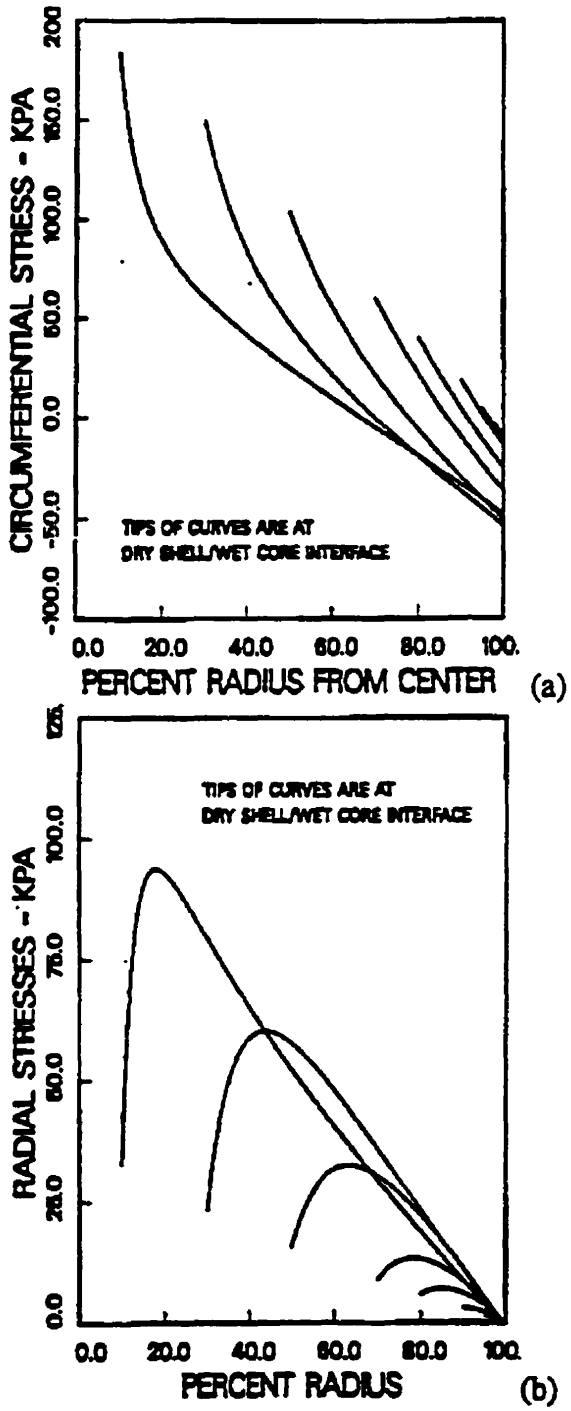


Figure 2.4.4.5.. Total Stress Distribution within Pellet: (a) Circumferential Stresses; (b) Radial Stresses [1].

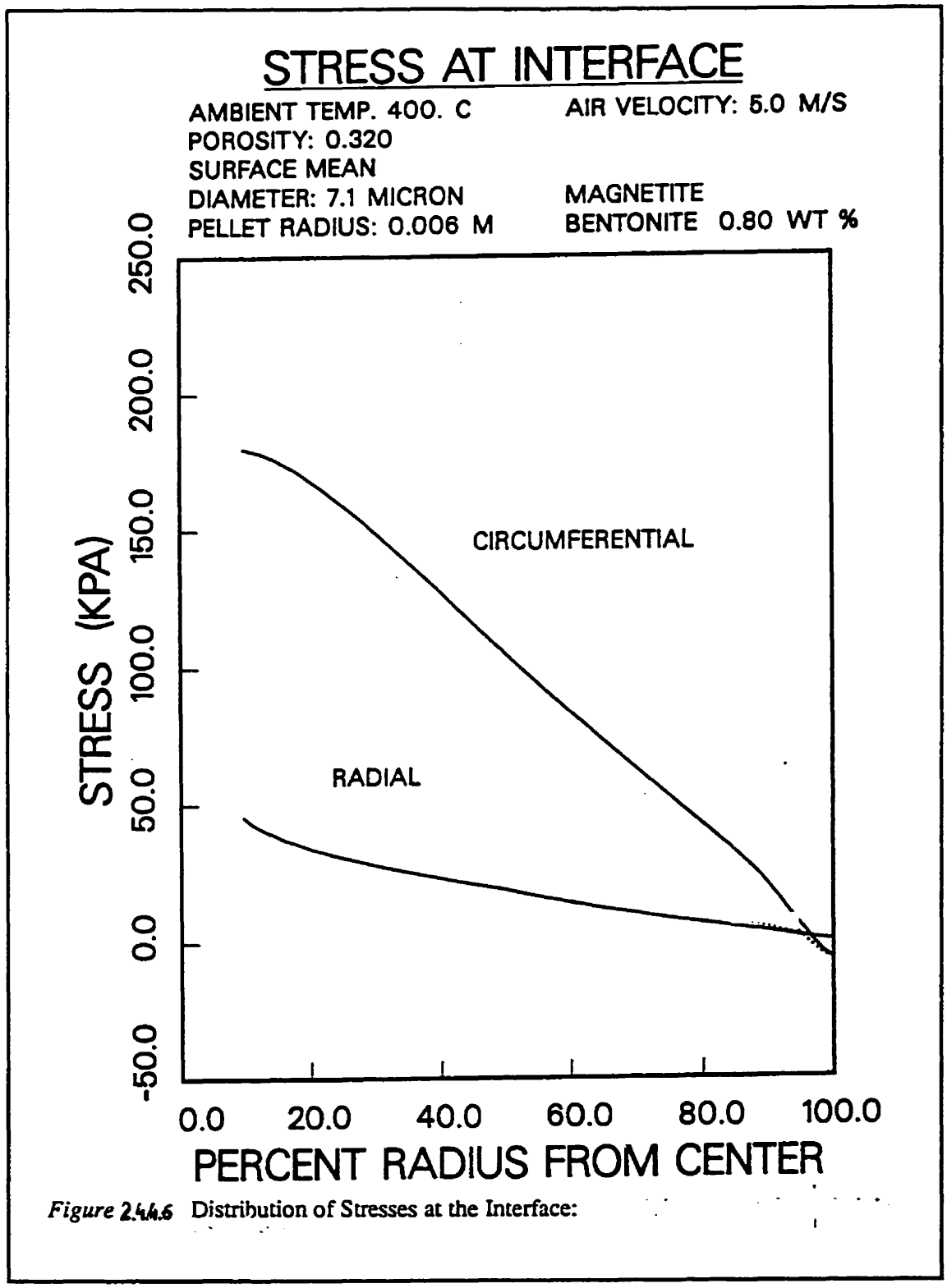


Figure 2.4.6 Distribution of Stresses at the Interface:

$$\sigma_T = \left[\frac{(1-\varepsilon)}{\pi d_p^2}\right] k^0 \cdot F \qquad (2.5.1.1)$$

In a dry agglomerate, where van der Waals forces dominate the bond strength, the bond force between two equal-sized spheres is given by equation (2.1.1) (see Section 2.1). Based on the experimental evidence Rumpf used the substitution $\pi / k^0 = \varepsilon$ in equation (2.5.1.1) to get:

$$\sigma_T = \left[\frac{(1-\varepsilon)}{\varepsilon}\right] \frac{F}{d_p^2} \qquad (2.5.1.2)$$

Other correlations between porosity and coordination number have been proposed [98] but the relationship by Rumpf remains the most commonly cited [9, 48, 51, 72, 88, 98].

Newitt and Conway-Jones [99] introduced the concept of a strength factor for spheres. They defined it as the ratio:

$$k = \frac{L}{D^2} \qquad (2.5.1.3)$$

where L represents the failure load and D is the sphere diameter. Haines [100] was the first to postulate that the origin of the tensile strength of a capillary state agglomerate is in the multitude of capillaries at the surface which cause a low liquid pressure p_l. It is equal to the entry suction:

$$\sigma_T = P_e \qquad (2.5.1.4)$$

where P_e is the entry suction of an agglomerate. Using this equality, Newitt and Conway-Jones argued that k should be directly proportional to the true tensile failure stress. They found experimentally that for wet, capillary-state, spherical pellets made from mono-sized silica sand

$$k = \frac{L}{D^2} = K \cdot P_e \qquad (2.5.1.5)$$

. The experimental proportionality constant K was found [99] to have a value of 0.7 for silica sands.

By combining eqns. 2.5.1.4 and 2.5.1.5 we get a relationship between the strength factor and the tensile strength of the capillary-state agglomerate:

$$L / D^2 = K \sigma_T \qquad (2.5.1.6)$$

A standard practice has been to measure agglomerate dry strength [51, 97, 101] by measuring the strength factor. The value of the proportionality constant was measured by different authors [51, 97, 102]. The value most relevant to our study was determined for Griffith iron-ore agglomerates [51] to be equal to 1.28.

The Zaharchuk model, presented in Chapter 2.4, includes calculation of the pellet dry strength. Model calculation is based on equation 2.5.1.2 taken from Rumpf [97]. In it the number-length mean particle diameter $d_{p\text{-}NL}$ is used as the characteristic particle size.

Calculation of a value of interparticle bond force in the eqn. 2.5.1.2 uses a correlating

equation obtained by a non-linear regression on the experimental points. It is based on the experimental data, obtained previously in our group for Griffith iron-ore agglomerates and reported in [51]. It includes the effect of the bentonite concentration B on the bond force F:

$$F = 0.141123 \cdot 10^{-6} + 0.101195 \cdot 10^{-5} \cdot B^{1.62951} \qquad (2.5.1.7)$$

The resulting tensile strength of a dry Griffith agglomerate is calculated in the Zaharchuk model by:

$$\sigma_T = \left(\frac{1-\varepsilon}{\varepsilon}\right)\left[\frac{0.141123 \cdot 10^{-6} + 0.101195 \cdot 10^{-5} \cdot B^{1.62951}}{d_{p-NL}^2}\right] \qquad (2.5.1.8)$$

2.5.2. Resistance to Spalling during Drying

When dried under intense drying conditions iron-ore agglomerates form concentric cracks. When drying conditions are excessively intense, the pellets disintegrate in a characteristic manner into shell-like fragments. The industrial term for such a disintegration is "spalling" [93, 94, 103]. The problem has been recognized in the early paper on iron-ore pelletization by Tigershiold and Ilmoni [103]. They observed that pellet spalling was dependent on the size of the particulate, matrix characteristics (microstructure), and drying temperature. Their results using two concentrates are reproduced in Table 2.5.2.1. Drying experiments were done on pellets produced by two methods of pelletization: one was the 'usual' batch balling. In the other, dry concentrate and then water were added in an alternating fashion throughout the pelletizing operation. Pellets were dried by placing twenty of them in a furnace (hydrodynamic flow conditions were not reported).

Table 2.5.2.1. Experimental Results of Tigerschiold and Ilmoni [103]

Concentrate	**1** (90% minus 325 mesh taconite)		**2** (54% minus 325 mesh 'crude')	
Pelletizing Mode	**Regular**	**Alternate**	**Regular**	**Alternate**
Blaine [cm^2/g]	990	990	3370	3370
Particle Size - % minus 250 mesh	19.7	19.7	85.2	85.2
Green Pellets: - Average Pore Size [μm] - % water -Crushing Strength [kg]	1.48 5.55 1.68	1.32 6.45 1.86	0.44 7.6 3.44	0.36 6.1 5.9
Dry Pellet Strength [kg] *Drying Conditions*: - 20°C, then to 100°C - 100°C, 8 hrs. - 200°C, 2 hrs. - 300°C, 2 hrs.	 0.38 0.34 0.28 2.55	 0.76 0.73 1.15 6.00	 1.58 1.62 5.35 All cracked	 2.03 2.65 7.35 All cracked

As noted in Table 2.5.2.1, pellets produced from the finer concentrate, *concentrate 2*, had the smaller pore size and higher strength. The dry strength of the pellets increased substantially with drying temperature, especially in pellets dried at 300°C. There was no explanation why this occurred. Experimental results, obtained by the author as a part of the present study and reported in Sections 6.2 and 6.3, are consistent with the observed phenomenon. In the present thesis, higher dry strength of intensively-dried pellets is interpreted in terms of microstructural evolution during drying (see Section 3.3).

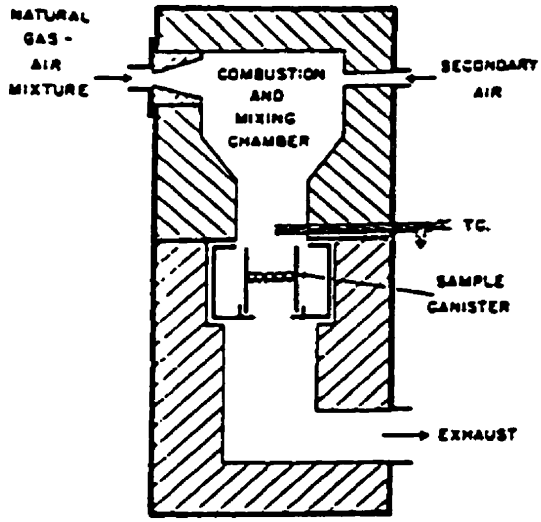
A more systematic study of pellet spalling was done by Schultz, Lex and Zetterstrom [93].

In the drying operation, a single layer of pellets on a screen was exposed to hot furnace gases (see Fig. 2.5.2.1(a)). The concept of *decrepitation resistance* was introduced to serve as a measure of the pellets' resistance to spalling under intense drying conditions. It was defined as the temperature at which 50% of the pellets in an assembly suffered spalling.

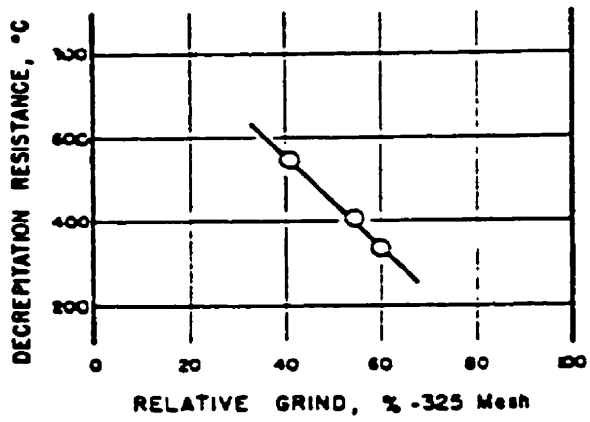
Decrepitation resistance for different particle size, bentonite and starch additions were determined. They are shown in Figure 2.5.2.1 b), c), and d) respectively. Figure 2.5.2.1 (b) confirms the phenomenon reported by Tigerschiold [86] that decrepitation temperature is inversely proportional to particle size. The effect of binders, shown in Figure 2.5.2.1 (c) and (d), indicates that the manner of bentonite addition – whether added on top of wet filter cake prior to pelletization (poorly mixed) or mixed thoroughly with the filter cake prior to pelletization (well mixed) -- makes a difference.

The important finding for the present purpose is that a maximum exists in the decrepitation temperature as a function of the amount of binder added (see Figure 2.5.2.1 (c)). A similar effect, although not as drastic as for bentonite, was observed for starch addition (see Figure 2.5.2.1 (d)). The optimal concentration of an additive in this case was ~0.15 %.

Another investigation of the effect of synthetic binders on the spalling resistance of agglomerates (in particular a comparison between the polymer trademarked 'Peridur' and Wyoming bentonite) was undertaken by Roorda et al. [94]. They used the term *shock temperature* as a measure of the pellets' resistance to spalling. The latter was defined as the temperature at which 10% of the pellets in a sample disintegrated due to spalling. Data on the concentrate properties, pellets and the measured shock temperatures are shown in Table 2.5.2.2.

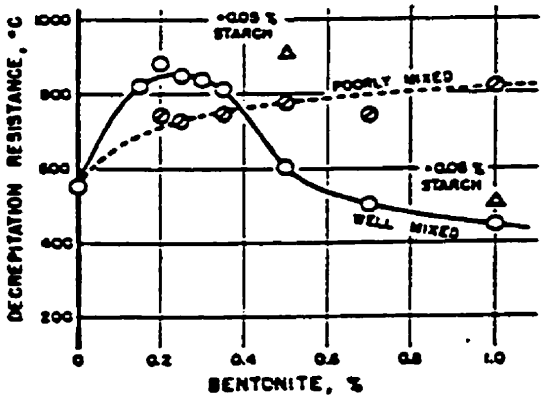


a)



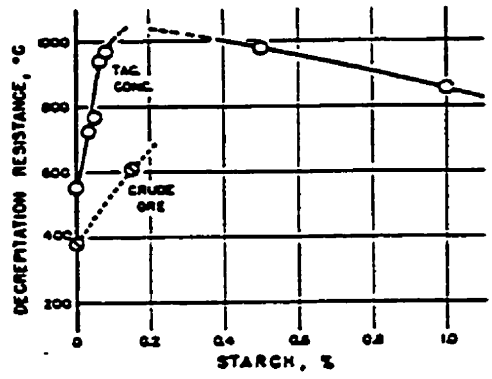
Decrepitation Resistance of ½-Inch Balls of Crude Ore As Function of Degree of Subdivision.

b)



Effect of Bentonite Additions on Decrepitation Resistance of ½-Inch Balls of Taconite Concentrate.

c)



Effect of Starch Additions on Decrepitation Resistance of ½-Inch Balls of Taconite Concentrate and Crude Ore.

d)

Figure 2.5.2.1. Spalling Behaviour; Experimental Results of Schultz et al. [93]: a) -- Drying Furnace; b) -- Decrepitation Resistance as a Function of Particle Size;c) -- Effect of Bentonite Additions on Decrepitation Resistance; d) -- Effect of Stach additions on Decrepitation Resistance.

Table 2.5.2.2. Experimental Results of Roorda et al. [94]

Material - Magnetite Concentrate	**Blaine [cm²/g]** 2010						**wt.% ≤40μm** 94.8		
	None	**Bentonite**		**Peridur XC3**			**Peridur XC7**		
Additive wt. %	0.0	0.5	1.0	0.1	0.2	0.3	0.1	0.2	0.3
- Water wt. %	8.8	9.2	10.1	9.4	9.8	10.0	9.9	10.8	11.3
- Green Strength [kg]	1.0	1.0	1.55	1.6	1.4	1.7	1.2	1.3	1.3
- Dry Strength [kg]	0.6	2.34	5.17	2.6	5.6	7.5	2.1	5.2	12.5
-Shock Temp.[°C]	400	575	375	650	475	200	575	200	100

Peridur has the capability of producing higher dry strength than bentonite at a given concentration. Again, the shock temperature improved with binder addition: from the 400°C characteristic of binder-free pellets to 650°C, 575°C, and 575°C for additions of 0.1% XC3, XC7, and 0.5% bentonite respectively. Significantly, a maximum was again observed for additions beyond the optimum. The shock temperature of excessive additives was below that of binder-free pellets. This is similar to the trends observed by Schultz et al. [93].

No explanation for the existence of a maximum in the decrepitation temperature versus additive concentration curve has yet been offered in the literature. A contribution of this thesis is a theoretical investigation of this phenomenon, and an explanation for it. Involved is the mathematical modelling of the internal stress buildup, and its comparison to the dry strength, using equations documented in Sections 2.4.3 and 2.5.1.The results of these investigations are reported in Section 4.5.

Chapter 3
CONTRIBUTIONS TO THEORY

This thesis work has made some original contributions to the fundamentals and theory of agglomerates. Also, additional theoretical contributions have been made to understanding the behaviour of agglomerates during intensive drying. These contributions are being documented in this Chapter.

3.1. Limitations of the Zaharchuk Model

The Zaharchuk model includes the vapour lock, or the loss of capillarity, as the cause for the surface/shrinking core transition during intense drying.

The issues and the nature of the vapour lock are illustrated in Fig. 3.1.1 and Fig. 3.1.2. Shown are the results of calculations, carried out by the author, using the Zaharchuk model. The set of pellet parameters and drying conditions used in this simulation was that of the 'typical' pellet (see Chapter 2.4.4). The liquid pressure and vapour pressure are plotted versus pellet saturation for an example case agglomerate, one with the average particle diameter 7.1μm. Also plotted is the drying rate predicted by the model for this set of parameters.

According to earlier arguments and equation (2.3.2.1), the loss of capillarity and thus the transition from the surface to the shrinking core regime should occur at the intersection of the two

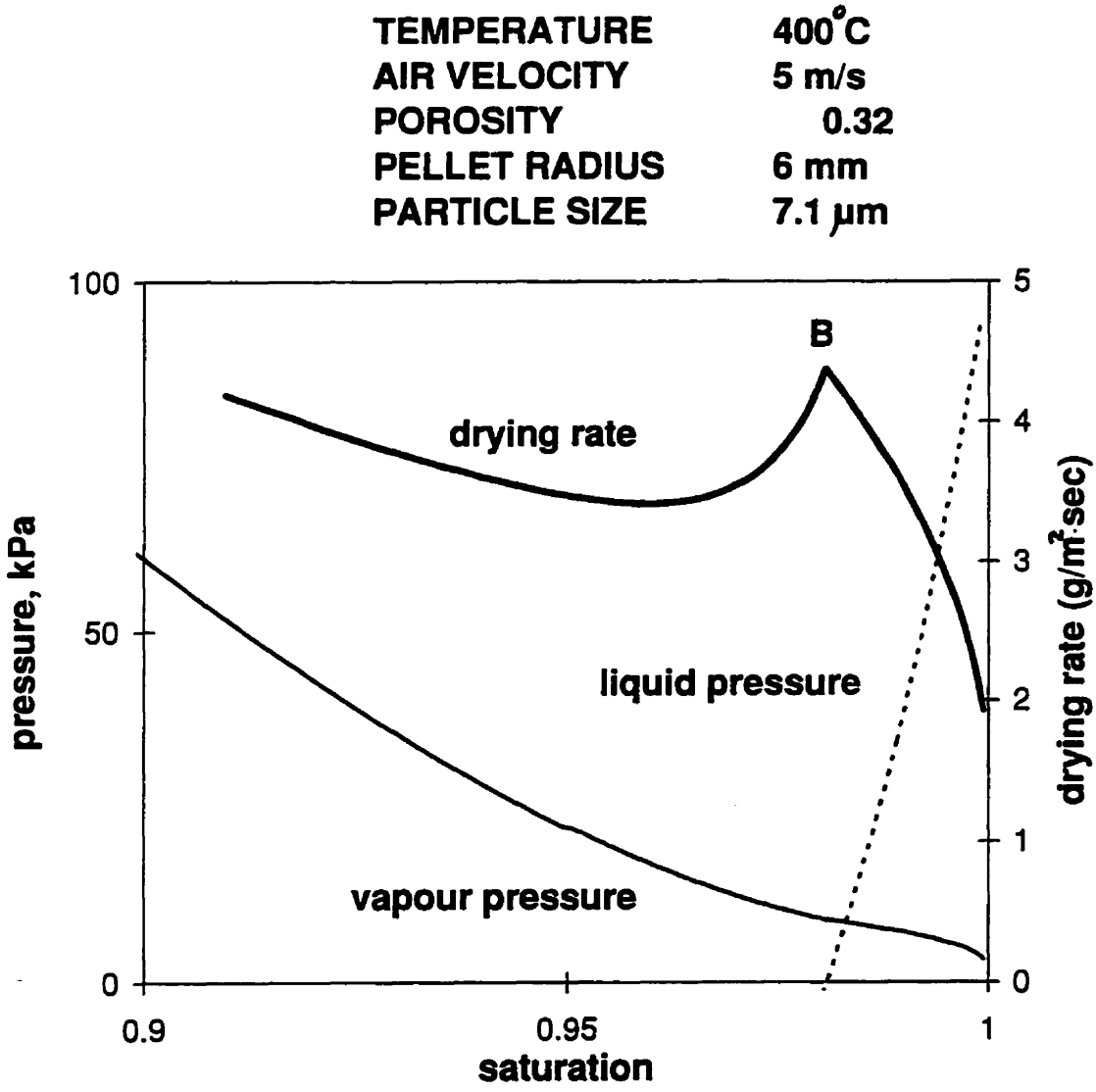


Figure 3.1.1. Model Predictions of : Drying Rate, Liquid Pressure and Vapour Pressure vs. Pellet Saturation (particle size 7.1 µm).

TEMPERATURE	300°C
AIR VELOCITY	1 m/s
POROSITY	0.32
PELLET RADIUS	6 mm
PARTICLE SIZE	17 μm

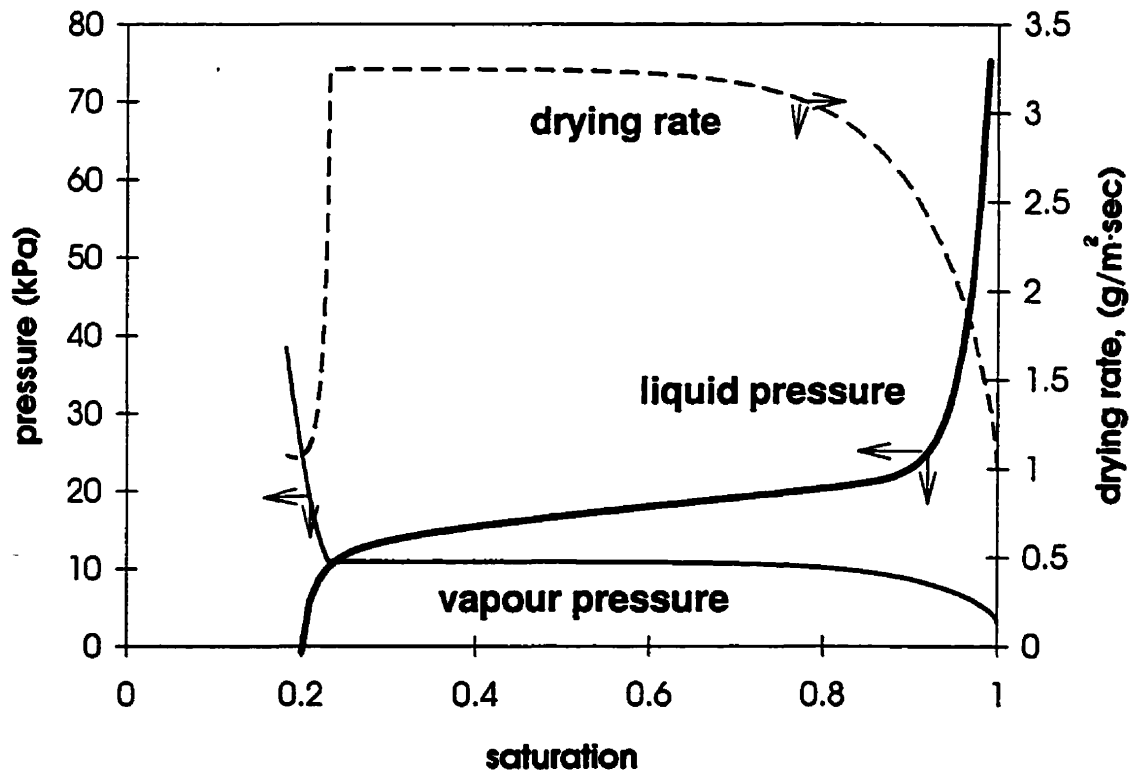


Figure 3.1.2. Model Predictions of : Drying Rate, Liquid Pressure and Vapour Pressure vs. Pellet Saturation (particle size 17 μm).

pressure curves. For the drying conditions in Figure 3.1.1, the intersection and transition is seen to occur early in the initiation period, when the degree of saturation is still above 95%, i.e. *before* the constant-rate period could be reached.

For the agglomerates of coarser particle size, the vapour-lock condition (eqn. 2.3.2.1) will occur later in the drying process. This scenario is illustrated in Fig. 3.1.2, in which the model results for a pellet with the average particle size 17μm and drying conditions somewhat milder than in Fig. 3.1.1 are plotted. For this d_p=17μm case, the model predicts a drying-rate-curve pattern which is similar to the mild-drying case: first, the existence of a constant rate period, and second, the delay of the transition to the shrinking core regime well into the constant-rate drying period.

Figure 3.1.3 represents additional Zaharchuk-model predictions for the same conditions as in Figure 3.1.1. Shown are the drying-rate curve and curves for the temperatures at the surface and the wet/dry interface (curves 2 and 3 respectively) as a function of time. Similar curves have been presented in Figures 2.4.4.2 and 2.4.4.3.

Drying begins with the initiation period (portion *AB* in Figure 3.1.3). As in the "classical" case, the rate here is controlled by the heat and mass transfer across the boundary layer. However, the rapid heat supply to the surface causes the temperature of the surface and the rest of the body to rise rapidly. Correspondingly, the equilibrium vapour pressure at the surface will rise exponentially. The vapour-lock condition (eqn. 2.3.2.1) is reached at point *B*. For the set of conditions in Figure 3.1.3 the surface temperature, at which the vapour lock condition is reached, is only 43.5^{0}C.

The shrinking-core drying regime, therefore, sets in starting at point *B*. In the Zaharchuk

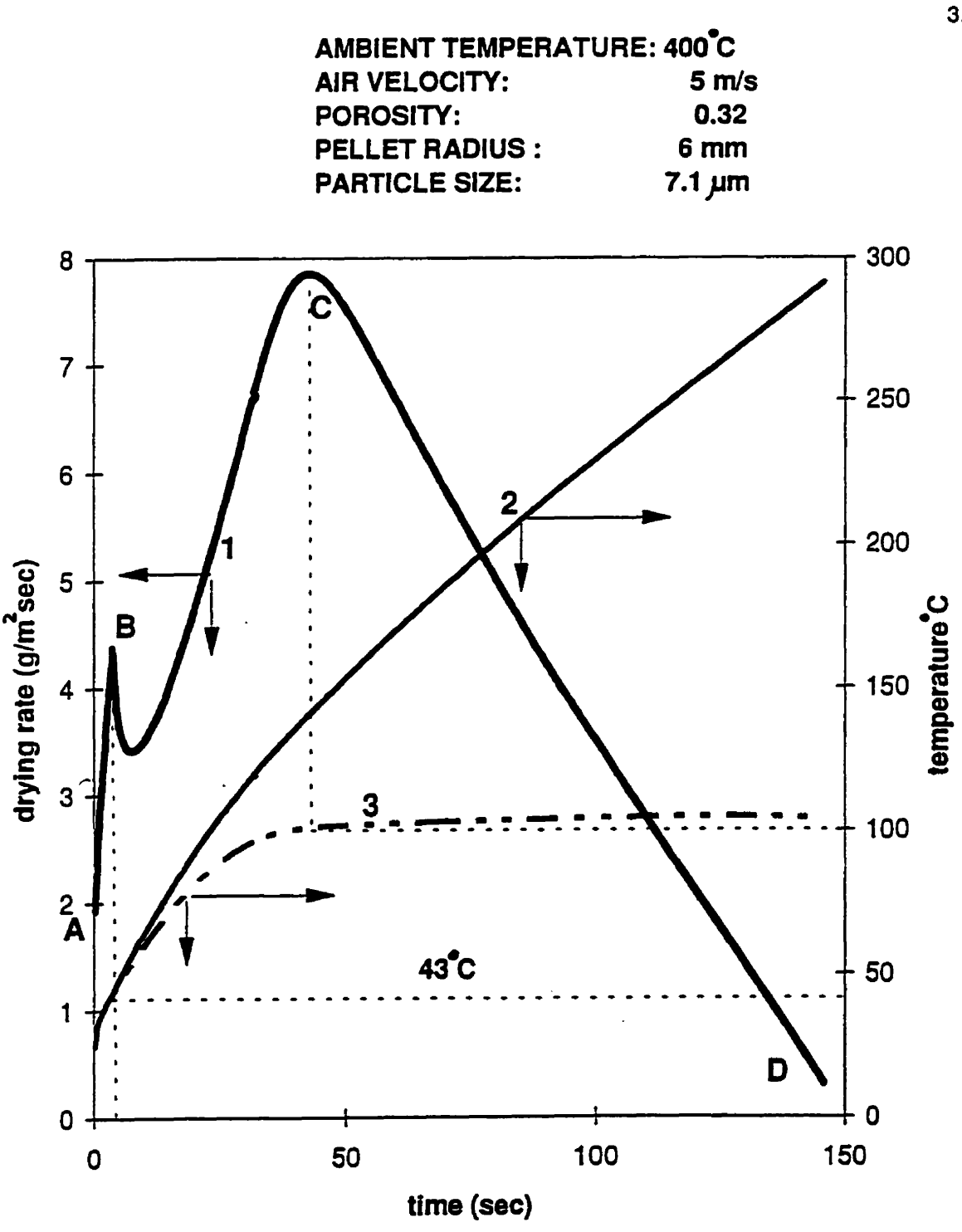


Figure 3.1.3. Drying Rate Curve (1); Temperature at the Surface (2) and at the Interface (3).

model, the transition between the surface and shrinking core drying periods is incorporated by assuming it to be an **instantaneous** event. The liquid pressure in the average pore size is calculated and compared to p_v^o. When the two become equal (see Figure 3.1.1), the calculation proceeds on the basis that the shrinking core period has begun. The sharp drop of the calculated drying-rate curve at point *B* in Figure 3.1.3 is to be noted. This is a direct result of the assumption that the surface/shrinking-core transition is instantaneous. Now, that the wet/dry interface has receded into the pellet interior, vapour diffusion through the dry shell becomes a significant contributor to the rate-control of the drying rate. The rate, therefore, shows the sharp instantaneous drop. The same effect is to be noted also in Figure 3.1.2, where there is a nearly vertical drop in the drying rate, following the constant-rate period. Such sharp rate changes, and a minimum in the drying rates, however, are simply unknown in practice. Clearly, a fault is in the assumption of the surface/shrinking-core transition being instantaneous.

The next important model prediction (see curves *2* and *3* in Figure 3.1.3) is that the temperature at the wet/dry interface continues to rise rapidly beyond the vapour-lock point. This results from the that the vapour pressure, the driving force for diffusion of the vapour through the dry shell, is increasing with temperature. Hence, the drying rate again begins to rise rapidly following the minimum near point *B*.

As the wet/dry interface temperature reaches 100^0C (point *C* in Figure 3.1.3), the water vapour pressure exceeds p_T, the surrounding gas pressure. Now the mechanism of vapour transport changes from diffusion to Darcy flow. Much smaller pressure differences between the interface and the surface (compared to the diffusion regime) suffice to remove the water vapour. Consequently, heat transfer alone becomes the rate-limiting factor. Since the resistance to heat

conduction through the dry shell increases with now rapidly increasing thickness of the latter, the drying rate begins to decrease. This starts at point *C* and the gradual decrease continues until the drying is complete (portion *CD* in Figure 3.1.3).

Granular agglomerates have a range of pore sizes. It is inherent to drying of these materials that the surface/shrinking core transition will occur during an extended period of time. An extended drying model has been developed in this study and is presented in the next Section. It resolves satisfactorily this limitation of the original Zaharchuk model.

3.2. Extended Drying Model

As a starting point of model development it is herewith asserted that, phenomenologically, the surface/shrinking-core transitional period for the intense drying conditions is somewhat similar to the first falling rate period in the 'classical' model. The key feature in both cases is that the liquid pressure is not maintained uniformly across the drying surface as more and more pores of certain sizes become drained. However, there is a crucial difference between the mechanism details in these two cases. In the first falling-rate period the liquid is being delivered to the surface through the interconnected system of the small pores (see Figure 2.3.1.2). This is so because the latter have the lower liquid pressures and thus provide a larger driving force for liquid flow. This process drains larger pores within the body, which are also interconnected and reach the surface.

A key proposition of the present model is that for intense drying the opposite takes place. This is illustrated in Figure 3.2.1, which is a replica of Figure 2.3.1.2. The smaller capillaries (capillary *B* in the Figure), having the lowest liquid pressure, will be the first to be the subject to the vapour-lock effect. Consequently, these smaller pores will be the first to become dry. While this occurs, the surface drying can continue, via the system of larger pores delivering water to the

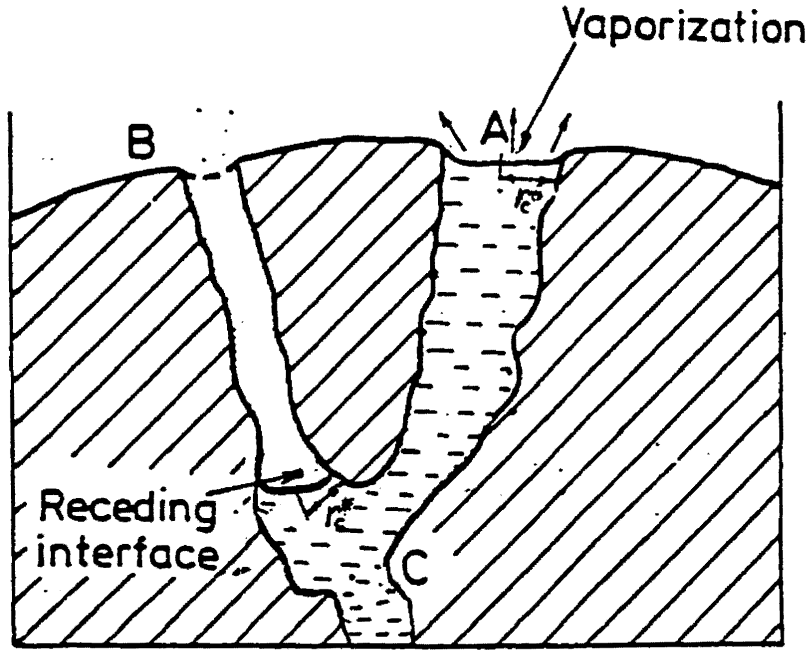


Figure 3.2.1. Simplified pore structure showing moisture migration for the intense drying conditions.

surface (capillary *A* in Figure 3.2.1).

This is the important, fundamental distinction between the mild and the intense drying mechanisms. It should also be the reason, and/or the mechanistic cause for any microstructural and physical property differences in the resulting agglomerates produced by these two drying techniques. Investigation of the latter point is one of the objectives of this research and will receive further elaboration in this thesis.

The extended mathematical model allows for the fact that a dispersion of the pore sizes exists. Further, it incorporates empirical information concerning the pore size distribution. The effect of the pore size distribution on the drying rate during the period of transition from the surface to the shrinking core regimes then becomes calculable. The operating assumptions are as follows. First, the vapour lock sets in when the local liquid pressure within a capillary becomes equal to the equilibrium vapour pressure in the gas phase above such a capillary. When the agglomerate has a wide pore-size distribution the above will apply to the smallest r_c at the pellet surface. Then, as this condition is reached, the liquid delivery through this capillary will terminate. As the surface temperature and, therefore, the vapour pressure keeps rising, more and more capillaries with a larger r_c at the surface become inoperative.

The data on pore size distribution in the pellet used in the model is based on the results of mercury porosimetry (see Chapter 2.2.3.1). An *if-* statement is included in each time step of the algorithm. It asks "*for which size* of r^*_c does the value of p_l equal to the value of p_v^0 ?". Then this fraction of the pore sizes is eliminated from consideration as liquid suppliers to the surface.

The physical picture of the intense drying process during the transitional period is shown

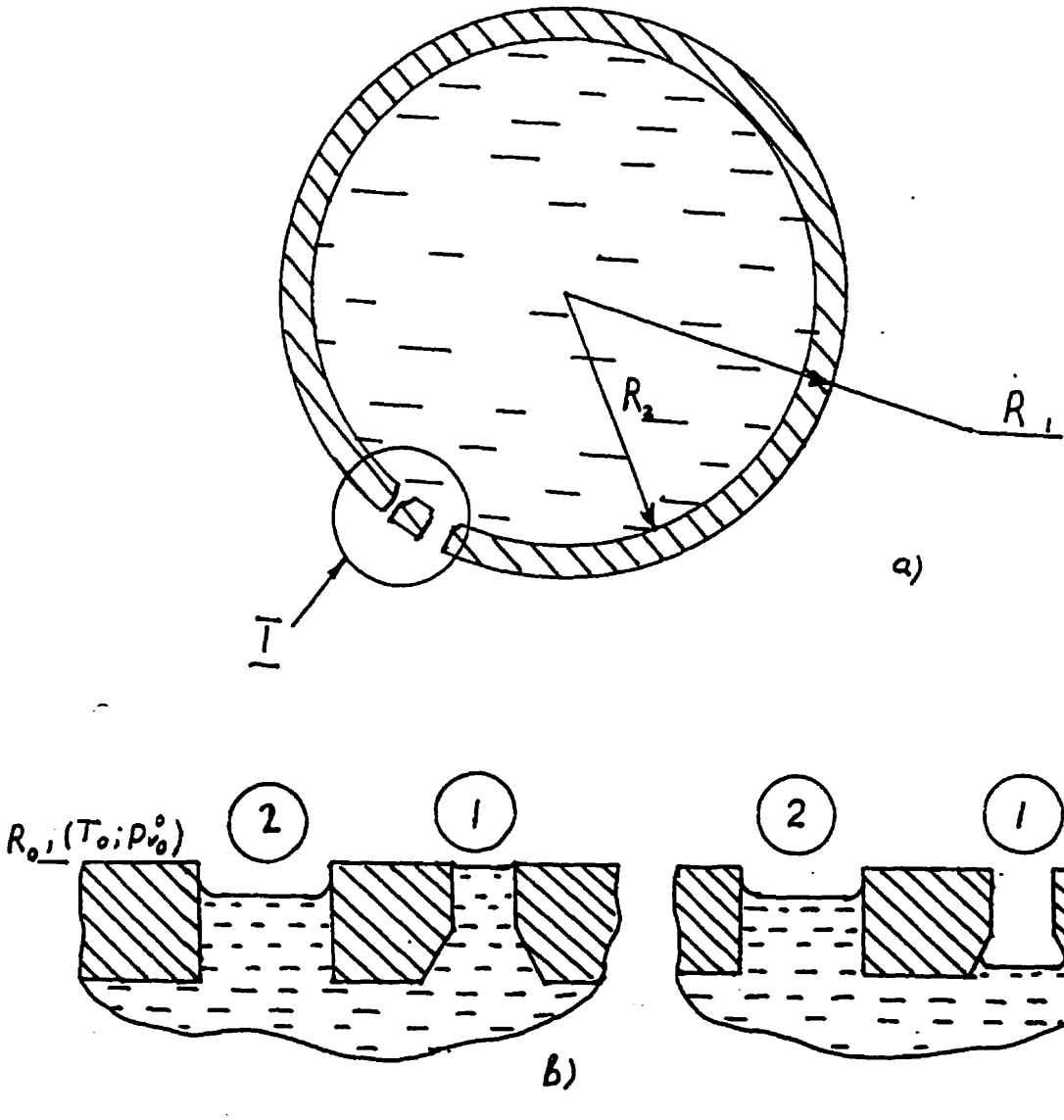


Figure 3.2.2. Simplified physical picture of the intense drying during the transitional period.

in Fig. 3.2.2. The pellet is represented as a water reservoir whose exterior surface is a porous shell pierced by a series of radial cylindrical capillaries (Fig. 3.2.2 a). A fundamental assumption is made that the capillary-radius distribution at the surface is equal to the pore-size distribution within the bulk of the pellet. The latter is, in this work, taken as being represented by the results of mercury porosimetry measurements.

Water from the inner reservoir is being continuously supplied to the surface through the capillaries by Darcy flow. During the early surface-drying period, the rate of water delivery to the surface (eqn. 2.4.14) is comparatively fast and, therefore, does not contribute to the drying-rate limiting factors. The vapour transport across the gas-phase boundary layer is the rate-limiting factor, determining the drying rate. As drying proceeds, the fraction of 'inactive' pores increases, and the water delivery rate decreases rapidly. At some point it will become rate-limiting. The model includes the calculation of the net water delivery rate G_{DF} (eqn. 2.4.14). This calculated G_{DF} value is compared to that of the effective drying rate in each iteration. As soon as it becomes smaller than the ability to diffuse across the boundary layer ($G_{DF} \leq G_{eff}$), the shrinking core drying regime is assumed to set in.

The following mechanistic assumptions are made in the present model. The symbols are defined in Figure 3.2.2:

1) The temperature gradients are always positive in the radial direction, i.e. for any $R_1 > R_2$ we have $T_1 > T_2$;

2) There are no temperature gradients in the circumferential direction at a given value of R, i.e. $dT/d\theta = 0$;

3) The water vapour pressure at the liquid surface is equal to equilibrium vapour pressure

at the effective, circumferentially uniform surface temperature T_1;

4) There are no circumferential vapour pressure gradients at a given value of R, i.e. $dp_v/d\theta=0$.

At $t=t_0$ all capillaries are filled with water in the entry suction sense. As drying proceeds, the condition is reached such that the vapour pressure over the capillary (1) in Fig. 3.2.2, which is the smallest capillary of the shell, becomes equal to p_l under its meniscus. At that instant the liquid delivery through capillary (1) is terminated and its water meniscus recedes from the surface to some new "equilibrium" position. Practically this will be to a larger radius in the same "channel" as shown in Figure 3.2.2 (c). Due to the positive radial temperature gradient, the temperature T_2 at the new location of the meniscus will be lower than that at the "surface" T_1. Correspondingly, the vapour pressure over the meniscus (p_{v2}), which is the equilibrium vapour pressure for temperature T_2, will be also lower than p_{v1}. Hence, there will be no positive vapour pressure gradient in capillary (1) to enable the vapour transport to the surface. Thus no evaporation at all will take place in capillary (1).

As drying proceeds, more and more capillaries reach the condition $p_{vi}=p_{li}$ and become inactive. Evaporation continues over the surfaces of the remaining *large* capillaries in which the menisci are still at the "surface". The process continues until the 'originally fast' rate of water delivery to the surface by Darcy flow (eqn. 2.4.14) through the smallest "still active" capillary size becomes less than the effective drying rate ($G_{DF} \leq G_{eff}$). At this instance the "surface" temperature T_1 shifts to a new, inward location of a smaller radius R_2. Thus, in effect, a wet/dry interface is generated within the matrix. Starting at this point, drying occurs in the shell interior, rather than

at the surface. In other words, the shrinking-core period technically sets in.

3.2.1 Program Algorithm

Based on the cumulative pore size distribution (see Figure 2.2.3.2 a), the value of w, the percentage of the specific r^*_c in the overall pore size distribution, is determined. This value defines the fraction of the pore-size spectrum deactivated in the capillary water transport at a particular drying time. The remaining fraction $(1-w)$, therefore, will represent the fraction of the pores through which water is still being delivered to the pellet surface.

Next, the value of effective drying rate is calculated from:

$$G_{eff} = G_{BL}(1-w) \qquad (3.2.1.1)$$

The value of G_{eff} thus includes a correction for the pores, which are inactive at the specific point in time. The fact that the drying rate has been effectively altered by this operation requires that the corresponding changes are made to the heat balance, equation 2.4.1.

This is done using an iterative technique. Since the approach of iterative calculation of the surface temperature and corresponding p_v^0 is already within the model, the changes introduced merely extend the iteration cycle. The convergence is defined to be complete when the difference between values obtained for p_v^0 in two iteration steps is less than 0.01 kPa and the surface temperature difference is less than 0.01^0C.

The following numerical method, called FINAL.FOR, has been developed to calculate the effective drying rate during the period of the surface-to-shrinking core transition. In each time step, the value G_{eff} is compared to the value of G_{DF} determined for pores larger than the smallest

"still active" pore size r_c*. The model FINAL.FOR runs until the point is reached where G_{DF} becomes smaller than the G_{eff}. This point is the criterion for the onset of the shrinking core drying period and is consistent with the physical considerations in the Section 3.2. Following this instant the calculations of the drying rate proceed via the original Zaharchuk model algorithm for the shrinking core regime.

The individual steps of the calculation procedure are given below. The steps are also itemized in the flow-chart in Figure 3.2.1.1.

1. The following information is read from the data file. It includes pellet parameters, initial conditions, external conditions, and other pertinent information.

- Pellet radius
- Porosity
- Cumulative pore size distribution function as described in Section 2.2.3.1.
- Initial saturation
- Initial pellet temperature
- External gas velocity
- External gas temperature
- Initial time step τ

2. Write all the pertinent data

3. Initial time $t^*=0$

4. Calculate the moisture content (MC) [kg H_2O]

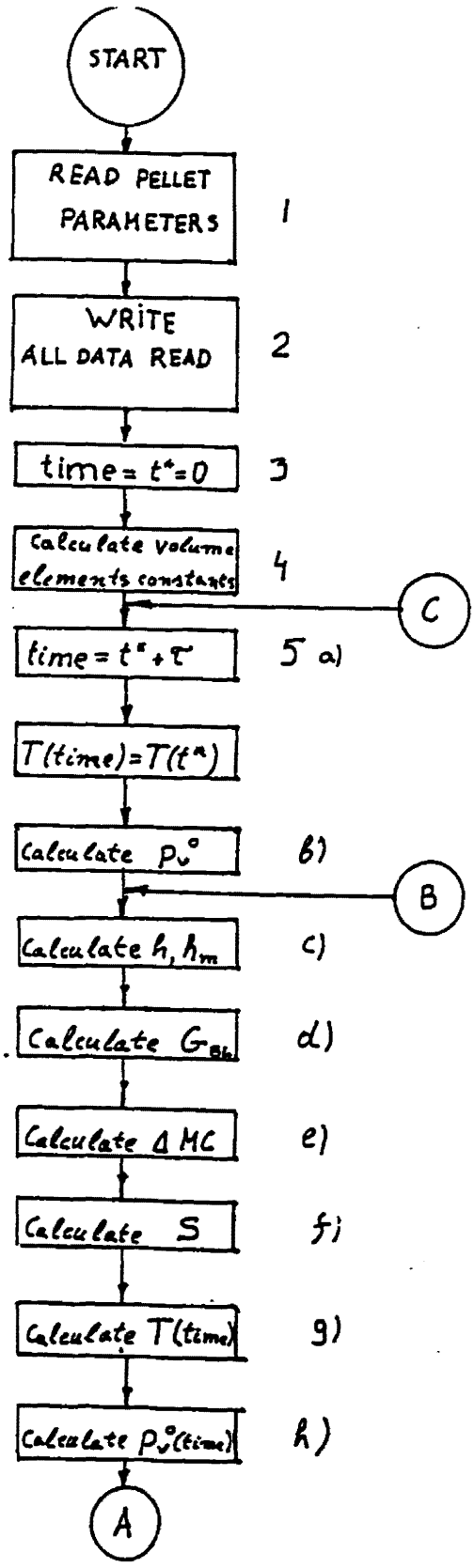


Figure 3.2.1.1. Program algorithm flow chart (part 1 of 2).

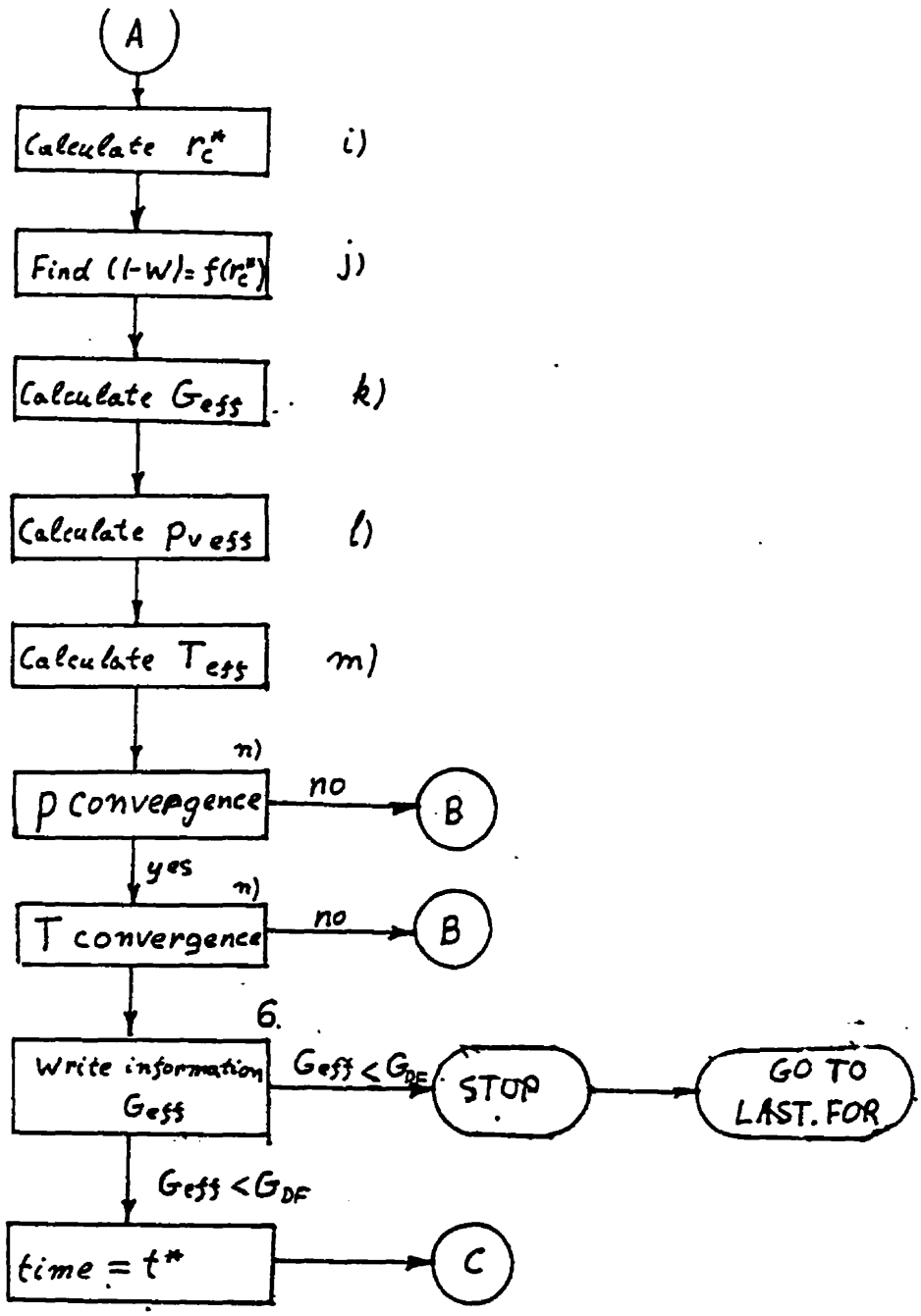


Figure 3.2.1.1. Program algorithm flow chart (part 2 of 2).

5. Surface Drying

a) New time $time = t^* + \tau$

b) The equilibrium vapour pressure p_v^0, corresponding to the surface temperature is calculated using eqn. 2.4.7. If this is the first iteration in this time step, temperature from the last time step is used.

c) The heat and mass transfer coefficients are calculated using the procedure of the Zaharchuk model.

d) Evaporation rate is calculated using the equation 2.4.6.

e) The amount of moisture evaporated during the time step τ is calculated using the equation:

$$\Delta MC = G \cdot \tau \qquad (3.2.1.2)$$

f) New saturation level is calculated subtracting ΔMC from the previous saturation level.

g) A heat balance is written. At the pellet surface it is given by eqn. 3.2.1.3:

$$k_{eff_{wet}} \left.\frac{dT}{dr}\right|_{r=R_p} = h(T_\infty - T|_{r=R_p}) + \sigma_{SB}\varepsilon_R(T_\infty^4 - T^4|_{r=R_p}) - \left(\frac{\Delta H_v \cdot G}{4\pi R_p^2}\right) - \left(\frac{G \cdot C_{P_l} \cdot}{R_p}\right)\left.\frac{\partial T}{\partial r}\right|_{r=R_p} \qquad (3.2.1.3)$$

h) The new equilibrium vapour pressure, corresponding to the new surface temperature is calculated, using eqn. 2.4.7.

i) Coefficient B_l from equation 2.4.19, is calculated, with p_l equal to p_v^0 from the previous step.

j) The pore radius r_c^* from eqn. 2.4.17 is determined by equating $(p_T - p_l)$ to the value of B_l in previous step.

k) Volume fraction $(1-w)$ of the pores larger than r_c^* is found from the cumulative pore size distribution function, which is described numerically by the polynomial fit or by Fourier's series.

l) Effective drying rate is calculated using eqn. 3.2.1.1.

m) Effective vapour pressure is found from the equation 2.4.6. by substituting the value of G_{eff} for G_{BL}.

n) A new surface temperature is calculated using the eqn. 3.2.1.3, corresponding to the effective vapour pressure at the surface. If the difference between it and the previous temperature is less than 0.010^0C and if the sum of the absolute value of the corrections of p_{veff} is less than 0.01 kPa, then convergence is assumed and iterations proceed for a new time step (i.e. item 5 a).

6. The pertinent data is recorded. The value of G_{eff} is compared to the value of G_{DF}. The latter is calculated from eqn. 2.4.14 using the final set of parameters from the current time step. If G_{eff} is smaller than G_{DF}, the iterations proceed to the new time step (i.e. item 5a). If $G_{eff} \geq G_{DF}$, FINAL.FOR routine stops and the calculations switch to the shrinking core routine taken from the Zaharchuk model.

3.2.2. Modelling the Shrinking-Core Drying Period

The new extended model, presented in the previous Section, deals with the non-instantaneous transition from the surface- to the shrinking core drying regimes. As soon as the wet/dry interface has shifted *entirely* into the pellet interior, the new model algorithm switches to the shrinking-core calculations according to the original Zaharchuk model. A basic assumption of the latter is a sharp interface between the wet core and dry shell of the pellet (see Fig. 2.4.4.1). Clearly, this assumption of the Zaharchuk model is unrealistic (see arguments in Sections 3.1 and 3.2), and it may cause significant deviations from experiment. An analogous model problem is the case of the surface/shrinking core transition. The model validation results reported in Section 6.1 showed that, in fact, such deviations can be quite substantial in certain cases.

In the present study an attempt has been made to extend the mathematical model of the shrinking-core drying period by including a non-sharp, or 'irregular' interface. It turns out that to incorporate a true irregular interface into the model algorithm is too complex a numerical problem and is not likely to be realistically solved [91]. An approximate solution, described below, was attempted. But even that was not successful.

In the original model algorithm, the saturation level is calculated for the entire wet-core region, i.e., it is uniform for all volume elements in this region (see Figure 2.4.4.1). The model modification attempted to decrease the saturation level of the volume element on the core side of the wet/dry interface. As a first approximation, the degree of saturation of this interface-containing element was set to the average between the two neighboring elements – the inner one fully within the wet core, and the outer one fully within the dry shell:

$$S_j = \frac{S_{j+1} + S_{j-1}}{2} \qquad (3.2.2.1)$$

However, when used in the algorithm, even this relatively simple model modification caused the numerical program to stall. This failure was attributed to the stiffness of the fundamental set of second-order partial differential equations describing the mass-, heat- and momentum balances, which have to be solved simultaneously for both the wet core and the dry shell regions of the pellet. This stiffness of the equation set causes instability and crashing of the numerical algorithm. Given its complexity, together with the time limitations of the current project, further attempts to solve this problem were discontinued.

3.3. Effect of Bentonite on Drying Behaviour

Upon drying, bentonite precipitates in the contacts between particles in the all important capillary sizes r_c [48]. By bridging these contacts, bentonite effectively alters the pore microstructure of the agglomerate. Such microstructural changes would be expected to become significant during the shrinking core regime, i.e., when local drying without liquid movement is taking place. The Zaharchuk model considers the effect of bentonite on drying behaviour only in connection with liquid immobilization. The latter results from the viscosity increase accompanying the concentration increase upon drying. The model does not include the consideration of the effect of bentonite precipitation on the microstructure of the pores.

In the present study, it was assumed that, for the purposes of modelling of the drying at the pellet surface (both during the initiation- and transitional periods), the effect of precipitation of bentonite on the microstructure within the pellet core can be neglected and the formalism

described in sections 3.1 – 3.2 is sufficient. The extended model, therefore, uses the same calculation of the viscosity of water-bentonite suspension as the original Zaharchuk model [49]:

$$\mu_d = \mu(1 - k_v\phi_d)^{-\frac{A_3}{k_v}} \qquad (3.3.1)$$

where μ and μ_d represent the viscosity of the pure solvent and the dispersion respectively, ϕ_d represents the volume fraction of the suspended solids in the dispersion, k_v represents the reciprocal of the maximum packing fraction at which flow can occur and A_3 is an empirical constant. Equation 3.3.1 is used to calculate the viscosity of the water-bentonite dispersion up to a maximum limit of 55,718,574 times the viscosity of water. The latter factor has been arbitrarily chosen in the Zaharchuk model as a limit to avoid the mathematical singularity that arises in equation 3.3.1 as the maximum viscosity level is approached.

In the extended model the result of the viscosity calculation in each time iteration is compared to the maximum viscosity value used in the Zaharchuk model. If it is still below the critical level, the calculated value is substituted into the mass balance equation (2.4.11) and the effective drying rate is calculated using the equation (3.2.1.1). When the value of viscosity becomes equal or larger than the critical one, the water-bentonite dispersion is assumed immobile and the algorithm switches to the shrinking core regime calculations at that instant.

Such a procedure accounts for the combination of either or both effects: of the critical capillary radius to cause local loss of capillarity AND of the effective immobilization of the water-bentonite suspension at this particular moment.

This thesis work has included parallel experimental research, conducted to study the character of the bentonite precipitation. The objective has been to establish the effect of bentonite

precipitation on overall drying behaviour, as well as to validate the values of the above model parameters. These results will be described in Section 6.4.

3.4. Matrix Expansion and a Hypothesis of its Cause

A hypothesis has been proposed in the course of this study to explain the volume increase in tumbled iron ore agglomerates during drying. It interprets this increase in terms of engulfment of the loose particles with the receding wet/dry interface (see Chapter 2.2.3.1).

The hypothesis is based on the findings of the volume measurements of Griffith iron ore agglomerates on the wet and dry basis, which have been conducted in our research group by D. Lisieczko [50]. Wet pellets were produced by two different methods: by usual tumbling procedure described elsewhere [47, 50, 51] and by pressure compaction in a 3/4" diameter double action mold. The densities of the individual wet pellets were measured. These pellets were then dried in the laboratory oven under the mild drying conditions (~80^{0}C) and their densities were measured again, now on a dry basis.

The results of these density measurements, which have not as yet been published, have been summarized by the author and are presented in the Table 3.4.1.

The data show conclusively that in the pellets produced by tumbling there is a significant (up to 15%) porosity increase upon drying. On the other hand, there is practically no such increase for the pressure-compacted tablets made of the same material.

We propose the hypothesis that the reason for the porosity increase in the tumbled pellets is associated with the skeletal network structure (see Chapter 2.2.3) of these pellets. It is assumed that the pressure compacted tablets do not possess such a structure and, hence, are unable to

exhibit such porosity increases.

Table 3.4.1. Volume Increase of Iron Ore Pellets upon Drying [50].

Pellet Description	Porosity ε		$(\Delta\varepsilon/\varepsilon_{wet})$x 100%
	wet basis	dry basis	
1. Plant pellets (0.8% bentonite)	0.302	0.343	13.4
2. Laboratory pellets (tumbled):			
- wet filter cake w/out bentonite	0.252	0.291	15.5
- dried f/c with 0.8% bentonite	0.290	0.328	13.2
- dried f/c with 1.2% bentonite	0.298	0.338	13.3
3. Pressure compacted pellets:			
- direct compaction (1.2% bent.)	0.286	0.292	2.10
- balling and recompaction (0.8% bentonite)	0.3048	0.3097	1.61

Next, we hypothesize that the reason for the volume increase in the tumbled pellets is the particle movement during drying, caused by the engulfment of the fine loose particles with the receding liquid/solid/gas interface (see Chapter 2.2.3.1). The essence of this hypothesis is illustrated in Fig.3.4.1. As drying proceeds, the smaller loose particles, which originally occupied positions in the voids of the pellet, i.e. which were not part of the skeletal-network structure, had low coordination numbers and were not anchored between others, are dragged into the interstices between the bigger, network-creating ones. As the pendular state of the agglomerate is approached, the amount of fines concentrated in the contact areas becomes large and the capillary radius, therefore, small. The consequently low liquid pressure tends to pull in the "surface particles" and thus, to pry apart the skeletal network structure of the agglomerate. The result is the observed increase in porosity.

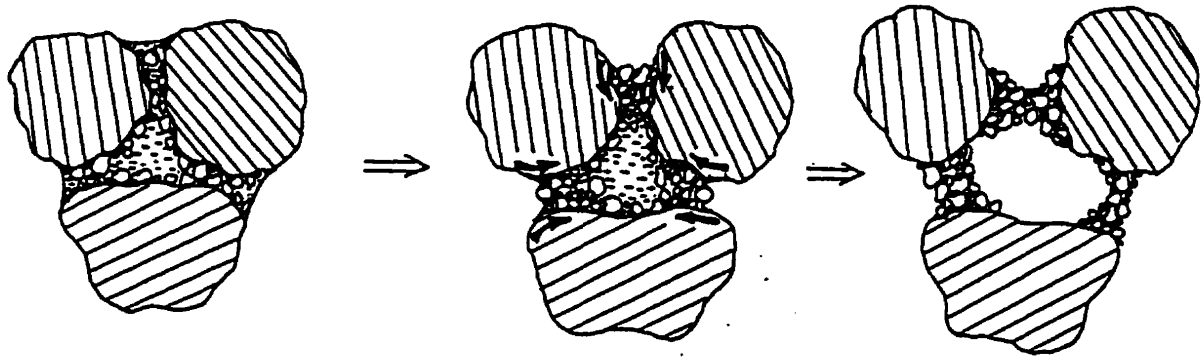


Figure 3. 4 .1. Schematic representation of pore expansion hypothesis.

The important thing to note is that the pore size increase was observed under mild drying conditions (drying in the oven at 80^0C). The particle engulfment phenomenon should be expected during such mild or 'slow' drying, where the solid-liquid-gas interface is receding from the larger to the smaller pores. The picture might, however, be quite different during the intense drying, based on the argument presented in Chapter 3.2. The contact areas between large particles, representing the necks in the ink-bottle structure, are likely to be the primary sites for the vapour lock. Creation of local gas/liquid interfaces in these areas will, consequently, hinder or prevent the engulfment process. It should be noted that the latter implication is a relatively new conceptual development. It was further studied experimentally and the results of this research are presented in Chapter 6.2.

Chapter 4

RESULTS OF MODELLING INVESTIGATIONS

In this Chapter a selected set of results of modelling of drying of agglomerate pellets is documented. A preliminary section, Section 4.1, is devoted to defining the relationship between the pore size of the agglomerate and external drying conditions, so as to define the onset of the vapour lock.

In the subsequent Sections, results of calculations using both the original Zaharchuk and the extended models are documented as follows:

(1) the effect of pore size of the agglomerate on the drying curve, and on the pattern of body temperatures reached under a 'typical' set of drying conditions.

(2) a definition of the range of pellet properties and drying conditions for the occurrence of the "intense" versus "mild" drying regimes.

(3) results of a theoretical investigation of the benefits achievable using "tumbling-and-drying". This is a potentially attractive modification of the industrial process of iron ore pelletizing, in that improvements in the spalling resistance under conditions of intensive drying -- and thus process capacity and economy improvement -- are possible.

4.1 Conditions for the Occurrence of the Vapour Lock

The theoretical analysis in Section 3.1 suggests that the occurrence of the vapour lock

should be limited to agglomerates of fine granular materials dried at relatively intensive conditions.

At issue is to quantify the range of pore size (r_c) in combination with the local temperature (T) and pellet saturation (S)) at which the vapour-lock condition is likely to set in. The following computation has been performed to establish the dependence of r^*_c, the critical pore radius at the instant of vapour lock ($p_l = p^0_v$) as a function of pellet's temperature T and pellet saturation S.

Equations 2.4.19 and 2.4.17 can be combined to obtain the following expression for r_c:

$$r_c = \frac{2 \cdot \gamma_{lv}(1 - \exp(-B_2 \cdot (1 - S))}{p_T - p_l - B_3(1 - S)^{B_4} - \dfrac{B_5(1 - S)}{(S - (S_p - 0.015))^{B_6}}} \qquad (4.1.1)$$

Recall that the parameters B are the constants in the capillary-pressure versus saturation equation, eqn. 2.4.19.

Next, in order to reflect the vapour-lock condition (eqn. 2.3.2.1), the expression for equilibrium vapour pressure (eqn. 2.4.7) was substituted for the liquid pressure in equation 4.1.1. Finally, the temperature dependence of the surface tension of the liquid (γ_{lv}), taken from Perry and Chilton [72], was substituted for γ_{lv}:

$$\gamma_{lv} = 2 \cdot (-0.002T + 0.1215) \qquad (4.1.2)$$

The resulting equation, giving the critical vapour-lock pore radius as a function of temperature and the degree of saturation, is:

$$r^*_c = \frac{2\cdot(-0.002T + 0.1215)\cdot(1-\exp(-B_2\cdot(1-S))}{p_T - p_v^0 - B_3(1-S)^{B_4} - \frac{B_5(1-S)}{(S-(S_p-0.015))^{B_6}}} \qquad (4.1.3)$$

The vapour-lock pore radius r^*_c in eqn. 4.1.3 was also connected to the particle diameter d_p by combining eqns. 2.4.15 and 2.4.18:

$$d_p = 4.33\cdot r_c^*\cdot\frac{1-\varepsilon}{\varepsilon} \qquad (4.1.4)$$

The important feature of this exercise is that it uses fundamental thermodynamical correlations among the parameters. Hence, the conclusions drawn from the results can be generalised to different drying systems.

The results of the calculations using eqns. 4.1.3 and 4.1.4 are presented in the form of three-dimensional graphs in Figure 4.1.1. The local temperature T and body saturation S are plotted as x- and y-axis respectively and the corresponding "vapour lock" pore radius r^*_c is plotted as the z-axis. Also plotted along a secondary z-axis are the corresponding values of particle diameter d_p, calculated using eqn. 4.1.4 for the 'typical' value of pellet porosity of 0.32.

Fig. 4.1.1 (a) shows that, for the range of saturation between 0.2 (the pendular state) and 1 (full saturation), and in the range of temperatures from 0^0C to 84^0C, the "vapour lock" pore radius is in the range of 1.0 to 2.8 μm. This corresponds to the range of mean particle diameters between 8 and 22 μm.

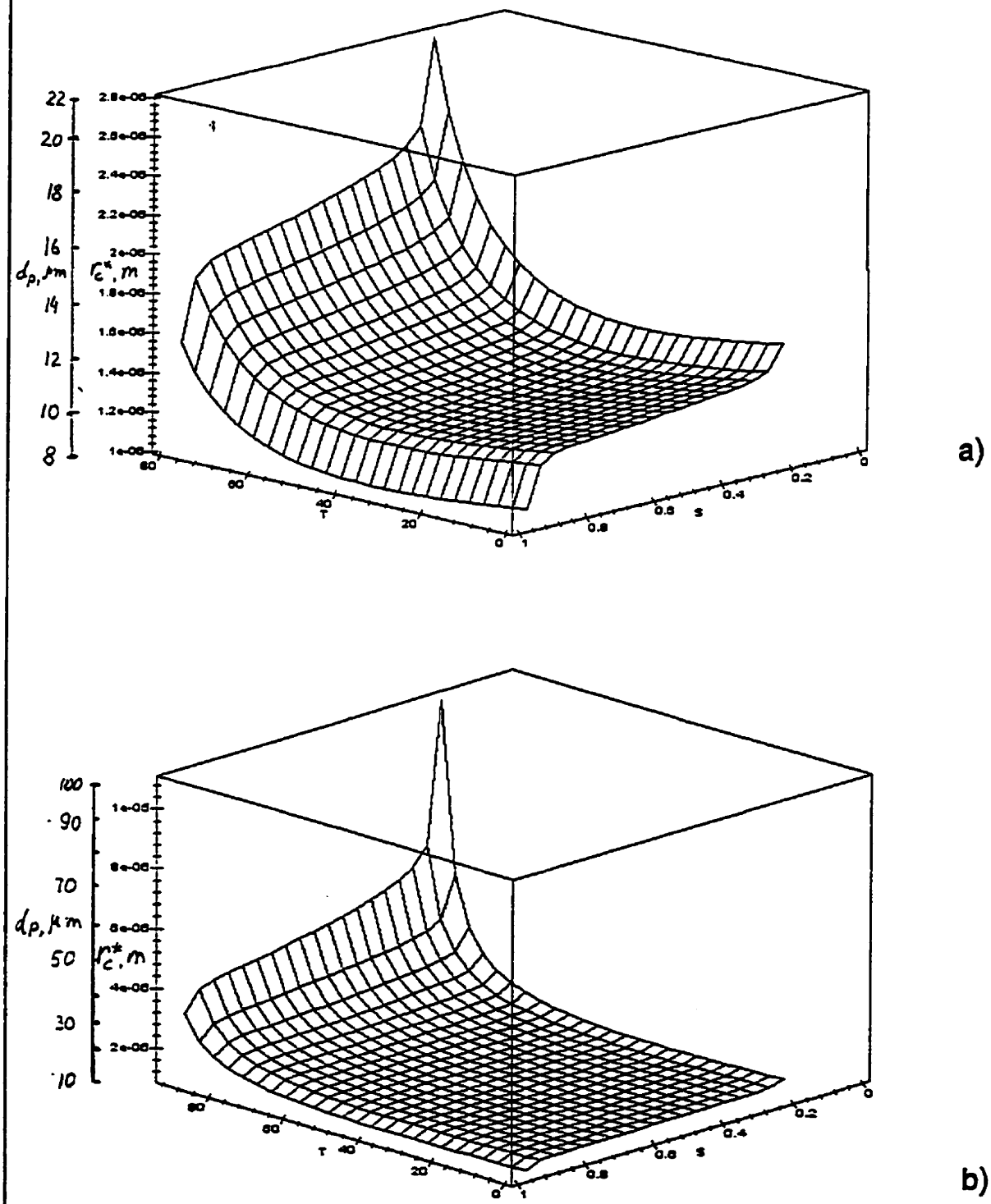


Figure 4.1.1. Dependence of critical pore radius and related particle diameter on surface temperature and saturation: a) over temperature range 0-80 deg.C; b) over temperature range 0 -94 deg.C.

It is of interest to provide a more detailed picture of the relationships in the extreme corners of the graph. It can be seen in Figure 4.1.1 (a) that, as saturation approaches the pendular state and surface temperature comes close to 100^{0}C, the equivalent pore radius "shoots up" to relatively high values. A compressed-axis graph is shown in Figure 4.1.1 (b). At 94^{0}C and saturation 0.22, i.e. the typical pendular-state value, r_c* is equal to 18 μm. This corresponds to a particle diameter of 165.6 μm. For conditions involving high pellet temperatures, therefore, the vapour lock may occur in packings of quite coarse particles.

Practical inferences can now be drawn with respect to the specific interests in this thesis: the drying of porous agglomerates. The first is that for agglomerates of fine particles the vapour lock sets in at relatively low body temperatures. For such agglomerates, the characteristic drying regime is likely to be the "intense" one (i.e. no constant-rate drying period), even under relatively "mild" drying conditions. This accounts for the observations in the available literature [59, 60] that, indeed, the absence of the constant-rate drying period was confined to agglomerates with fine pores.

The second is the behaviour of agglomerates of large particles (e.g. >20 μm mean particle diameter). For the vapour lock to occur here, a high local temperature, e.g. 80^{0}C, is required. Thus, a set of conditions, which would produce an intense drying regime for most ore agglomerates, would result in a typically mild regime in this case. However, another aspect of this evidence is that the constant-rate drying period can be brought to an end by the rise of the body temperature during its latter part. Thus, the large-pore vapour lock is likely to be important in the mechanism of the breaking-up of the liquid phase continuum in cases where the body reaches the pre-pendular stage of drying.

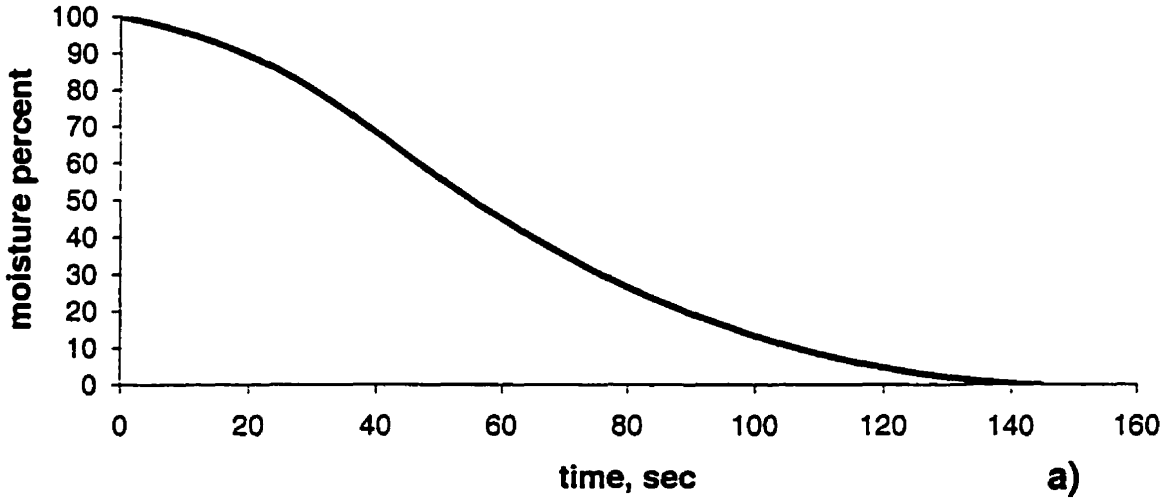
Of interest is the "lower limit" of the occurrence of the vapour lock. Calculations show that the minimum pore size for the vapour lock to occur at conditions near zero temperature, e.g. at T_S=0.001^{0}C and S=0.999, is $5.211 \cdot 10^{-8}$ m (particle diameter 0.4804 μm). Much attention has been devoted to the question of whether macroscopic thermodynamic equations are still applicable at such low pore sizes [77-82]. Fisher [82] reports that the force of adhesion for water, calculated from macroscopic thermodynamics, agrees with experiment for meniscus radii above 5 nm. Thus, for water, a pore size of 10-15 molecular diameters is sufficient to establish its macroscopic properties. This is, still, an order of magnitude lower than the lower limit of the applicability of the vapour lock noted above. Consequently, our approach of applying the vapour lock effect to the drying of fine (e.g. pore size of 0.1-10μm, or particle diameter of ~1-100 μm) granular materials is valid.

4.2. Modelling of Drying Behaviour

The extension to the drying model was documented in Chapter 3.2. In this Section the modelling results are presented for two sets of pore-size parameters of the agglomerate. The purpose is to specifically demonstrate the limitation of the Zaharchuk model and the ability of the extended model to better deal with the onset of the vapour lock in general, but in particular with the agglomerates featuring pore sizes in excess of about 2 μm.

Figures 4.2.1 and 4.2.2 present weight-loss curves and drying rate curves both plotted versus time. Figure 4.2.3 presents the calculated temperatures at the pellet surface, at the interface and the center plotted versus time. The 'typical pellet' parameters and drying conditions [1] were

AMBIENT TEMPERATURE	400 C
AIR VELOCITY	5.0 m/s
PELLET RADIUS:	6.0 mm
POROSITY:	0.32
BENTONITE	0.0 %
PARTICLE SIZE	7.1 um



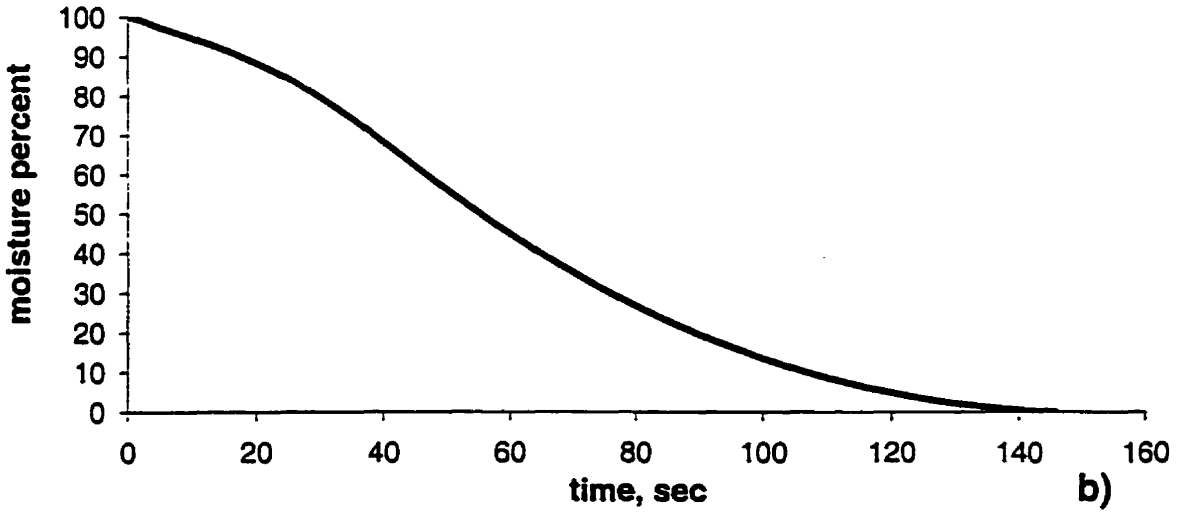
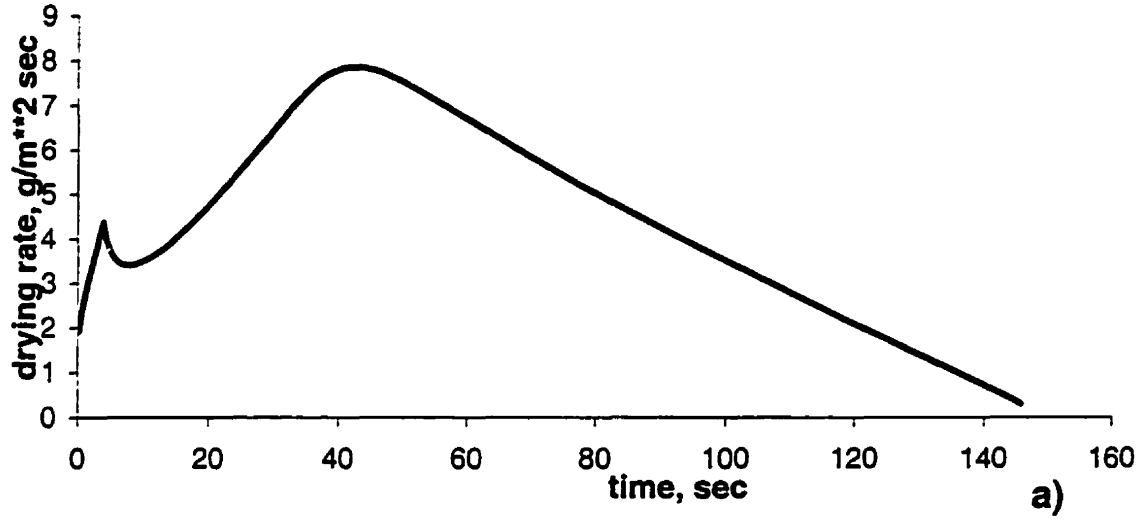


Figure 4.2.1 Drying Curve Predicted by: (a) - the Zaharchuk Model ;
(b) - by the Extended Model: Particle Diameter 7.1 um.

AMBIENT TEMPERATURE 400 C
AIR VELOCITY 5.0 m/s
PELLET RADIUS: 6.0 mm
POROSITY: 0.32
BENTONITE 0.0 %
PARTICLE SIZE 7.1 um



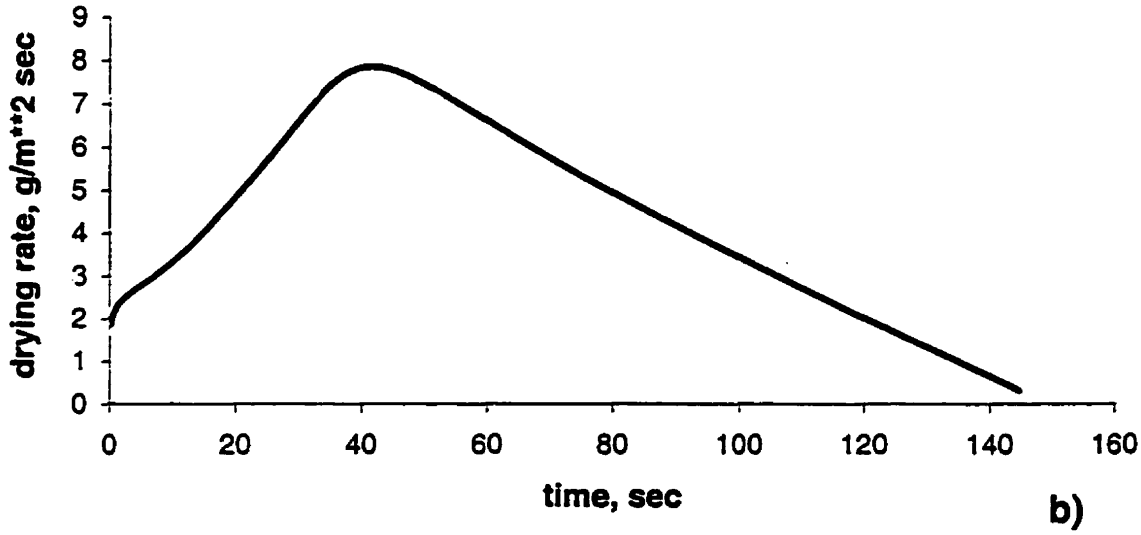
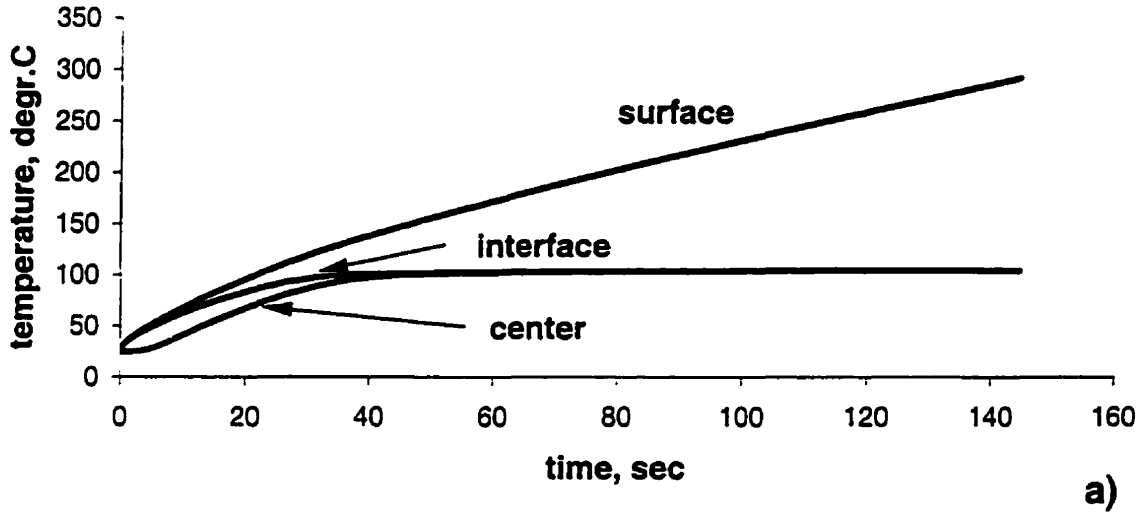
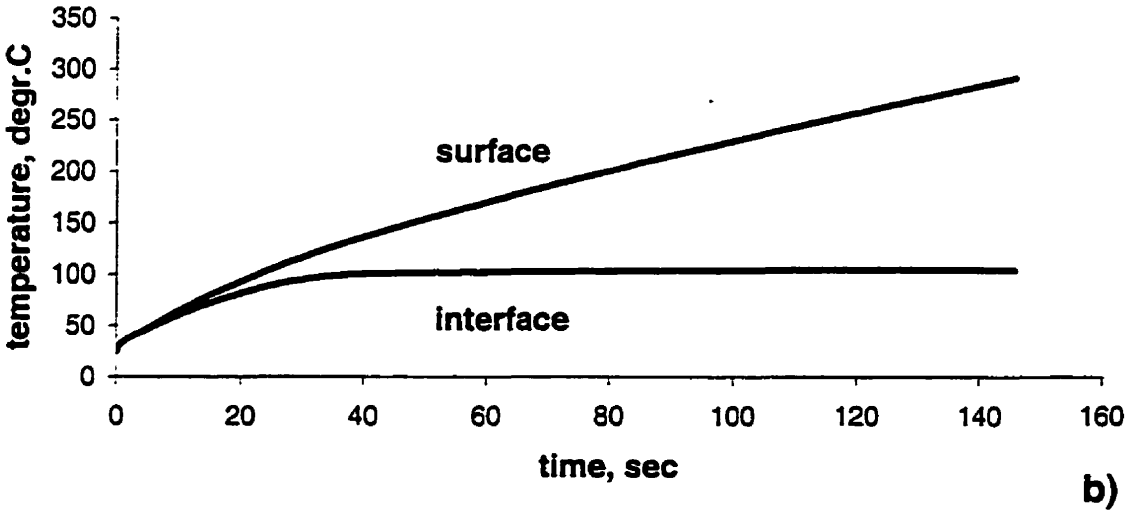


Figure 4.2.2 Drying Rate vs.Time Curve Predicted by:
(a) - Zaharchuk Model; (b) - by the Extended Model: Particle Diameter 7.1um.

AMBIENT TEMPERATURE 400 C
AIR VELOCITY 5.0 m/s
PELLET RADIUS: 6.0 mm
POROSITY: 0.32
BENTONITE 0.0 %
PARTICLE SIZE 7.1 um



a)



b)

Figure 4.2.3.(a) - Surface- , Interface- and Centre Temperature vs. Time Curves Predicted by the Zaharchuk Model; (b) - Surface- and Interface Curves Predicted by the Extended Model: Particle Diameter 7.1um.

used in these simulations (see Section 2.4.4). The upper graphs in the Figures correspond to the results using the Zaharchuk model and the lower ones - to those using the extended model. Note that the extended model algorithm does not incorporate the prediction of temperature at the pellet center. Hence, there are only two curves in Figure 4.2.3 *b* corresponding to temperatures at the pellet surface and at the interface.

For an average particle size of 7.1 μm there is practically no difference in the shape of drying curves between the original and the extended model results(Figure 4.2.1 *a* and *b* respectively). The *drying-rate* curves calculated using the Zaharchuk model show the odd "saddle-shape" portion in the initiation period. This is direct consequence of theassumption of an instantaneous-transition (Section 3.1). This 'saddle' is absent in the extended-model plot. This fact is an obvious improvement over the original model. For this set of pellet parameters however, the benefit achieved by the model extension is not that significant. This is because the transition between the surface- and shrinking core drying regimes occurs early in the drying process. Therefore, the transition period here is relatively short.

The latter point is reflected also in Figure 4.2.3, where practically no difference in the shape of the respective temperature curves is visible. The departure of the interface temperature curve from the surface curve, signaling the onset of the shrinking core drying period, occurs at ~42^{0}C.

In order to highlight the significance of the improvements to the model, additional model simulations were carried out with the average particle size d_p of 20 μm instead of 7.1 μm. For this case, the transition to the shrinking-core drying regime is delayed and the difference between two

models becomes appreciable. Weight loss curves, drying rate curves and pellet temperature curves predicted by the two versions of the model are shown in Figures 4.2.4 to 4.2.6 respectively. As previously, the upper graphs in the Figures present the Zaharchuk model predictions and the lower ones -- those of the extended model.

Both drying curves in Figure 4.2.4 exhibit a discontinuity, a new feature absent in the fine-particle pellet modelling (see Figure 4.2.1). The significance of the discontinuities is better seen on the respective drying-rate curves in Figure 4.2.5. For the coarser-particle agglomerate the Zaharchuk drying model (Fig.4.2.5 *a*) predicts a distinct constant-rate drying period. The latter is terminated by an instantaneous drop of drying rate at 51 sec drying time. This drop reflects the instantaneous transition to the shrinking core regime. The vertical drop corresponds to the observed inflection on the drying curve in Fig. 4.2.4 *a*. After this rapid drop, the drying rate rises again to a maximum at 68 sec, and then, finally, decreases until the end of the drying process.

Significantly, the extended model predicts no constant-rate drying rate period. Instead, Fig.4.2.5 *b* exhibits a distinct maximum at a drying time of 25 sec, followed by a gradual decrease of the drying rate until a drying time of 65 sec. The minimum, characteristic of the Zaharchuk model, is eliminated. A sharp discontinuity of slope in Figure 4.2.5 *b* is introduced, which reflects the completion of the transition to the shrinking core drying regime. In time, this inflection corresponds to the change in slope of the drying curve in Figure 4.2.4 *b*. After a very brief rise following the inflection, the drying rate decreases until drying is complete.

The temperature curves for the above set of pellet parameters are presented in Figure 4.2.6. An extensive constant temperature period, at 63^0C, is evident in Figure 4.2.6 *a*. This stage

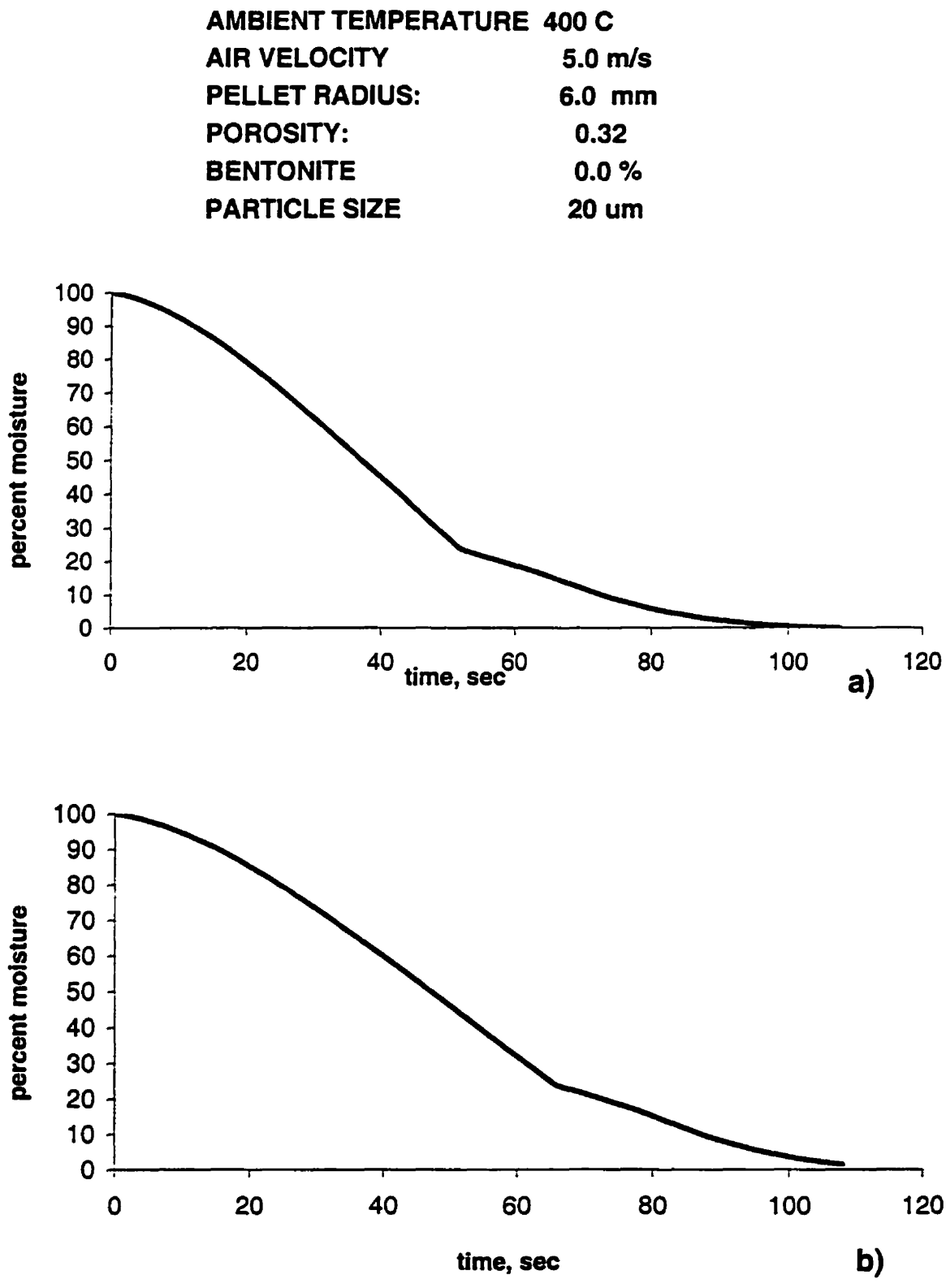


Figure 4.2.4 Drying Curve Predicted by: (a) - the Zaharchuk Model ;
(b) - by the Extended Model : Particle Diameter 20um.

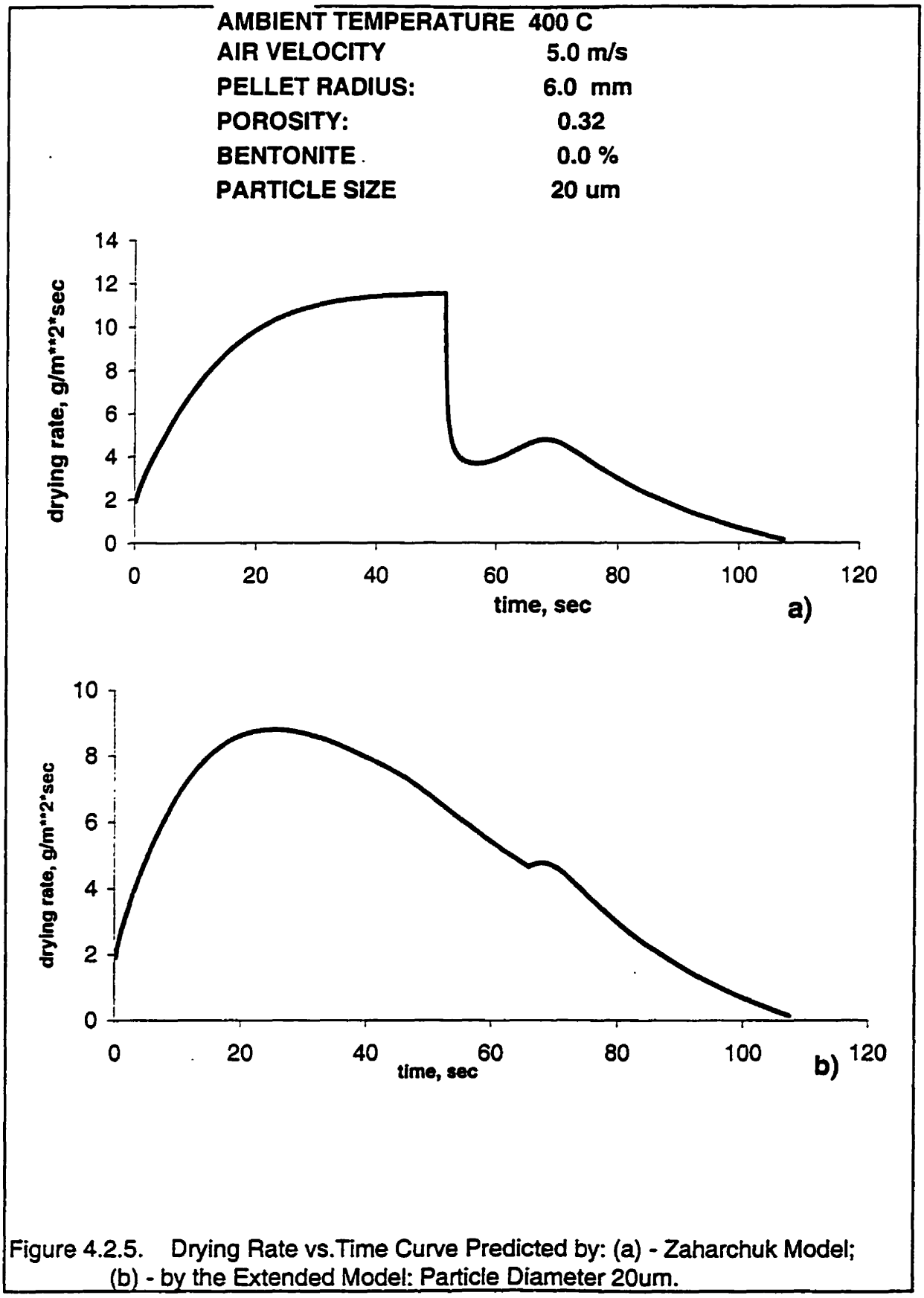


Figure 4.2.5. Drying Rate vs.Time Curve Predicted by: (a) - Zaharchuk Model; (b) - by the Extended Model: Particle Diameter 20um.

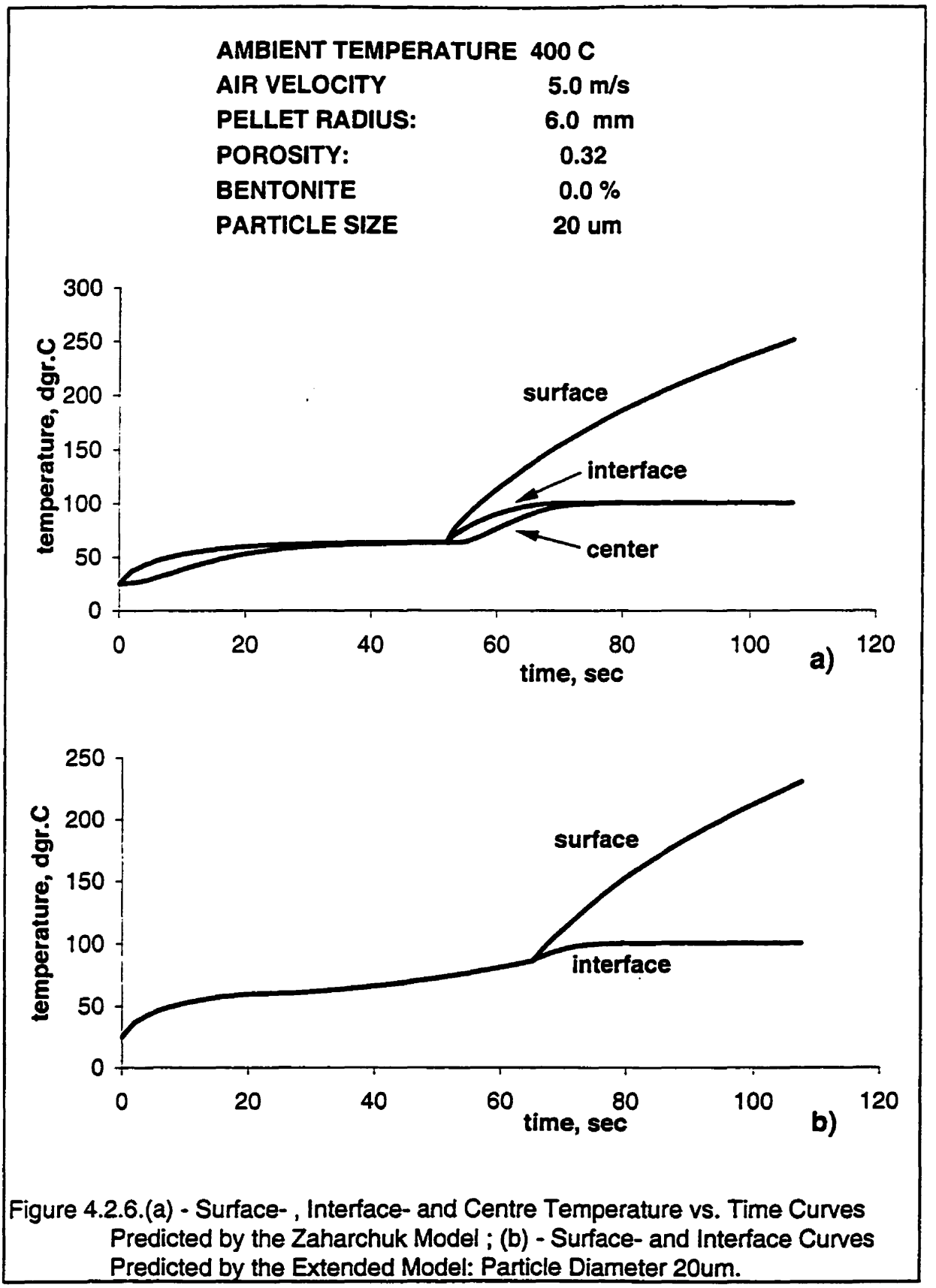


Figure 4.2.6.(a) - Surface- , Interface- and Centre Temperature vs. Time Curves Predicted by the Zaharchuk Model ; (b) - Surface- and Interface Curves Predicted by the Extended Model: Particle Diameter 20um.

corresponds to the constant rate drying in Figure 4.2.5 *a*. According to the Zaharchuk model, a surface drying regime sets in following the temperature rise during initiation period, and continues until 51 sec. After the instantaneous transition to the shrinking core drying regime at 51 sec (see the corresponding vertical drop in drying-rate curve in Fig. 4.2.5 *a*) the surface temperature rises rapidly. The interface temperature also increases, although at a slower pace. Importantly, this causes the driving force for the product vapour diffusion through the dry shell to increase. Vapour diffusion controls the drying rate at this stage (see Section 3.1), and this fact explains the rising drying rate in Figure 4.2.5 *a* between the ~55 and 68 sec marks. The interface temperature in Figure 4.2.6 *a* reaches the 100^{0}C mark at 68 sec time. This corresponds to the 'lower' local maximum on the drying rate curve (see Fig. 4.2.5 *a*). At this point the rate-controlling mechanism changes from vapour diffusion to heat transfer through the dry shell (see Section 3.1). Afterwards, both interface- and center temperatures stay constant just above 100^{0}C for the remainder of the drying process. This stage corresponds to the final decline of the drying-rate curve in Figure 4.2.5 *a* , caused by the resistance to the heat conduction through the dry shell increasing with the receding wet/dry interface.

According to the improved model (Fig. 4.2.6 *b*), surface temperature also rises during the initiation period. After reaching the value of around 60^{0}C at 20 sec, the temperature rise slows down, as the smallest pores at the surface start to experience the vapour lock. Contrary to the predictions of the Zaharchuk model, a constant temperature is never established at the surface. After 25 sec of drying (which corresponds to the maximum on the drying rate curve in Figure 4.2.5 *b*), the surface temperature continues to increase gradually. The reason for this rise is that,

as a progressively larger fraction of the pores is becoming vapour-locked (and therefore inoperative as surface-drying sites), an increasing fraction of heat input is being used for heating up the pellet.

The surface-temperature rise in Figure 4.2.6 *b* continues until the value of 87^0C is reached at 65 sec drying time. At this point the area of the remaining unlocked pores, and, thus, the rate of water delivery to the surface by Darcy flow (determined by eqn. 2.4.14 in Section 2.4.1) becomes too small to consume the heat input to the surface. Hence, after the 65 sec mark, the shrinking core period effectively sets in. The surface temperature therefore, rises sharply, while the temperature of the interface, reaches the 100^0C mark, and stays almost constant for the rest of the drying process. This stage corresponds to the decline of drying rate in Figure 4.2.5 *b* beyond the second small maximum. As in the Zaharchuk model, temperature behaviour is explained by the increasing resistance to heat transfer through the ever-thickening dry shell.

4.3. The Concepts of Mild and Intense Drying and Transition Between them

As stated in the previous chapters the term "intense drying" was chosen to describe a drying regime which deviates from the 'classical' or mild-drying regime, i.e., is characterized by a complete absence of the constant-rate drying period. The basic postulate of this study is that, in the intense drying case, the vapour lock interrupts the surface drying stage *before* conditions for the constant-rate drying period can be established. In turn, it was shown in Sections 4.1 and 4.2 that the pore size of the agglomerate plays a very significant role. The objective of this Section, therefore, is to identify the combinations of pellet parameters (those controlling the pore

size, i.e., particle size and porosity), and drying conditions (e.g., temperature), so as to define the distinction between intense and mild or normal drying regimes. Also to be identified are the issues in the transition between the two drying regimes.

Figure 4.3.1 shows a series of drying-rate versus time curves calculated using the original Zaharchuk model. The pellet-property parameter in the figure is particle diameter of the constituent powder and, therefore, the pore size of the agglomerate. Otherwise, the pellet properties and drying conditions were the 'typical' ones. (Note that the model allows for the dependence on particle size of the relevant pellet properties, e.g., the diffusivity and thermal conductivity).

The Zaharchuk model was used for the calculations, because it is best suited to demonstrate the phenomenon of concern presently, namely the existence of a pattern of the highest achievable surface-drying rates as distinct from the maximum overall, or absolute, drying rates.

In Figure 4.3.1 the *absolute* maximum drying rates are indicated by the B_i while the maximum *surface-drying* rates are the sharp maxima, familiar from Figures 4.2.2(a) and 4.2.4 (a), and indicated by the A_i. The latter are the values of the drying rates at the instant when the drying front shifts from the surface to the receding interface (recall that in the Zaharchuk model this shift is instantaneous). One notes that there is a definite pattern to the relative magnitudes of these two maximum drying rates. For the fine particle-size pellets (curves *1* and *2*) the overall maximum rate is higher than the maximum surface rate. For the coarser-particle pellets, when the surface/shrinking-core transition shifts to later stages of drying (curves *3* and *4*), these two maximum rates approach each other and/or become identical at high enough pore sizes (curves

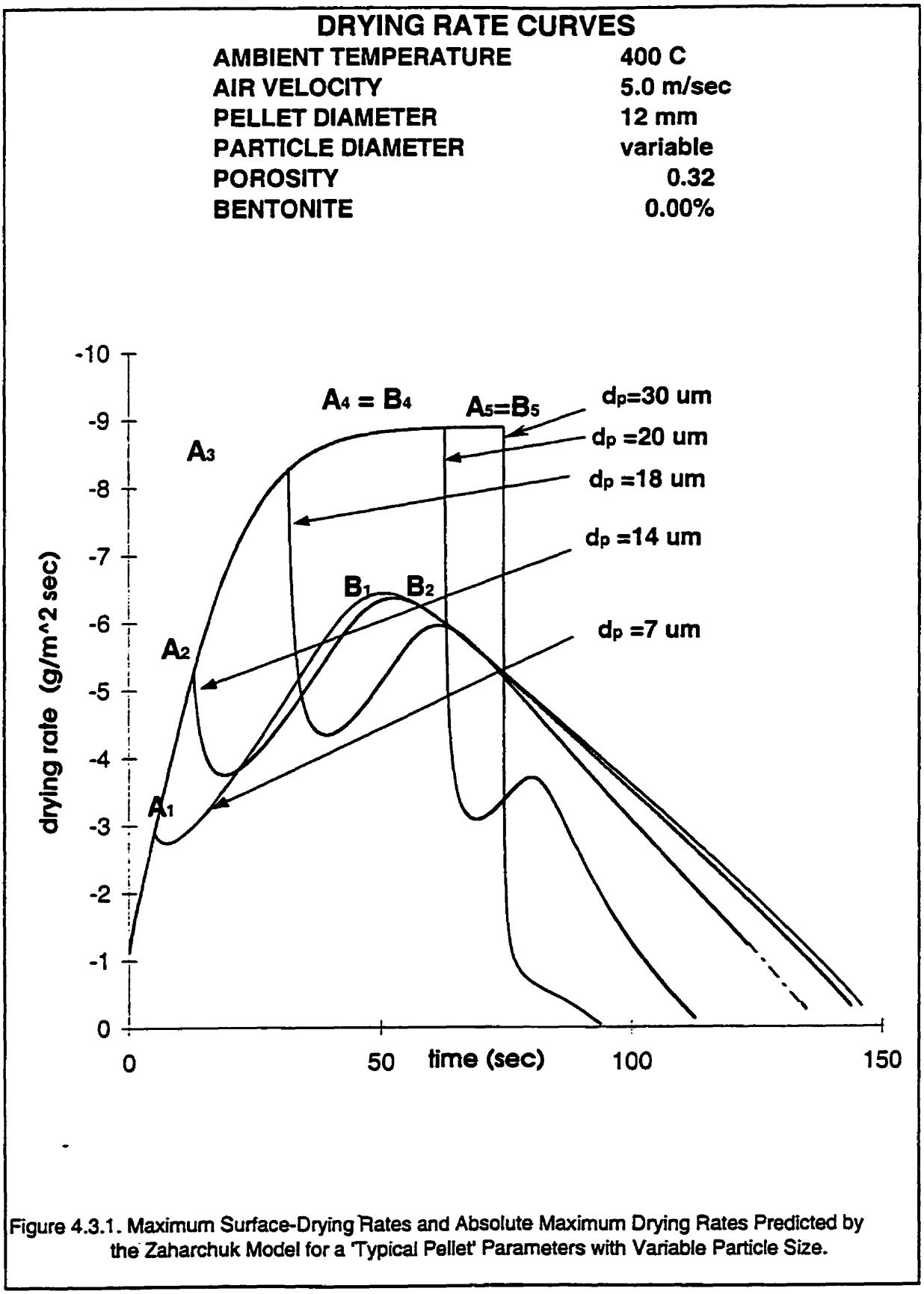


Figure 4.3.1. Maximum Surface-Drying Rates and Absolute Maximum Drying Rates Predicted by the Zaharchuk Model for a 'Typical Pellet' Parameters with Variable Particle Size.

4 and *5*). This makes the drying-rate during the constant-rate period also the absolute maximum drying rate for the particular drying conditions. Clearly, when a constant-rate period exists, the drying-rate is both the maximum absolute drying rate, and the maximum surface-drying rate.

What has so far been referred to as intense drying is associated with the non-existence of a constant-rate period. Under these conditions, the heat and mass transfer rates within the porous body of agglomerate are slowed down by the vapour lock. The actual maximum drying rate under "intense" drying conditions therefore, turns out to be less than that potentially possible, e.g., where the heat and mass transfer across the boundary layer are the only rate limitations. To further document and illustrate these generalizations the results of additional modelling have been plotted in Figures 4.3.2 and 4.3.3.

The maximum surface- and maximum overall drying rates achievable for a 'typical' pellet are plotted against the pore-size-controlling variables, the particle diameter d_p and matrix porosity ε, respectively. The plots are for three drying temperatures which cover the range of drying intensity of interest presently.

Figure 4.3.2 now shows systematically the trends which are merely suggested in Figure 4.3.1: for small particle sizes (including the 'typical' 7.1μm) the maximum surface-drying rate (shown with dotted lines) increases rapidly with the particle size (and, therefore, pore size!), while the overall-maximum drying rates stay relatively constant or increase slightly. At a critical particle size, e.g. 15 μm, 18 μm and 22 μm respectively for the 200, 400 and 600^{0}C temperatures, the two become equal (compare the trends of the curve for d_p=18 μm in Figure 4.3.1 at point A_3 and beyond). Both maximum drying rates, now equal, rise rapidly with increasing particle size. Again, these trends continue at all drying temperatures until a horizontal

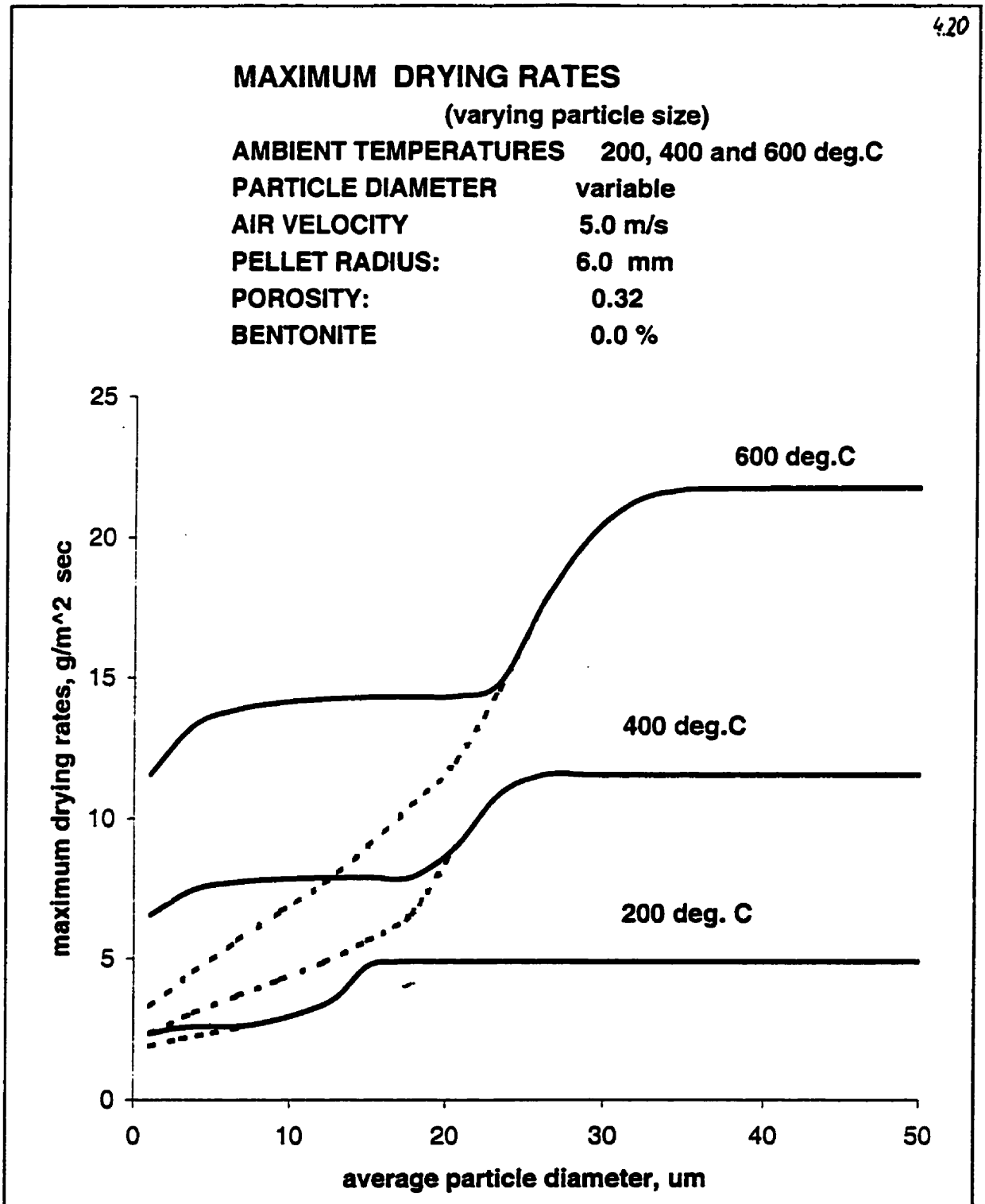


Figure 4.3.2. Dependence of Model-predicted Maximum Drying Rates on Particle Diameter and Drying Temperature. Maximum Surface-Drying Rates are Shown with Dotted Lines; Solid Lines are the Absolute Maximum Drying Rates.

condition, a limiting maximum drying rate, is reached. The latter portions of the curves, of course, correspond to the drying rates of the constant-rate periods in each case.

Similar trends are also observed in the series of model simulations, plotted in Fig. 4.3.3, where pellet porosity is the variable. Similarly to Figure 4.3.2, the absolute maximum drying rate first stays essentially unchanged, and then rises with increasing porosity. When the latter reaches the value of typically 0.5, 0.54 and 0.62, the constant rate drying period sets in, for the drying temperatures 200^{0}C, 400^{0}C and 600^{0}C, respectively. Such high values of porosity are unrealistic in agglomeration practice. In the literature [15] this range of porosity values is, however, reported in connection with the very loose random packing obtained by fluidization (see Table 2.2.1.1 in Section 2.2.1).

A general and important observation is that, by increasing the drying temperature, i.e., the intensity of the drying conditions, the maximum absolute drying rates do become significantly higher, so that their values even when there is failure to reach the constant rate drying regime, are still the highest values achievable.

The other important observation from these results is that the values of maximum absolute drying rates for the cases of the so-called intense drying regimes (left portions of the curves) are in fact smaller than those at the constant-rate drying level. Yet the latter is to be identified as a 'mild' drying regime. This observation may be somewhat discomforting with respect to the chosen terminology. Yet, it is simply a fact that, under a given set of conditions, the drying rate at the pellet surface is always potentially faster than at the receding wet/dry interface.

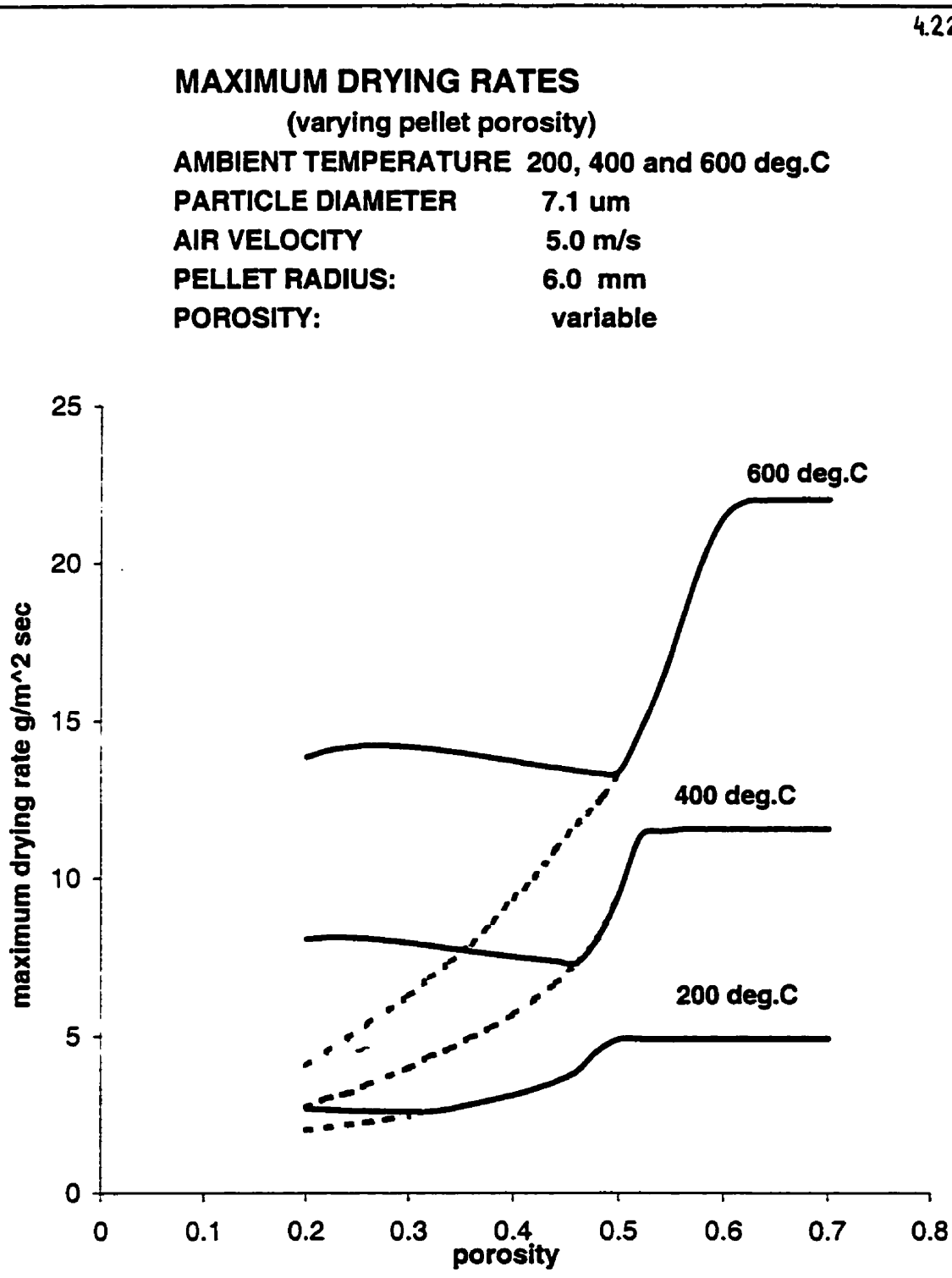


Figure 4.3.3. Dependence of Model-predicted Maximum Drying Rates on Porosity and Drying Temperature. Maximum Surface-Drying Rates are Shown with Dotted Lines; Solid Lines are the Absolute Maximum Drying Rates.

4.4. Tumbling-and-Drying Investigations

Tumbling-and-drying is a term used to describe the operation of a balling drum with simultaneous injection of heated air to dry the pellets while they 'tumble'. It has been shown in earlier studies [86, 103] that the pellet matrix densifies uniformly in the process, i.e. the pellet porosity decreases. Tumbling-and-drying, therefore, is potentially a method to increase the dry strength and spalling resistance of the pellets and thus is an attractive operation in the industrial production of the high-grade iron ore agglomerates. Another task addressed in this project, therefore, was to generate both model and experimental results to assess quantitatively the effect of the tumbling-and- drying operation on the resulting dry strength of the pellets, on stresses built up in these pellets during intense drying, and thus the increase in their shock temperature. The latter term will be defined further in this Chapter.

4.4.1. Existing Experimental Data Base

Six groups of pellets have been produced previously in our group by tumbling-and-drying [50, 92] using a laboratory pelletizing drum. The blowing of heated air over the pellet charge in the rotating pelletizing drum was interrupted six times and pellet samples were collected for later analysis. The sample pellets from each group were dried completely in the laboratory oven at 85^0C, and their dry strengths were determined using the diametral compression test (see Section 5.5). The results of this investigation are summarized in Table 4.4.1.1.

Table 4.4.1.1 Results of Tumbling-and-Drying Experiment [92].

Group #	No. of Pellets Tested	Porosity (dry basis)	Initial Saturation	Dry L/D^2 (kPa)	Dry Strength (eqn. 2.5.1.6) (kPa)
1	2	0.325	0.8952	40.5765 (1.2127)*	31.7004 (0.9474)*
2	1	0.2501	0.9995	84.373	65.9164
3	2	0.2441	0.8941	94.1055 (9.1563)	73.5199 (7.1534)
4	3	0.289	0.8599	101.5415 (15.3421)	79.3294 (11.9860)
5	1	0.2555	0.968	129.395	101.0898
6	3	0.2615	0.8008	130.308 (29.0784)	101.8031 (22.7175)

* Values in brackets represent standard deviations (where applicable)

The presented results show that porosity of the dried pellets has decreased significantly with the degree of tumbling-and-drying. Also, the values of dry strength in these pellets are correspondingly higher. The initial degree of saturation shows a significant scatter, presumably related to errors during handling.

The increase in dry strength can be seen better in Figure 4.4.1.1, where the experimental values are plotted as a function of porosity. A linear regression fit is shown with a dashed line. Also shown is the trend line predicted by the Zaharchuk model (see eqn. 2.5.1.8 in Section 2.5.1). The latter underpredicts the observed increase in dry strength in tumbled-and-dried pellets by as much as 50%. This fact implies that some other mechanism, not included in the model, may be responsible for the observed increase of these pellets' dry strength. A possible origin of such a mechanism is the additional strengthening, resulting from extensive particle rearrangements,

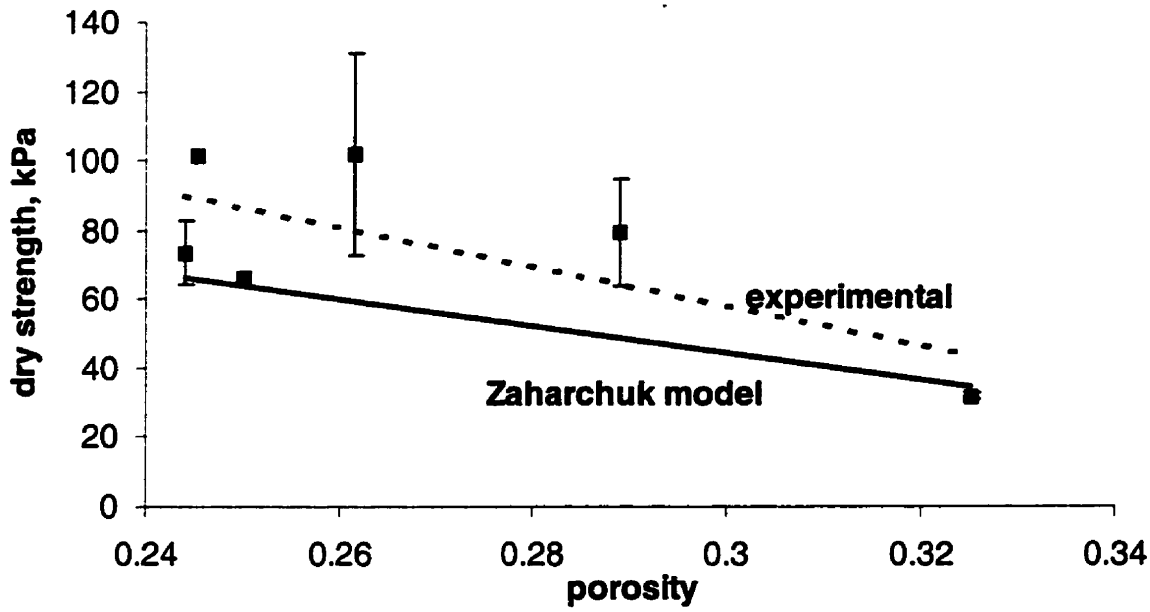


Figure 4.4. 1. 1. Experimental Results of Dependence of Dry Strength on Porosity in Tumbled-and-Dried Pellets.

the destruction of the particle network structure (see Section 3.4) and of the ink-bottle effect and thus an increase in the co-ordination number. Also, interparticle contacts due to particle migration during drying (see Chapter 3.4) may be a factor.

4.4.2. Modelling the Drying Behaviour of Tumbled-and-Dried Pellets

In the modelling of the drying behaviour of tumbled-and-dried pellets during intense drying, properties of representattive pellets from groups 1, 4 and 6 were used. These represent a sufficient range of degrees of tumbling-and-drying exposure. Key properties of these pellets are listed in Table 4.4.2.1.

Table 4.4.2.1. Parameters of Tumbled-and-Dried Pellets [52]

Group #	Density, g/cc	Moisture %	Porosity dry basis	Diameter mm	Mass g	Initial Saturation	Dry Strength kPa
1	3.292	8.76	0.3296	12.1	3.052	0.875	32.37
4	3.444	7.47	0.2986	12.16	3.241	0.862	70.854
6	3.656	5.79	0.2554	9.09	1.437	0.829	110.62

'Typical' rapid drying conditions, 400^{0}C and air velocity 5 m/sec, were used in the simulations. The resulting drying-rate curves are shown in Figure 4.4.2.1. The densest *Pellet* 6 can be dried much faster than the other two. Its total drying time was 62 seconds, which is two times shorter than that of *pellet* 4. Gains in drying time attained in *pellet* 6 over *pellet* 1 are even more pronounced - 2.25 times.

Next is the evaluation of the resistance to spalling of the pellets densified by the tumbling-and-drying operation. Results of the calculation of the maximum drying stresses for the three pellets are shown in Figure 4.4.2.2. Plotted are the total circumferential stresses at the wet/dry interface versus percent radius. The circumferential stresses are the highest (see argument in Section 2.4.4) and, hence, they are considered as the primary cause of pellet spalling [1].

The differences in stress levels built up in the pellets are relatively minor. The stress curve for *pellet 6* at first exhibits a higher slope and then a lower one compared to the curves for *pellets 1* and *4*. The horizontal lines in Figure 4.4.2.2 are the experimentally measured values of dry strengths of the pellets, taken from Table 4.4.2.1.

The susceptibility of pellet to spalling is indicated by the points of intersection of the

MODEL DRYING RATE CURVES OF THE TUMBLED-AND-DRIED PELLETS

MATERIAL	**GRIFFITH CONCENTRATE**		
PARTICLE DIAMETER	**7.1 um**		
AMBIENT TEMPERATURE	**400 deg. C**		
AIR VELOCITY	**5.0 m/s**		
Pellet Parameters:	Pellet 1	Pellet 4	Pellet 6
PELLET RADIUS:	**6.05 mm**	**6.18 mm**	**4.54 mm**
POROSITY:	**0.3296**	**0.2986**	**0.2554**
SATURATION	**0.875**	**0.862**	**0.829**

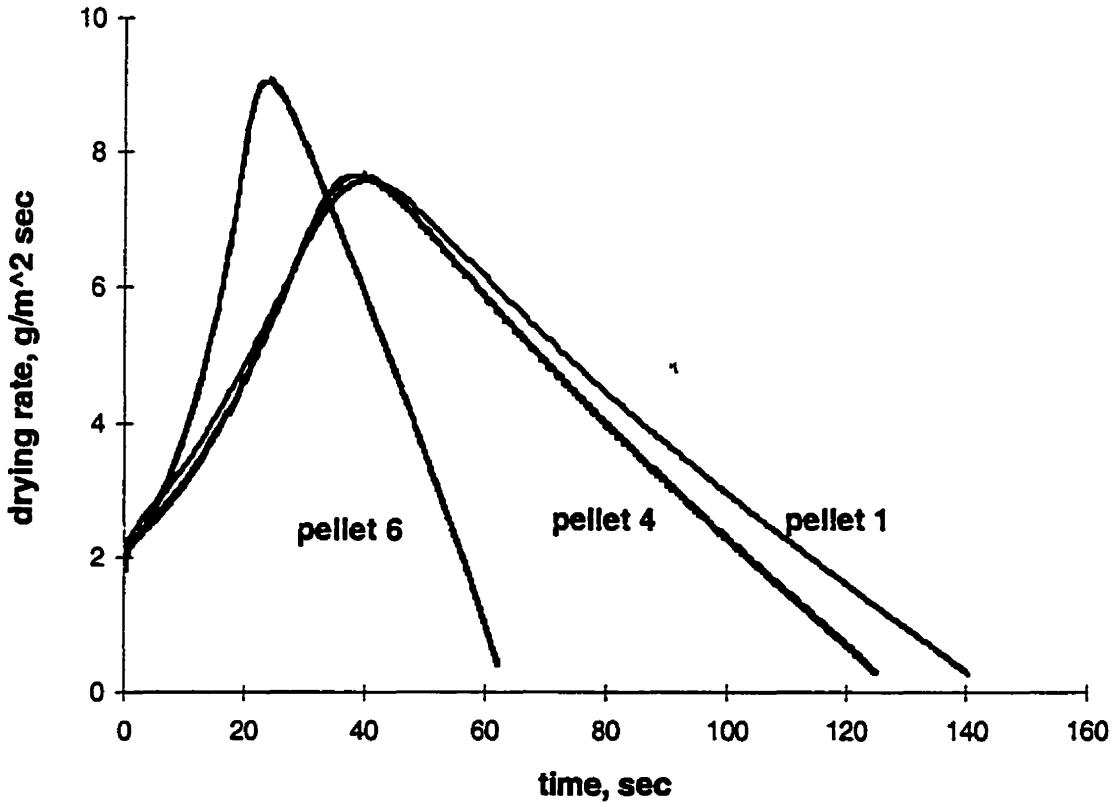


Figure 4.4.2.1.Model Drying Rate Curves of Pellets Produced by Tumbling-and-Drying.

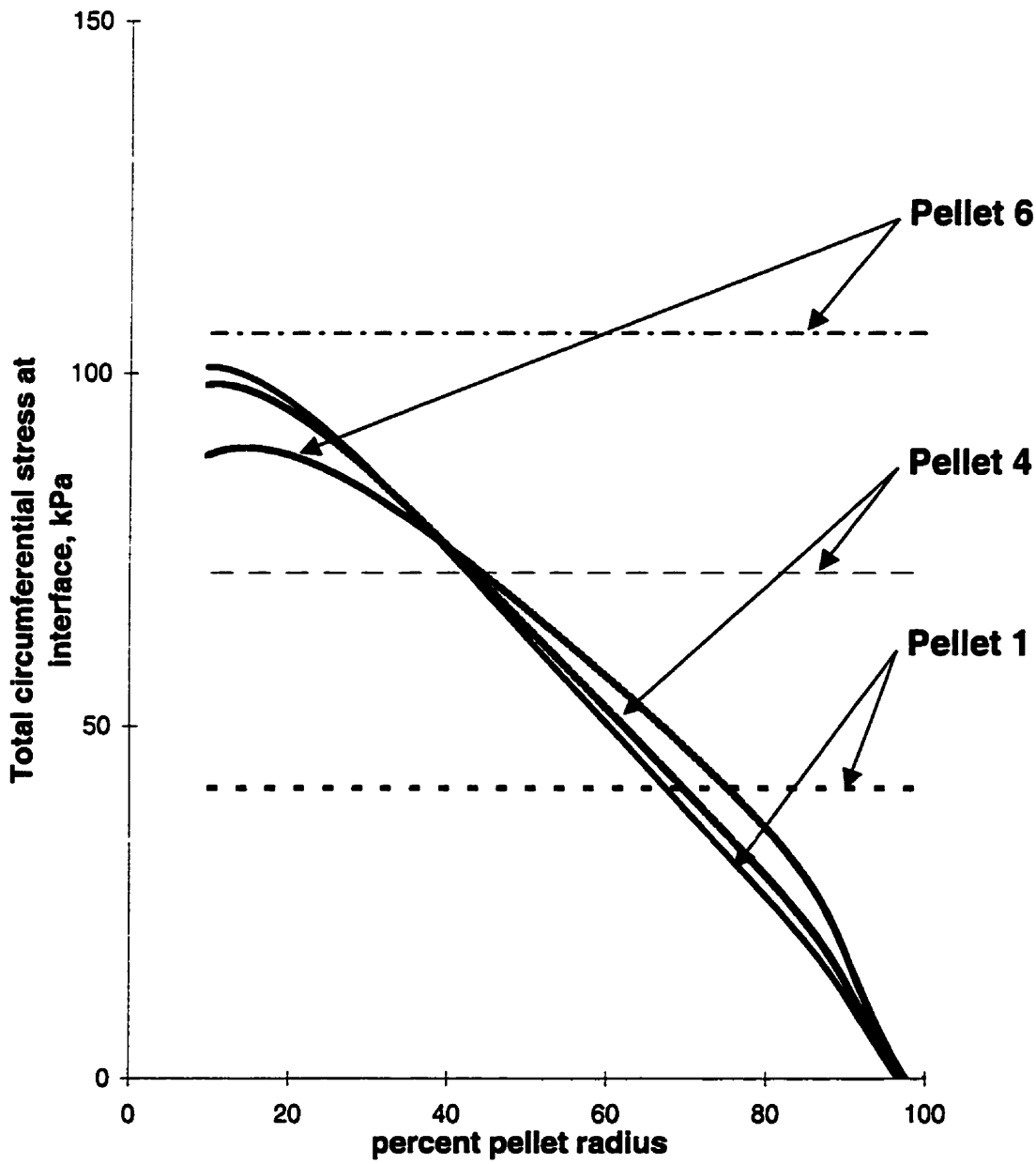


Figure 4.4.2.2. Total Circumferential Stresses at Interface during Drying at 400 deg.C of the Tumbled- and-Dried Pellets.

respective stress- and strength lines. According to Figure 4.4.2.2, *pellet 1*, being mechanically weaker, will likely experience spalling at the early stages of drying at 400^{0}C. Its wet/dry interface is still close to the pellet's surface. *Pellet 4*, and especially *pellet 6* are not likely to spall at this drying temperature. Their dry strengths are substantially higher and intercepts of the strength lines with the respective stress curves occur when the wet/dry interface is deep in the pellet's interior, or, in case of *pellet 6*, does not occur at all.

The above results show clearly that there are significant prospective benefits of the tumbling-and-drying operation. These advantages are two-fold: the first is that part of the moisture is removed prior to the drying operation, making the latter technological process easier. The second is a significant degree of strengthening of the pellets due to their densification. Even though the stress buildup in the pellets is not changed greatly, the improved tensile strength increases resistance to spalling. This fact would allow the drying operation to be carried out under more intense conditions, thus improving the capacity of the indurating machines *and* reducing the operating cost.

4.4.3 Modeling of the Spalling Resistance during Intense Drying

A more systematic model simulation of the stress buildup in pellets produced by tumbling- and-drying was performed as described below. The purpose was to predict the limiting drying conditions at which spalling can be avoided.

The concept of a *shock temperature* is used in the literature [93-96] to provide a measure of the pellet's spalling resistance (see Chapter 2.5.2). In our study we arbitrarily defined the shock temperature to be the drying temperature at a 'typical' air flow of 5 m/sec, at which the level of total circumferential stress at the wet/dry interface location of 50% of the

pellet's radius exceeds the value of the pellet's dry strength.

Simulations of drying at different drying temperatures were performed on a pellet with 0.8% bentonite and varying porosity values but otherwise 'typical' parameters and drying conditions (see Table 2.4.4.1). The strengths were calculated using eqn. 2.5.1.8. Results of these simulations are presented as a plot of the shock temperature against pellet's porosity in Figure 4.4.3.1.

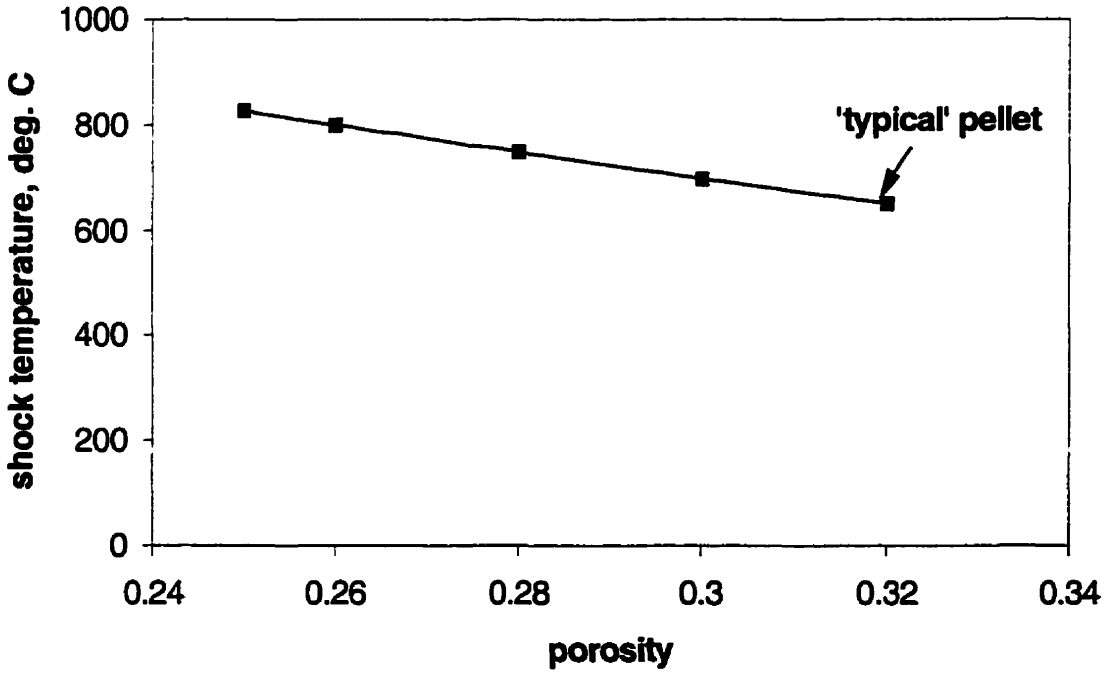


Figure 4.4.3.1. Model Dependence of Shock Temperature on Pellet's Porosity.

The graph shows clearly the beneficial effect of pellet's densification that can be achieved by tumbling-and-drying. The densification would enable increasing the drying temperature by

as much as 30%, typically from 600 to 800^{0}C, while still avoiding the spalling problem.

4.5 Modelling of the Effect of Bentonite on Spalling Resistance

The conventional way of improving the spalling resistance of the pellets, which has been used extensively for decades, is by adding bentonite [93-96, 103].

The effect of bentonite additions on shock temperature was modelled in this study. The model simulation procedure used was analogous to that used previously (see Section 4.4.3), except here the bentonite content, instead of porosity, was the variable. Results of model simulations are given graphically in Figure 4.5.1, which presents the dependence of shock temperature on weight percent bentonite added.

According to our results, there is significant increase in spalling resistance as bentonite is being added. However, after bentonite concentration reaches 0.8wt.% (which happens to be a standard amount used in industry), this effect reverses itself. Any further additions of bentonite have a detrimental effect on the shock-temperature. This trend is consistent with the results of Schultz et al. [93] and Roorda et al. [94] (see Chapter 2.5.2).

In order to investigate this peculiar phenomenon, further model simulations were performed. Their aim was to establish the dependence of maximum stress levels at different temperatures and pellet's strength on the amount of bentonite added, and thus the reason for the maximum in Figure 4.5.1. The results of these model simulations are summarized graphically in Figure 4.5.2. The curves represent the dependence of maximum tensile stresses arising at a wet/dry interface located at 50% radius of a 'typical' Griffith pellet at three different drying temperatures - 600^{0}C, 620^{0}C and 650^{0}C, as a function of amount of bentonite added. These

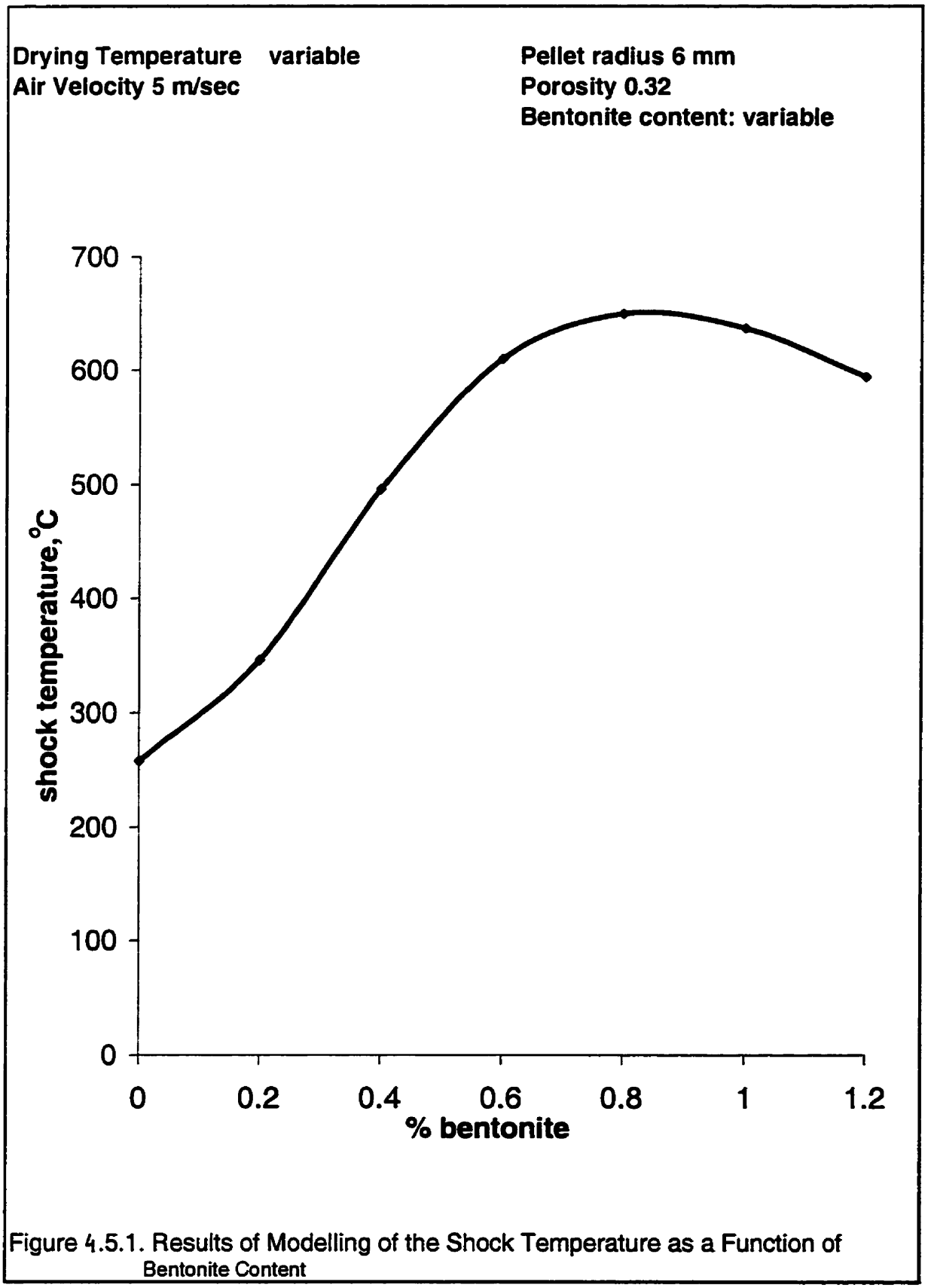


Figure 4.5.1. Results of Modelling of the Shock Temperature as a Function of Bentonite Content

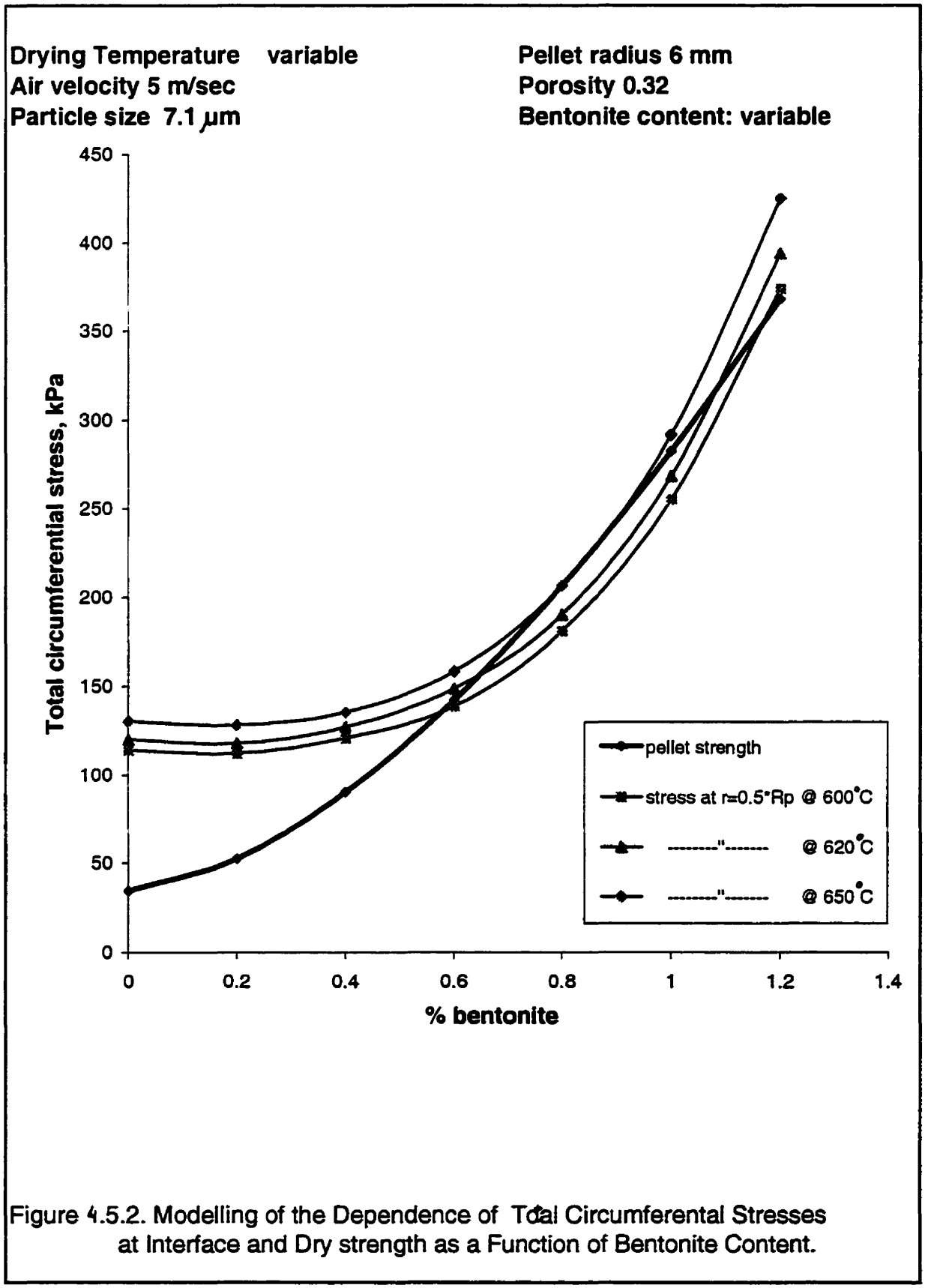


Figure 4.5.2. Modelling of the Dependence of Total Circumferental Stresses at Interface and Dry strength as a Function of Bentonite Content.

temperatures were chosen because they are adjacent to the shock-temperature peak in Figure 4.5.1. Also plotted in the same graph is the pellet's dry strength, also calculated by the model (eqn. 2.5.1.8), as a function of bentonite content.

At low bentonite concentrations the stress level is rising much slower than the pellets' strength. As the concentration of bentonite approaches 0.8%, however, this trend inverts, with stress curves rising faster than the pellet strength. It is this inversion of slopes that is responsible for the leveling-off the shock temperature near 0.8% bentonite content.

Lower drying temperature stress curves yield two intersection points with the strength curve: one below and one above the 0.8% bentonite content. These points signify the highest temperatures, at the corresponding bentonite concentrations, at which no spalling can be expected.

As noted in Figure 4.5.1, the maximum temperature at which a pellet containing 0.8% bentonite can be dried 'safely' is 650^0C. At this temperature and bentonite level stress and strength curves in Figure 4.5.2 are tangent. Any further increase in the drying temperature would result in the stress curve exceeding the strength curve at all % bentonite and thus ultimately lead to pellet's spalling.

Chapter 5

EXPERIMENTAL MATERIALS AND PROCEDURES

5.1 Experimental Materials

Much of the previous experimental work in our group has been done using the magnetite concentrate from the Griffith Mine at Red Lake, Ontario. Although the Griffith Mine was shut down, a sizeable sample of the concentrate has been available since 1982.

At the Griffith Mine the raw concentrate was beneficiated by screening, magnetic separation and floatation. The resulting wet filter cake contained ~9% water on a wet basis. Griffith bentonite was used as binder, added at the level of 0.8% by weight. It was mixed with the filtered concentrate in a pug-mill mixer prior to feeding into a balling drum. Particle size analysis of a typical sample of the Griffith concentrate is presented in Figure 5.1.1 [51]. The mean surface particle diameter of these samples was determined to be 18 μm which corresponds to the number-mean diameter of 7.1 μm [1].

Two kinds of samples were obtained from the Griffith pelletizing plant and used in this project:

- filter cake without bentonite;

- balling drum feed containing 0.8 wt.% bentonite.

In order to produce pellets with the coarser average particle size the finer fraction of the

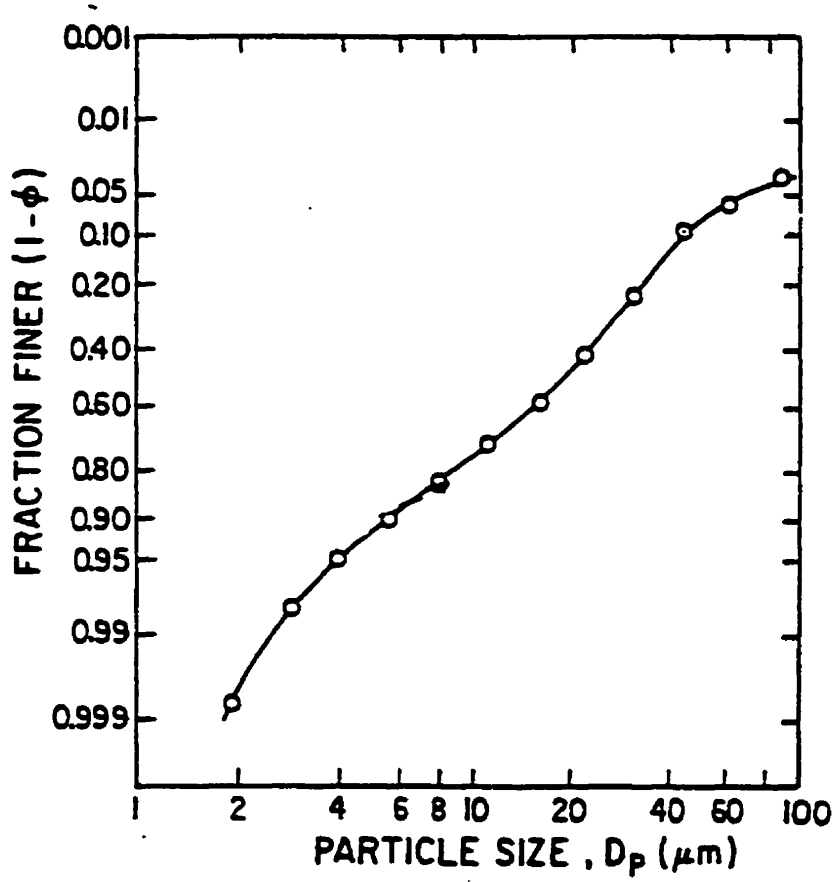


Figure 5.1.1. Particle size analysis of the Griffith concentrate by CANMET.[31]

samples were removed by screening. The resulting samples had a number-mean particle size of 17 – 20 μm.

Other materials being used in this project included the monosized nickel beads (particle size 7.5 μm) supplied by Sherritt Gordon Mines Ltd. and monosized glass spheres (particle size 200 μm) obtained from Sigma-Aldrich Ltd.

Laboratory pellets were produced using the 200 mm diameter and 250 mm deep laboratory pelletizing drum, described previously [47].

5.2. Drying Apparatus

The available thermogravimetric drying apparatus has been originally designed by Zaharchuk [1] and was further improved by the author [2]. It is shown schematically in Figure 5.2.1. The apparatus consists of three parts:

- an air heater/dryer column to carry out the drying under well-defined temperature and Reynolds number conditions;
- an air supply blower and air heating facility, equipped with instrumentation to measure and control the flow rate and temperature of the drying air;
- a Cahn electrobalance, to continuously monitor the pellet weight during drying.

The source of the air is a blower (Spiral model SL 2EA2, supplied by Roton Manufacturing Co.); air flow is controlled by a rotameter (type 4-HCF-1827, supplied by S&K Co.; float type 40-J). The heater/dryer column is a 750mm high pyrex tube attached to two pairs of cylindrical guides travelling on vertical rods (not shown in the Figure). The whole column is lifted up towards a pellet suspended from the Cahn electrobalance, so as to enable the pellet to

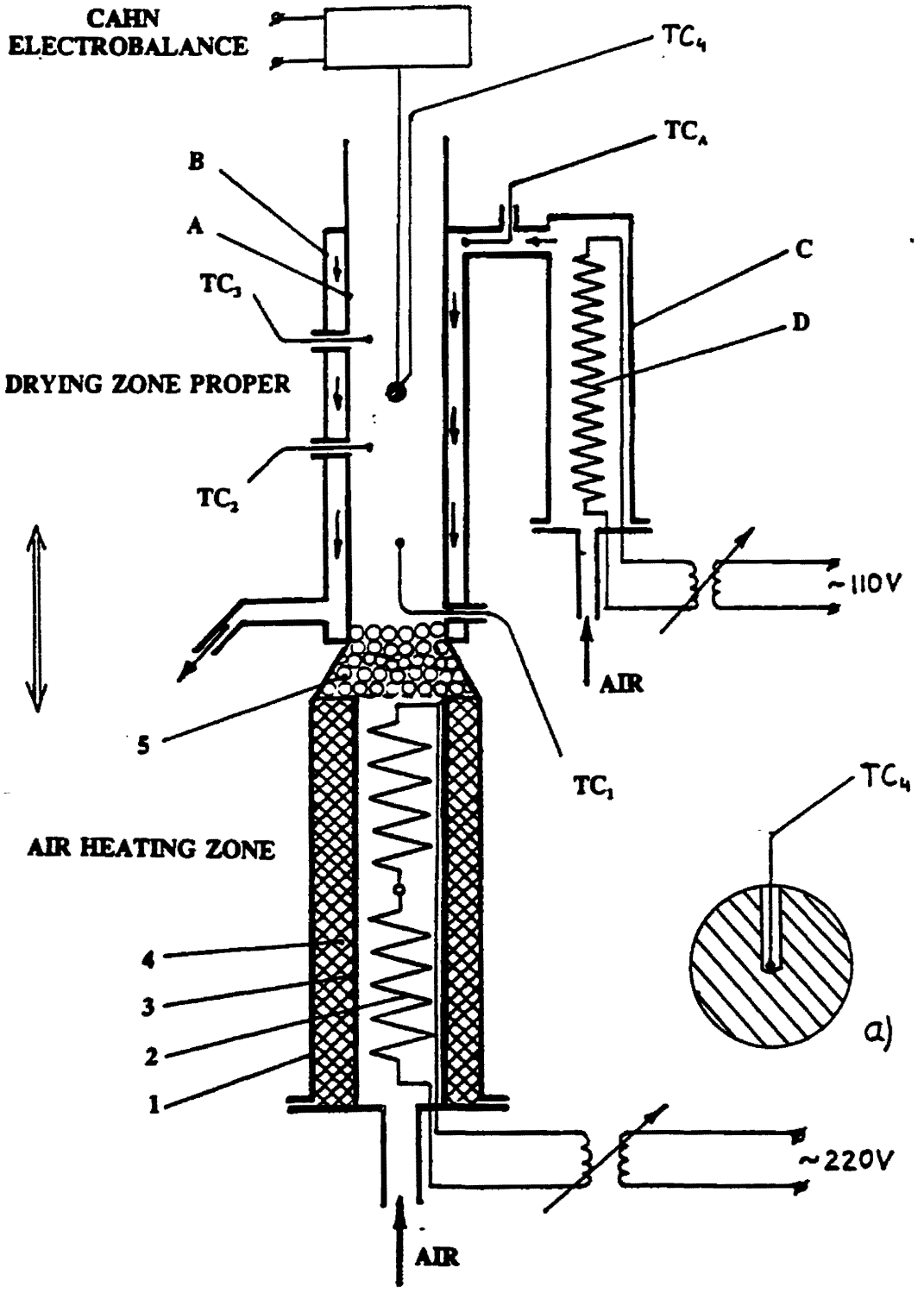


Figure 5.2.1. Schematic representation of drying apparatus.

be rapidly placed into the drying zone.

The heater/dryer column, schematically shown in Figure 5.2.1, consists of two functional zones:

- the air heating column;

- the drying zone column.

The air heating column is constructed from an outer 250 mm high by 90 mm inside-diameter pyrex tube, identified as (1) in Figure 5.2.1. Two electric heating elements (2) (type HG-751, supplied by Electro-Sonic Co.), connected in series are positioned in the lower part of the dryer column. The voltage impressed onto the heating coils is controlled manually by 210V 25A powerstat (type 1256D from Superior Electric Co.). The heating elements are placed into a 38-mm diameter quartz tube (3). The space between the tubes is filled with fibreglass wool (4) to minimize heat losses to the exterior. This two-layer insulation insures that the temperature of the pyrex glass (1) does not rise above its annealing temperature (~590^{0}C). A stainless steel grate with the 50mm deep bed of ceramic beads, resting on top of it (5), is located at top of the tube (3). The purpose of this bed of beads is to ensure air mixing and to achieve temperature and flow uniformity across and along the height of the drying zone. Another purpose is to eliminate radiation from the heating coils to the drying zone.

The drying zone is a 500-mm high by 50-mm inside diameter pyrex tube, constructed as an annulus, so designed to minimize temperature gradients throughout its height. The inner wall *A* of the pyrex tube is joined to the top of the outer tube (1) of the air-heating zone. Tube *A* is surrounded by another pyrex tube *B* (75 mm inner diameter) forming an annulus. Air, heated to the same temperature as the air in the air-heating column, enters near the top of the annulus and

exits near its bottom. The temperature of this air is controlled by a heater *D* located in a separate column *C*. The heater is connected to a manually controlled powerstat. The outside of the dryer and heater columns is insulated by a fibreglass wool blanket (not shown in Figure 5.2.1, but shown in the photos in Fig.5.2.3).

The drying zone temperature is preset by setting the electrical potential of the powerstat for a particular air flow desired. Chromel-alumel thermocouples (type K) are used for temperature control in the drying zone. Temperature calibration curves are shown in Figure 5.2.2. The thermocouple TC_1 is located at the bottom of the drying zone and measures the temperature of the entering air. Two other thermocouples are placed 50 mm below (TC_2) and above (TC_3) the level at which the pellet is positioned during drying. The temperature of the air entering the annulus is controlled by thermocouple TC_A.

The hot air stream exits the drier column at its top. In order to separate the Cahn electrobalance from this hot stream a stainless steel shield, shown in Figure 5.2.3, is installed between them. Also an additional moving lid, also shown in Figure 5.2.3, to prevent excessive convective heating of the surroundings between the drying runs, is affixed closely to the top of the dryer column.

Weight loss measurement results from the Cahn electrobalance were recorded by means of the data acquisition/control unit, supplied by Hewlett-Packard Co. (model 3421A). An average of 5 consecutive readings with a time step of 0.1 seconds was taken as a single data point. The programm "COLLECT.ROB" (copyright Hewlett-Packard 1984,1985) was used to take readings from the data acquisition unit into the IBM XT computer. All data were saved on a hard disk.

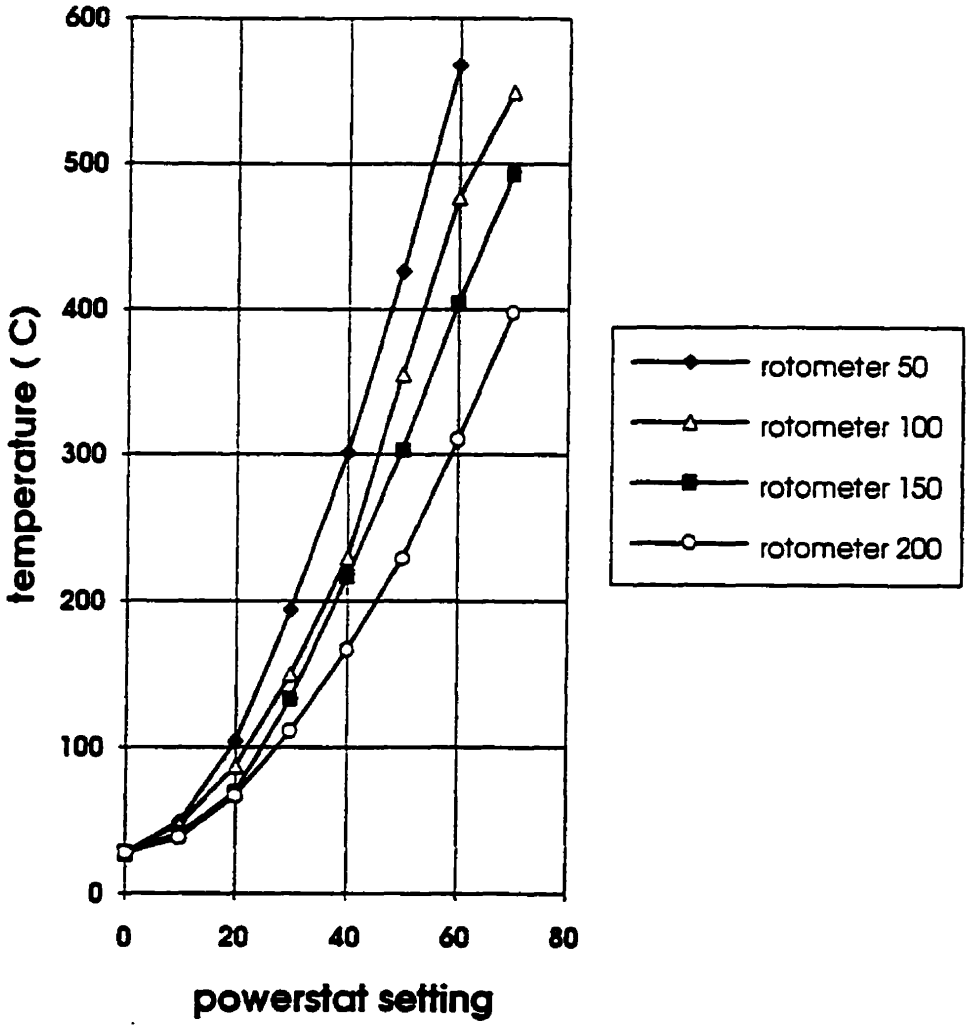


Figure 5.2.2. Drying zone temperature calibration chart.



Figure 5.2.3. Drying Apparatus.

5.3 Direct Measurement of Pellet-Centre Temperature

A series of experiments designed specifically to measure the internal temperature profiles during drying was carried out. For this purpose the experimental apparatus was modified to include an extra thermocouple, TC_4 (see Fig. 5.2.1 a) to measure the temperature of the pellet centre during drying. Chromel-alumel (type K) thermocouples made from 0.005mm diameter wires were used. Such fine thermocouple wires allowed the size of the hole drilled into the pellet core to be less than 1mm in diameter, thus minimizing the damage to the pellet matrix. After the hole was drilled and the thermocouple inserted in it, the residual concentrate (produced by the drilling) was packed carefully into the remaining space between the thermocouple and the walls of the hole.

The procedure of recording the pellet-centre temperature was similar to the simultaneous weight-loss measurements, as described above.

5.4 Scanning Electron Microscopy

This section details the procedures used for preparing samples for the study under the scanning electron microscope (SEM). Also, the SEM-analysis instrumentation is described in this section.

The samples were studied using the JEOL Corp. JSM 840 scanning electron microscope. The images obtained on the electron microscope were photographed using Kodak Panatomic-X 35mm film of 32 ASA. This film produces a negative of very fine grain which allows highly detailed enlargements.

An important requirement of the samples to be used in the SEM analysis is that they be

electrically conductive and resistant to damage under vacuum. The specimens were placed on standard SEM stubs covered with liquid graphite solution, and were coated with gold using the SPI sputter metal-coating technique. An issue is the heaviness of such coatings. Studies of Hodgkin and Murr [84] indicate that gold coatings of between 100 and 200Å are appropriate, but these results were obtained using flat surfaces. For the highly irregular surfaces of the agglomerated materials, it has been found by Markievicz [85] that thicker coatings were more appropriate. However, such coatings can cover up minute topographical features, thereby reducing the ability to resolve the very finest detail. The duration of the sputter deposition was chosen such as to produce a 400Å-thick coating.

In the quantitative study of bentonite deposits the energy dispersive spectroscopy (EDS) technique was applied. Silicon was chosen as the characteristic element and component of the bentonite. The X-ray energy range was 0-20 keV. Quantitative analysis, using the QX20-XAN-0190 software provided by Link Analytical Ltd., was applied.

There were two tasks in these studies:

1) to determine the amount of bentonite at particular points of the sample's microstructure, i.e. the deposits at contact points between particles. The point analysis (at x5000 magnification), was used here allowing the amount of bentonite in a small area of a sample around a certain point to be determined;
2) to determine quantitatively the distribution of bentonite deposits throughout a diametral cross section, in particular along the pellet's radial direction. The beam-scanning analysis was used here. It enabled to determine the average amount of bentonite deposited over large areas of the agglomerate as seen on the monitor of the

microscope.

5.5 Porosity and Dry Strength Measurements

Pellet porosity was determined from the measurements of volume and weight, using the formula:

$$\varepsilon = \frac{\rho_s - m/V}{\rho_s} \tag{5.5.1}$$

where ρ_s represents the density of solid magnetite, and m and V are the pellet mass and volume respectively.

The pellet dry strengths were determined using the procedure described in Section 2.5.1. Since a precise diameter measurement was required for determining pellet porosity and strength, the pellets were shaped into spheres using the cutting tools, shown in Figure 5.5.1 and described elsewhere [47, 51]. The shaping was performed in a plexiglass 'glove-box' enclosure -- this was done to prevent moisture loss. A relative humidity close to 100% was maintained by passing an air stream through water and discharging into the atmosphere of the box. Slight condensation on the plexiglass provided the basis for humidity control. Diameters of the spheroidized pellets were measured in six locations and an average was recorded.

Breaking loads L were measured using an Instron universal machine at a constant stressing rate of 2.0 mm/min. The strength factor L/D^2 was then calculated. Finally, dry strengths

of the individual pellets (σ_T) were evaluated using eqn. 2.5.1.6 (see Section 2.5.1).



Figure 5.5.1. Cutting Tools Used to Shape Pellets into Spheres [47, 51].

Chapter 6

EXPERIMENTAL RESULTS AND MODEL VALIDATION

6.1 Drying Experiments to Validate the Model

In this chapter the results of model-validation experiments are documented. Results of two independent series of validation experiments are reported:

1) drying experiments, aimed at validation of drying rate curves predicted by the model (Section 6.1.1), obtained prior to introducing the temperature-measuring technique;

2) immersed-thermocouple experiments, coupled with drying-rate measurements, aimed at validation of wet-core temperature profiles predicted by the model (Section 6.1.2).

6.1.1 Drying of Coarser-Particle-Size Pellets

The Zaharchuk model has been validated experimentally by this author as part of his M.A.Sc. work [2] for a limited number of specific conditions. The Griffiths iron ore agglomerates with a number-average particle size of 7.1 μm were used. An example case of the drying-rate curve of a pellet without bentonite has been reproduced in Fig.6.1.1.1. Evidently, the agreement between the model and experiment is excellent, thus validating the

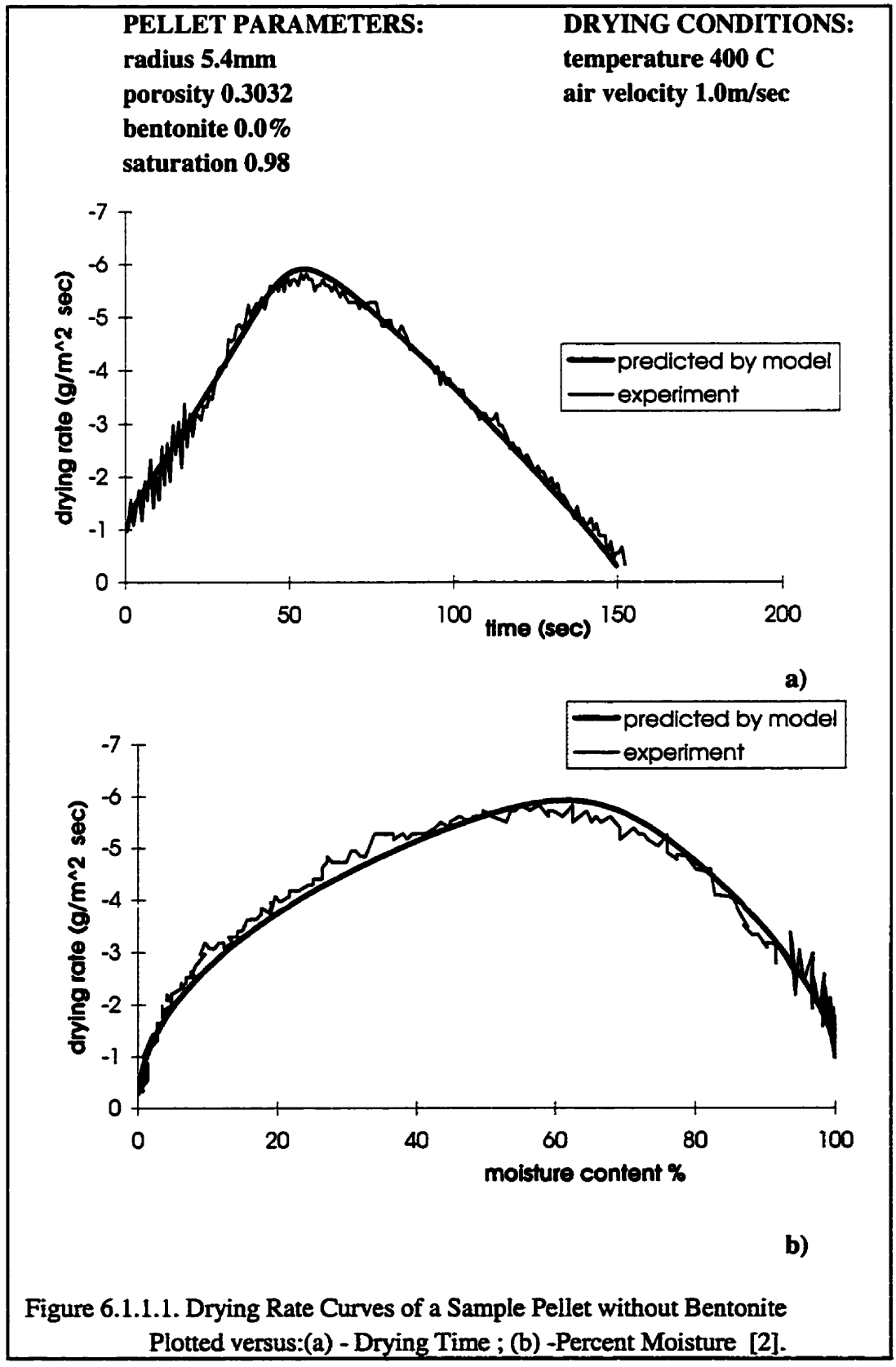


Figure 6.1.1.1. Drying Rate Curves of a Sample Pellet without Bentonite Plotted versus:(a) - Drying Time ; (b) -Percent Moisture [2].

former. These results, moreover, showed conclusively that under the intense-drying conditions there was no constant-rate period. The transition from the surface to the shrinking core regime occurred early in the initiation period. This occurred before the conditions which are inherent to the onset of the constant-rate drying could be achieved. For these conditions the surface/shrinking-core transition period may be considered short or non-existent (see modelling results in Sections 4.2 and 4.3). As a result, the fact that the Zaharchuk model ignores this period does not detract from the quality of the overall drying-rate curve.

It was discovered in other experimentation, as part of the present program, that, when agglomerates of a coarser particle size, e.g. 17μm, are being dried rapidly, the assumption of instantaneous transition in the original model may cause substantial deviations of model predictions from experimental data. The experimental drying rate curves for this case are shown in Figures 6.1.1.2 to 6.1.1.6. A guide to these graphs is presented in Table 6.1.1.1. The pellets were prepared from the coarser-particles powder sample, a screening product of the original Griffith concentrate (see Section 5.1). In Figs. 6.1.1.2 to 6.1.1.6 the results obtained using the original Zaharchuk model are shown in the upper graphs, and those using the extended model are shown in the lower graphs in each case.

The experimental curves show a steeply rising curve and a clear maximum, which is then followed by a falling-rate period. There is generally good agreement between experiment and both models during the initiation period and in the prediction of the total drying time. The discrepancy between the Zaharchuk model and experiment is in the middle of the drying rate curves. As noted in Section 4.2, the original model predicts the beginning of a constant-

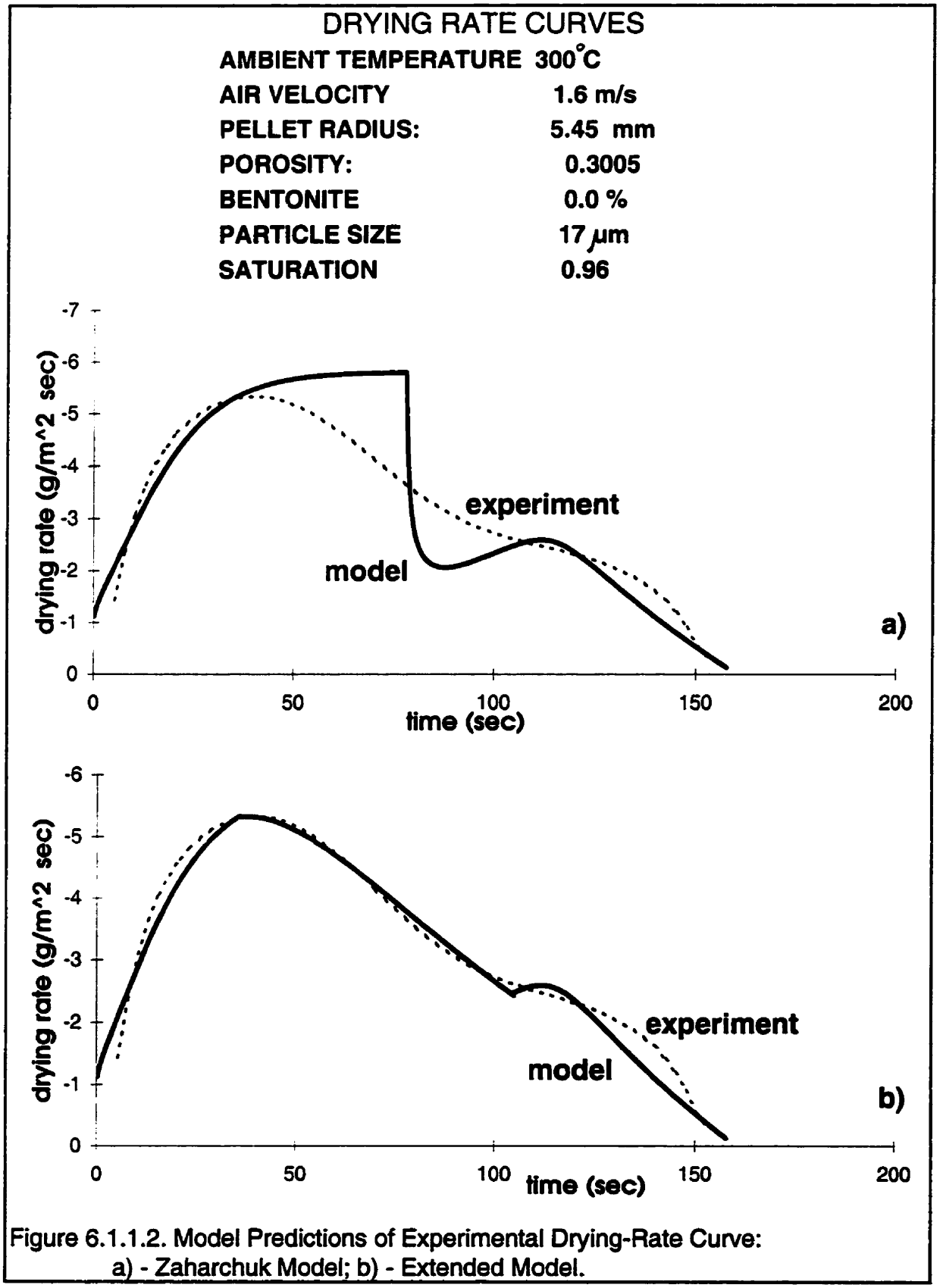


Figure 6.1.1.2. Model Predictions of Experimental Drying-Rate Curve:
a) - Zaharchuk Model; b) - Extended Model.

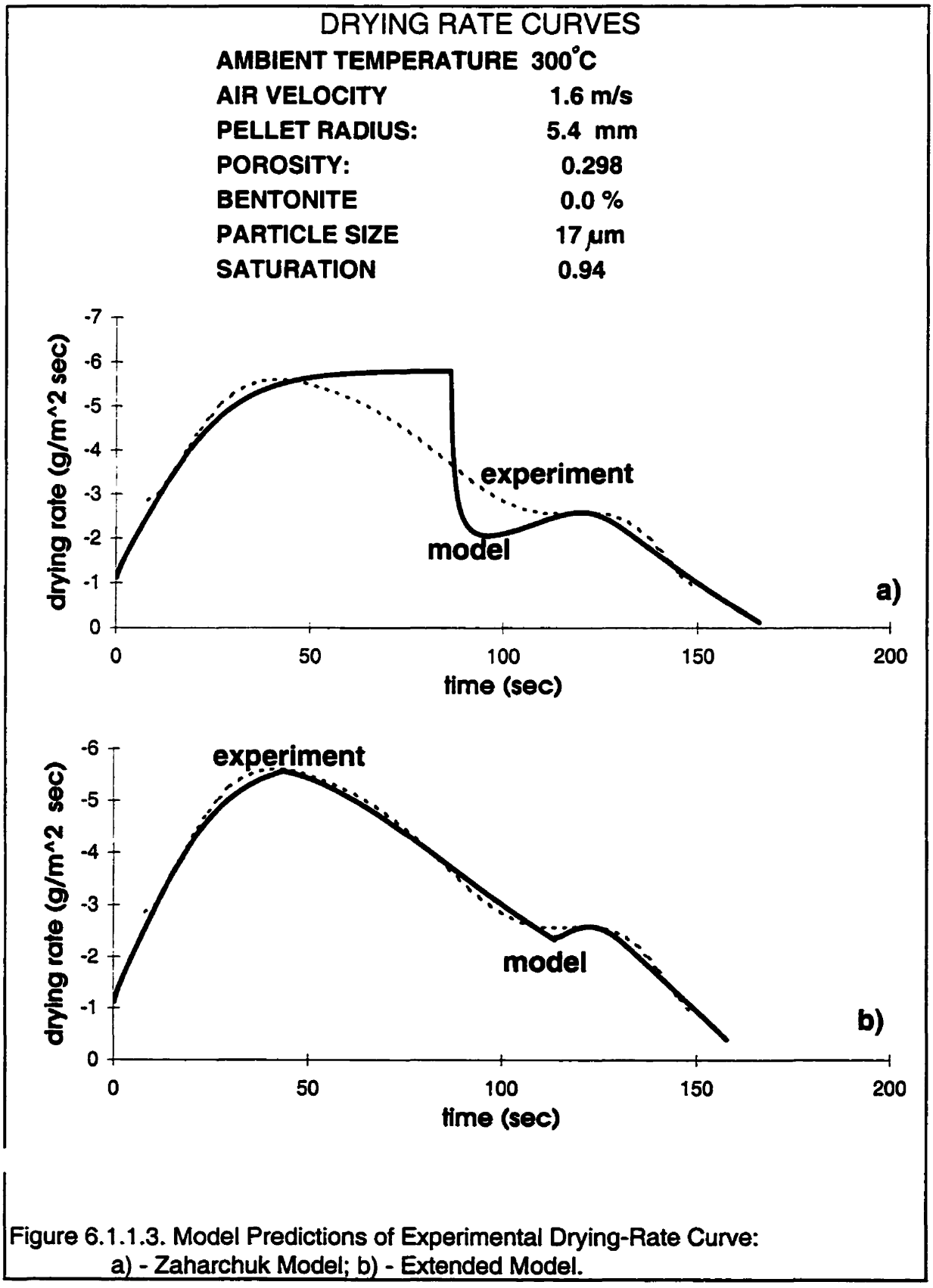


Figure 6.1.1.3. Model Predictions of Experimental Drying-Rate Curve:
a) - Zaharchuk Model; b) - Extended Model.

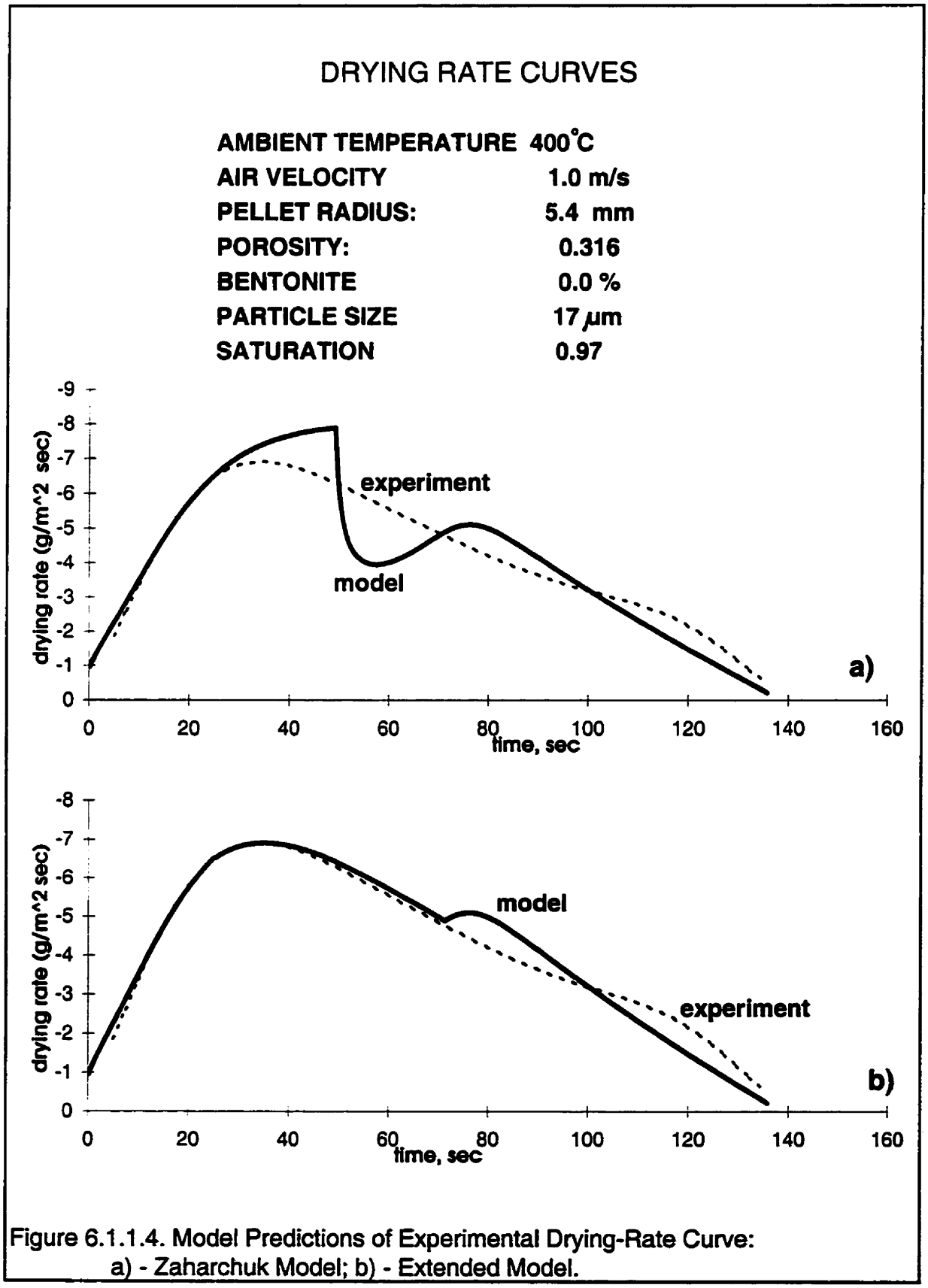


Figure 6.1.1.4. Model Predictions of Experimental Drying-Rate Curve:
a) - Zaharchuk Model; b) - Extended Model.

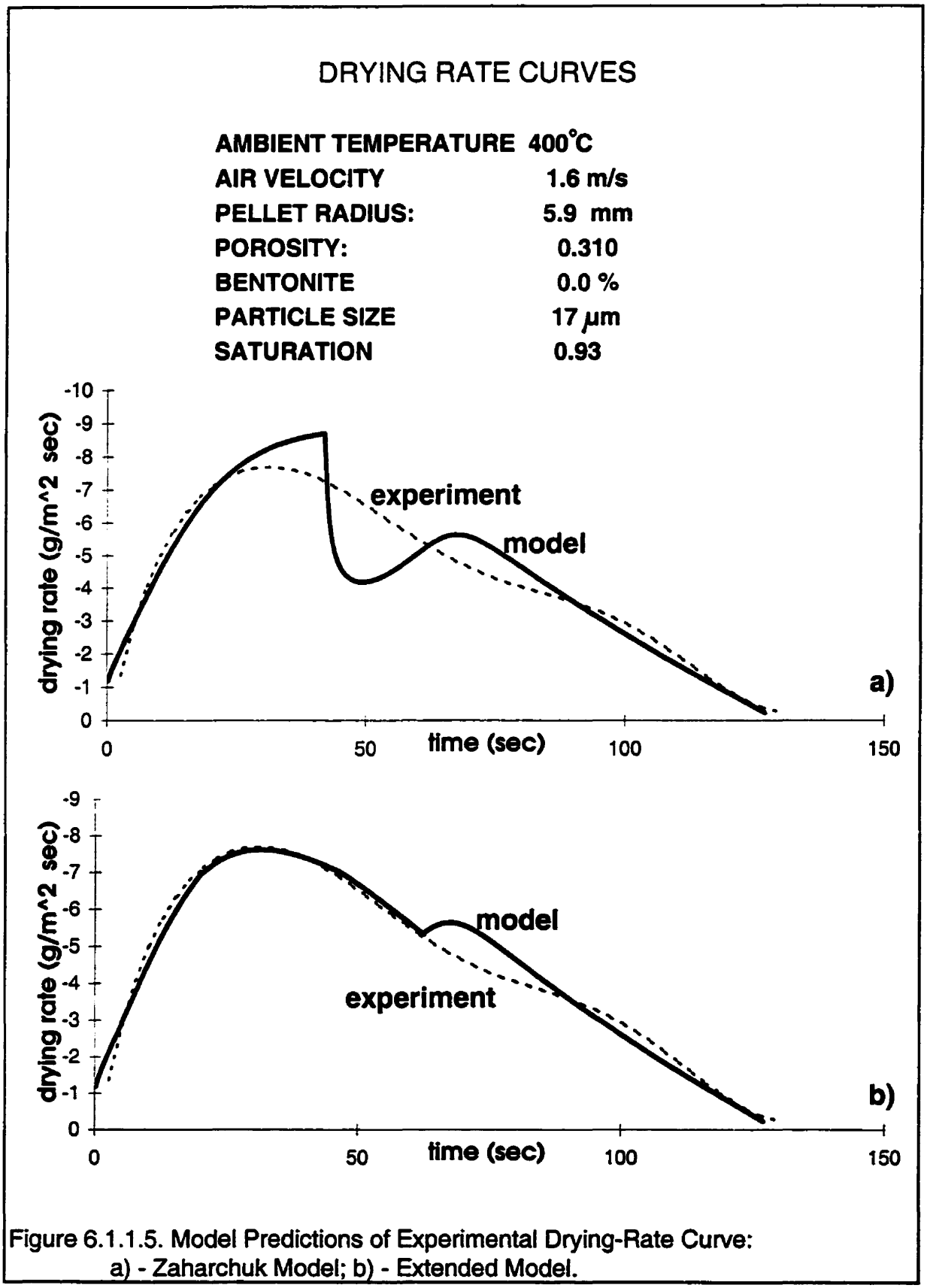


Figure 6.1.1.5. Model Predictions of Experimental Drying-Rate Curve:
a) - Zaharchuk Model; b) - Extended Model.

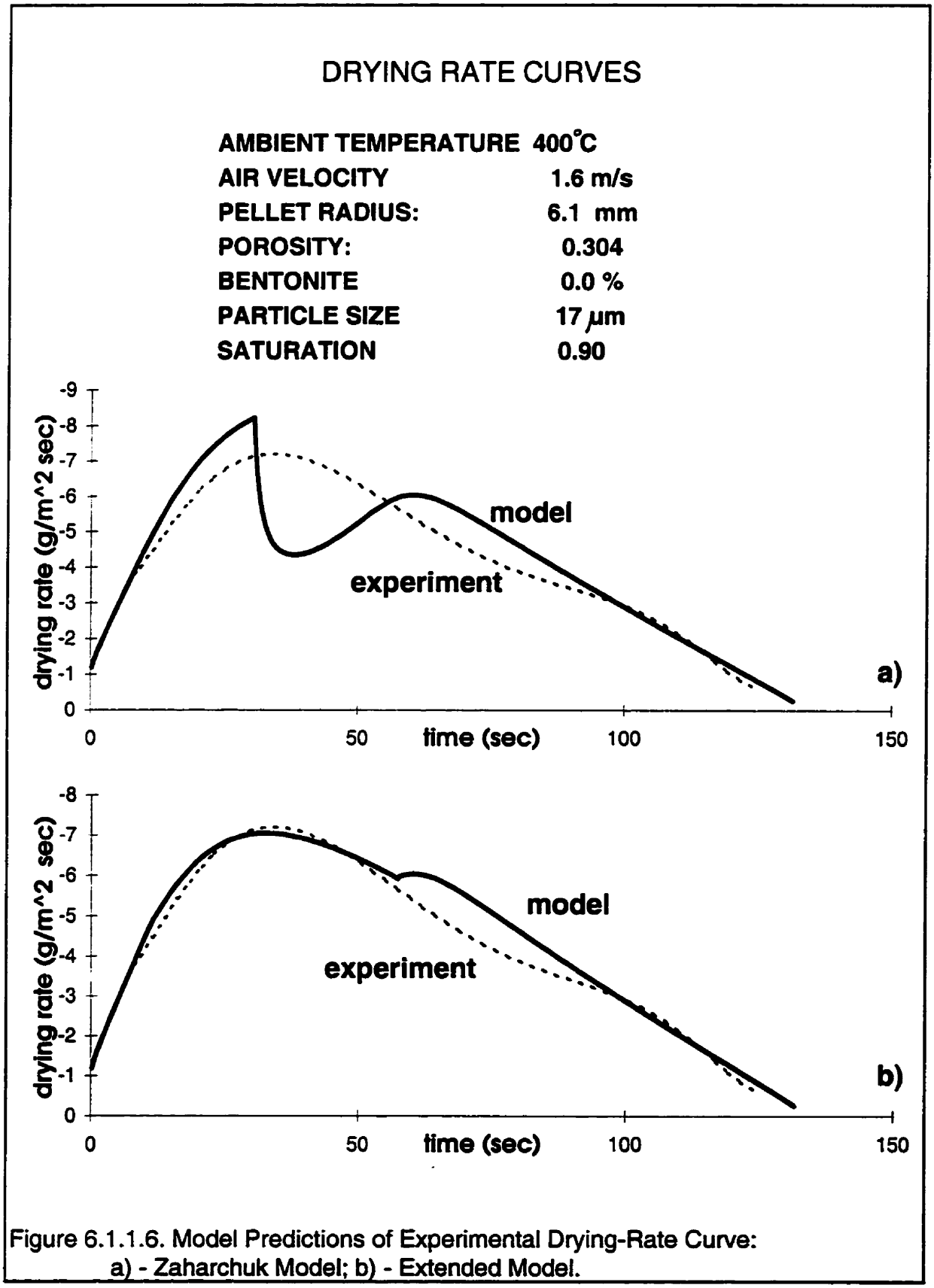


Figure 6.1.1.6. Model Predictions of Experimental Drying-Rate Curve:
a) - Zaharchuk Model; b) - Extended Model.

rate period (a horizontal portion of the drying-rate curves), which is then interrupted by the sharp, near-vertical drop, identical to that discussed in connection with Figure 4.2.5 *a*. This is shown in Figures 6.1.1.2 *a* to 6.1.1.6 *a*.

Table 6.1.1.1. Guide to the Results of Drying Experiments
Griffith Concentrate
Pellet Radius: 5.4 - 6.1 mm
Porosity: 0.298 - 0.316
Average particle diameter: 17μm
Bentonite content: 0.0 %
Pellet Saturation: 0.90 - 0.97

Temperature	**300°C**	**400°C**	
Air Flow Rate	**1.6 m/s**	**1.0 m/s**	**1.6 m/s**
Figures	Fig. 6.1.1.2 and Fig. 6.1.1.3	Fig. 6.1.1.4	Fig.6.1.1.5 and Fig. 6.1.1.6

The extended model predicts the experimental drying-rate patterns much more successfully. Evidently, the inclusion in the model of a gradual transition between the surface- and shrinking-core drying regimes is a key improvement of the Zaharchuk model. As was the case in Figure 4.2.5 *b*, the drying-rate curves predicted by the extended model shown in Figures 6.1.1.2 *b* to 6.1.1.6 *b* exhibit a distinct maximum, immediately followed by the falling rate period. That part of the curves is in excellent agreement with experiment.

Next, one should note that the experimental drying-rate curves in Figures 6.1.1.2 - 6.1.1.6 exhibit an inflection during the falling rate period. According to theoretical considerations (see arguments in Section 4.2) this inflection should occur during the

transition from the transition period- to the shrinking core regime. The extended-model curves show a discontinuity which corresponds to this transition (see also Figure 4.2.5 *b* in Section 4.2). To be noted is that in Figure 6.1.1.3 and, to some degree, - in Figure 6.1.1.2 this inflection occurs in the same period as an inflection in the experimental curve. In the other graphs, however, the inflections on the experimental and the extended-model curves do not coincide in time. Modelling modifications to eliminate the discontinuity and this discrepancy with experiment was considered (see Section 3.2.2) but eventually left beyond the scope of this thesis.

Generally, the agreement of the extended model with experiment is quite good and thus the extended model can be considered as validated.

6.1.2 Center-Temperature Measurement

Drying investigations which comprised drying experiments with the thermocouple immersed in the interior of the pellets (see Section 5.3) were carried out in the course of this study. Their objective was to provide an independent experimental validation of the model, in this case -- the prediction by the latter of the temperature patterns at the pellets' center.

Several groups of pellets were made of Griffith concentrate of two different average particle sizes (7.1 and 17μm). They were dried at two sets of drying temperatures and gas flow conditions. Their temperature-at-the-center data were recorded versus time and shown in lower graphs in Figures 6.1.2.1 and 6.1.2.2. Also shown for easier correlation are the corresponding drying rate curves of the pellets (upper graphs). The guide to these graphs is presented in the Table 6.1.2.1.

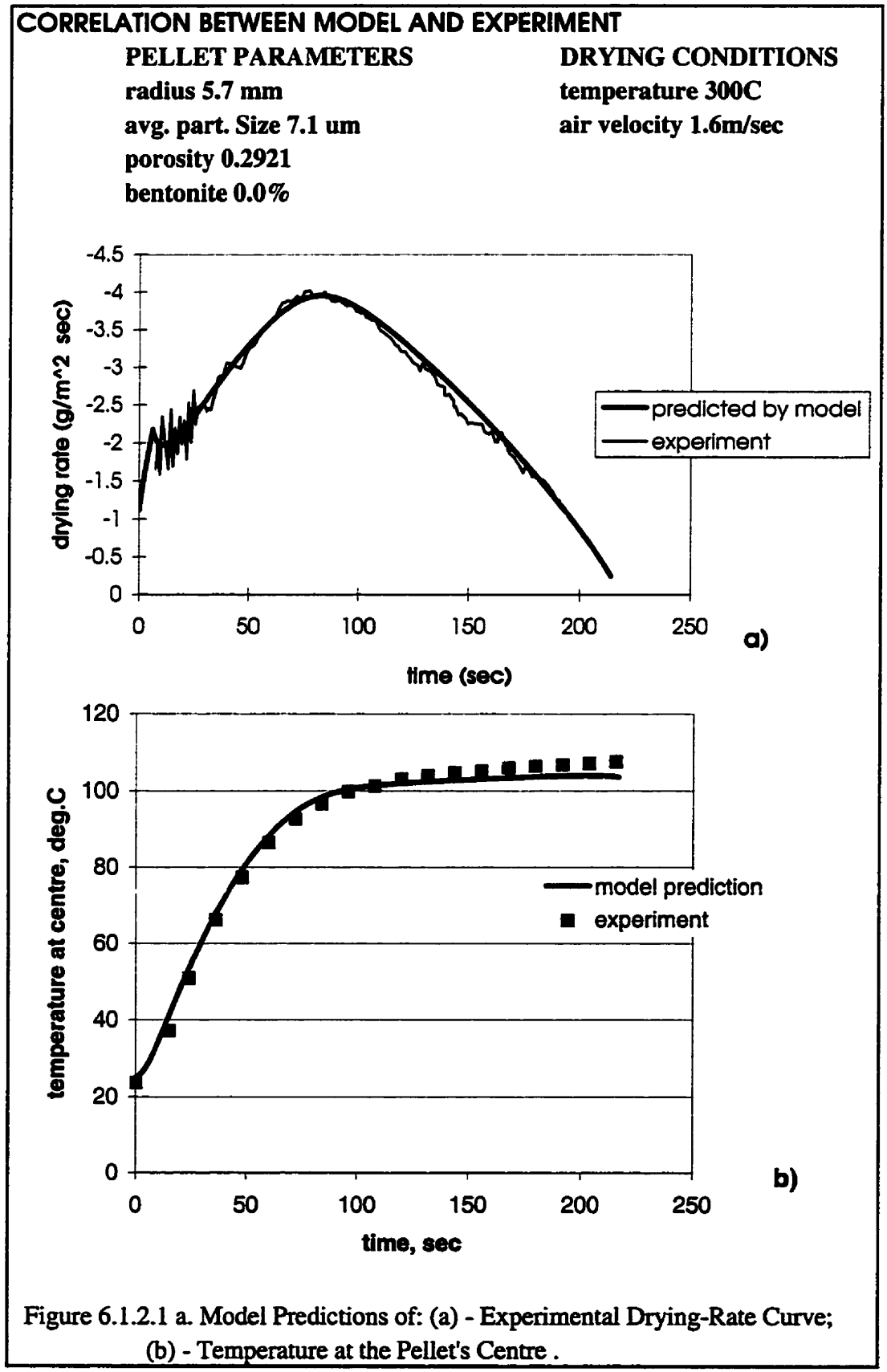


Figure 6.1.2.1 a. Model Predictions of: (a) - Experimental Drying-Rate Curve; (b) - Temperature at the Pellet's Centre .

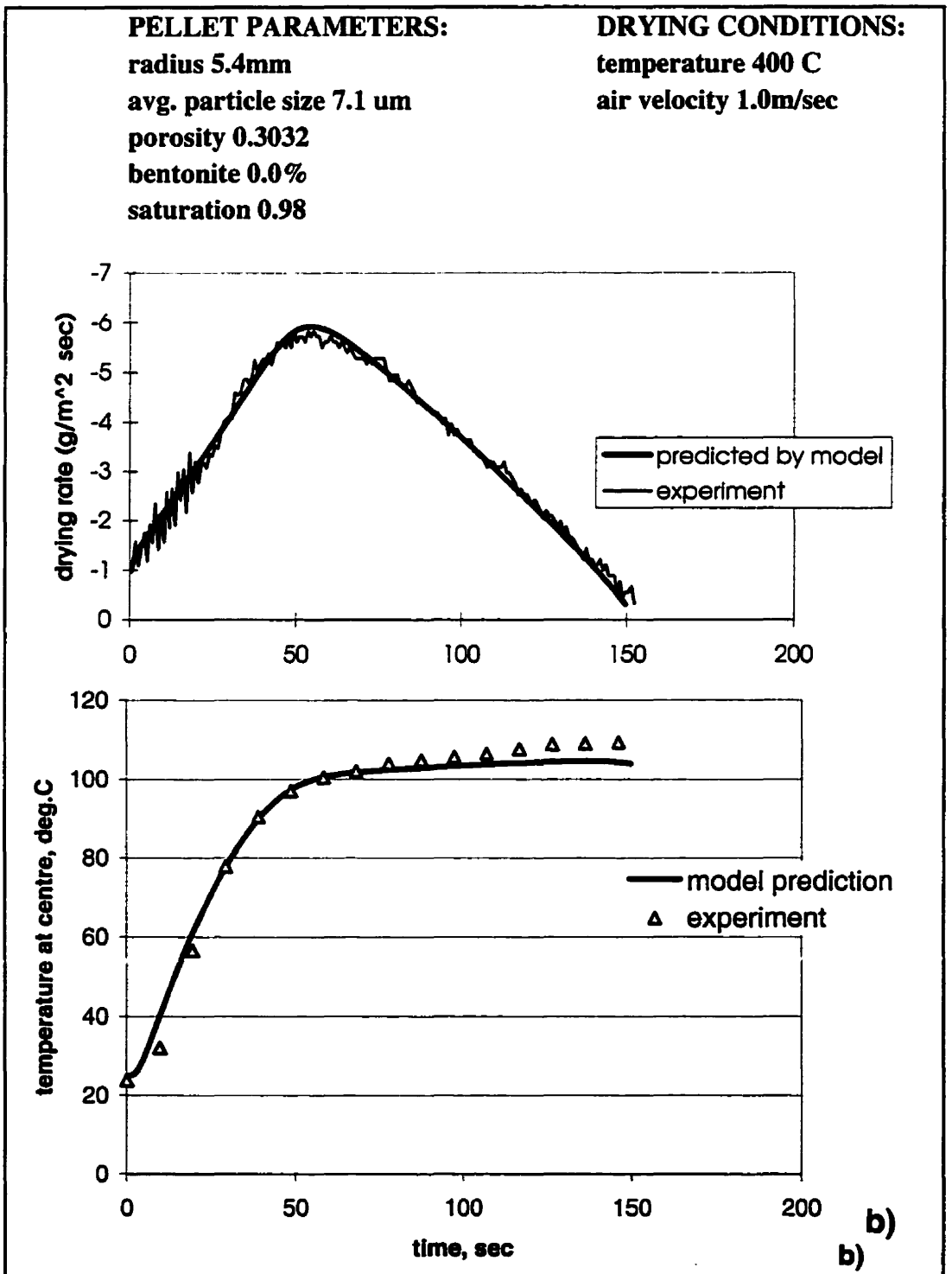


Figure 6.1.2.1 b. Model Predictions of: (a) - Experimental Drying-Rate Curve; (b) - Temperature at the Pellet's Centre .

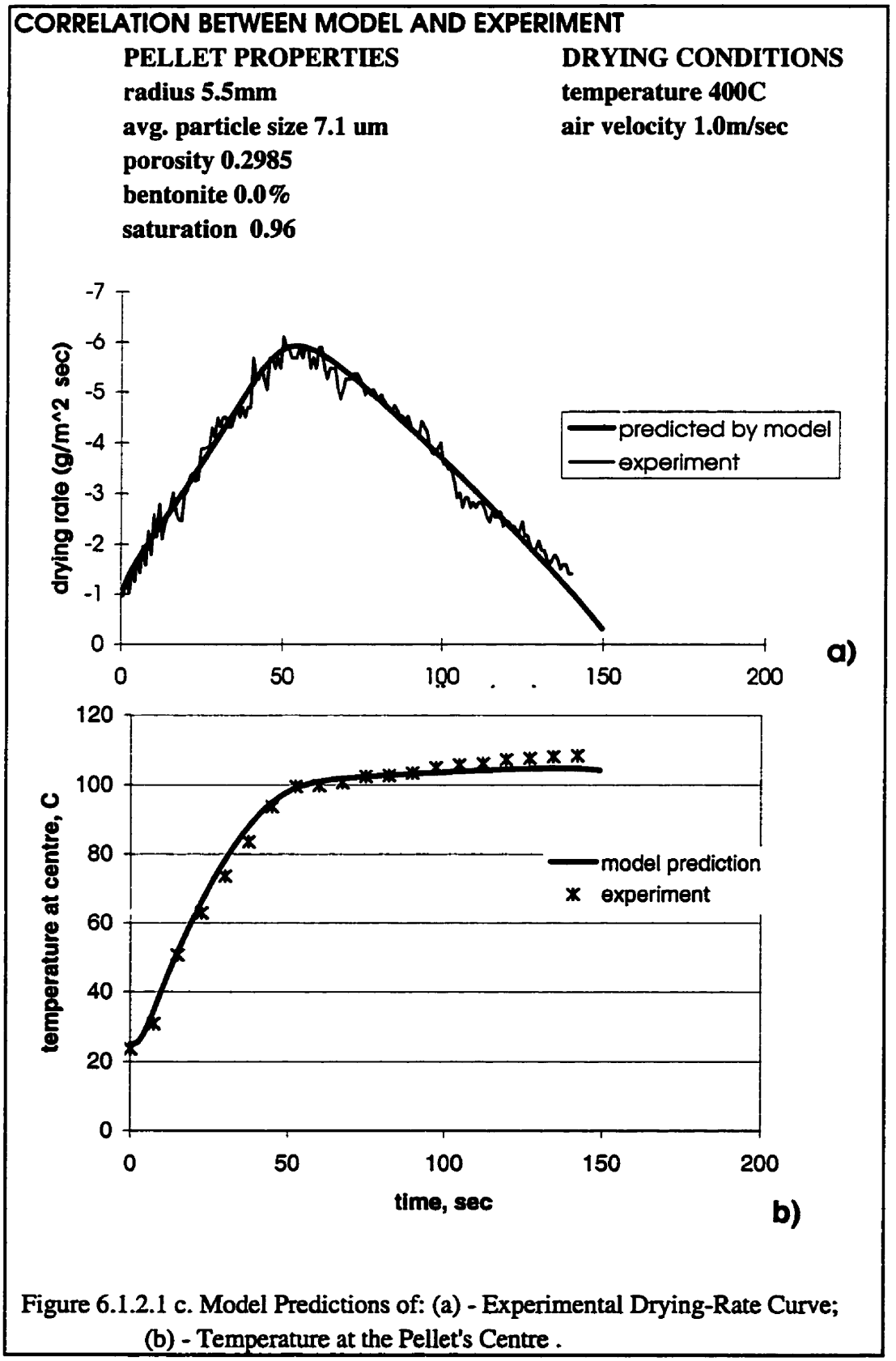


Figure 6.1.2.1 c. Model Predictions of: (a) - Experimental Drying-Rate Curve; (b) - Temperature at the Pellet's Centre .

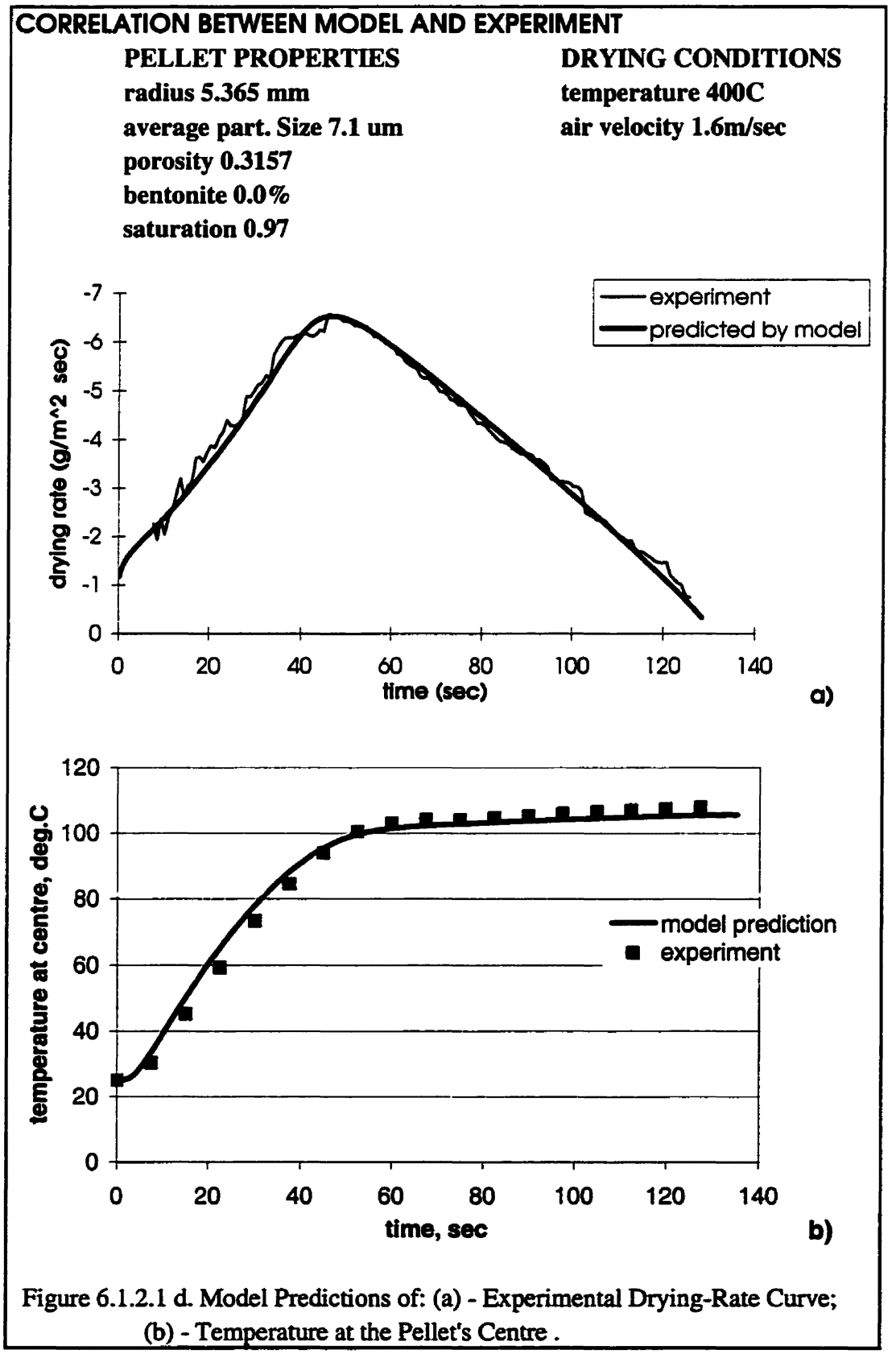


Figure 6.1.2.1 d. Model Predictions of: (a) - Experimental Drying-Rate Curve; (b) - Temperature at the Pellet's Centre .

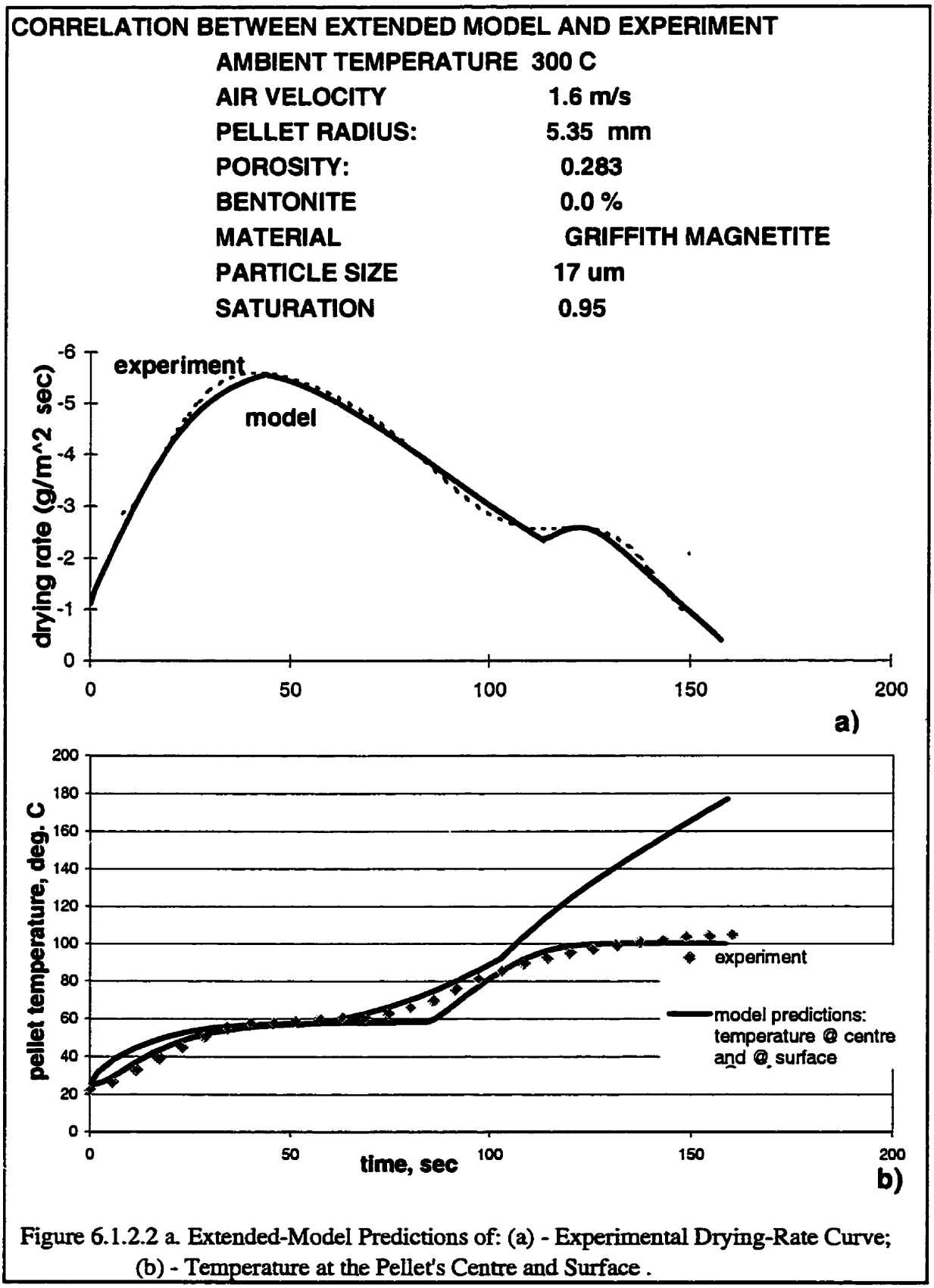


Figure 6.1.2.2 a. Extended-Model Predictions of: (a) - Experimental Drying-Rate Curve; (b) - Temperature at the Pellet's Centre and Surface .

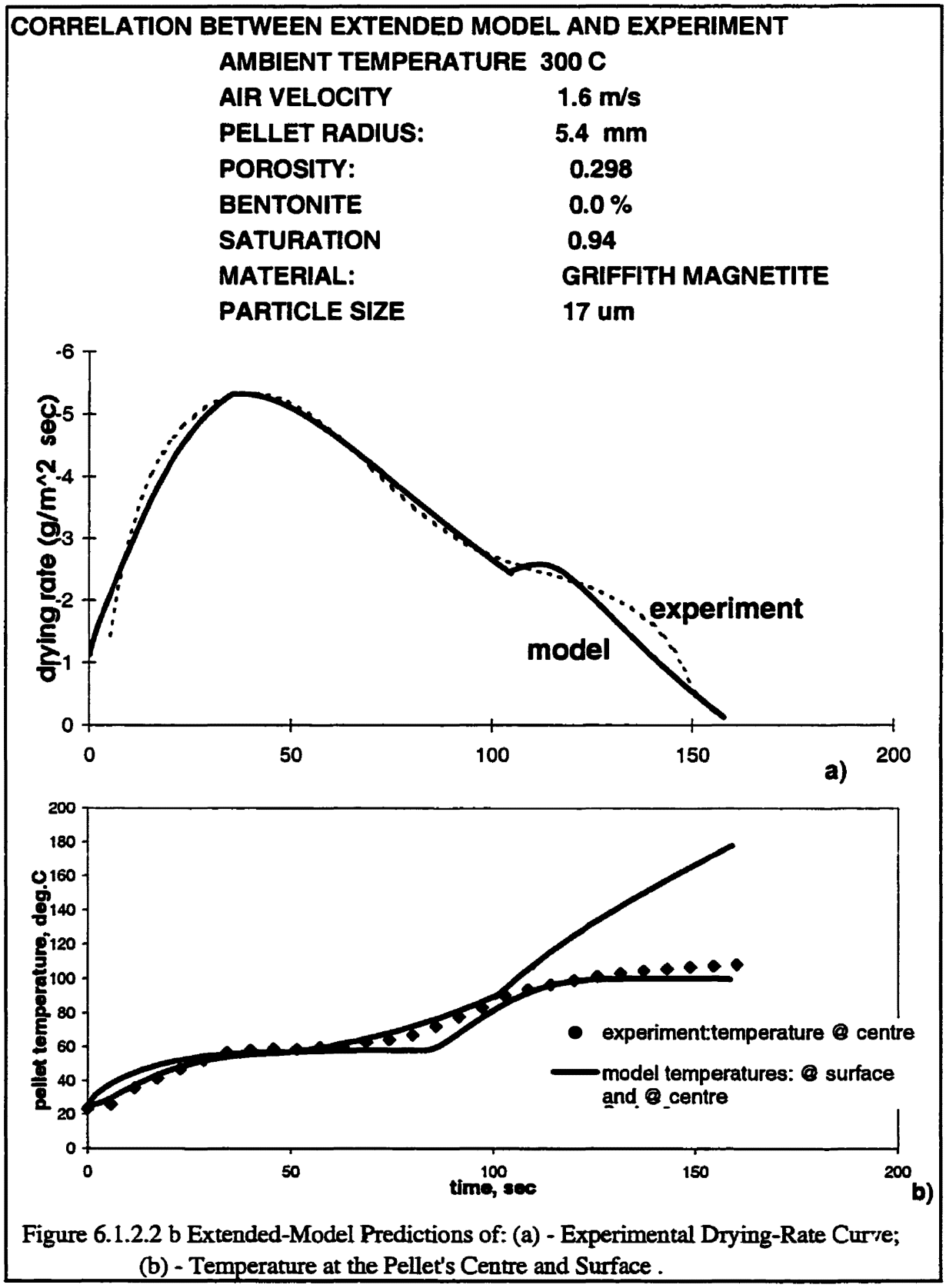


Figure 6.1.2.2 b Extended-Model Predictions of: (a) - Experimental Drying-Rate Curve; (b) - Temperature at the Pellet's Centre and Surface .

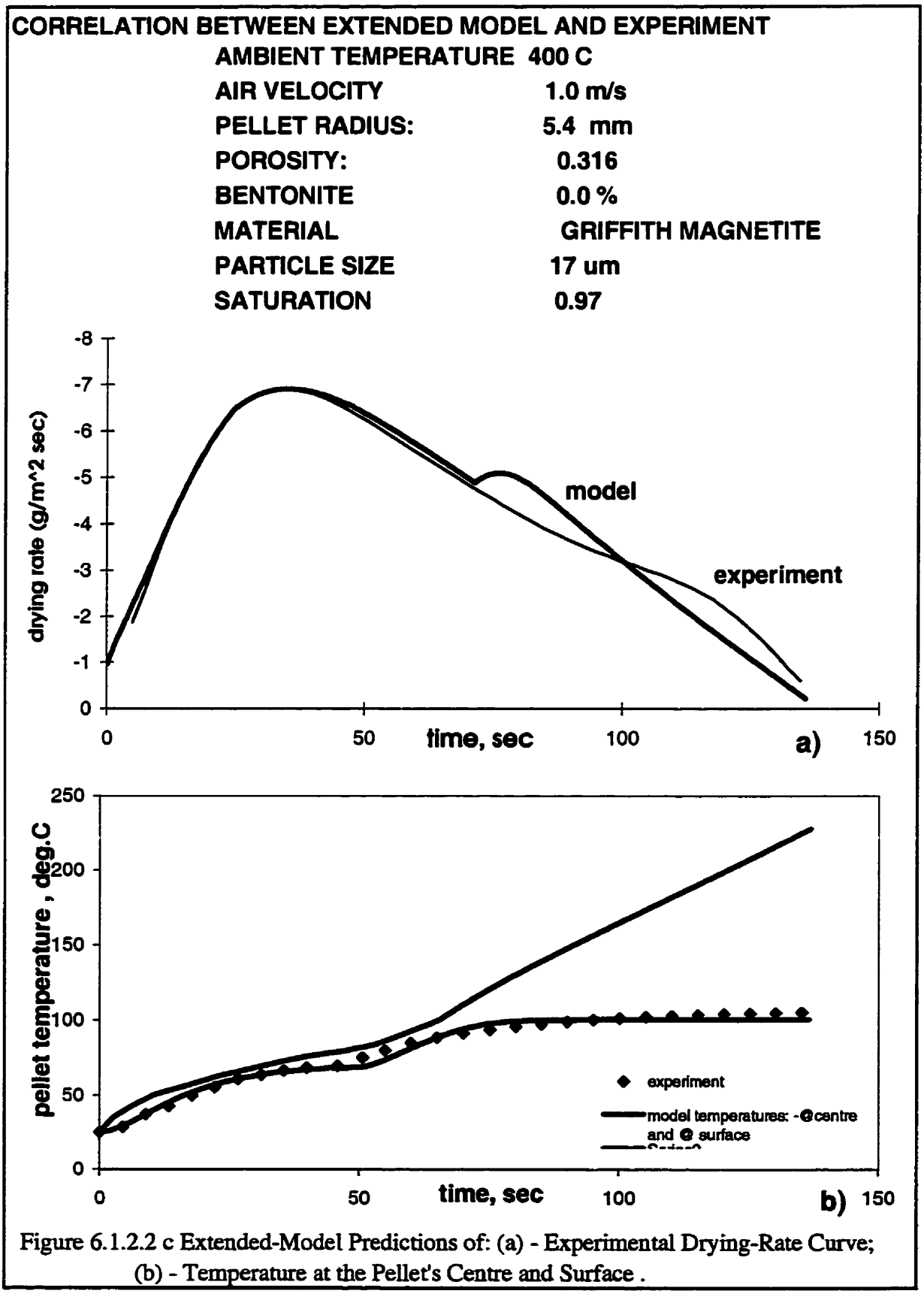


Figure 6.1.2.2 c Extended-Model Predictions of: (a) - Experimental Drying-Rate Curve; (b) - Temperature at the Pellet's Centre and Surface .

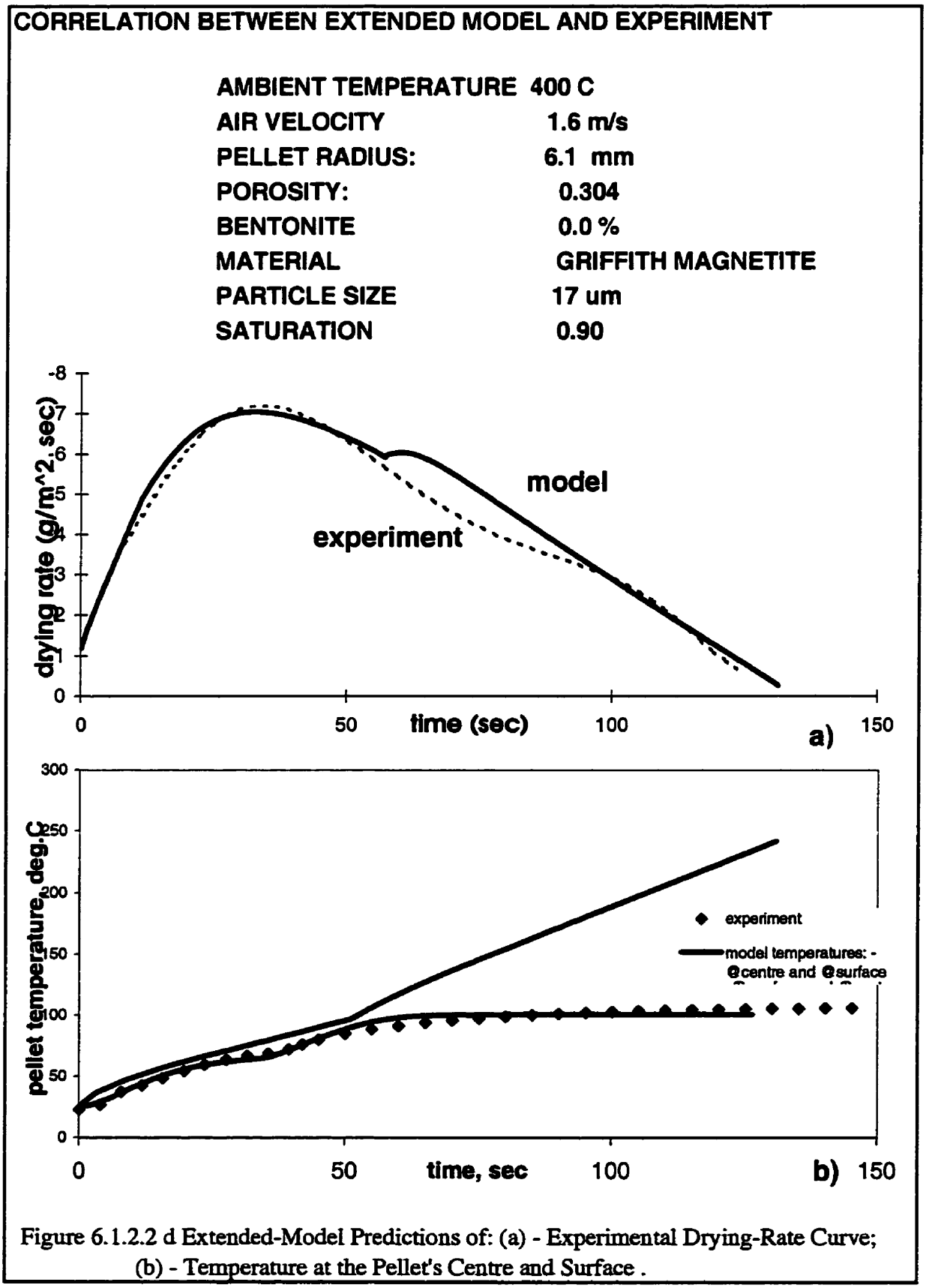


Figure 6.1.2.2 d Extended-Model Predictions of: (a) - Experimental Drying-Rate Curve; (b) - Temperature at the Pellet's Centre and Surface .

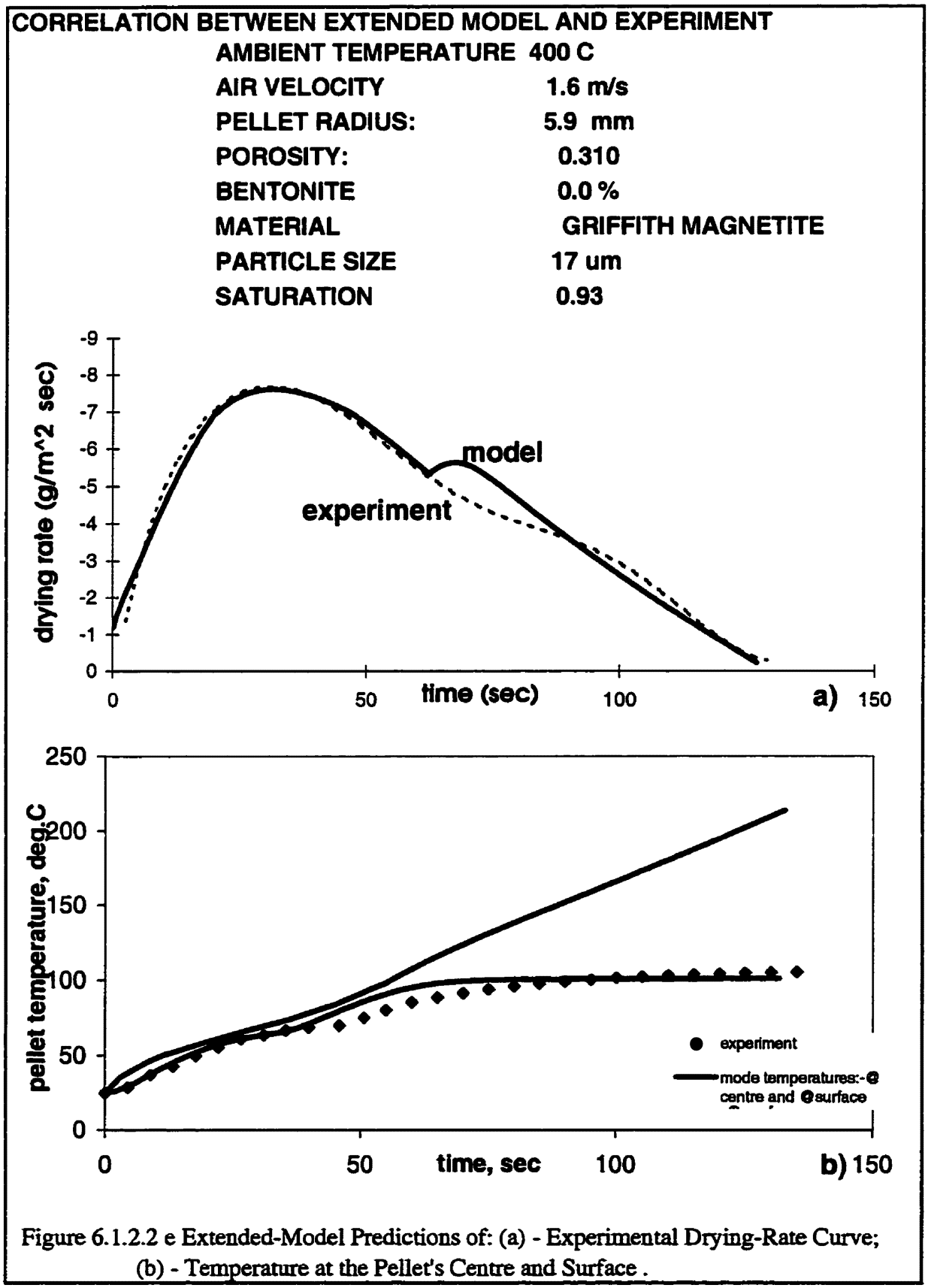


Figure 6.1.2.2 e Extended-Model Predictions of: (a) - Experimental Drying-Rate Curve; (b) - Temperature at the Pellet's Centre and Surface .

Table 6.1.2.1. Guide to the Results of Center-Temperature Measurements
Griffith Concentrate
Pellet Radius:5.365 -6.1 mm
Porosity:0.2773 - 0.316
Pellet Saturation : 0.90 - 0.98

	300°C		400°C	
	1.0 m/s	**1.6 m/s**	**1.0 m/s**	**1.6 m/s**
-Pellets with average particle size **7.1μm**	-	Fig.6.1.2.1 *a*	Figs.6.1.2.1 *b, c*	Fig. 6.1.2.1 *d*
-Pellets with average particle size **17μm**	-	Figs.6.1.2.2 *a, b*	Fig.6.1.2.2 *c*	Figs.6.1.2.2 *d, e*

When pellets made of fine particles (7.1μm) are being dried (Figs. 6.1.2.1 *a-d*), the temperature at the pellet center (lower graphs) rises steeply until it reaches 100°C and then stays approximately at the constant level. Significantly, this point coincides in time with the maximum on the corresponding drying-rate curves in the upper graphs. This validates our theoretical considerations (see Section 3.1) that, for these fine-particle-size agglomerates, the drying-rate maximum is associated with the transition of the mechanism of vapour-transport through the dry shell from diffusion to Darcy flow. The latter occurs when the temperature at the wet/dry interface reaches 100°C, and the water-vapour pressure becomes super atmospheric.

Also shown in the graphs are the Zaharchuk model predictions of the pellet-center temperature curves[1]. They are in remarkable agreement with the experimental data.

For the pellets made of the coarser particles (17μm)(see Figs. 6.1.2.2 *a-d*) the shapes of the temperature curves and the corresponding drying-rate curves are quite different. As in

---

1

As mentioned previously (see Section 4.2) the extended model algorithm does not include the calculation of the temperature at the pellet center. Hence, the temperature results in this Section are correlated with the original Zaharchuk model.

the previous case, temperature curves (lower graphs) and corresponding drying-rate curves (upper graphs) rise at first. However, the maximum drying rate in coarser agglomerates is reached at much lower pellet temperatures compared to fine agglomerates - around 60^{0}C as opposed to 100^{0}C. Afterwards, the drying rate declines gradually while temperature at the pellet center is still rising. All drying-rate curves exhibit inflections during the falling rate period, which coincide with the temperature of the pellet center reaching 100^{0}C.

These observations are in remarkable agreement with our theoretical considerations (see Section 4.2) that the drying-rate maximum in coarser agglomerates is associated with the surface/shrinking core transition period, whereas the drying-rate inflection during the falling rate period is associated with the wet/dry interface reaching 100^{0}C and the corresponding changeover of the vapour-transport mechanisms.

The extended-model predictions of the pellet-surface temperature curves and the corresponding prediction for the drying-rate curves are shown in the respective graphs. The pellet-center temperature curves predicted by the Zaharchuk model are also shown. In most experiments the model/experiment agreement is quite satisfactory. The experimental results and their good agreement with model predictions ultimately validate the extended-model formalism described in Sections 3.1 - 3.2.

6.2 Matrix Expansion Studies

Investigations of pore structure evolution during drying have been initiated and a matrix expansion hypothesis has been suggested (see Section 3.4). The latter is based on the findings of the volume measurements of Griffith iron ore pellets (see Table 3.4.1) before and

after their drying in the oven (drying temperature 80^0C). The volume increase is seen as being caused by the engulfment of loose fine particles with the receding wet/dry interface. The smaller loose particles, which occupied positions in the voids of pellet porous matrix and are not part of the skeletal-network structure, are dragged during drying into the interstices between the bigger, network-creating ones. As the pendular state of the agglomerate is approached, the amount of fines concentrated in the contact areas becomes large, and the capillary radius, therefore, small. The consequently large capillary pressure tends to pry apart the rigid particle network structure of the agglomerate. The result is the observed increase in porosity.

This particle engulfment phenomenon should be expected during mild drying, where the solid-liquid-gas interface is receding from the pore center to the contact areas. The picture is quite different during the intense drying, as the contact areas between large particles, representing the necks in the ink-bottle structure, are the primary sites of the vapour lock. Creation of such local gas/liquid interfaces in these areas will, consequently, prevent the particle drag into the contact areas.

In order to investigate the latter conjecture and, ultimately, to validate experimentally the matrix expansion hypothesis, two independent approaches were taken:

- direct volume and porosity measurements of the pellets on both wet and dry basis, initiated in our previous work;

- repetitive drying of the pellets at varying drying conditions and comparing their drying rate curves

6.2.1 Porosity Measurements

Experimental measurements of volume change the pellets undergo upon drying were conducted. The objective was twofold. Firstly, to increase our experimental data base for the mild drying conditions in order to validate the matrix expansion hypothesis. Secondly, the volume measurements on the pellets were also conducted following their drying under intense conditions. The purpose was to confirm that the vapour lock would prevent the porosity increase observed under mild drying conditions.

6.2.1.1 Griffith Iron Ore Agglomerates

Pellets under investigation were made from Griffith iron ore concentrate with the average particle size 7.1μm. They were prepared by tumbling in the laboratory pelletizing drum. They were subsequently dried in the drying apparatus at 100°C and 400°C. The air flow rate was 1.0 m/s in both cases. Volume and mass measurements were conducted on these pellets before and after drying and their porosities on wet and dry basis were calculated (see Section 5.5). Results are summarized in Table 6.2.1.1.1.

Table 6.2.1.1.1 Porosity Measurements of Iron Ore Pellets upon Drying

Pellet Description	No. of Pellets Tested	Drying Temperature	Average Porosity		% increase
			wet basis	dry basis	
-Griffith iron ore pellets (avg. part. diam.7.1μm	40	100°C	0.3181	0.3631	14.183 (± 2.776)
	36	400°C	0.3061	0.3074	0.441 (± 1.3052)

Our results show a significant porosity increase for drying at 100°C. The results are in good agreement with those obtained in our group previously for oven-dried pellets (see Table 3.4.1).

For the rapidly dried pellets the picture is drastically different. There is practically no porosity increase upon drying. Moreover, some individual pellets within this group exhibited a slight porosity *decrease* upon drying.

These results establish that the matrix expansion phenomenon is limited to the mild drying conditions. This, in turn, provides the first step in the confirmation of our hypothesis that the expansion occurs as a result of the engulfment drag.

6.2.1.2 Porosity Measurement throughout a Drying Run

In order to investigate the matrix expansion phenomenon during mild drying in greater detail the following experiment was conducted. Drying of a pellet at 100^0C was interrupted every 25 sec to measure its volume and mass, followed by a resumption of drying at the same conditions. This procedure was repeated until there was no change in pellet's mass, meaning that drying was complete. Values of the porosities at different times and of the corresponding degrees of saturation were then calculated and analyzed.

The results of the experiment are shown in Figure 6.2.1.2.1. The percent increase in the pellet porosity is plotted against degree of saturation. From the beginning of the drying process, until about S=0.4, there is only a small increase in porosity of the pellet. However, porosity starts to increase drastically as the pendular saturation level is approached. These results show that the porosity increase coincides with the final stages of drying, consistent with the mechanism postulated in Section 3.4.

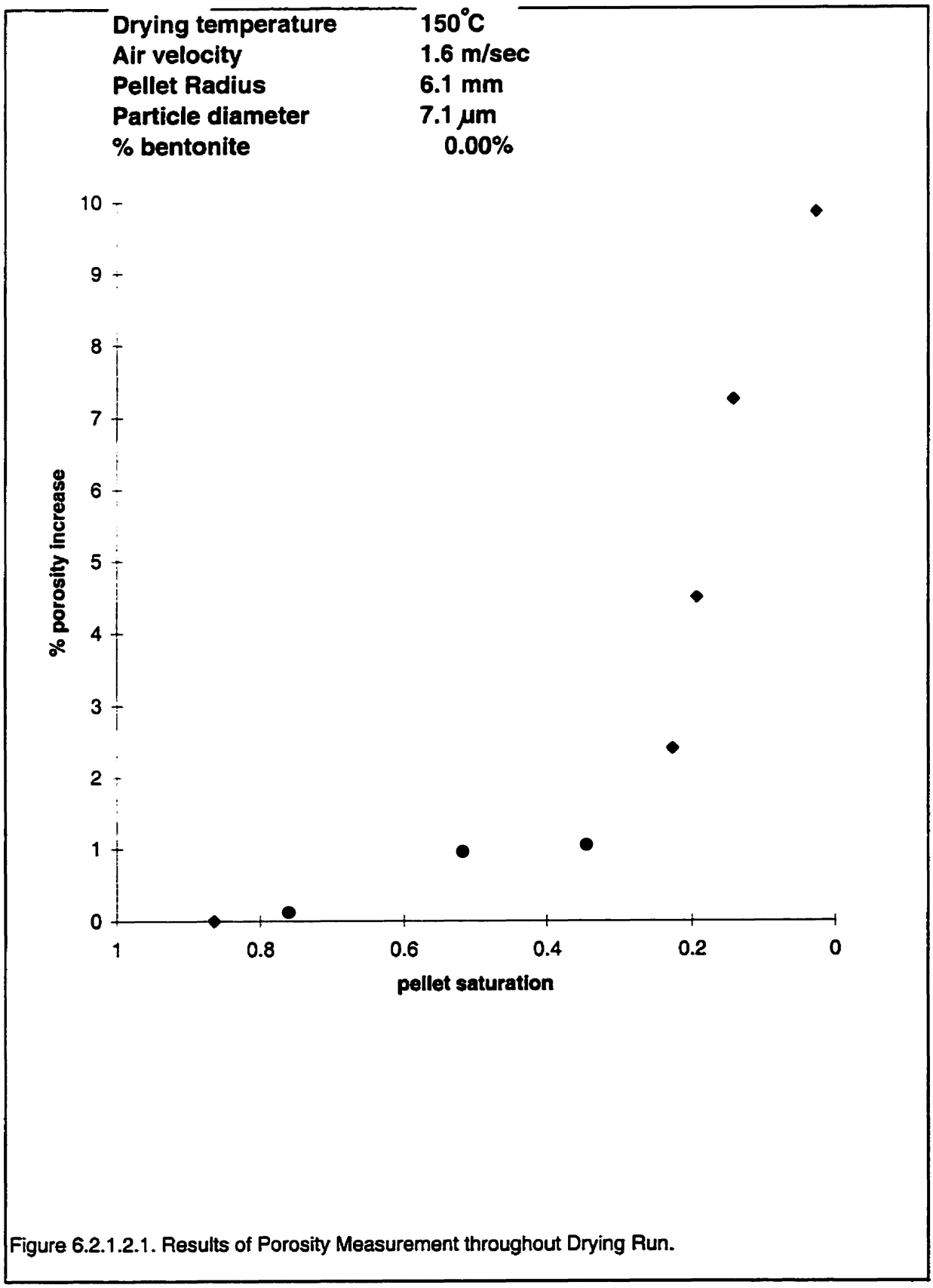


Figure 6.2.1.2.1. Results of Porosity Measurement throughout Drying Run.

6.2.2 Repetitive Drying

The matrix expansion hypothesis implies (and our results from the previous sections corroborate this) that pellets dried under mild conditions should possess a microstructure significantly different from that of the wet pellets. This means that, if rewetted and redried again, the pellets dried mildly the first time should exhibit a drying rate pattern different from that observed during the first-time drying. At the same time, when pellets are dried under conditions of intense drying, their microstructure does not experience any drastic alterations. This suggests that pellets dried rapidly during the original run, should exhibit similar drying behaviour during repeated drying. In addition, the other possible combinations of the first-time / second-time drying can provide additional valuable information regarding the phenomenon of matrix expansion.

A series of repetitive drying experiments was conducted on Griffith iron ore agglomerates to further substantiate the pore expansion hypothesis. The guide for the resulting experimental drying rate curves is presented in the Table 6.2.2.1.

One set of pellets (see Figure 6.2.2.1 (a-c)) was originally dried at 150^{0}C (no drying-rate curves were determined for this step), then rewetted and redried again at 400^{0}C. The latter drying-rate curves are shown with dotted lines. Also plotted in the Figures are drying-rate curves obtained for the freshly prepared pellets dried for the first time at 400^{0}C. The latter curves are shown with thick lines on the respective graphs.

REPETITIVE DRYING RATE CURVES

DRYING TEMPERATURE	**400°C**
AIR VELOCITY	**1.6 m/s**
PELLET RADIUS	**5.09 mm**
BENTONITE CONTENT	**0.00%**
PARTICLE SIZE	**7.1 μm**

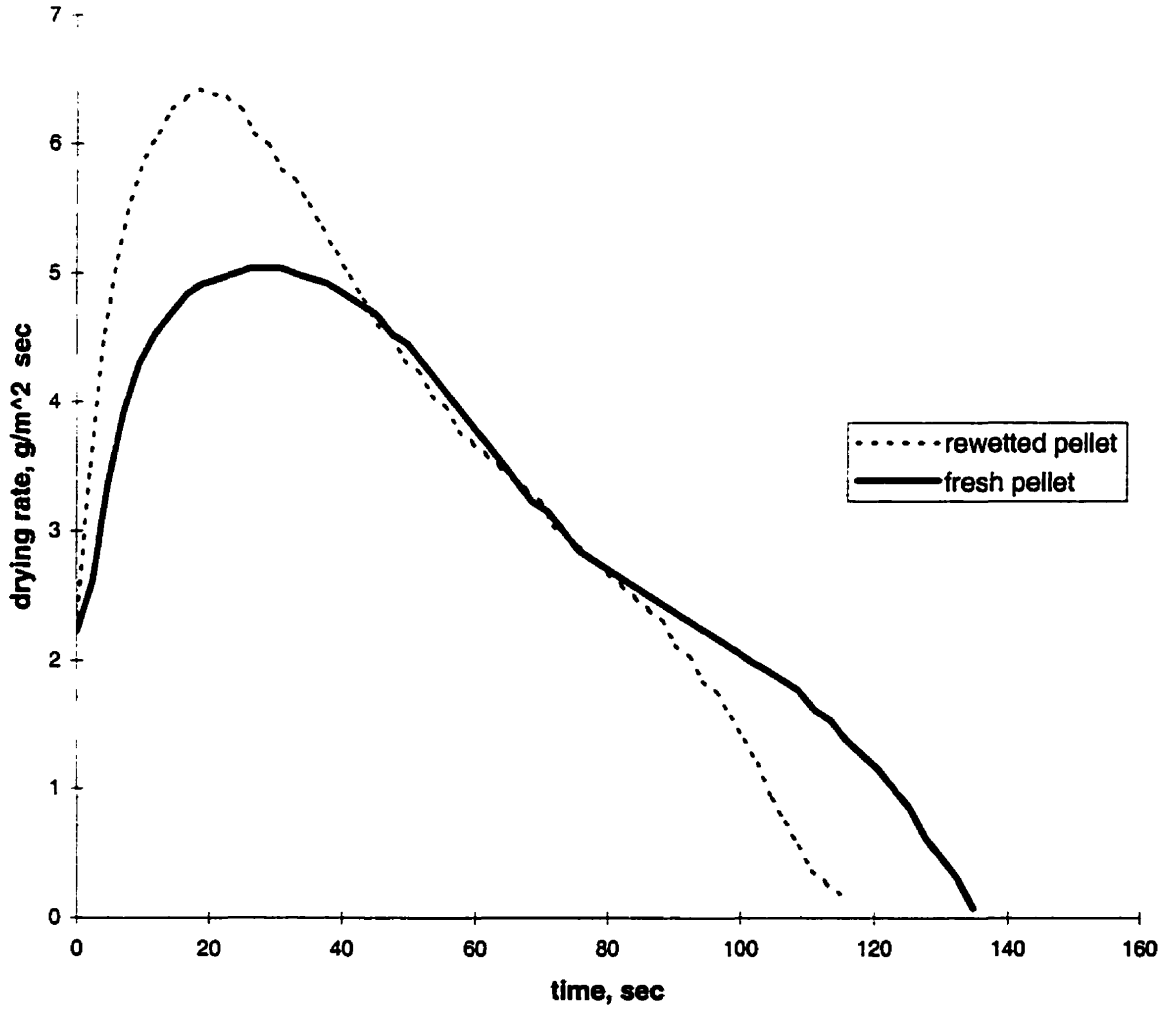


Figure 6.2.2.1 a. Comparison of Drying Rate Curve of the Fresh Pellet without Bentonite Dried at 400°C to that of the Rewetted Pellet Originally Dried at 150°C, then Rewetted and Re-Dried at 400°C.

REPETITIVE DRYING-RATE CURVES

DRYING TEMPERATURE	**400°C**
AIR VELOCITY	**1.6 m/s**
PELLET RADIUS	**5.447 mm**
BENTONITE CONTENT	**0.00%**
PARTICLE DIAMETER	**7.1 μm**

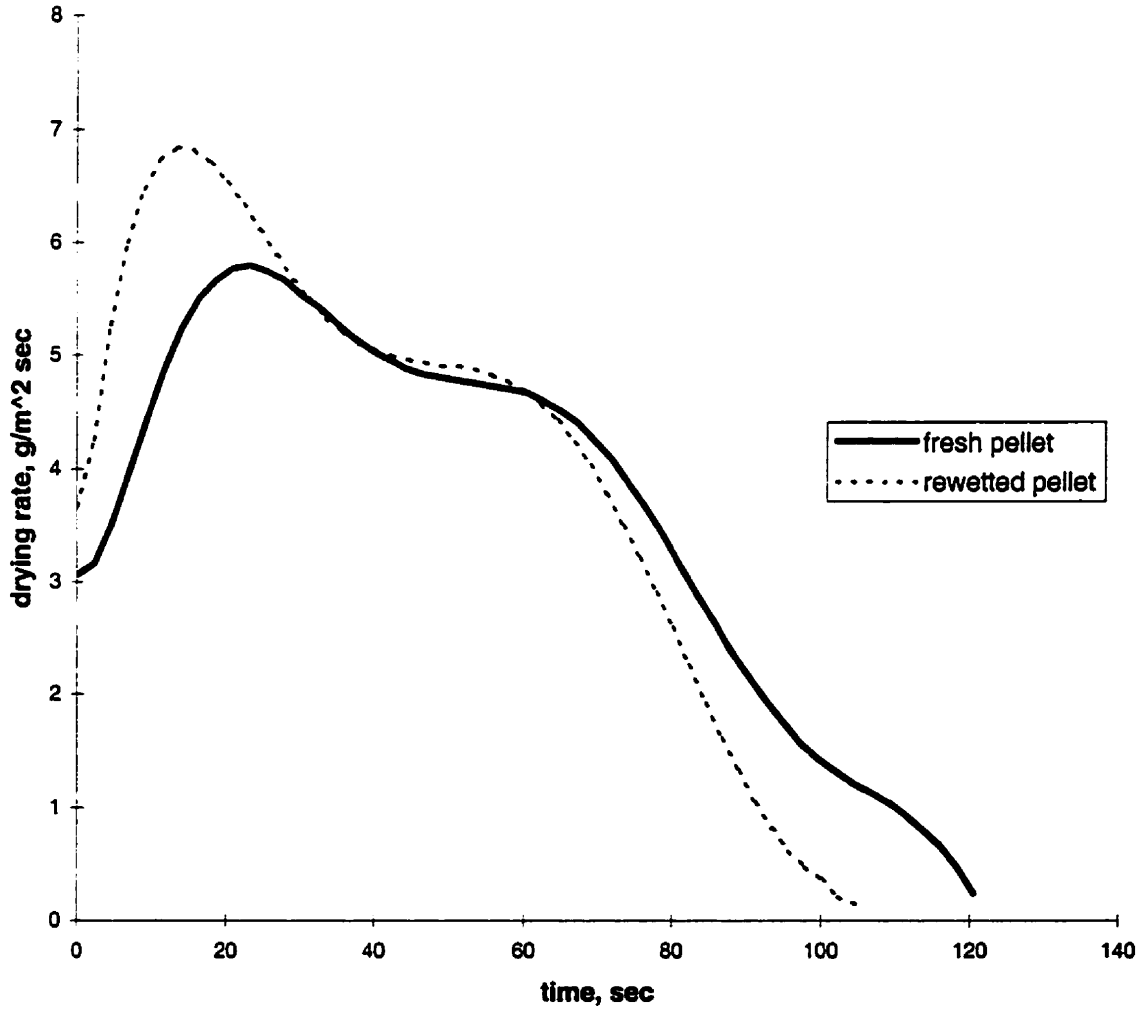


Figure 6.2.2.1 b. Comparison of Drying Rate Curve of a Fresh Pellet without Bentonite Dried at 400°C to that of the Rewetted Pellet Originally Dried at 150°C, then Rewetted and Re-Dried at 400°C.

REPETITIVE DRYING RATE CURVES

DRYING TEMPERATURE	**400°C**	
AIR VELOCITY	**1.6 m/s**	**REMARKS: "rewetted pellet"**
PELLET RADIUS	**5.778 mm**	**was originally dried at 150°C,**
BENTONITE CONTENT	**0.00%**	**then rewetted and redried**
PARTICLE SIZE	**7.1 μm**	**again at 400°C**

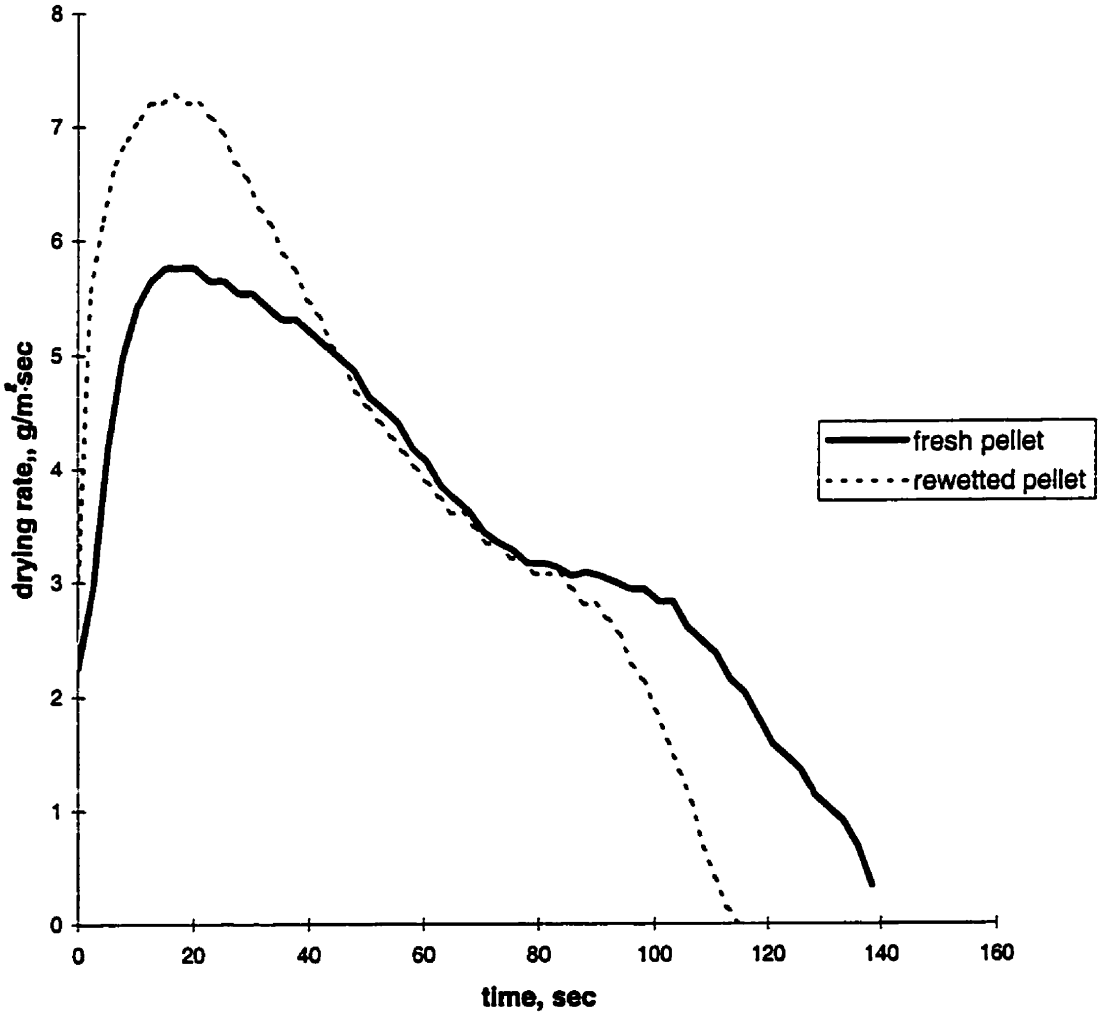


Figure 6.3.2.1 c. Comparison of Drying Rate Curve of the Fresh Pellet without Bentonite Dried at 400°C to that of the Rewetted Pellet Originally Dried at 150°C, then Rewetted and Re-Dried at 400°C.

Table 6.2.2.1. Guide to the Results of Repetitive Drying Experiments Griffith Concentrate

		FIRST-TIME DRYING	
		150°C	400°C
SECOND-TIME DRYING	150°C	Fig. 6.2.2.3	Fig. 6.2.2.4
	400°C	Fig. 6.2.2.1 (a-c)	Fig. 6.2.2.2

Drying rate curves of all rewetted pellets exhibited a steeper initiation period, and higher maximum drying rates than the fresh ones.

Second set of pellets was originally dried at 400°C (thick line). These pellets were then rewetted and redried again at the same drying conditions. Resulting drying-rate curves for the first- and second-time drying are shown in Figure 6.2.2.2 with a solid and a dotted line respectively. The two curves are practically identical.

Yet another pellet was dried at 150°C, then rewetted and redried at the same temperature. Results are shown in Figure 6.2.2.3 with a thick and a dotted lines respectively. The fresh and rewetted drying rate curves are practically identical. Characteristic feature of drying-rate patterns in this group is a well-established constant-rate drying period in both curves.

The final series of repetitive-drying experiments was performed on freshly-prepared pellets dried at 150°C. Their drying-rate curves (shown with thick lines) were compared to those of the rewetted pellets dried under the same conditions (shown with dotted lines). The latter pellets, before being rewetted and tested in this experiment, have been originally dried at 400°C.

REPETITIVE DRYING RATE CURVES

DRYING TEMPERATURE	**400°C**
AIR VELOCITY	**1.6 m/s**
PELLET RADIUS	**6.933 mm**
BENTONITE CONTENT	**0.00%**
PARTICLE SIZE	**7.1 μm**

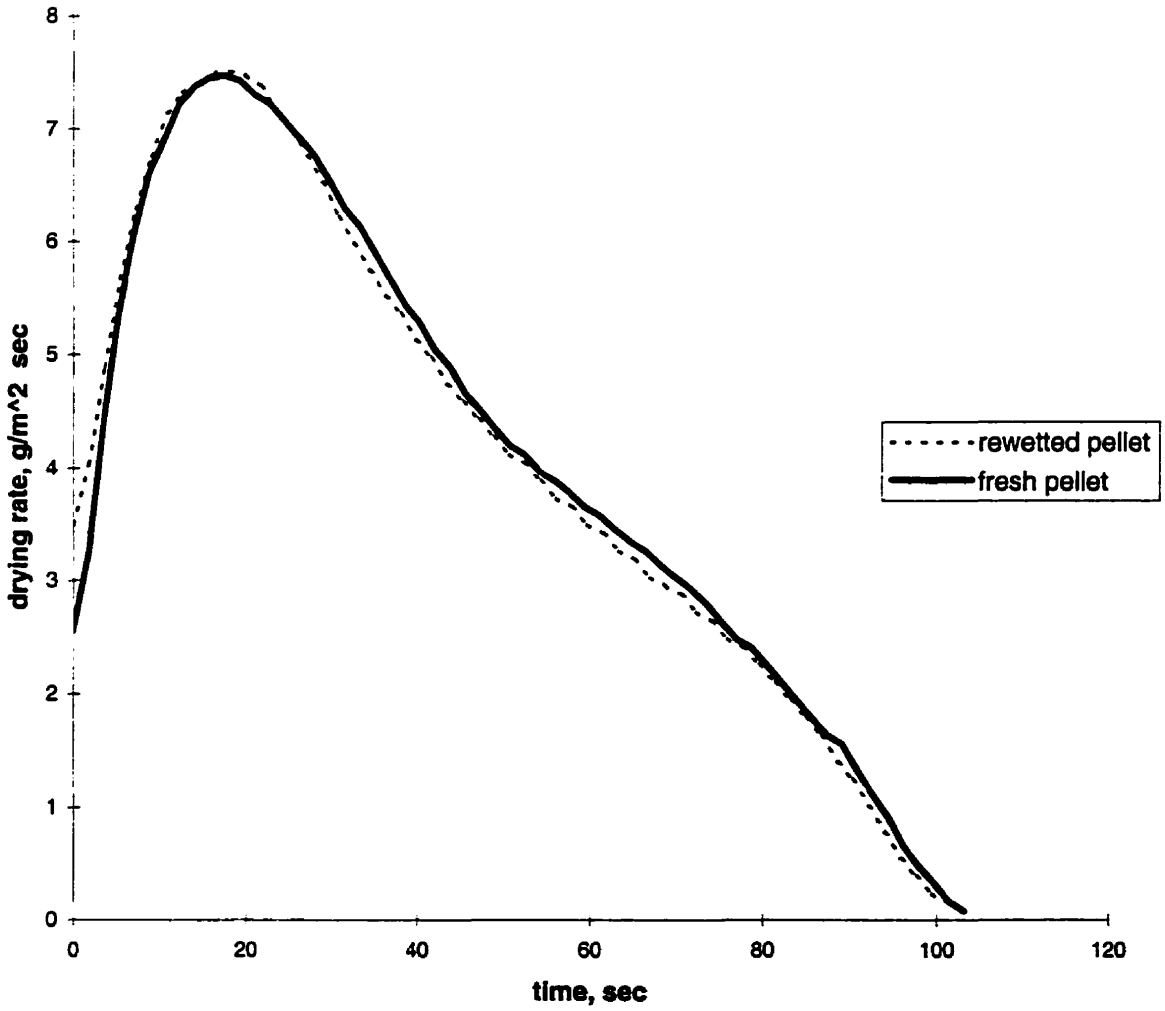


Figure 6.2.2.2 . Comparison of the Drying Rate Curves of a Pellet without Benonite Dried at 400°C then Rewetted and Re-dried at the Same Temperature

REPETITIVE DRYING RATE CURVES

DRYING TEMPERATURE	**150°C**
AIR VELOCITY	**1.6 m/s**
PELLET RADIUS	**5.646 mm**
BENTONITE CONTENT	**0.00%**
PARTICLE SIZE	**7.1 μm**

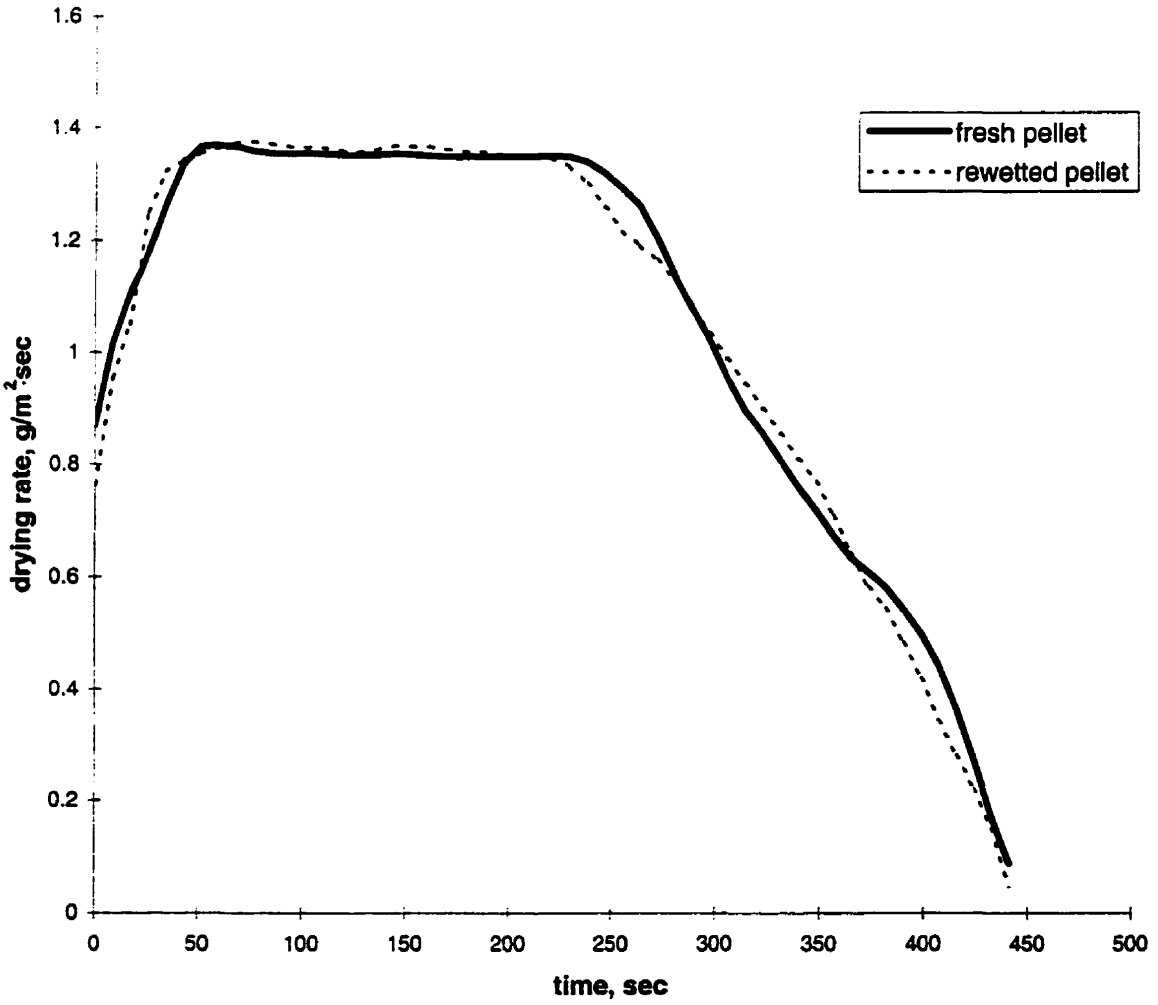


Figure 6.2.2.3. Comparison of the Drying Rate Curves of a Pellet without Benonite Dried at 150°C then Rewetted and Re-dried at the Same Temperature

REPETITIVE DRYING RATE CURVES

DRYING TEMPERATURE	**150°C**
AIR VELOCITY	**1.6 m/s**
PELLET RADIUS	**5.673 mm**
BENTONITE CONTENT	**0.00%**
PARTICLE SIZE	**7.1 μm**

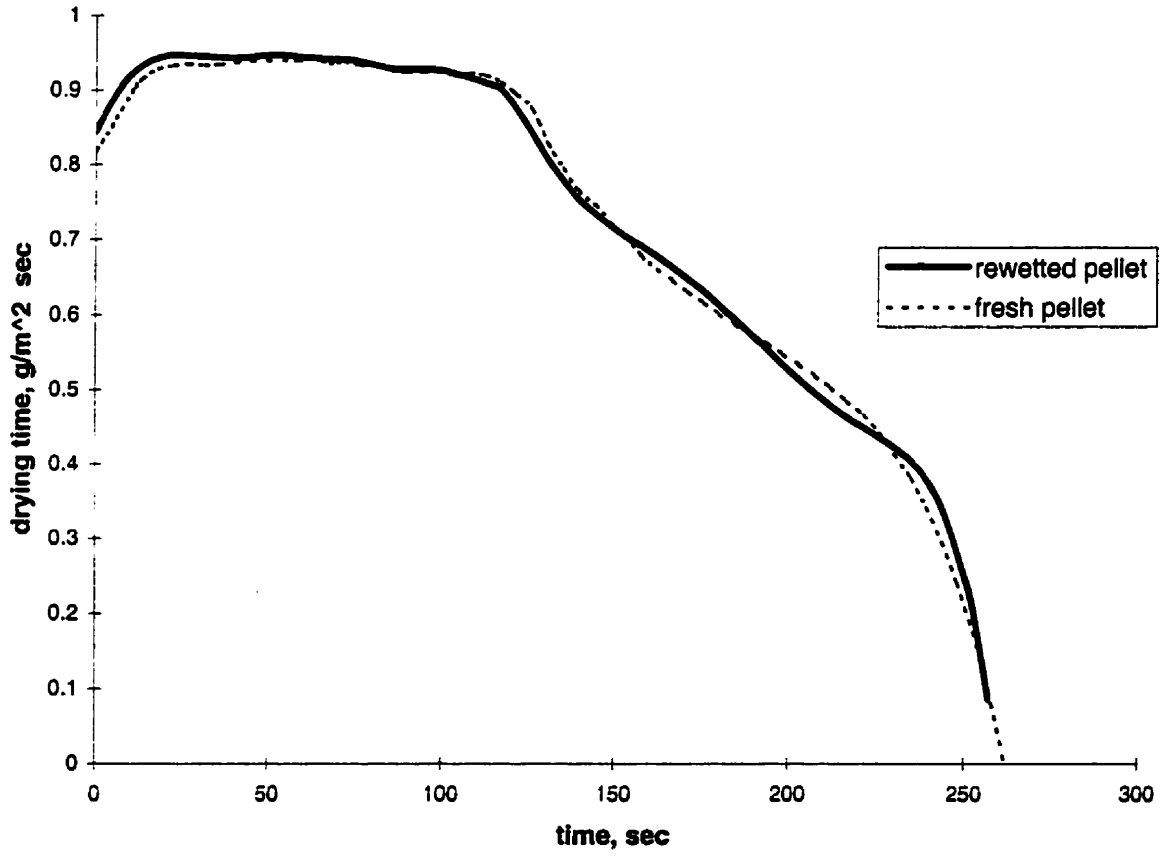


Figure 6.2.2.4. Comparison of Drying Rate Curve of the Fresh Pellet without Bentonite Dried at 150°C to that of the Rewetted Pellet Originally Dried at 400°C, then Rewetted and Re-Dried at 150°C.

Results are shown in Figure 6.2.2.4. It is strikingly similar to Figure 6.2.2.3. Not only are the fresh and rewetted drying rate curves very close, but also relative duration of the constant-rate drying period proportionally to the total one is roughly the same in both cases.

We interpreted the results of the repetitive drying experiments in line with our previous considerations. When pellets are originally dried at mild drying conditions, their microstructure is significantly modified due to matrix expansion phenomenon. That is why, when rewetted and redried again at 400^{0}C (Fig. 6.2.2.1), these pellets exhibited drying behaviour different from the one observed in fresh pellets.

Pellets, which were dried initially at 400^{0}C (Figs. 6.2.2.2 and 6.2.2.4), did not experience any significant structural modifications due to occurrence of vapour lock, which prevented liquid engulfment into the contact areas. Therefore, when dried for a second time, they exhibited drying-rate curves practically identical to those of the fresh pellet.

In this respect results obtained in Figure 6.2.2.3 were somewhat problematic. Pellets in this series were originally dried at 150^{0}C, which, according to our hypothesis, implies that substantial alteration of their microstructure had occurred. Yet, when redried again at the same temperature, they exhibited the drying rate curve very similar to the one of the first-time drying.

The reason for such behaviour can be found when rate controlling mechanisms during drying are analyzed. During the initiation period, and later, during the constant-rate drying, the rate of liquid supply to the surface, which among other parameters depends on pellet porosity (see eqns. 2.4.14 and 2.4.15), is rapid, and thus does not control the drying rate. The

latter is determined, instead, by the 'slow' vapour transport across the boundary layer (eqn. 2.4.6), which is independent of pellet's porosity.

These considerations are validated in Figure 6.2.2.5. It represents the results of the Zaharchuk model simulation of initiation and constant-rate drying periods performed for the same pellet dried at 150^{0}C but with two different porosities - 0.32 and 035. The latter values represent typical increase in porosity during mild drying. Resulting drying rate curves are identical. This validates our observation that apparent matrix expansion upon mild drying does not affect the drying rate during repeated drying run.

6.3 Dry Strength Measurement

Experimental results reported in previous sections imply that significant differences in microstructure arise between pellets dried rapidly as opposed to those dried under milder conditions.

Measurement of dry strength was performed on these two groups of pellets. Its objective was to verify if the microstructural differences among these two groups would be reflected in their mechanical properties.

Griffith concentrate laboratory pellets were spheroidized in the wet state to enable their accurate volume measurements (see Section 5.5). These pellets were then dried on an individual basis in the drying apparatus under well defined drying conditions. Although more time-consuming than drying in batches, this approach insured that all pellets within one group were dried under conditions which were exactly the same and that there was no interference between pellets as a result of physical contact or deviating drying conditions. The first group of pellets was dried at 100^{0}C and an air velocity 1.6 m/s, while the second group was dried at

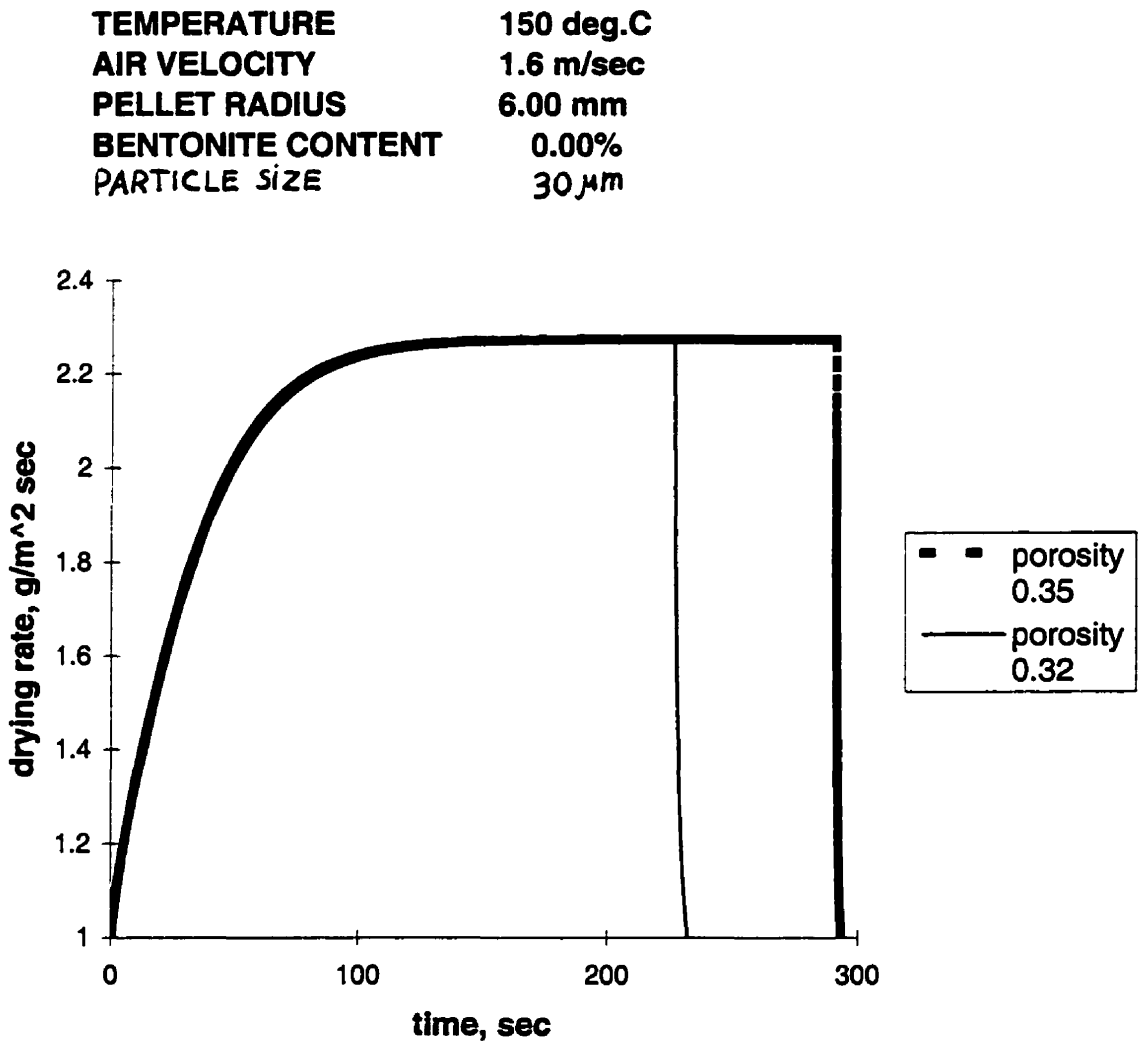


Figure 6.2.2.5. Drying-rate Curves Predicted by the Model for Two Different Porosities: 0.32 and 0.35

400°C and the same air velocity (comprising mild- and intensive-drying environments respectively).

Dry strength was determined using the correlation between strength and L/D^2 (see Section 5.5). Results of these measurements are summarized in Table 6.3.1.

Table 6.3.1. Results from Dry Strength Measurements

Pellet Description	No. of Pellets	Drying Temperature	Porosity	Dry Strength (Eqn. 2.5.1.6) [kPa]
Laboratory Pellets made of Griffith Concentrate (avg. part. diam. 7.1μm)	29	100°C	0.3722 (0.0339)	21.655 (5.081)
	29	400°C	0.3368 (0.0283)	25.442 (6.523)*

*Values in brackets represent the standard deviations

The dry strength of the mildly dried pellets are in good agreement with those found previously in our group for the oven-dried pellets [48]. The latter value was 21.6497 kPa. Also, porosity of the mildly-dried pellets was higher than in the intensively-dried ones, which is consistent with the results reported in Section 6.2.1.1.

The important result of this investigation is that the mean value of dry strength for the pellets dried at 400°C is larger than for those dried at 100°C. In percentage terms, the difference between the two groups is 17.5%. These results are consistent with those of Tigerschiold and Ilmoni [103] discussed in Section 2.5.2.

These results can be explained only by the microstructural differences among these groups of pellets which originate in their respective drying regimes. Pellets which have been dried slowly, as our matrix expansion hypothesis suggests, experienced significant microstructural evolution via the particle engulfment at the late stages of the mild drying process. This resulted in larger values of porosity, and, consequently, in lower dry strength.

In the group of pellets dried at 400^{0}C, on the other hand, particle engulfment in the contact areas during drying has been hindered by the occurrence of vapour lock in these very sites. Consequently, no porosity increase in these pellets is observed, and the average value of dry strength of pellets in this group is higher.

6.4. Binder-Additive Behaviour

Objective of this Section is to document the results concerning the effect of a binder-additive, namely bentonite, on drying behaviour of the agglomerates. This includes the results of microstructural investigations on bentonite precipitation during drying, porosity and dry-strength measurements of agglomerates with bentonite.

Also included in this Section are the results of drying experiments performed on pellets with bentonite, and their modelling using the extended drying model.

6.4.1. Microstructural Investigation of Bentonite Precipitation

In order to study effects of bentonite precipitation on the pore structure, SEM microstructural studies of synthetic agglomerates, prepared by tumbling of monosized spheres[2] with bentonite and dried under different conditions, have been undertaken. Another objective was to study experimentally the character and distribution of bentonite precipitates, throughout the pellet interior, for the intense drying conditions as opposed to the mild ones.

2

Previous studies of bentonite precipitates in the 'regular' iron ore pellets showed that, because of the irregular shape and wide size distribution of the constituent particles, drawing any consistent conclusions about the nature of these precipitates is rather problematic. At the same time, using synthetic agglomerates with bentonite added makes precipitates of the latter much more visible.

The ultimate objective of this particular investigation was to establish the effect (if any) the vapour lock would have on precipitation of bentonite during intense drying.

Particulates used were nickel beads (provided by Sheritt Gordon Ltd.) with a narrow particle size range of 5 -10μm. Pellets were produced using these beads with addition of 1.0 wt.% bentonite (batch #6) [48] and dried at 100^{0}C (representing mild drying environment) and 400^{0}C (the intensive one).

Drying rate curves of pellets *NB21* (dried at 100^{0}C) and *NB23* (400^{0}C) are shown in Figure 6.4.1.1 and 6.4.1.2 respectively. While the former drying rate curve exhibits a distinct constant-rate drying period (i.e. prolonged surface drying), in the latter one this period is completely absent. This feature of the latter drying-rate curve implies that the surface drying has been interrupted early and the reason for this early transition to shrinking core drying regime was the vapour lock.

In order to investigate the microstructure of the above samples their diametrical cross sections were prepared for SEM analysis. Also, a diametrical cross-sectional sample of a glass-bead pellet *GB1* with particle size 200μm, also containing 1.0 wt.% bentonite, was prepared. In the latter sample, which has been dried at 400^{0}C, occurrence of vapour lock during drying is not expected due to its coarser particle size and, correspondingly larger pore structure (see Section 4.1). Hence, the glass-beads pellet was used as a reference point of what would be the character of bentonite deposits in a pellet with the foreknown absence of the vapour lock during drying.

The sample microstructures of the glass-beads pellet *GB1* are shown in Figure 6.4.1.3. Deposits of bentonite are concentrated mainly in the contacts between particles.

TEMPERATURE	100°C
AIR VELOCITY	1.6 m/s
MATERIAL	nickel beads
PELLET RADIUS	5.504 mm
PARTICLE SIZE	5-10 μm
POROSITY	0.3547
BENTONITE	1.0 wt. %

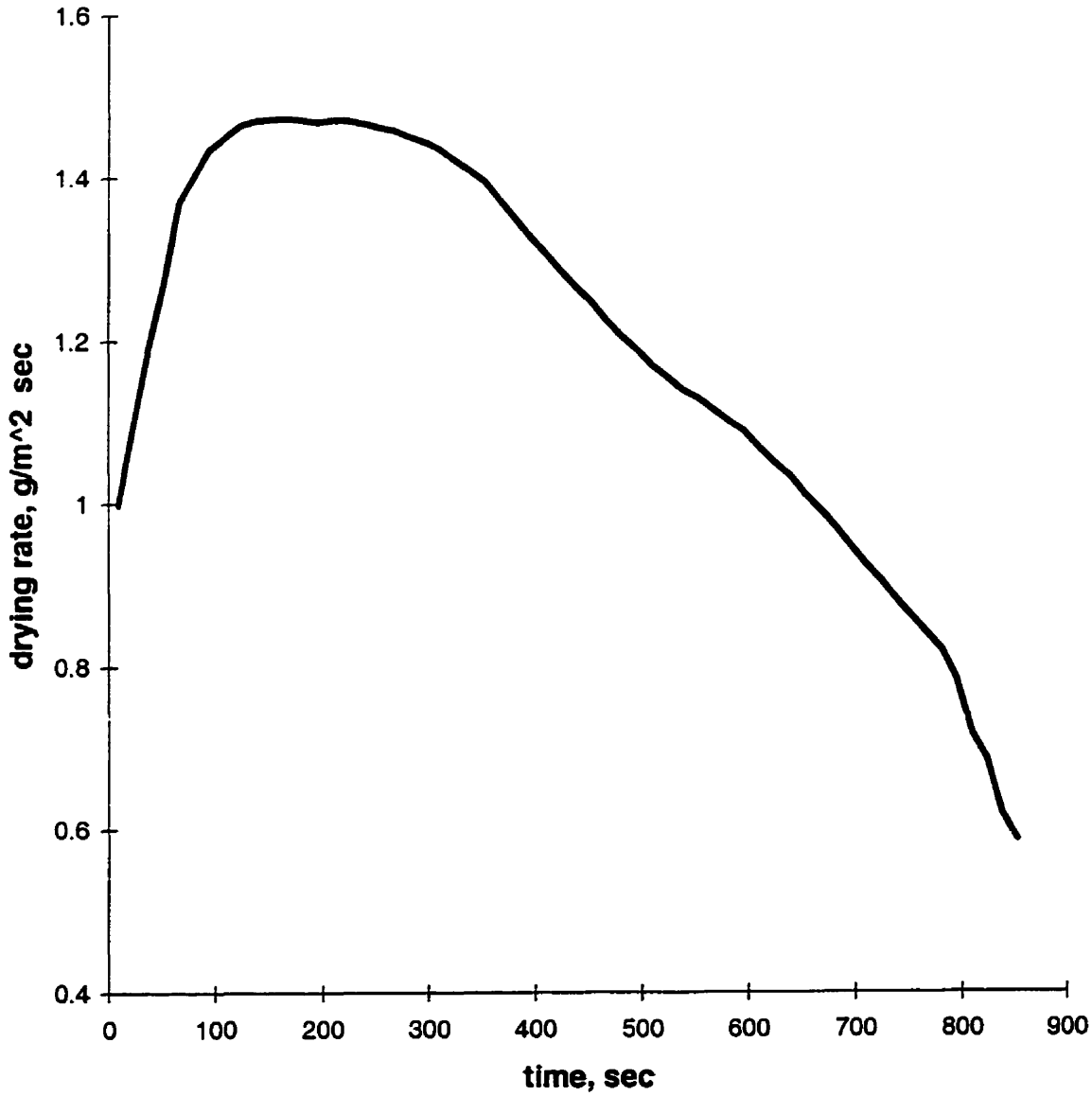


Figure 6.4.1.1. Experimental Drying-rate Curve of a Sample Nickel-beads Pellet Dried at Mild Conditions.

TEMPERATURE	400 deg.C
AIR VELOCITY	1.6 m/s
MATERIAL	nickel beads
PELLET RADIUS	6.29 mm
PARTICLE DIAMETER	5-10 μm
POROSITY	0.3692
BENTONITE	1.0 wt. %

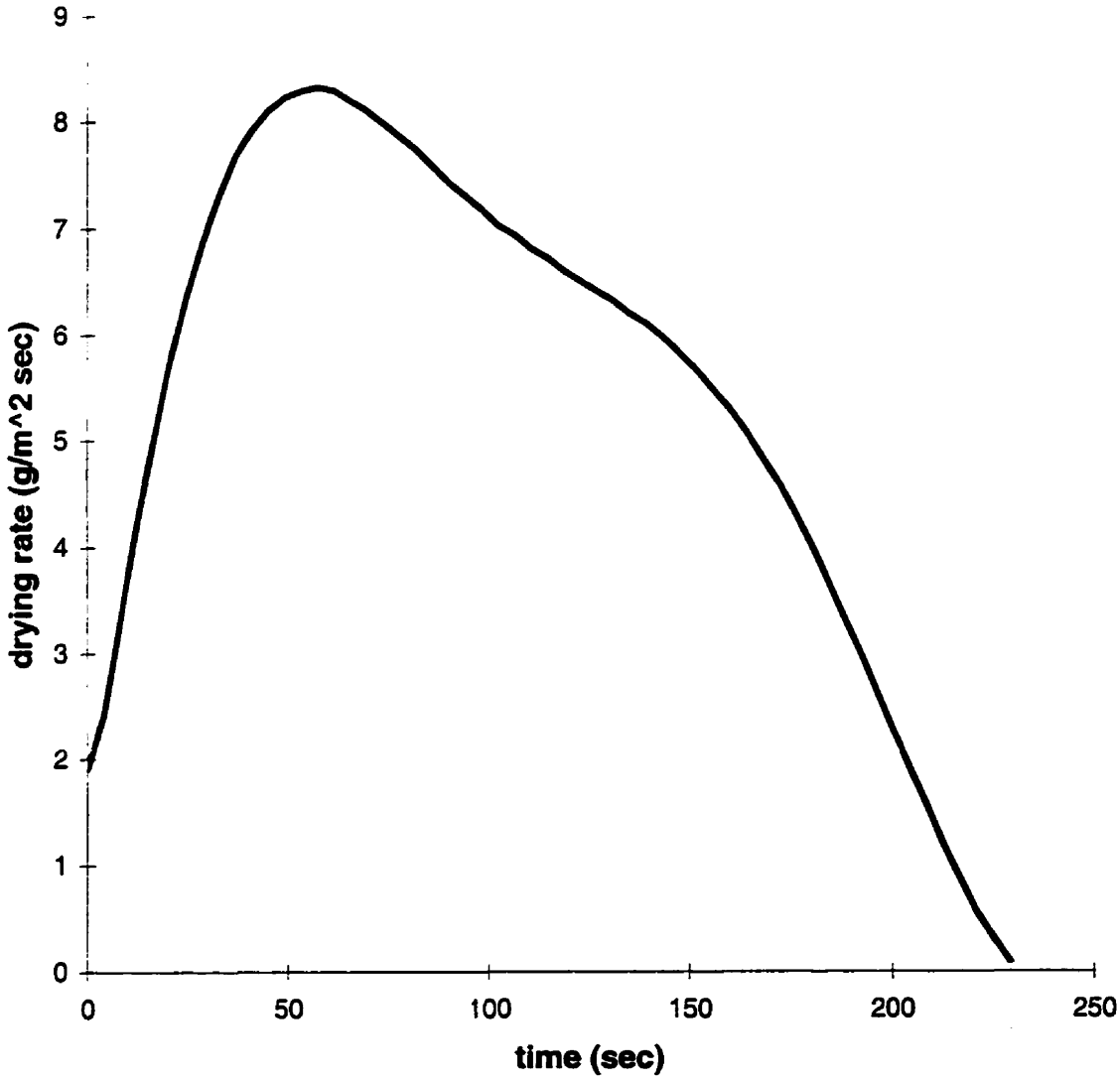


Figure 6.4.1.2. Experimental Drying-rate Curve of a Sample Nickel-beads Pellet Dried under Intense Conditions.

Microstructures of the pellet *NB21* agglomerated from nickel beads (particle size 5-10 μm) and dried at 100°C are shown in Figure 6.4.1.4. Unlike in sample *GBI*, bentonite precipitates not only in the contact areas between the particles, but also across the particles' surface in the large pore spaces.

Finally, Figure 6.4.1.5 depicts microstructures typical of the nickel-beads pellet *NB23* dried at 400°C. Deposits of bentonite in this sample look quite similar to those in samples *NB21*. It appears that bentonite is spread even more across the particles' surface instead of being concentrated exclusively in the contact areas.

In order to investigate these qualitative observations in greater detail the SEM elemental analysis was performed at the characteristic points of samples *NB21* and *NB23*. The point analysis technique, described in Section 5.4, was applied in this experiment.

Table 6.4.1.1 summarizes the results of this analysis. It shows the wt.% of silicon (the main and distinctive component of bentonite) at different locations on the surface of nickel particles. References to the specific micrographs at which the probes were taken are given in brackets.

Table 6.4.1.1 Results of Elemental Analysis of Bentonite Deposits on Nickel-Beads Pellets with Particle Size 5 -10μm

Pellet ID	Drying Temperature	Position of Probe	% Bentonite
NB21 (Fig.6.4.1.4 a)	100°C	1. at the peak of bentonite deposit 2. to the right of the peak 3. to the left from the peak 4. aside from bentonite deposit	5.021 ± 0.158 1.405 ± 0.129 1.256 ± 0.114 0.294 ± 0.079
NB23 (Fig.6.4.1.5 a)	400°C	1. at the peak of deposit 'ring' 2. inside the deposit 'ring' 3. outside the deposit 'ring' 4. aside the deposit 'ring'	3.294 ± 0.124 0.825 ± 0.093 1.699 ± 0.112 1.159 ± 0.095

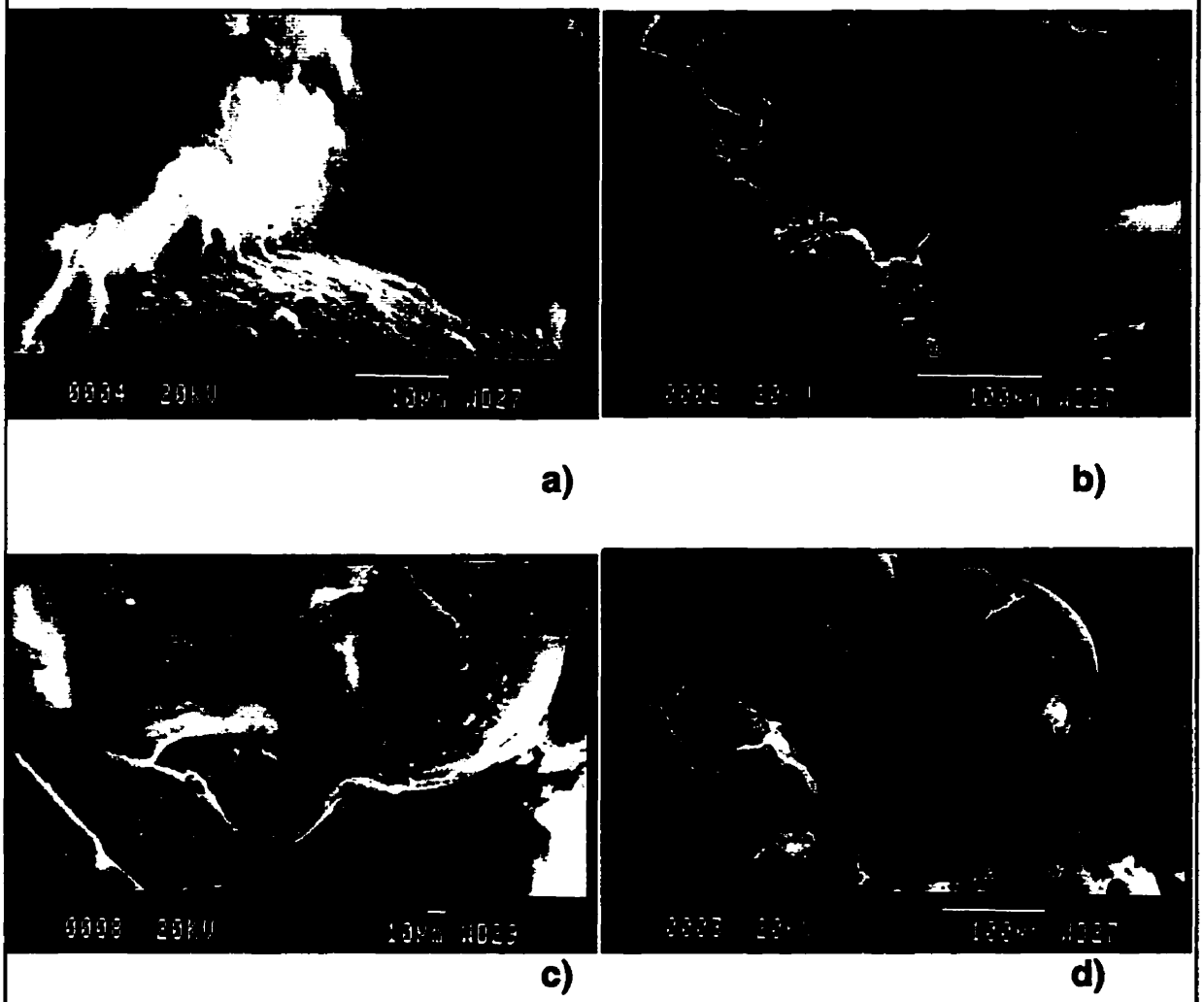


Figure 6.4.1.3.Photomicrographs of a Glass-beads Pellet with the Particle Diameter 200um and 1.0% bentonite Dried at 400 Degrees C: (a,b) - Pellet Interior; (c, d) - Near-the-Surface Area .

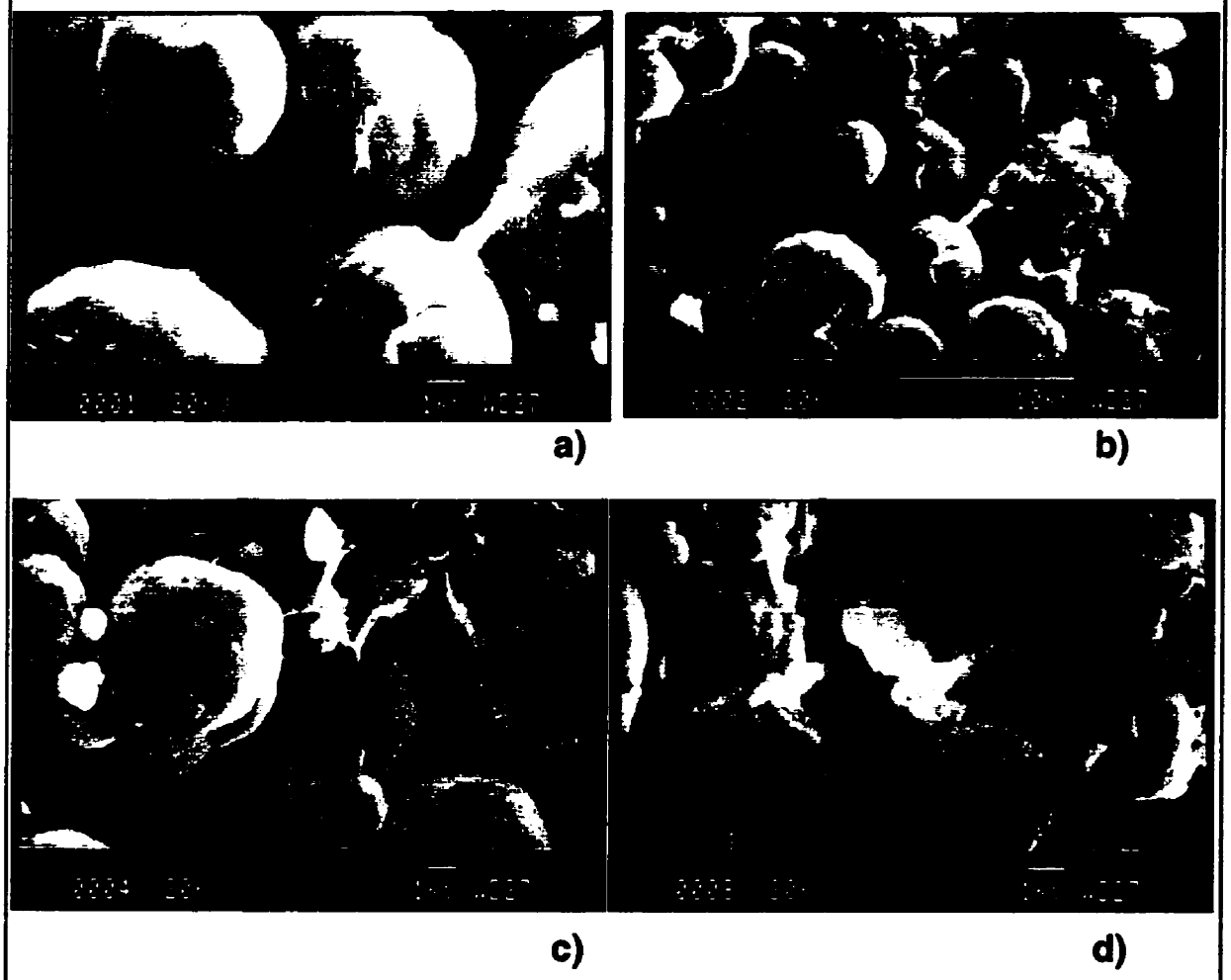


Figure 6.4.1.4 Photomicrographs of a Nickel-beads Pellet with the Particle Diameter 7.5 um and 1.0% bentonite Dried at 100 Degrees C:(a-c) - Pellet Interior; (d) - Near the Surface Area .

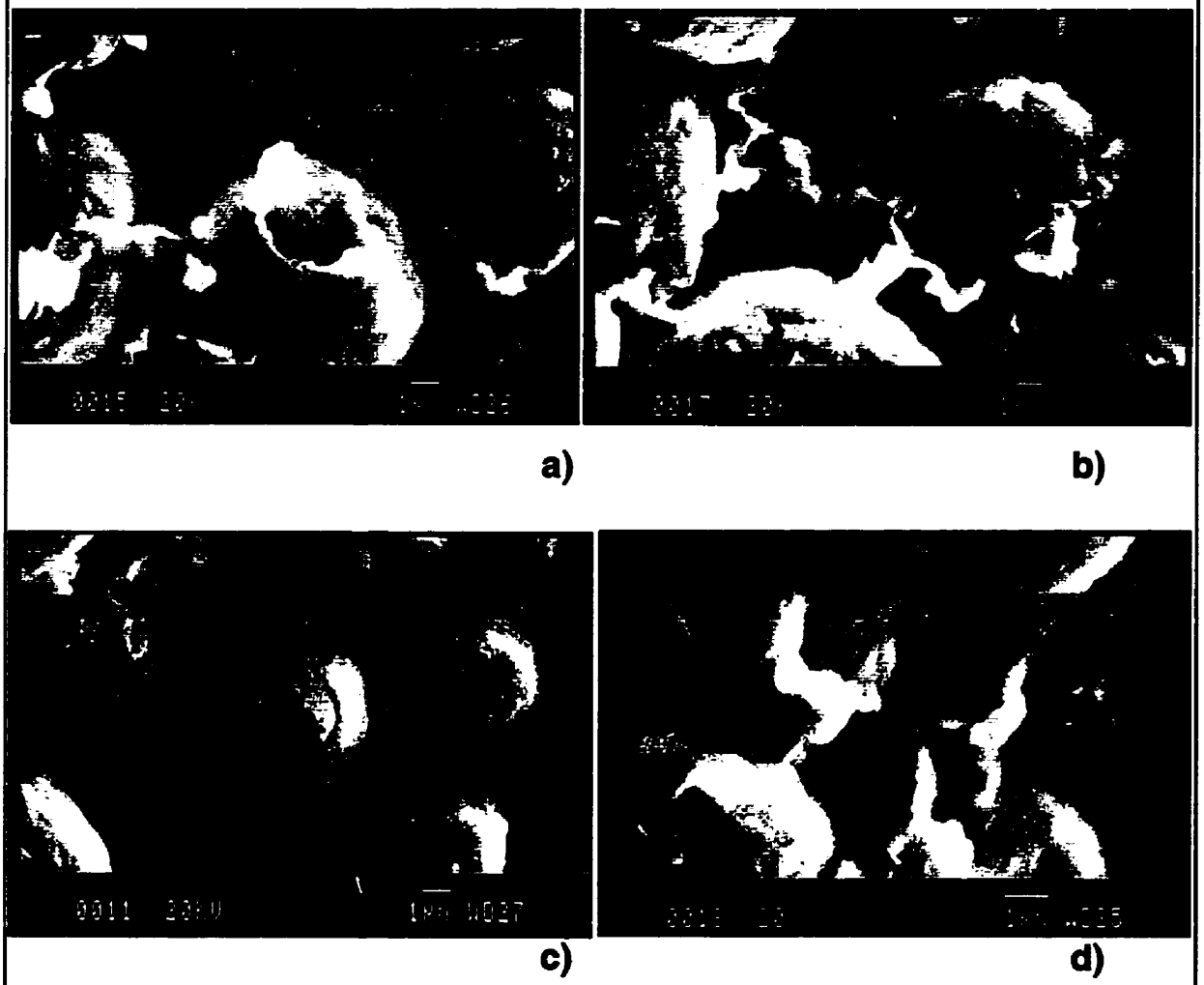


Figure 6.4.1.5. Photomicrographs of a Nickel-beads Pellet with the Particle Diameter 7.5 um and 1.0% bentonite Dried at 400 Degrees C:(a,b) - Pellet Interior; (c,d) - Near-the-Surface Area .

It follows from these results that bentonite deposits in a pellet dried at 100^{0}C distribute evenly on both sides of a bentonite deposit 'peak' in Fig.6.4.1.4(a). Also, there is relatively little bentonite located aside from this peak.

In a pellet dried at 400^{0}C (Fig. 6.4.1.5(a)), on the other hand, the distribution of bentonite is more uneven, with more bentonite located on the outer side of a deposit 'ring' (probe 3) than on its inner side (probe 2). Most significantly, the amount of bentonite aside from the 'ring' (probe 4) is substantially higher than inside the deposit 'ring'. It is also much higher than analogous figure in pellet dried at 100^{0}C.

It seems that such differences in character of bentonite depositions can be explained in terms of the occurrence of the vapour lock. Drying of the pellet *NB21* proceeds along the 'classical path' with most of the drying occurring at the pellet's surface (see Figure 6.4.1.1). In this case precipitation of bentonite occurs when the pendular stage is reached locally or when water-bentonite suspension becomes locally immobile. Deposition of bentonite, therefore, occurs mainly in the areas immediately adjacent to the contact points between the particles.

When pellet is dried rapidly (pellet *NB23),* the vapour lock condition is reached at high saturation level (see drying-rate curve in Figure 6.4.1.2); i.e., when pores are still filled with liquid. The vapour lock occurs *within* the liquid phase at the narrowest pore necks, i.e. at the contacts between particles. Hence, the possibility of bentonite precipitation in these contact points will be limited. Instead, precipitation of bentonite will occur mostly along the circular liquid-gas-solid interface that forms around the contact between neighboring spherical particles (see *point1* in Figure 6.4.1.5 (a)), as well as in the pore areas away from the contact points, whereto the liquid-gas interface will eventually recede.

Another part of the microstructural investigation included analyzing the distribution of bentonite deposits in these pellets' radial direction. The purpose of this investigation was twofold. First of all -- to establish if there is efflorescence of bentonite during the surface drying regime at mild drying conditions. Secondly, if efflorescence of bentonite is taking place during mild drying, then how it would be affected by the occurrence of the vapour lock under intense-drying conditions.

The beam-scanning elemental analysis, described in Section 5.4, was applied to determine silicon (and, therefore, bentonite) distribution in radial direction inside the pellets *NB21* and *NB23*.

The results of this analysis are presented graphically in Figure 6.4.1.6. Normalized content of silicon (the amount of silicon at a particular point divided by the average amount throughout the sample) is plotted against radial distance from the sample's surface. The dotted line represents the average normalized amount of bentonite.

The radial distribution of bentonite deposits in pellet *NB21* is shown in the upper graph. Evidently, the amount of bentonite in the vicinity of this pellet's surface is more than twice as high as its average amount in the interior, implying that efflorescence of bentonite during mild drying is quite significant.

On the other hand, pellet *NB23*, dried at 400^0C, shows no signs of bentonite efflorescence with bentonite deposits distributed evenly in radial direction.

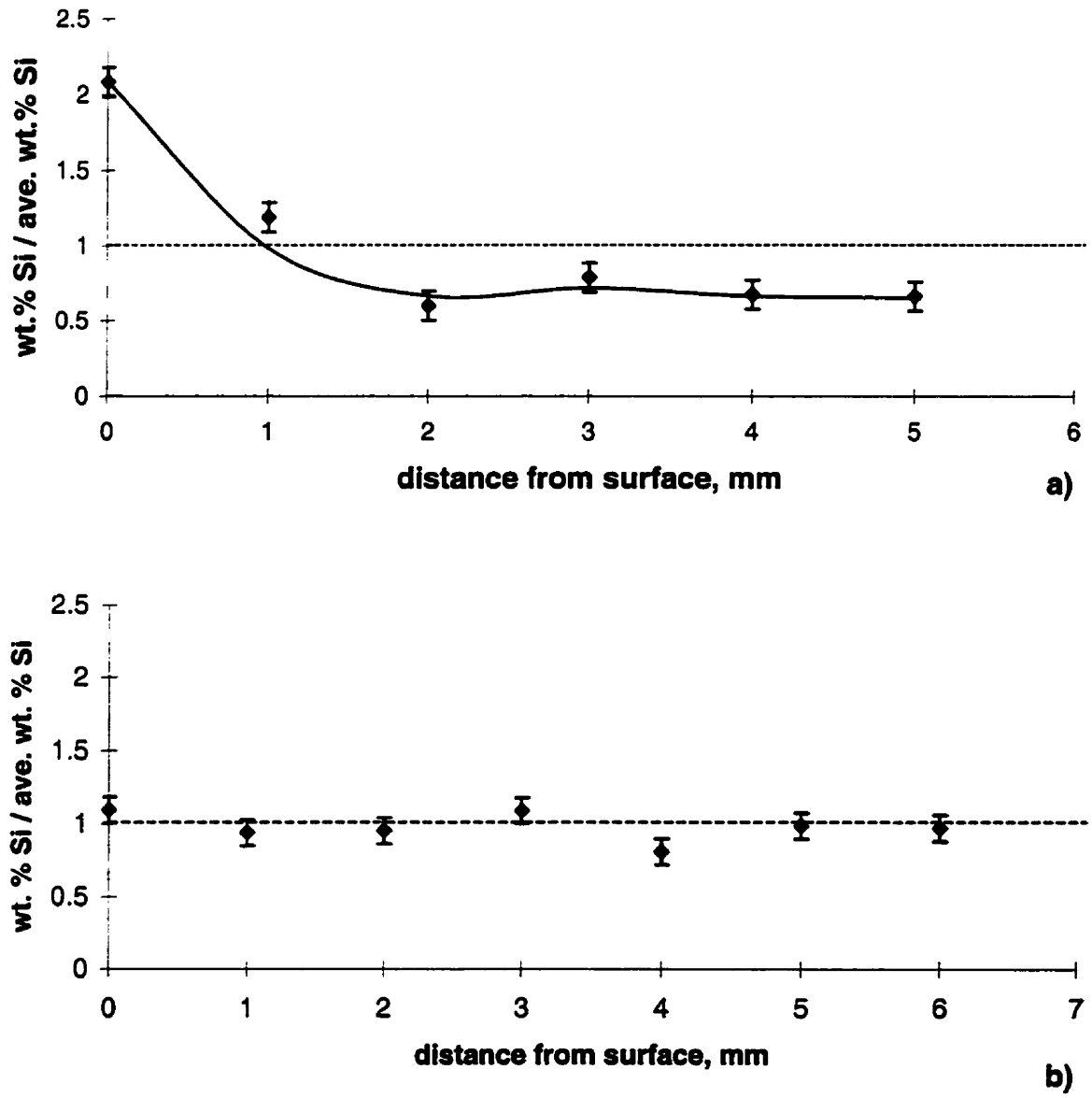


Figure 6.4.1.6. Distribution of Bentonite inside Nickel-beads Pellets Dried at: a) - 100 deg. C; b) - 400 deg. C.

6.4.2 Porosity and Dry Strength Measurements

Measurements of pellet porosity on a wet and dry basis and measurement of these pellets' dry strength were performed on three groups of pellets contaning bentonite. The first group of pellets was made from Griffith iron ore concentrate with the wide particle size distribution (avg. particle diameter 7.1μm) and an addition of 0.8 wt.% bentonite. Second and third groups comprised the synthetic agglomerates made from monosized spherical particles, both with addition of 1.0% bentonite. In the second group *(GBI)* pellets were made from monosized glass beads, 200μm in diameter, and used in the experiments described in Section 6.4.1 of the thesis. The third group of pellets *(NB3)* was made from monosized nickel beads, 16μm in diameter.

Procedures were identical to those reported in Sections 6.2.1 and 6.3 for the bentonite-free pellets. Each kind of pellets was divided into two groups: one was dried at 100^{0}C and an air velocity 1.6 m/s, while another group - at 400^{0}C and the same air velocity (comprising mild- and intense-drying environments, respectively). Results of these measurements are summarized in Table 6.4.2.1.

Presented results show that there is a significant porosity increase in Griffith iron-ore pellets dried at 100^{0}C, and practically no such effect for those dried at 400^{0}C. This effect is similar to that reported in Section 6.2.1 for pellets without bentonite, although the absolute value of porosity increase in pellets with 0.8% bentonite is somewhat smaller (14.183% and 10.584%, respectively).

Values of the dry strength of the mildly-dried iron ore pellets are in good agreement with those found previously in our group for the oven-dried pellets [48] -- 176.005 kPa for the pellets with 0.8% bentonite. Another important observation is that the mean value of dry

strength for the pellets dried at 400°C is larger than for those dried at 100°C. In percentage terms the difference between the two groups is 7%.

Table 6.4.2.1. Porosity and Dry Strength Measurements of Pellets with Bentonite

Pellet Description	No. of Pellets	Drying Temperature	Average Porosity		% Porosity Increase	Dry Strength (eqn.2.5.1.6) [kPa]
			wet basis	dry basis		
Griffith Iron-ore Pellets *avg. d_p=7.1*µm + 0.8% bentonite	28	100°C	0.3230	0.3569	10.584 (2.565)	175.480 (25.6529)
	29	400°C	0.3097	0.3165	0.7062 (1.323)	187.657 (24.9124)
-Glass beads' pellets *(GB1)* *d_p=200*µm *+1.0% bentonite*	54	100°C	0.4266	0.4276	0.253 (0.314)	n/a
		400°C	0.4155	0.4175	0.319 (0.479)	n/a
-Nickel beads' pellets *(NB3)* *d_p=16*µm *+1.0% bentonite*	65	100°C	0.3547	0.3578	0.874 (1.0378)	n/a
		400°C	0.3727	0.3761	0.912 (0.9231)	n/a

*Values in brackets represent the standard deviations

As in the case of bentonite-free pellets, these results can be explained by the microstructural differences among these groups of pellets which originate in their respective drying regimes (see argument in Section and 6.3).

Results of porosity measurements on synthetic agglomerates made from monosized spheres (groups *2* and *3* in Table 6.4.2.1) show that there is only a slight porosity increase upon drying for pellets in either group regardless of the drying conditions.

The results of the porosity measurements reported in this Section, as well as in Sections 6.2.1 for the bentonite-free pellets, substantiate our hypothesis that matrix expansion

occurs due to engulfment of loose fine particles into the contacts between the larger structure-creating ones. This migration occurs at the late stages of the mild drying process as the liquid phase recedes into pendular bridges between the larger, structure-creating particles (see Sections 3.4 and 6.2.1.). In agglomerates that do not contain a substantial fraction of fine particles, matrix expansion upon drying does not take place.

6.4.3 Drying Experiments and Modelling

In this Section the results of drying experiments of Griffith iron-ore pellets with bentonite, as well as their modelling, are documented. Results of two independent series are reported:

1) drying experiments of both fine-particle-size and coarser-particle-size pellets containing bentonite;

2) center-temperature measurements of these pellets.

6.4.3.1 Drying of Fine-Particle-Size Pellets with Bentonite

An important limitation of the Zaharchuk model, discovered by the author during his MASc studies [2], relates to intense drying of the fine-particle-size agglomerates (avg. part. size 7.1μm) containing bentonite. For such pellets the Zaharchuk model overpredicts the maximum drying rate and then underpredicts the total drying time by as much as 15% (see example in Figure 6.4.3.1.1), as opposed to an excellent model/experiment agreement for the bentonite-free pellets (see Fig. 6.1.1.1). Part of the present project, therefore, was a search for an explanation for this phenomenon. The working hypothesis is that bentonite precipitation during the shrinking core regime modifies both the pore microstructure and

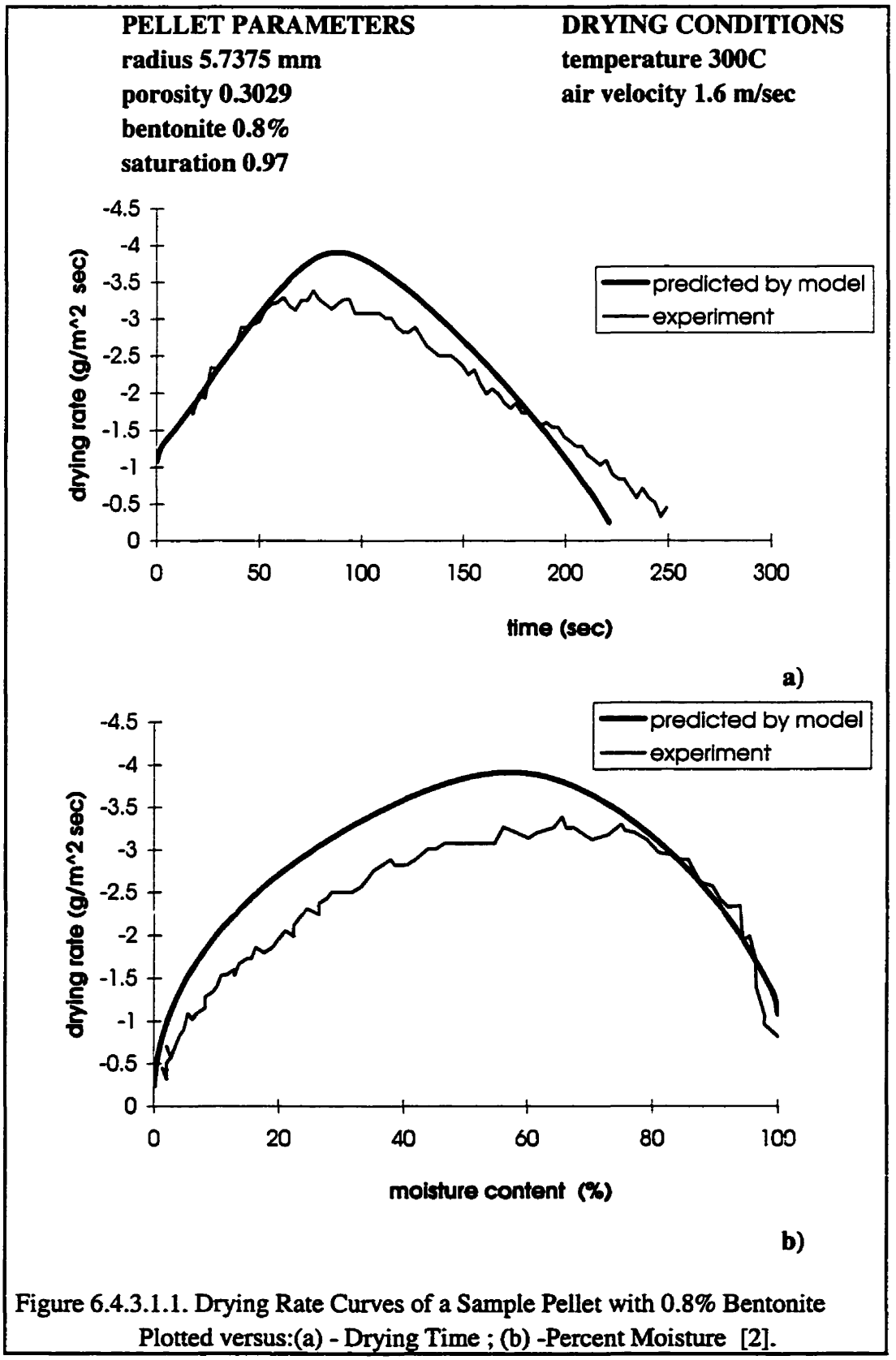


Figure 6.4.3.1.1. Drying Rate Curves of a Sample Pellet with 0.8% Bentonite Plotted versus:(a) - Drying Time ; (b) -Percent Moisture [2].

physical properties (e.g., dry-shell thermal conductivity) of pellet's matrix, thus affecting the drying rate.

Several modelling programs to incorporate more discriminating elements into the model were part of these investigations. In the process some of the parameters such as pore tortuosity and temperature dependence of the equilibrium vapour pressure were shown to have a minimal effect on shape of the model-predicted drying-rate curves. The only parameter that did minimize the deviations of model-predicted curve patterns was found to be the effective thermal conductivity of the dry shell. When the value of the latter is decreased from 0.5 W/mK (as used for bentonite-free pellets) to 0.35 W/mK, the model-predicted drying rates exhibited much better agreement with experiment. This is demonstrated in Figures 6.4.3.1.2 - 6.4.3.1.5, which show the experimental results, the original and the corrected model predictions. In the upper graphs the drying rates are plotted against time and in the lower -- against the decreasing total moisture content of the pellets (or saturation). The guide for these graphs is presented in Table 6.4.3.1.1.

Table 6.4.3.1.1. Guide to the Results of Drying Experiments
Griffith Concentrate
Pellet Diameter: 10.475 - 12.2 mm
Porosity: 0.2773 - 0.3029
Average particle diameter: 7.1μm
Bentonite content: 0.8 %
Pellet Saturation: 0.94 - 0.98

Temperature	**300°C**	**400°C**	
Air Flow Rate	**1.6 m/sec**	**1.0m/sec**	**1.6 m/sec**
Figures	Fig.6.4.3.1.2	Figs. 6.4.3.1.3 and 6.4.3.1.4	Fig. 6.4.3.1.5

Clearly, the model-experiment agreement is much better when the corrected value of effective dry-shell conductivity of 0.35 W/mK is being used in the model.

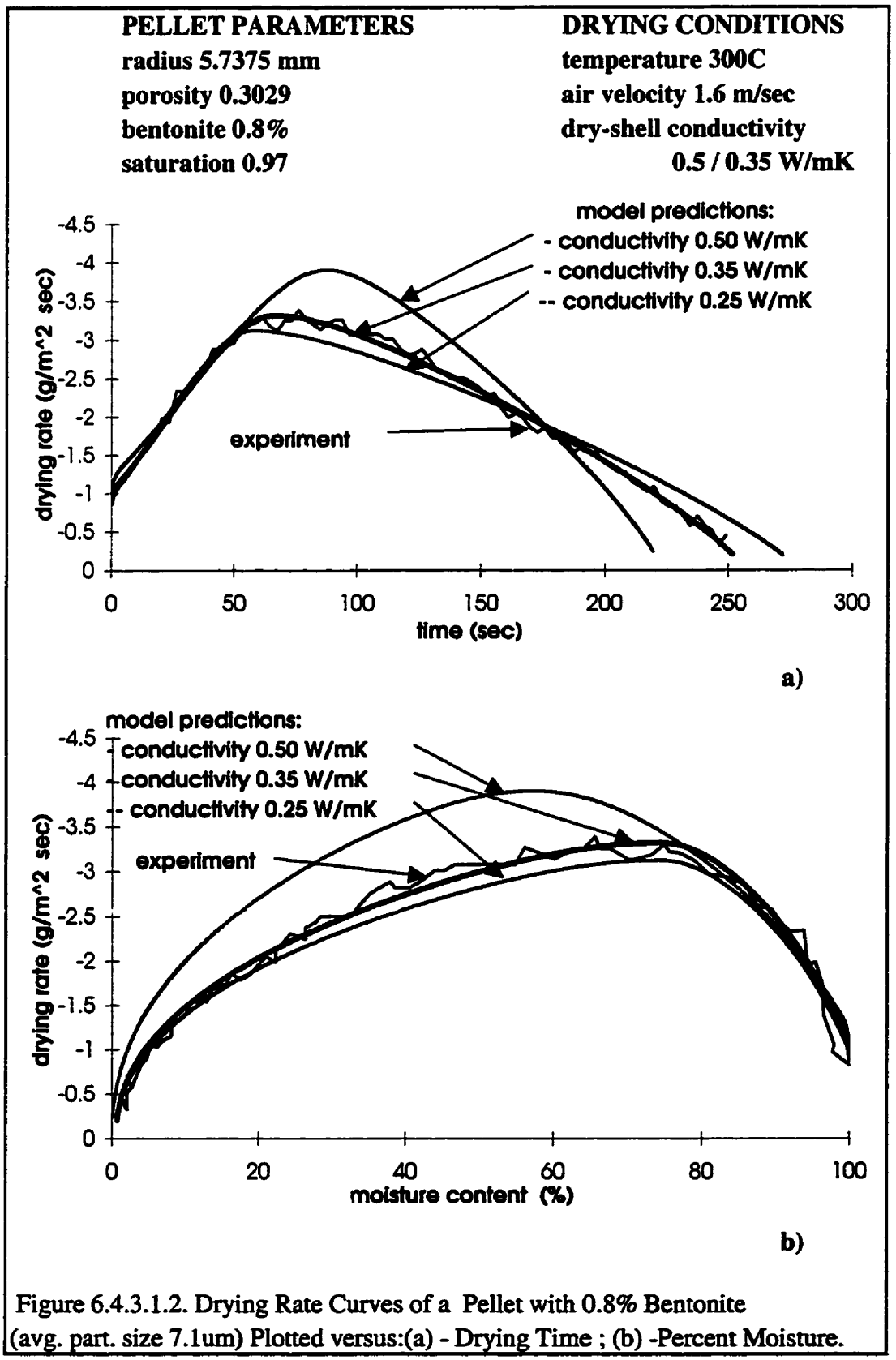


Figure 6.4.3.1.2. Drying Rate Curves of a Pellet with 0.8% Bentonite (avg. part. size 7.1um) Plotted versus:(a) - Drying Time ; (b) -Percent Moisture.

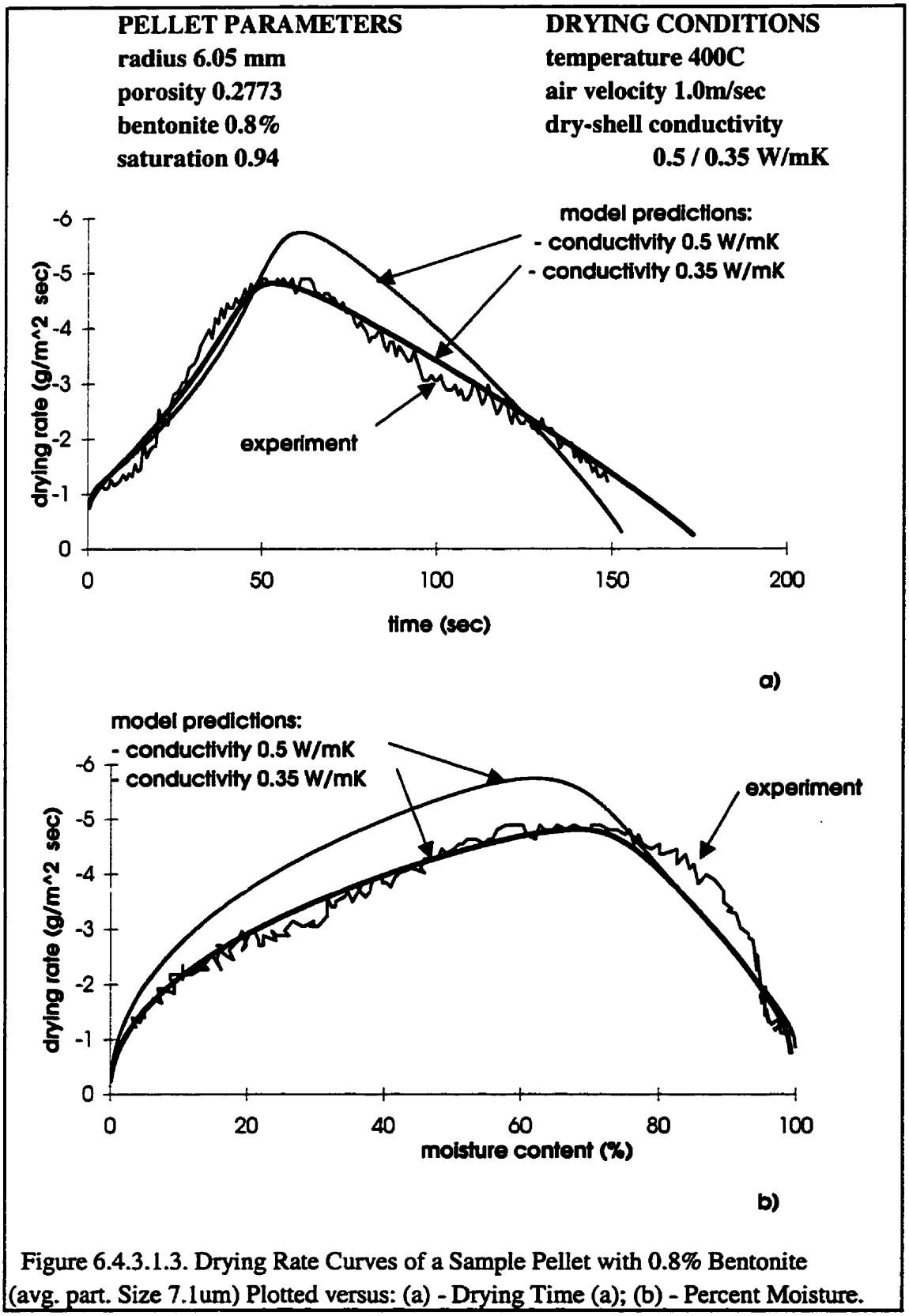


Figure 6.4.3.1.3. Drying Rate Curves of a Sample Pellet with 0.8% Bentonite (avg. part. Size 7.1um) Plotted versus: (a) - Drying Time (a); (b) - Percent Moisture.

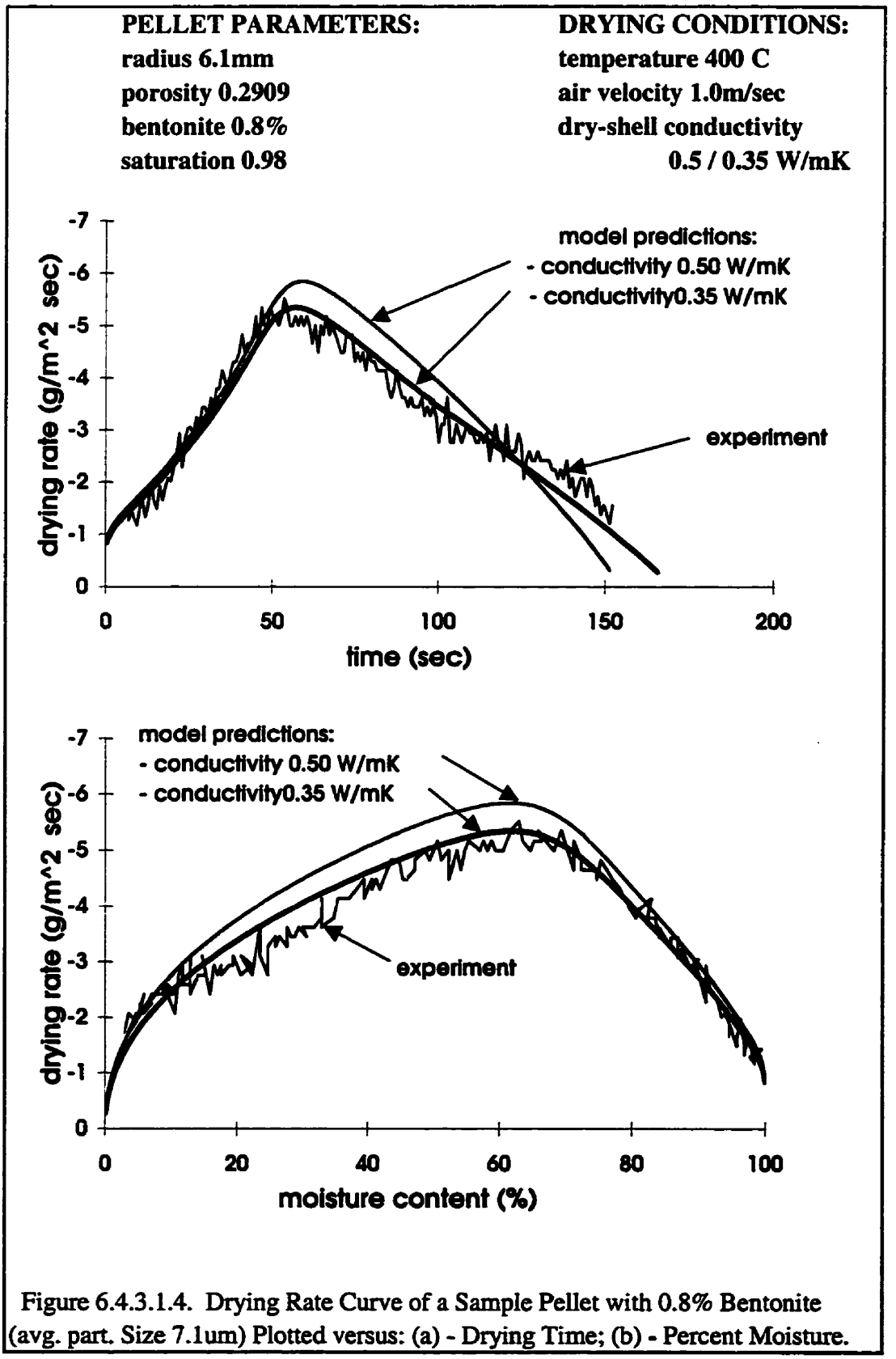


Figure 6.4.3.1.4. Drying Rate Curve of a Sample Pellet with 0.8% Bentonite (avg. part. Size 7.1um) Plotted versus: (a) - Drying Time; (b) - Percent Moisture.

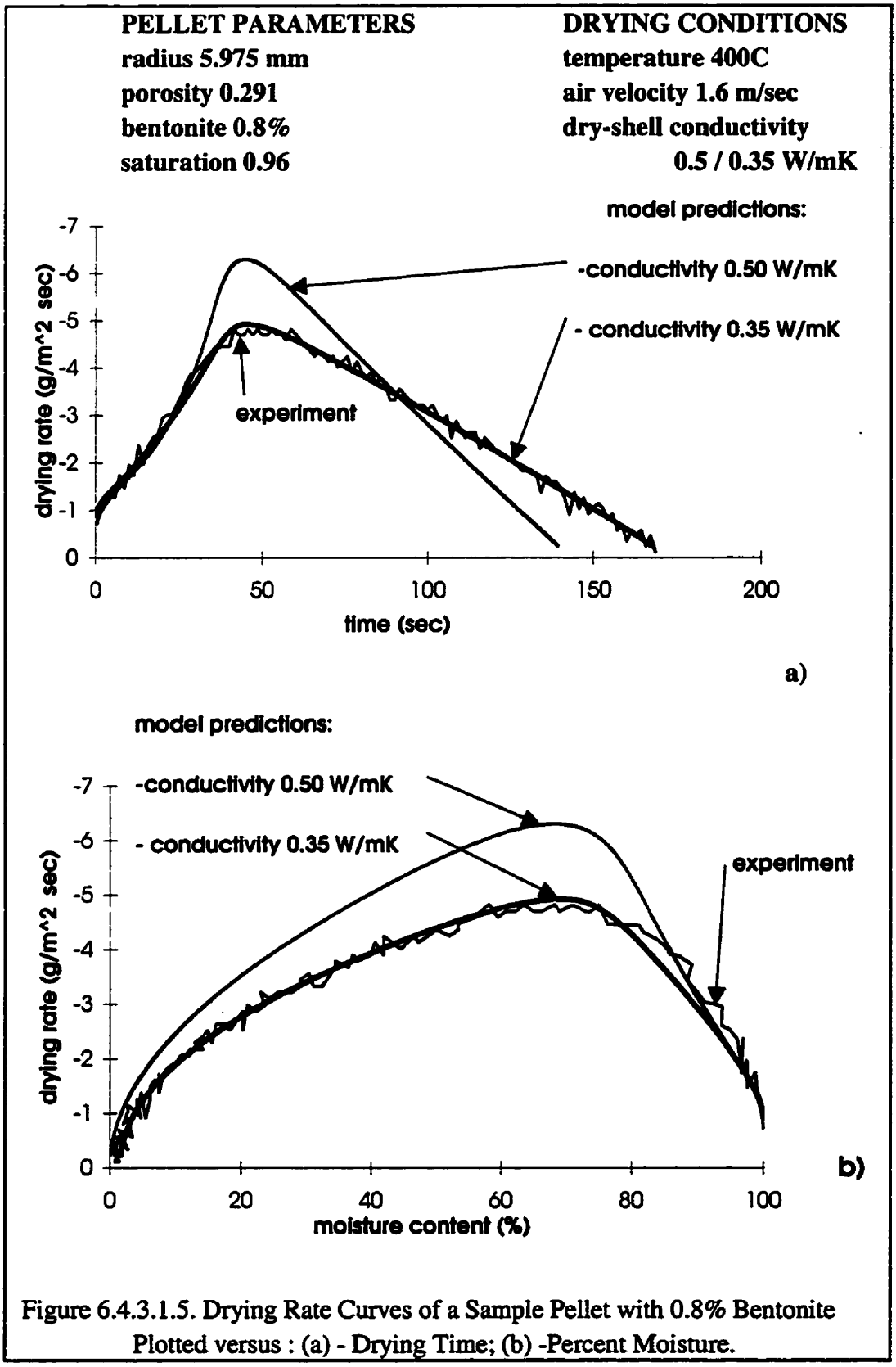


Figure 6.4.3.1.5. Drying Rate Curves of a Sample Pellet with 0.8% Bentonite Plotted versus : (a) - Drying Time; (b) -Percent Moisture.

The model prediction based on a *decrease* in the thermal conductivity in bentonite-containing pellets is somewhat unexpected and needs further experimental validation. Based on the very limited experimental data cited in the Zaharchuk thesis [1], bentonite should increase, rather than decrease, the thermal conductivity of the dry shell. Further elaborations on how and why bentonite would have the effect observed in Figures 6.4.3.1.2 - 6.4.3.1.5 will be left beyond the scope of this work.

6.4.3.2 Drying of Coarser-Particle-Size Pellets with Bentonite

The extended model in its present form uses the same calculation of the viscosity of water-bentonite suspension as the original Zaharchuk model (eqn. 3.3.1). However, the calculated value for each time iteration is then substituted into the mass balance equation (eqn. 2.4.11) and effective drying rate is calculated using eqn. 3.2.1.1. This accounts for the combined effect of either or both of the vapour lock AND of the effective immobilization of the water-bentonite suspension (see Section 3.3).

The correlations of the original- and of the extended models with the experiments for pellets with the average particle size 19.9μm and 0.6 wt.% bentonite dried at various rapid drying conditions are shown in Figures 6.4.3.2.1 - 6.4.3.2.8. In the upper graphs the original model results are shown. The lower graphs show the modified-model predictions. Figures 6.4.3.2.9 - 6.4.3.2.15 represent analogous results but for pellets made of Griffith concentrate with the average particle size 18.6μm and with 1.2% bentonite added. The guide for these graphs is presented in Table 6.4.3.2.1.

MATERIAL	GRIFFITH CONCENTRATE
AMBIENT TEMPERATURE	300 C
AIR VELOCITY	1.0 m/s
PELLET RADIUS:	5.3 mm
POROSITY:	0.318
BENTONITE	0.6 %
PARTICLE SIZE	19.9 um
SATURATION	0.82

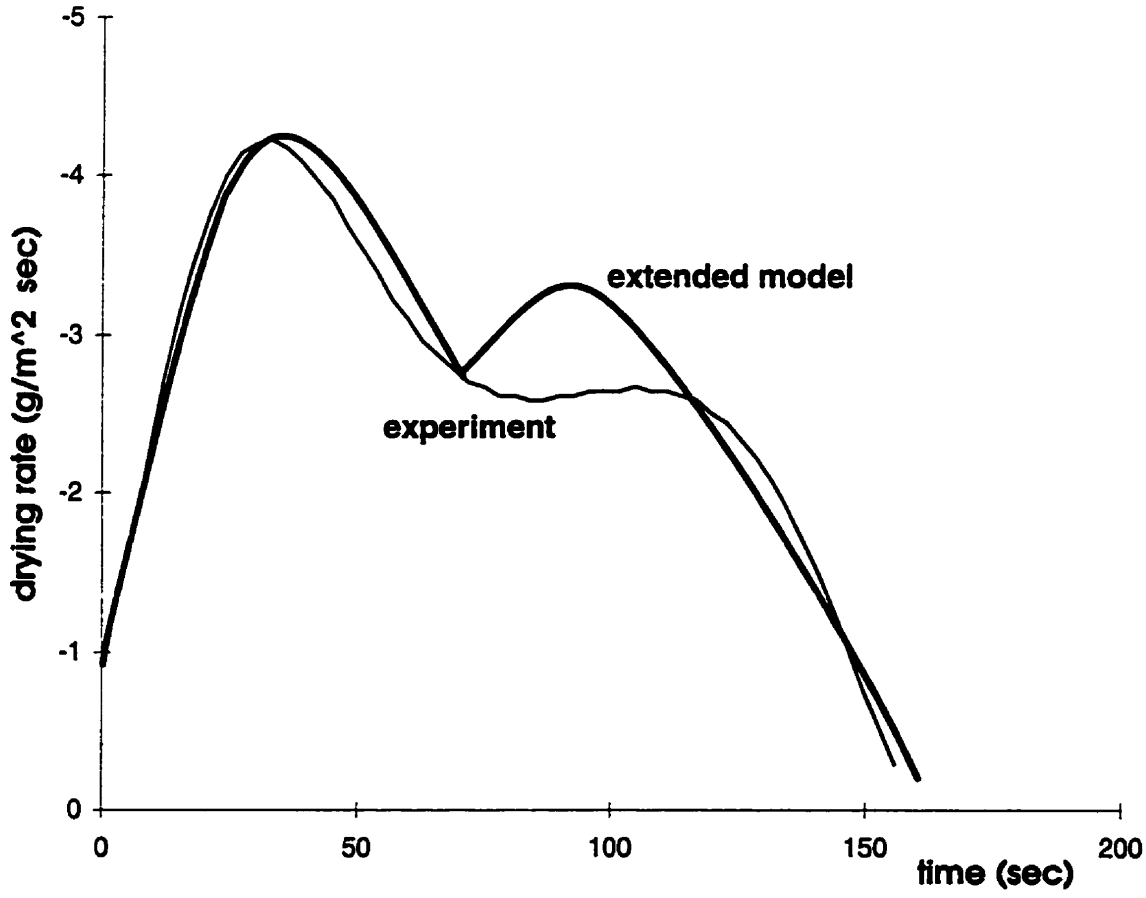


Figure 6.4.3.2.1. Model/experiment Correlation for a Drying Rate Curve of a Pellet with 0.6% Bentonite.

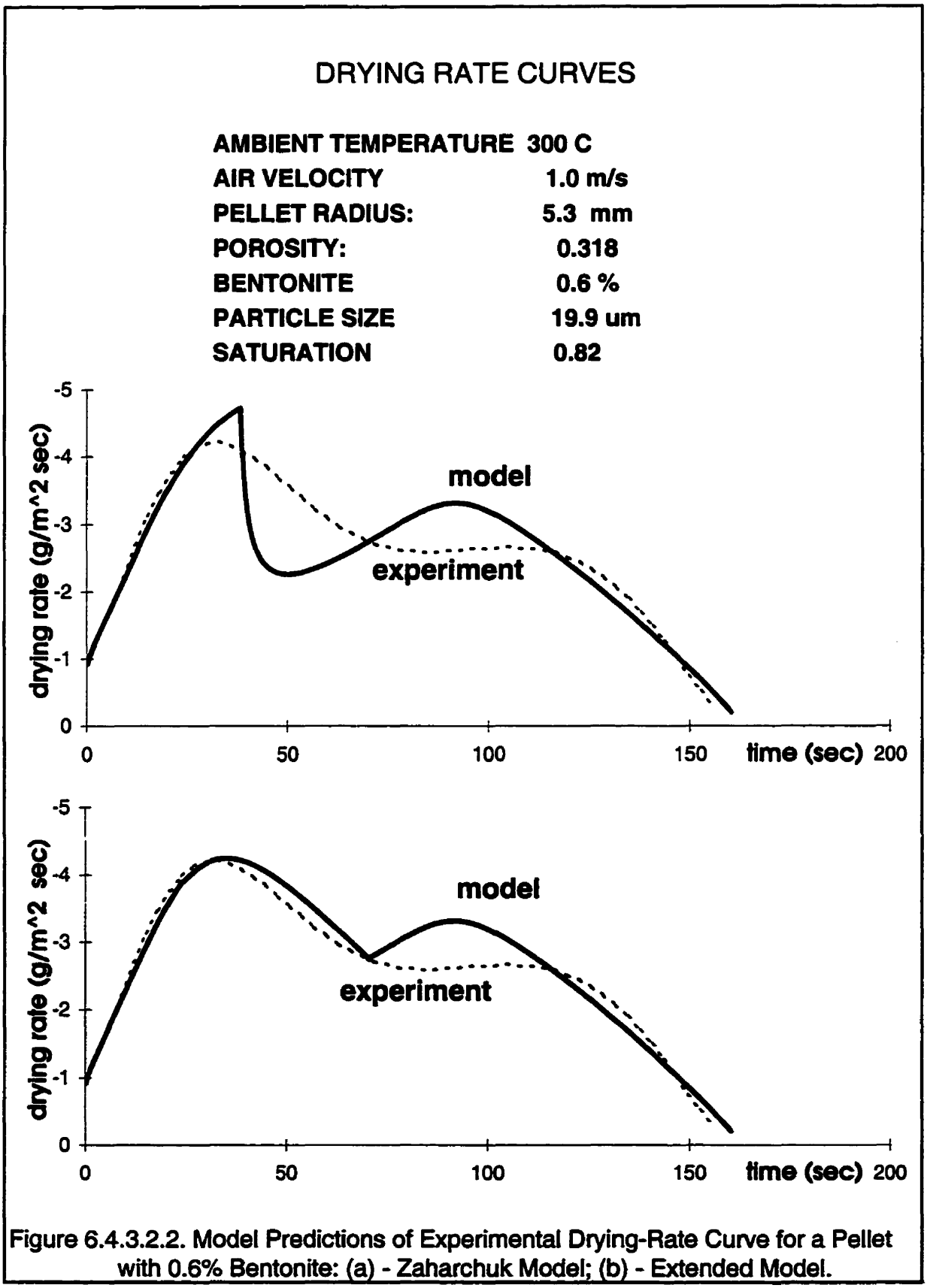


Figure 6.4.3.2.2. Model Predictions of Experimental Drying-Rate Curve for a Pellet with 0.6% Bentonite: (a) - Zaharchuk Model; (b) - Extended Model.

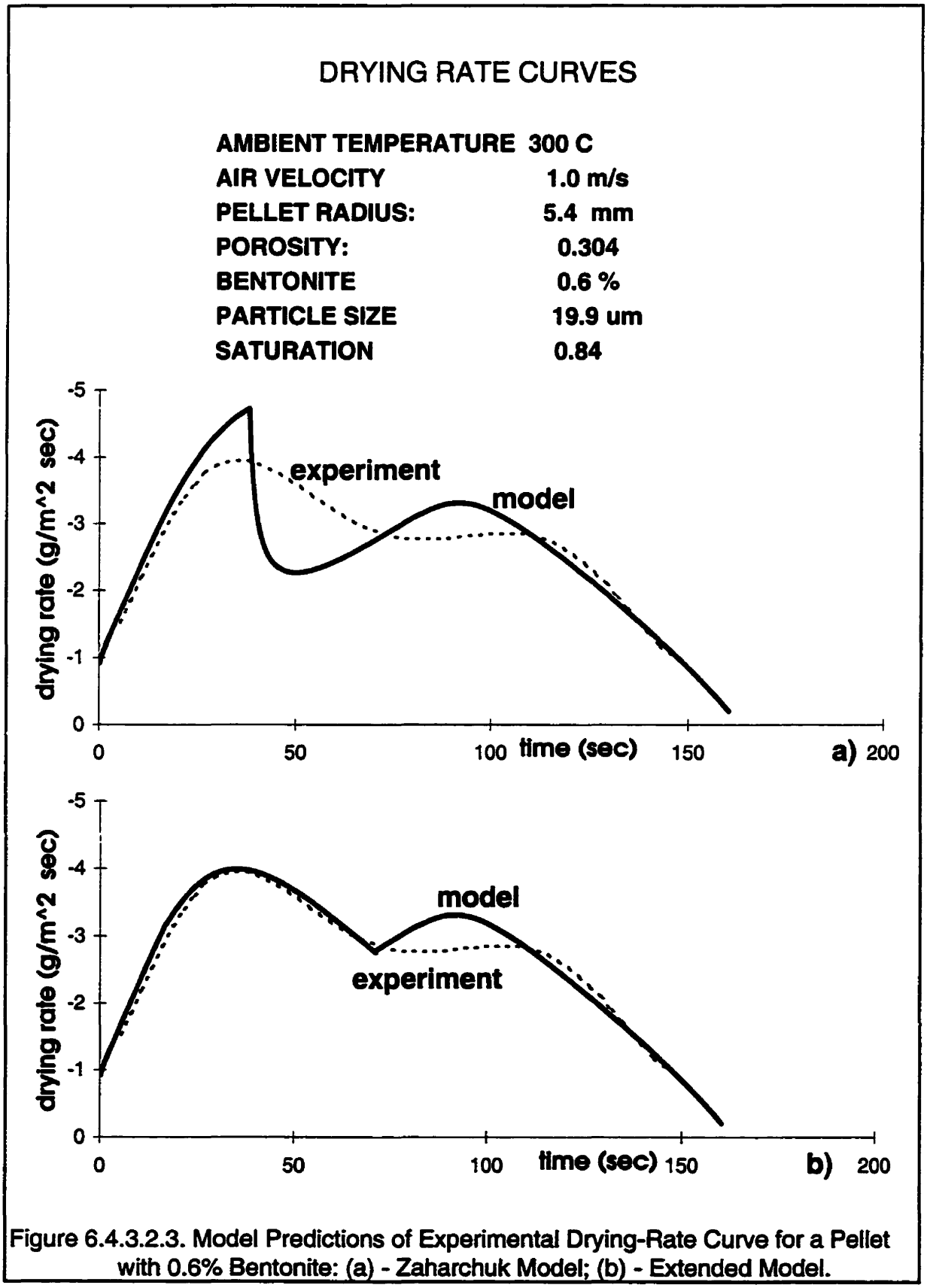


Figure 6.4.3.2.3. Model Predictions of Experimental Drying-Rate Curve for a Pellet with 0.6% Bentonite: (a) - Zaharchuk Model; (b) - Extended Model.

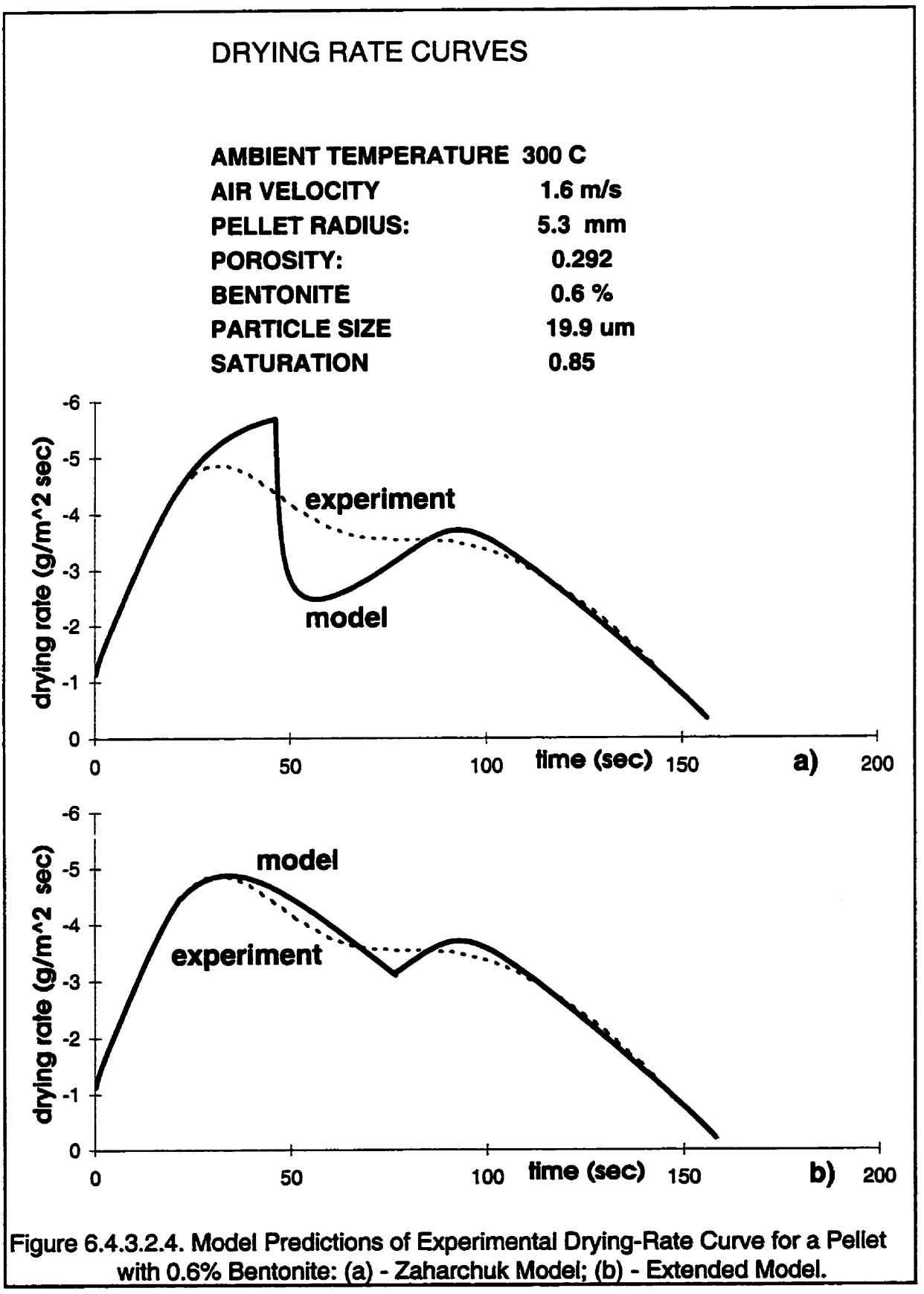


Figure 6.4.3.2.4. Model Predictions of Experimental Drying-Rate Curve for a Pellet with 0.6% Bentonite: (a) - Zaharchuk Model; (b) - Extended Model.

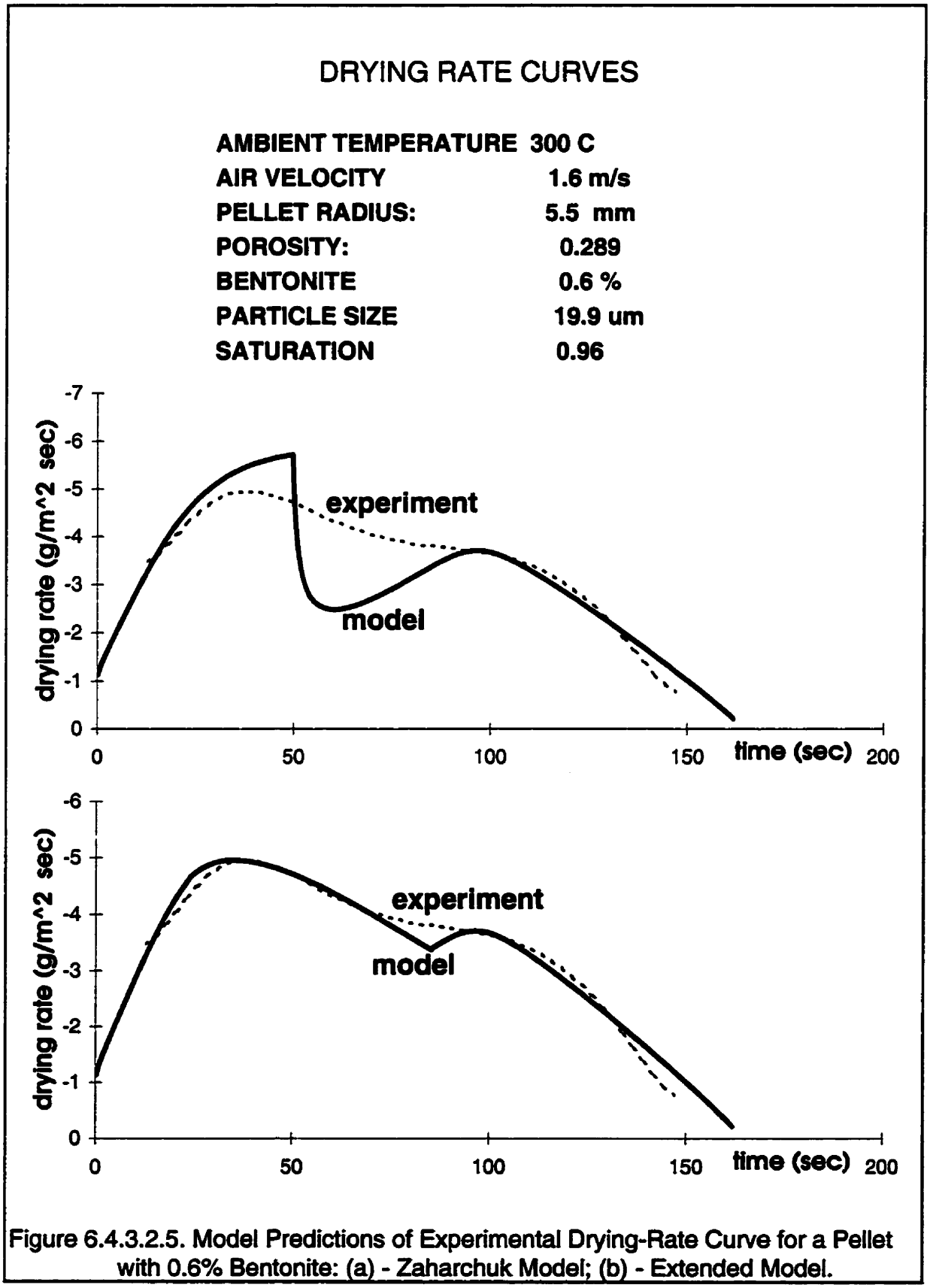


Figure 6.4.3.2.5. Model Predictions of Experimental Drying-Rate Curve for a Pellet with 0.6% Bentonite: (a) - Zaharchuk Model; (b) - Extended Model.

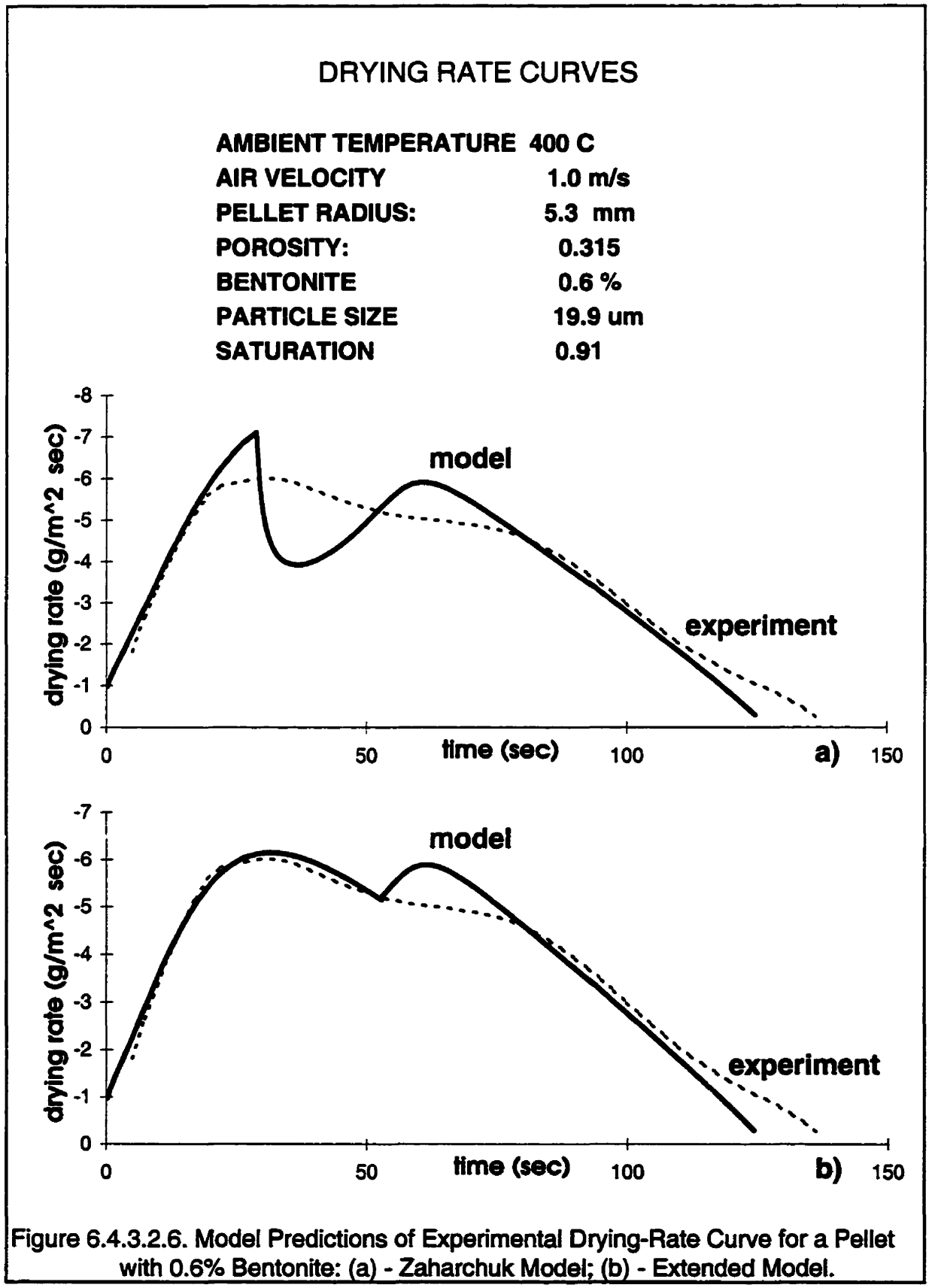


Figure 6.4.3.2.6. Model Predictions of Experimental Drying-Rate Curve for a Pellet with 0.6% Bentonite: (a) - Zaharchuk Model; (b) - Extended Model.

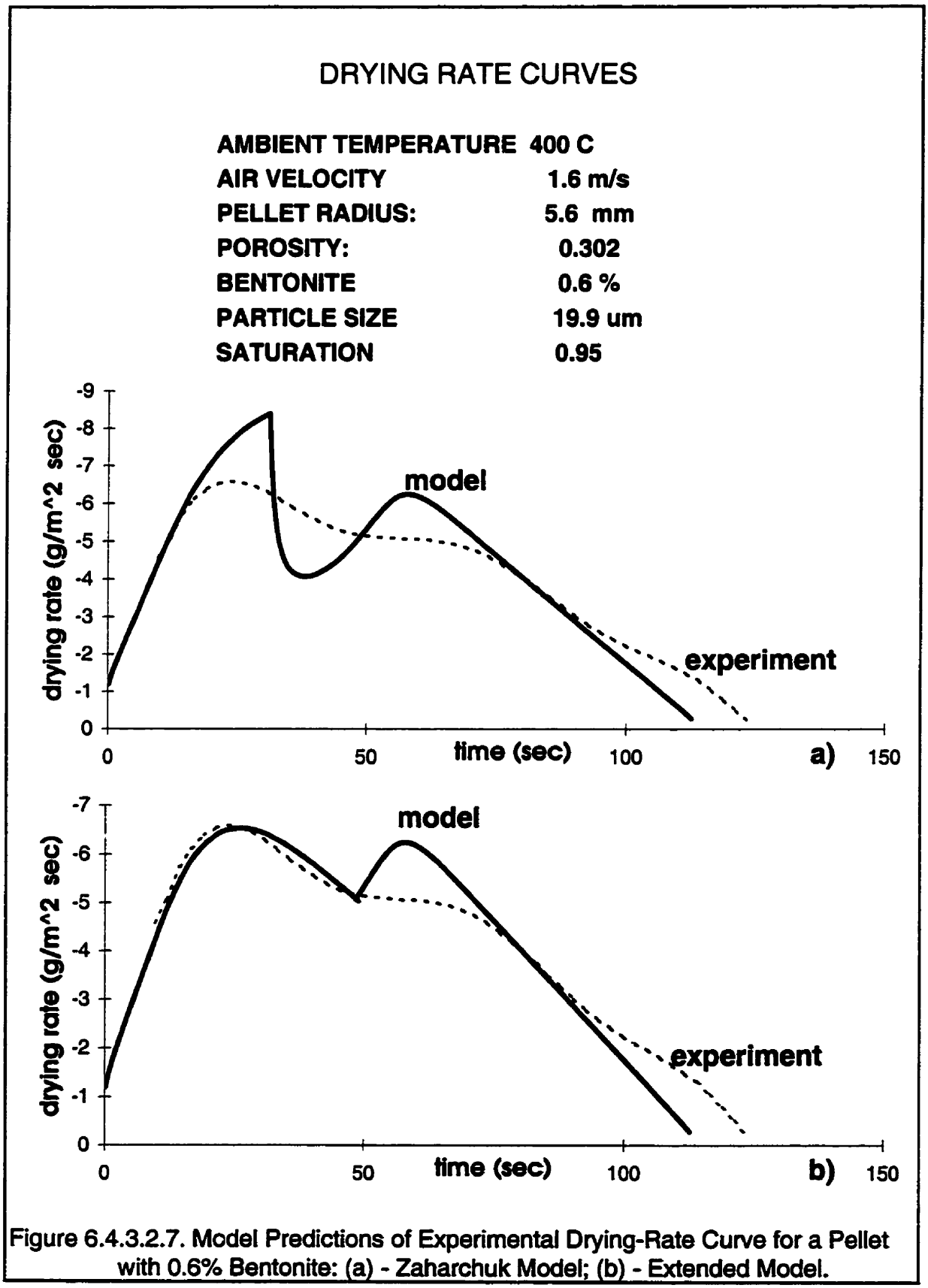


Figure 6.4.3.2.7. Model Predictions of Experimental Drying-Rate Curve for a Pellet with 0.6% Bentonite: (a) - Zaharchuk Model; (b) - Extended Model.

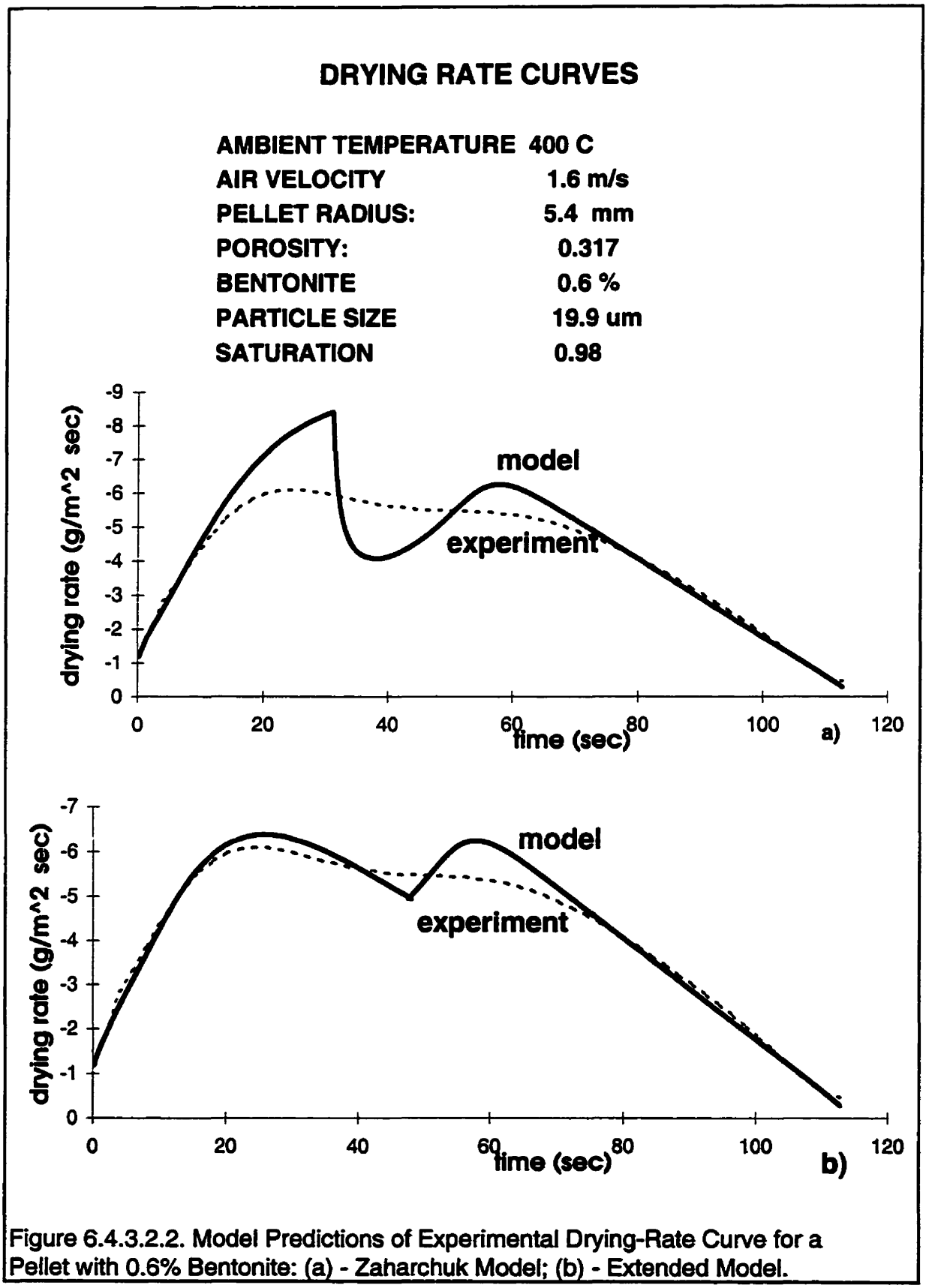


Figure 6.4.3.2.2. Model Predictions of Experimental Drying-Rate Curve for a Pellet with 0.6% Bentonite: (a) - Zaharchuk Model; (b) - Extended Model.

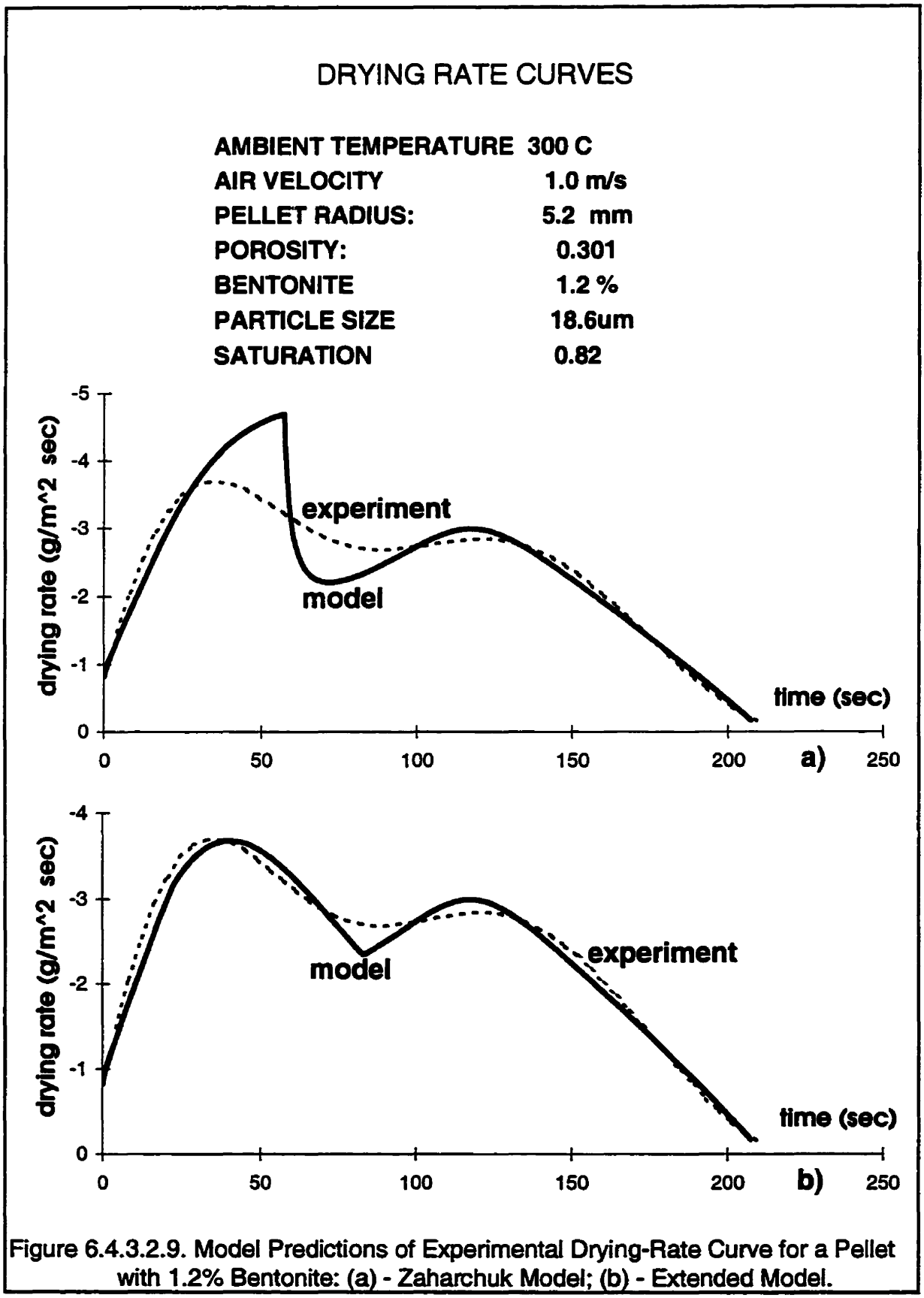


Figure 6.4.3.2.9. Model Predictions of Experimental Drying-Rate Curve for a Pellet with 1.2% Bentonite: (a) - Zaharchuk Model; (b) - Extended Model.

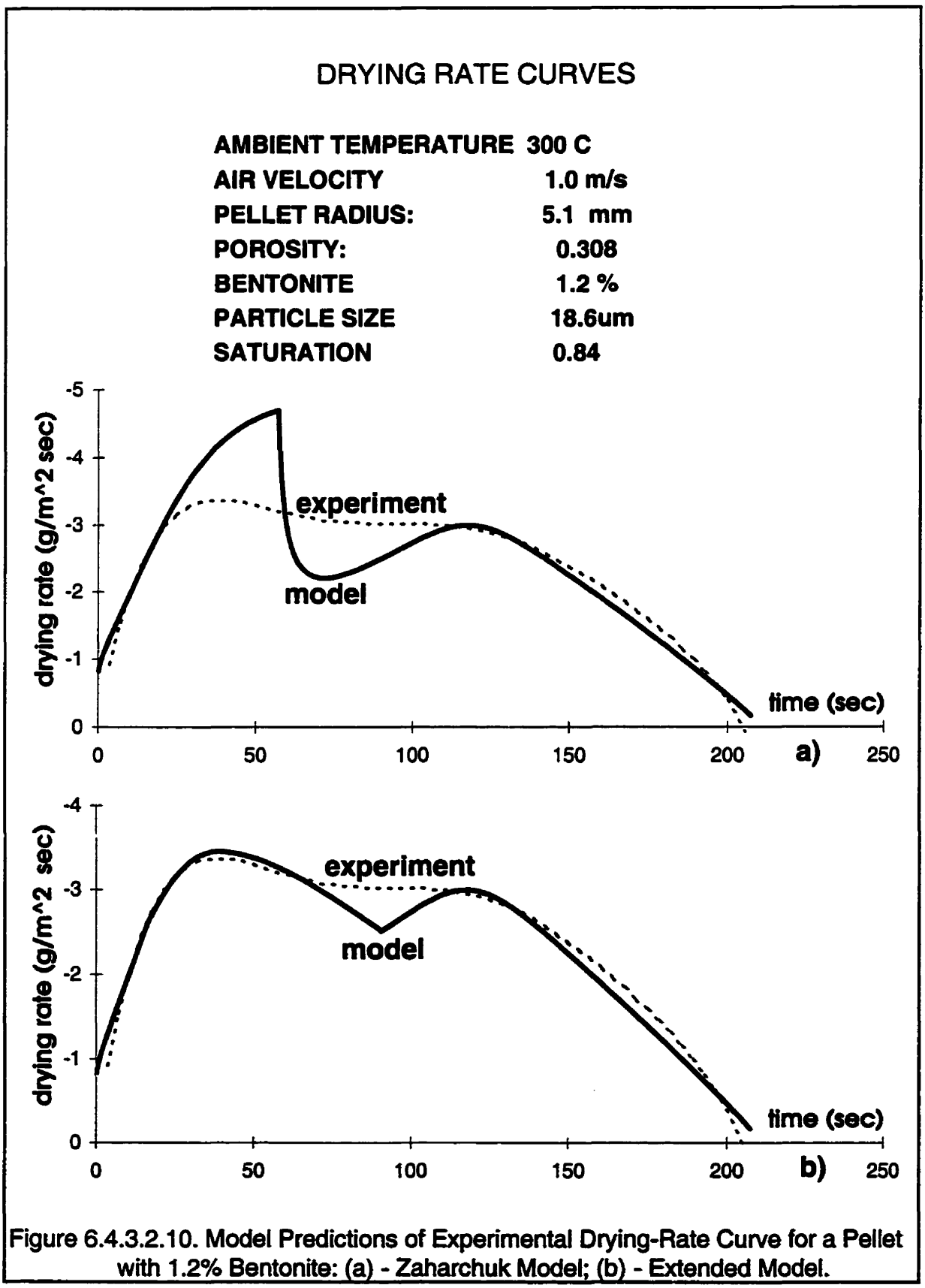


Figure 6.4.3.2.10. Model Predictions of Experimental Drying-Rate Curve for a Pellet with 1.2% Bentonite: (a) - Zaharchuk Model; (b) - Extended Model.

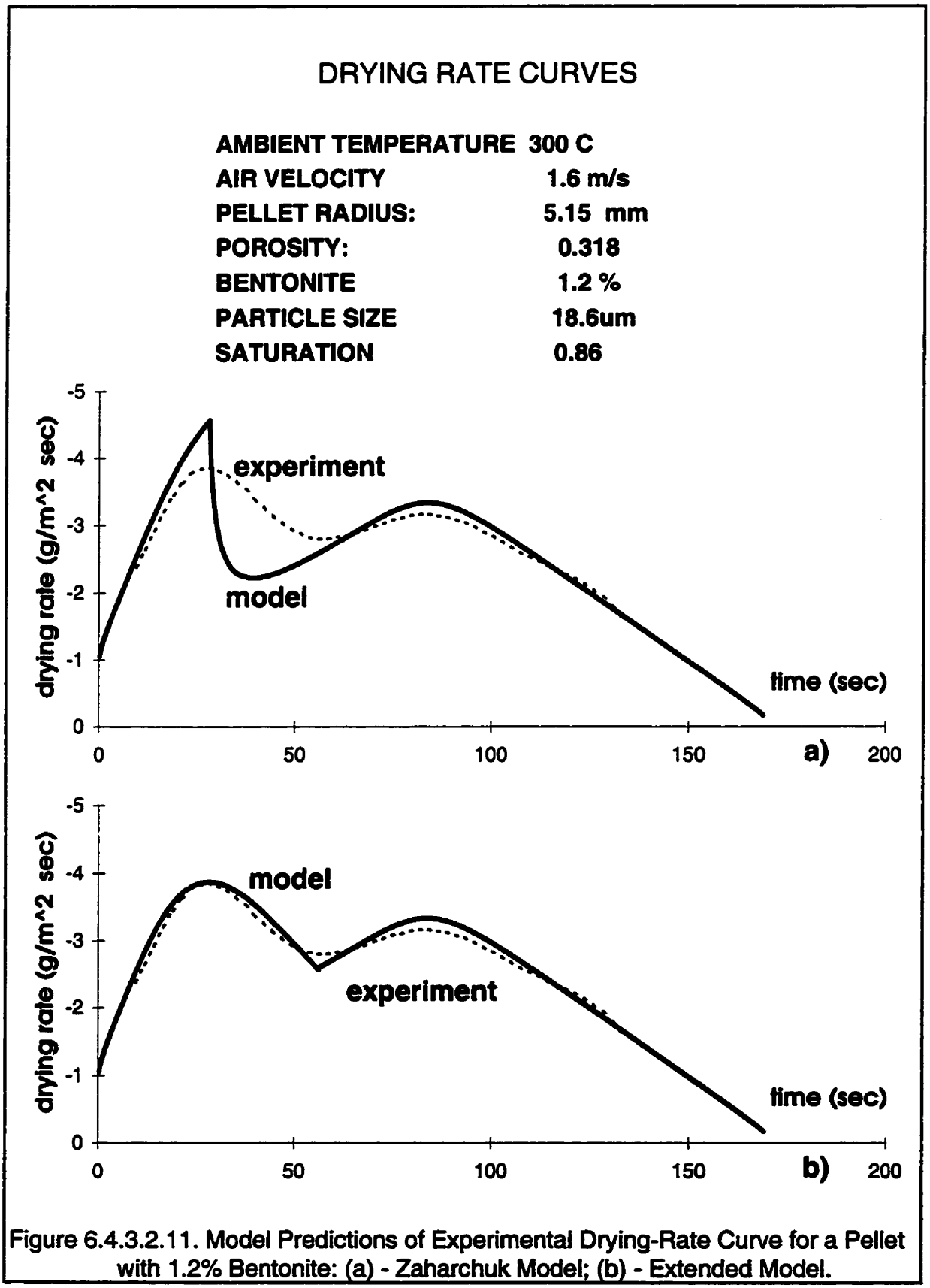


Figure 6.4.3.2.11. Model Predictions of Experimental Drying-Rate Curve for a Pellet with 1.2% Bentonite: (a) - Zaharchuk Model; (b) - Extended Model.

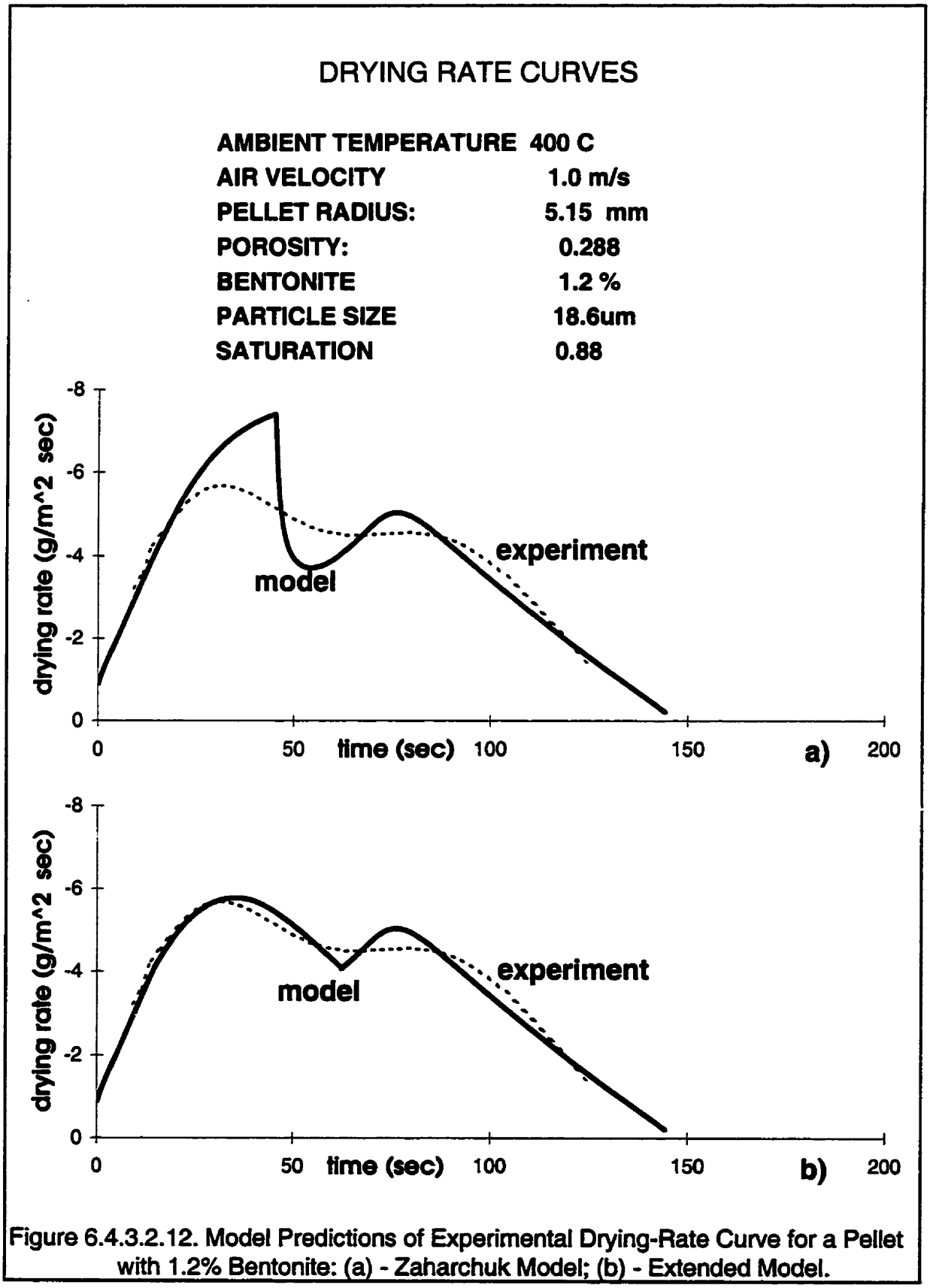


Figure 6.4.3.2.12. Model Predictions of Experimental Drying-Rate Curve for a Pellet with 1.2% Bentonite: (a) - Zaharchuk Model; (b) - Extended Model.

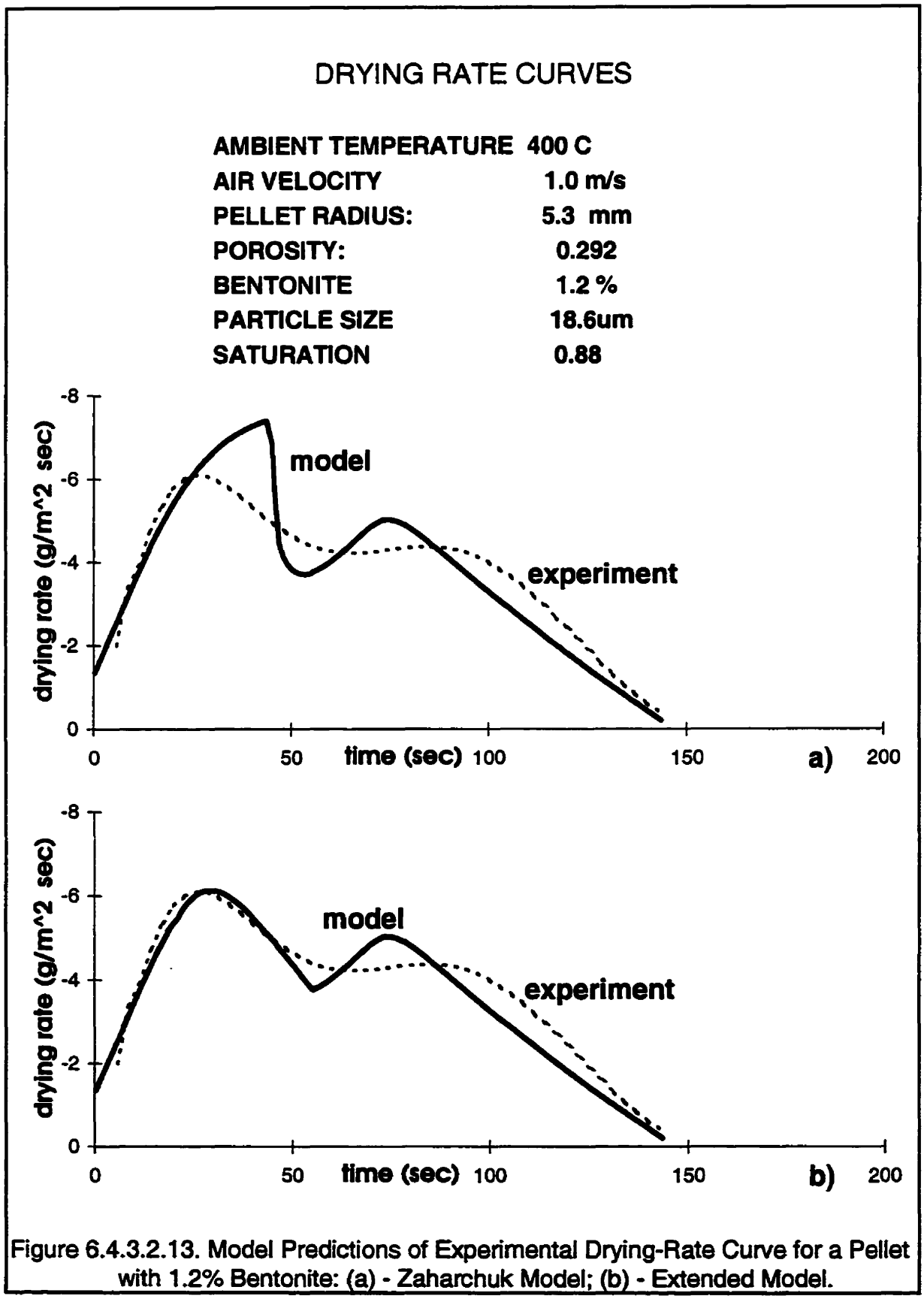


Figure 6.4.3.2.13. Model Predictions of Experimental Drying-Rate Curve for a Pellet with 1.2% Bentonite: (a) - Zaharchuk Model; (b) - Extended Model.

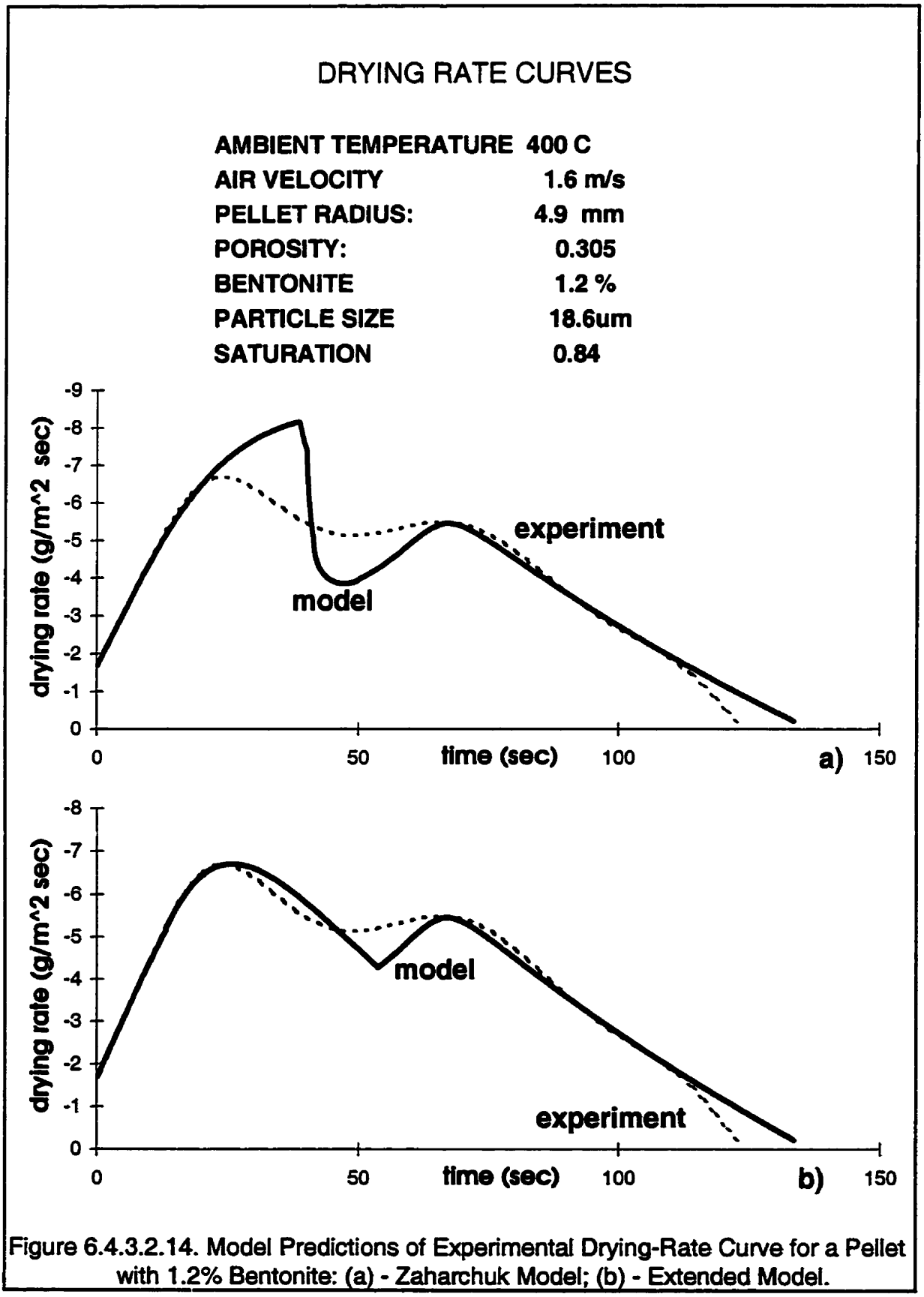


Figure 6.4.3.2.14. Model Predictions of Experimental Drying-Rate Curve for a Pellet with 1.2% Bentonite: (a) - Zaharchuk Model; (b) - Extended Model.

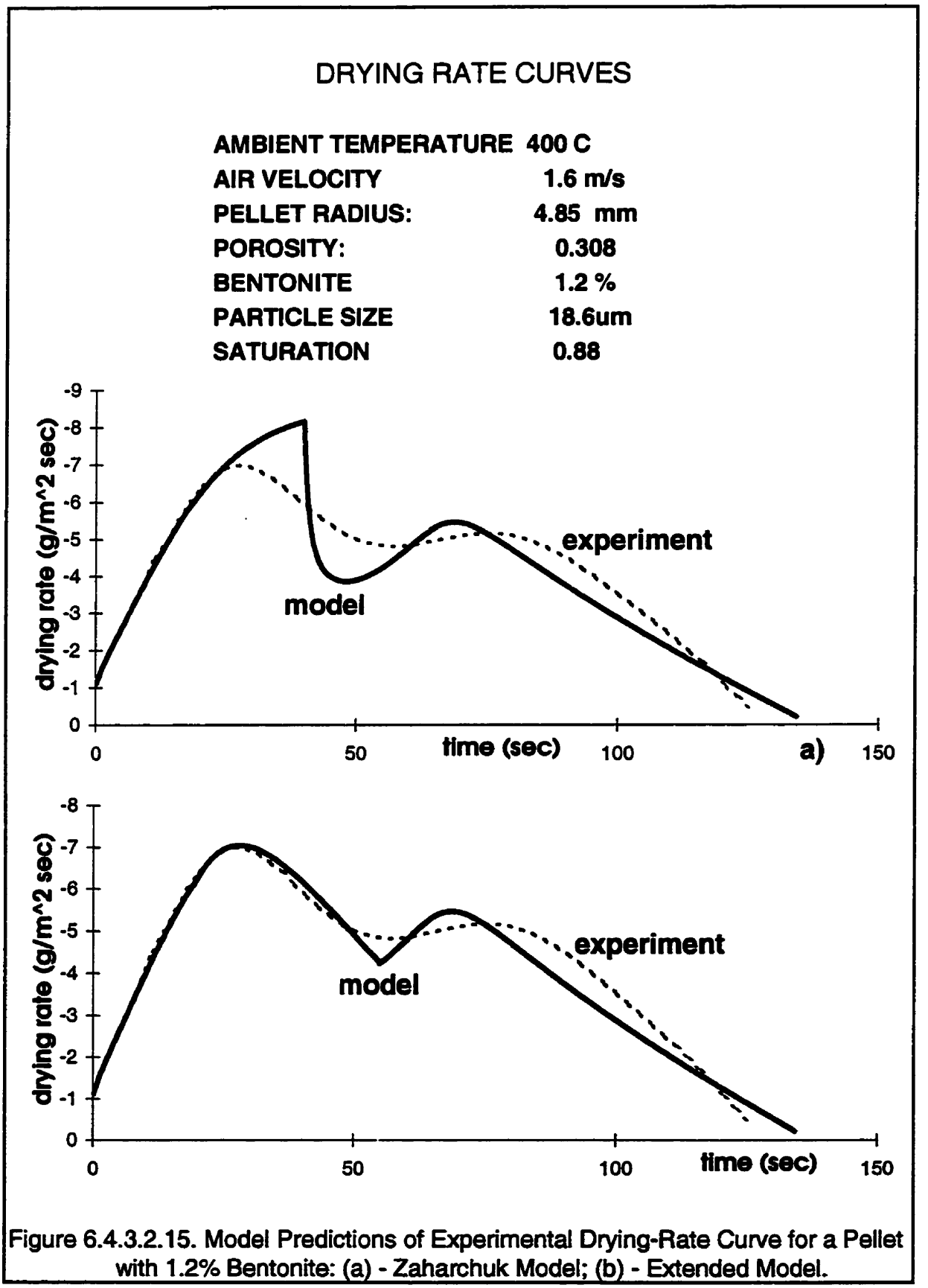


Figure 6.4.3.2.15. Model Predictions of Experimental Drying-Rate Curve for a Pellet with 1.2% Bentonite: (a) - Zaharchuk Model; (b) - Extended Model.

Table 6.4.3.2.1. Guide to the Results of Drying Pellets with Bentonite
Griffith Concentrate
Pellet Radius: 4.65 - 6.1 mm
Porosity: 0.288 - 0.332
Average particle diameter: 18.6μm and 19.9μm
Bentonite content: 0.6 wt. % and 1.2 wt.%
Pellet Saturation: 0.82 - 0.98

Temperature	**300°C**		**400°C**	
Air Flow Rate	**1.0 m/s**	**1.6 m/s**	**1.0 m/s**	**1.6 m/s**
-Pellets with 0.6% bentonite Average Particle size **19.9μm**	Fig. 6.4.3.2.1 - Fig.6.4.3.2.3	Fig. 6.4.3.2.4 and Fig.6.4.3.2.5	Fig. 6.4.3.2.6	Fig. 6.4.3.2.7 and Fig.6.4.3.2.8
-Pellets with 1.2% bentonite Average particle size **18.6μm**	Figs. 6.4.3.2.9 and 6.4.3.2.10	Fig. 6.4.3.2.11	Figs. 6.4.3.2.12 and 6.4.3.2.13	Figs. 6.4.3.2.14 and 6.4.3.2.15

Similarly to the case of pellets without bentonite (see Figs. 6.1.1.2 -6.1.1.6 in Section 6.1.1), the Zaharchuk model predicts adequately the drying rate pattern during the initial and the late stages of drying, but substantially overpredicts the drying-rate maximum. Another observation was that, according to Zaharchuk model, the interruption of surface drying regime occurs earlier for pellets with 0.6% bentonite as opposed to those without bentonite. This effect is even more pronounced in pellets containing 1.2% bentonite. The reason for earlier termination of surface drying is liquid-phase immobilization effect in pellets containing bentonite.

The extended model, on the other hand, predicts the drying rate pattern during the *entire* drying process quite adequately. Unlike the Zaharchuk model, it predicts gradual surface/shrinking core transition due to combination of two factors: the vapour lock and liquid immobilization. It also predicts an inflection during the falling rate period observed on the experimental curves. In some cases (Figs. 6.4.3.2.4 and 6.4.3.2.5 for pellets with 0.6%

bentonite, and Figs. 6.4.3.2.9 and 6.4.3.2.11 for pellets with 1.2% bentonite) the model/experiment agreement during the falling rate period is remarkable. In other cases the model drying-rate inflections do not coincide in time with the experimental ones.

Generally, as in the case of the bentonite-free pellets (Figures 6.1.1.2 to 6.1.1.6), the agreement with the experiment for pellets with bentonite is much better when the extended model in its present form is being used.

6.4.3.3 Center-Temperature Measurement

Center-temperature measurements, similar to those reported in Section 6.1.2 but for the pellets containing bentonite, were carried out in the course of this study.

Several groups of pellets were made from the Griffith concentrate of three different average particle sizes (7.1, 18.6 and 19.9μm) and with three different bentonite contents (0.6, 0.8 and 1.2%). They were dried at two drying temperatures and gas flow conditions. Their temperature-at-the-center data were recorded versus time and shown in lower graphs in Figures 6.4.3.3.1 - 6.4.3.3.3. Also shown for easier correlation are the corresponding drying rate curves of the pellets (upper graphs). The guide for these graphs is presented in the Table 6.4.3.3.1.

When pellets made of fine particles (7.1μm) with 0.8% bentonite are being dried (Figs. 6.4.3.3.1 *a-d*) there is no constant rate drying period (upper graphs). The temperature at the pellet center (lower graphs) is rising steeply until it reaches 100^{0}C and then stays approximately at the constant level. Significantly, this point coincides in time with the maximum on the corresponding drying rate curves.

Similarly to bentonite-free pellets (see Section 6.1.2), experimental temperature

curves are in excellent agreement with those predicted by the model.

Table 6.4.3.3.1. Guide to the Results of Center-Temperature Measurements
Griffith Concentrate
Pellet Diameter: 9.7 - 12.2 mm
Porosity: 0.288 - 0.332
Pellet Saturation : 0.82 - 0.99

	300°C		400°C	
	1.0 m/s	**1.6 m/s**	**1.0 m/s**	**1.6 m/s**
-Pellets with average particle size 7.1μm and 0.8% bentonite	-	Fig.6.4.3.3.1 *a*	Figs.6.4.3.3.1 *b, c*	Fig. 6.4.3.3.1 *d*
-Pellets with average particle size 19.9μm and 0.6% bentonite	Figs.6.4.3.3.2 *a, b*	Figs.6.4.3.3.2 *c, d*	Fig.6.4.3.3.2 *e*	Figs.6.4.3.3.2 *f, g*
-Pellets with average particle size 18.6μm and 1.2% bentonite	Figs.6.4.3.3.3 *a, b*	Figs.6.4.3.3.3 *c, d*	Figs.6.4.3.3.3 *e, f*	Figs.6.4.3.3.3 *g, h*

For the pellets made of coarser particles (18.6 - 19.9μm) with 0.6 and 1.2% bentonite (see Figs. 6.4.3.3.2 - 6.4.3.3.3), the shape of the temperature curves and the corresponding drying rate curves is quite similar to those reported in Section 6.1.2 for the bentonite-free pellets. As in the previous case, temperature curve (lower graphs) and corresponding drying rate (upper graphs) rise at first. However, the maximum drying rate in coarser agglomerates is reached at much lower pellet temperatures compared to fine-particle agglomerates - around 60°C as opposed to 100°C. Afterwards, the drying rate declines gradually while temperature at the pellet's center is still rising. All drying rate curves exhibit inflections during the falling rate period, which coincide with the temperature of the pellet center reaching 100°C.

These observations are in remarkable agreement with our theoretical considerations (see Section 4.2) and with the model predictions.

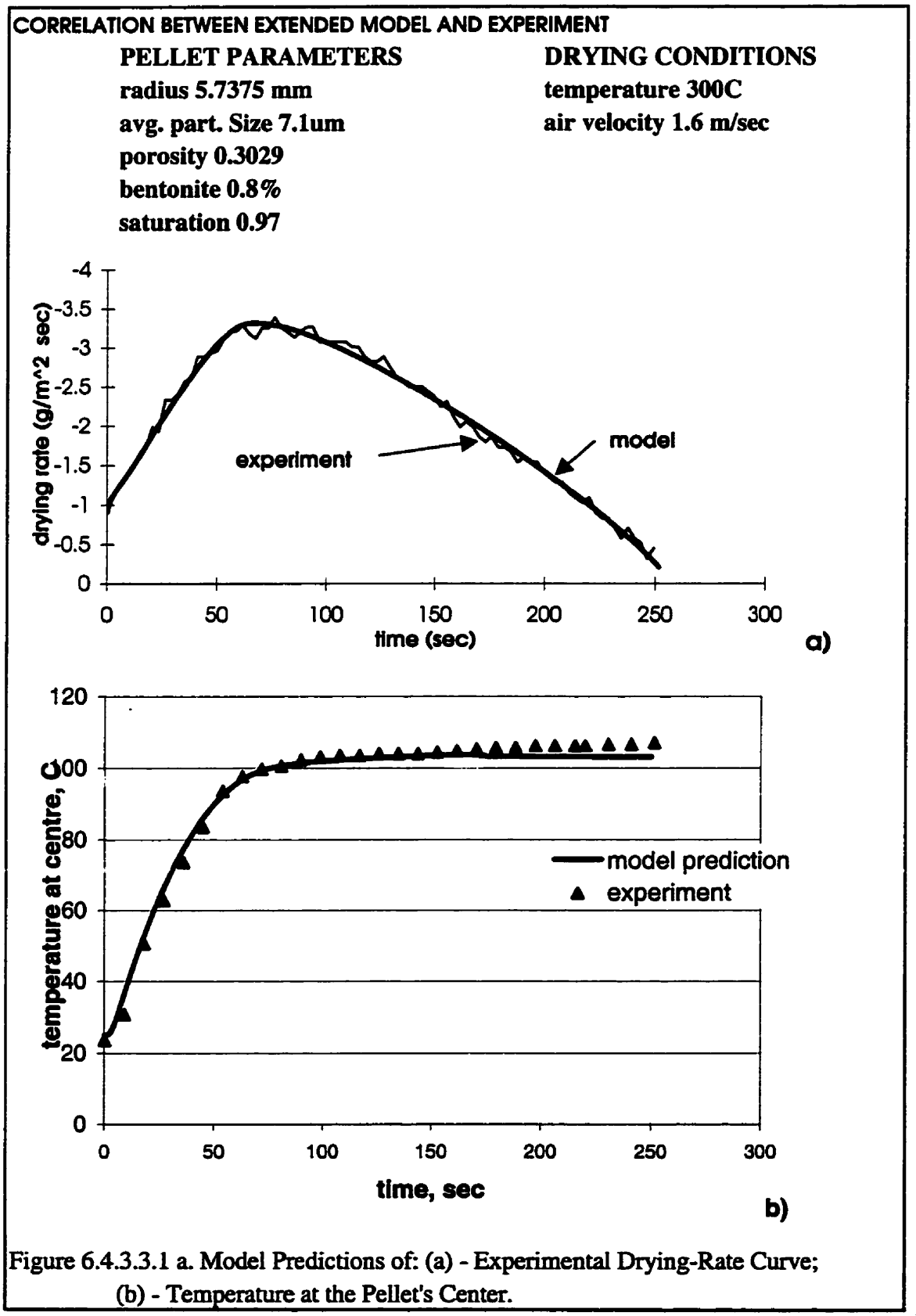


Figure 6.4.3.3.1 a. Model Predictions of: (a) - Experimental Drying-Rate Curve; (b) - Temperature at the Pellet's Center.

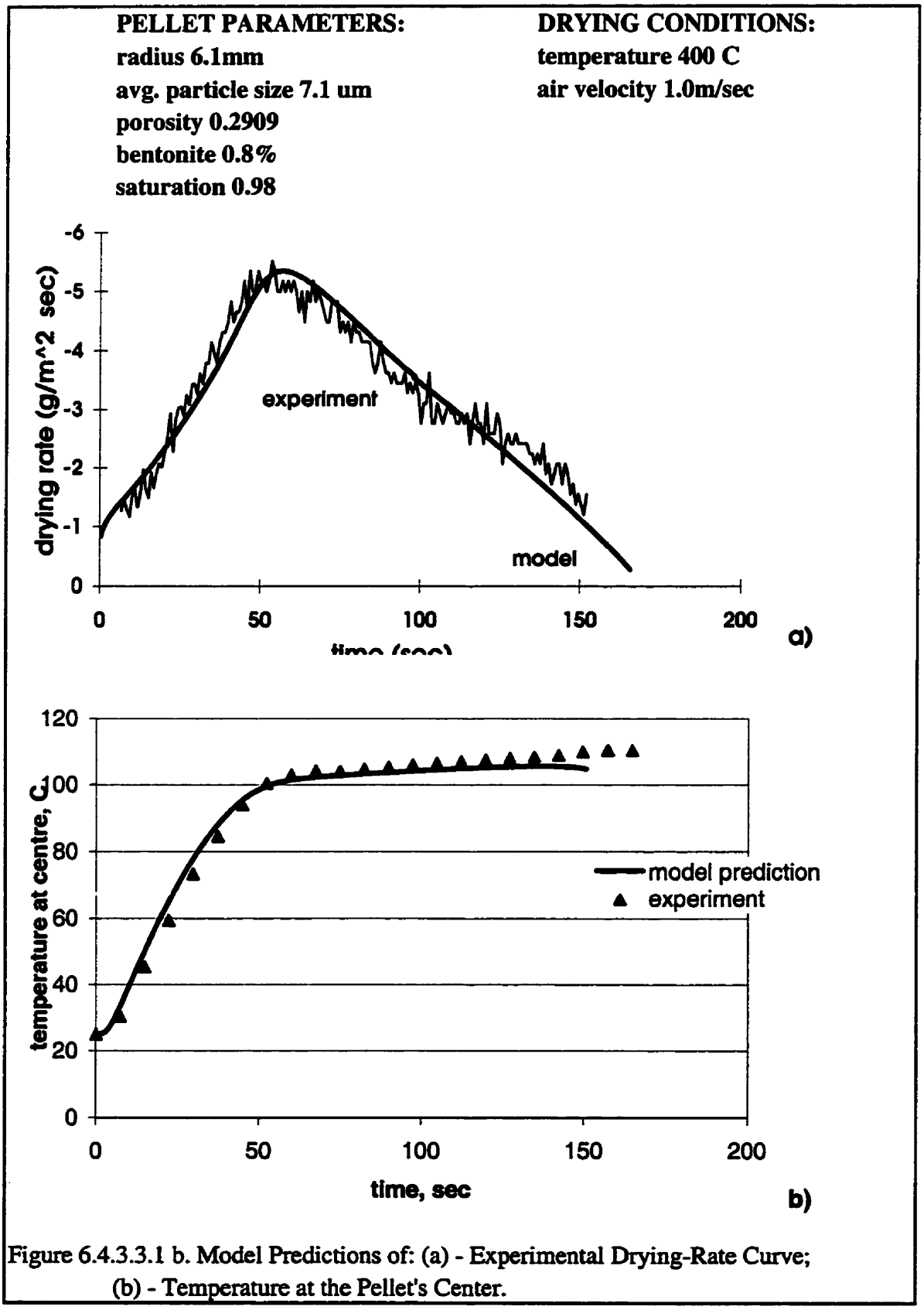
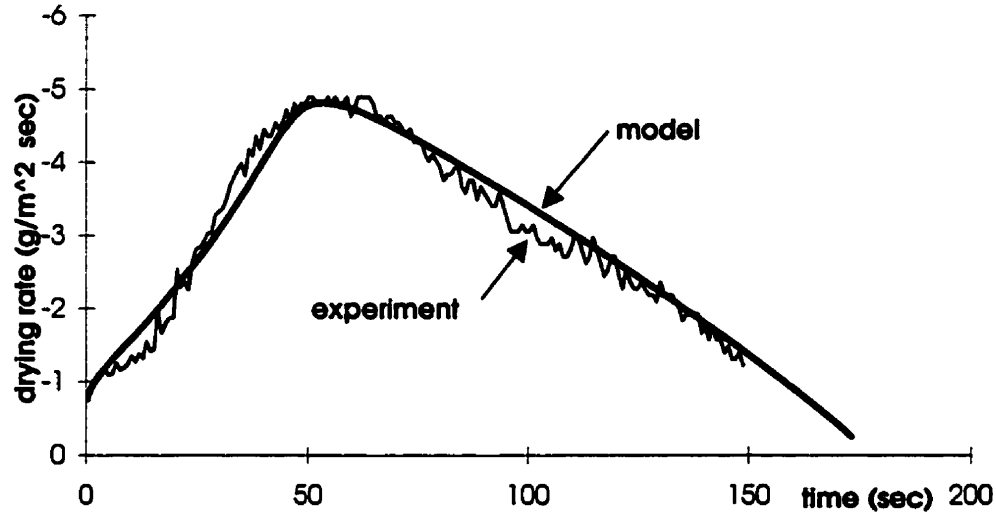


Figure 6.4.3.3.1 b. Model Predictions of: (a) - Experimental Drying-Rate Curve; (b) - Temperature at the Pellet's Center.

CORRELATION BETWEEN MODEL AND EXPERIMENT

PELLET PARAMETERS
radius 6.05 mm
avg. particle size 7.1 um
porosity 0.2773
bentonite 0.8%
saturation 0.94

DRYING CONDITIONS
temperature 400C
air velocity 1.0m/sec



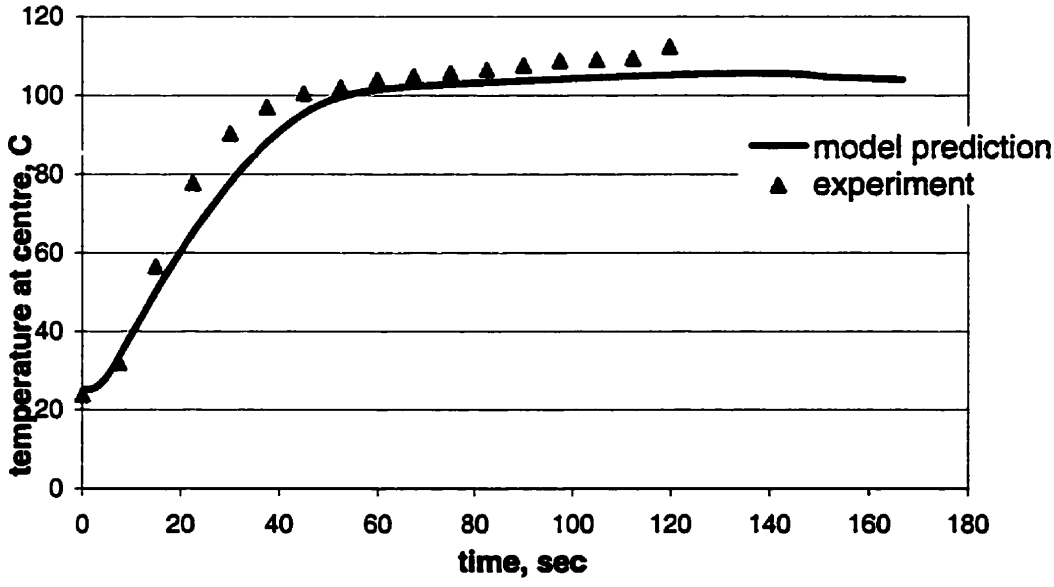


Figure 6.4.3.3.1 c. Model Predictions of: (a) - Experimental Drying-Rate Curve; (b) - Temperature at the Pellet's Center.

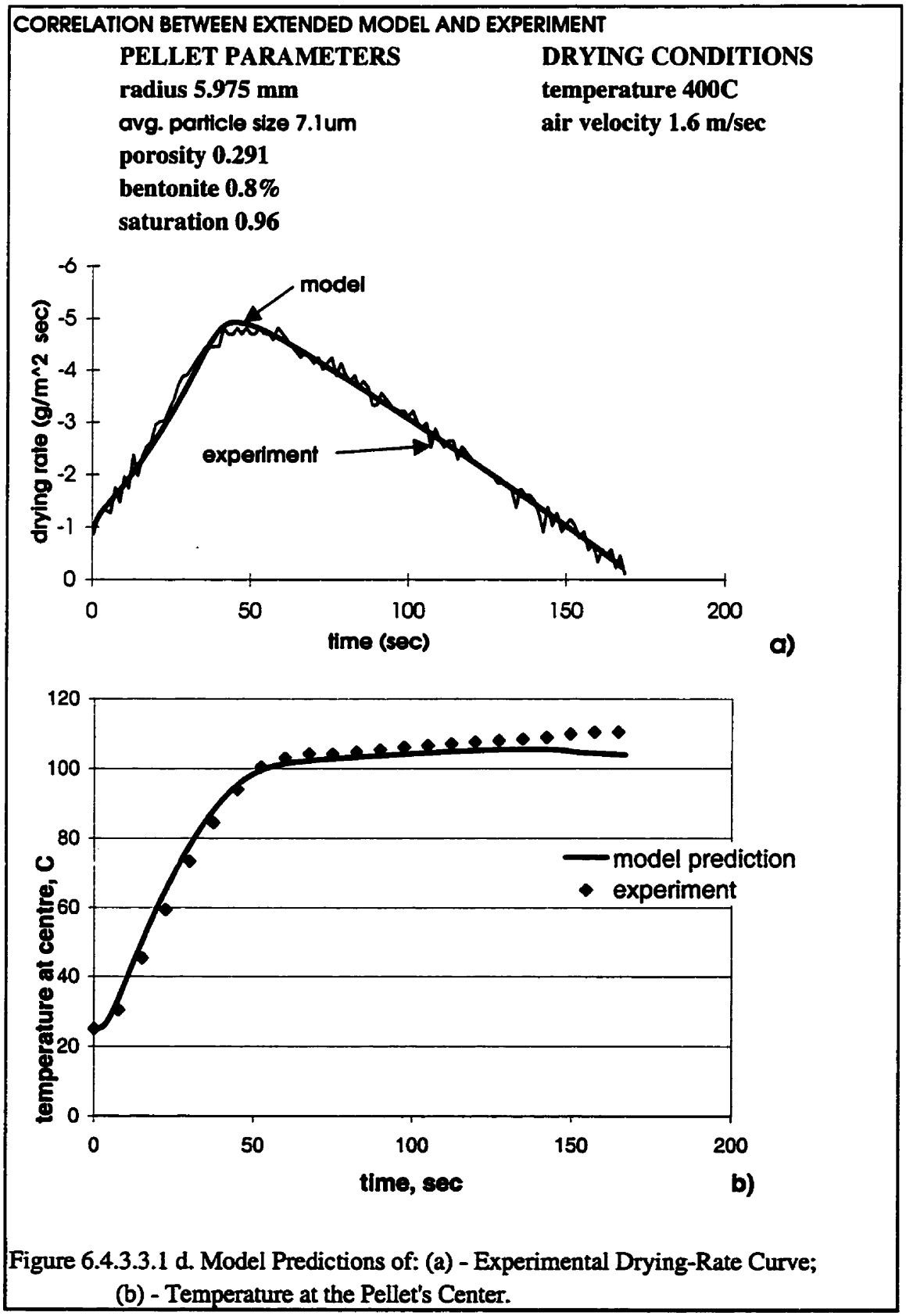
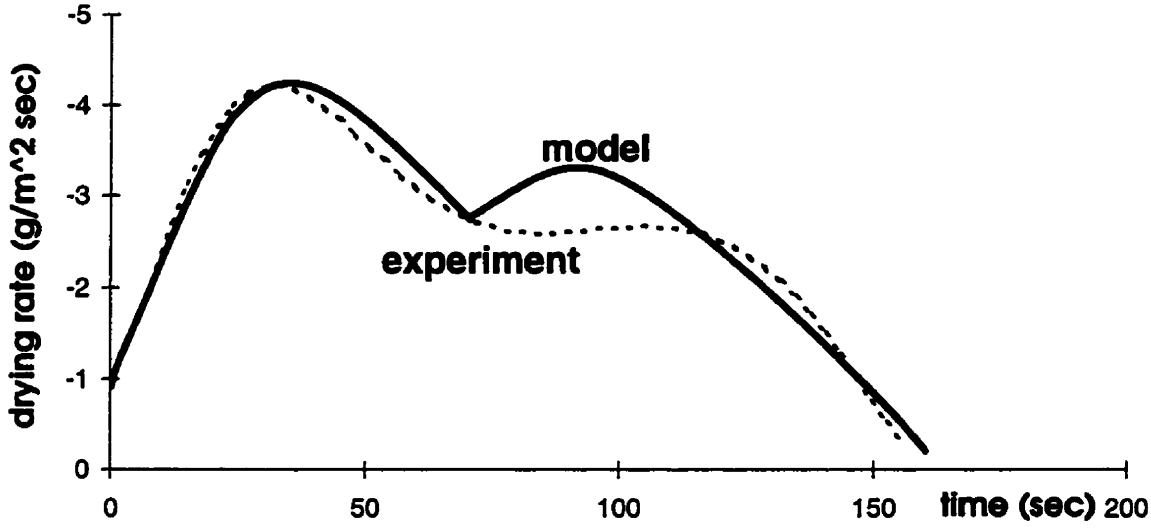


Figure 6.4.3.3.1 d. Model Predictions of: (a) - Experimental Drying-Rate Curve; (b) - Temperature at the Pellet's Center.

CORRLATION BETWEEN EXTENDED MODEL AND EXPERIMENTt

AMBIENT TEMPERATURE	300 C
AIR VELOCITY	1.0 m/s
PELLET RADIUS:	5.3 mm
POROSITY:	0.318
BENTONITE	0.6 %
MATERIAL	GRIFFITH MAGNETITE
PARTICLE SIZE	19.9 um
SATURATION	0.82



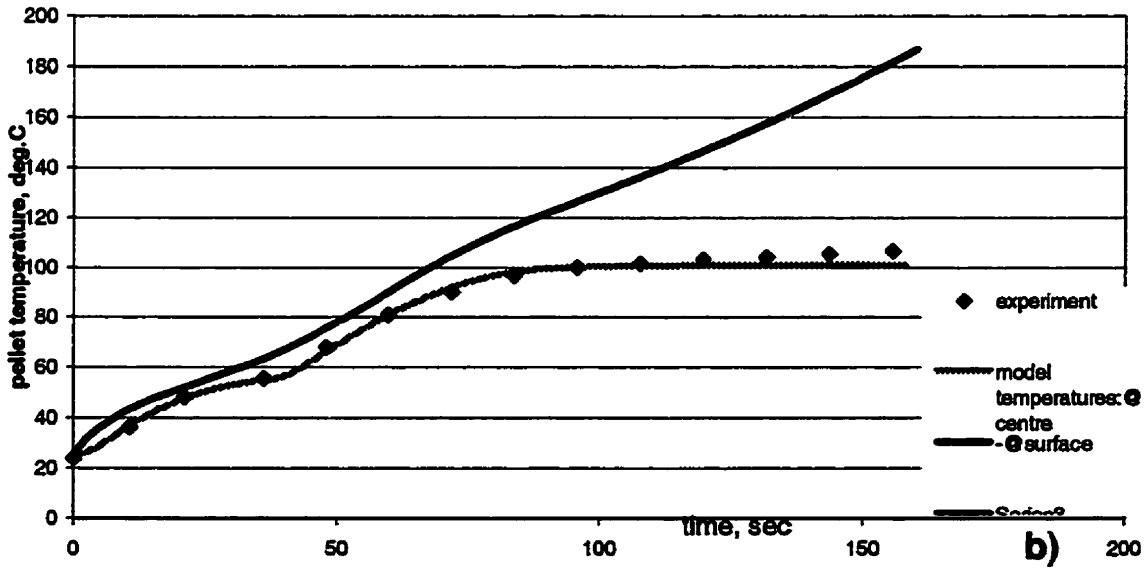
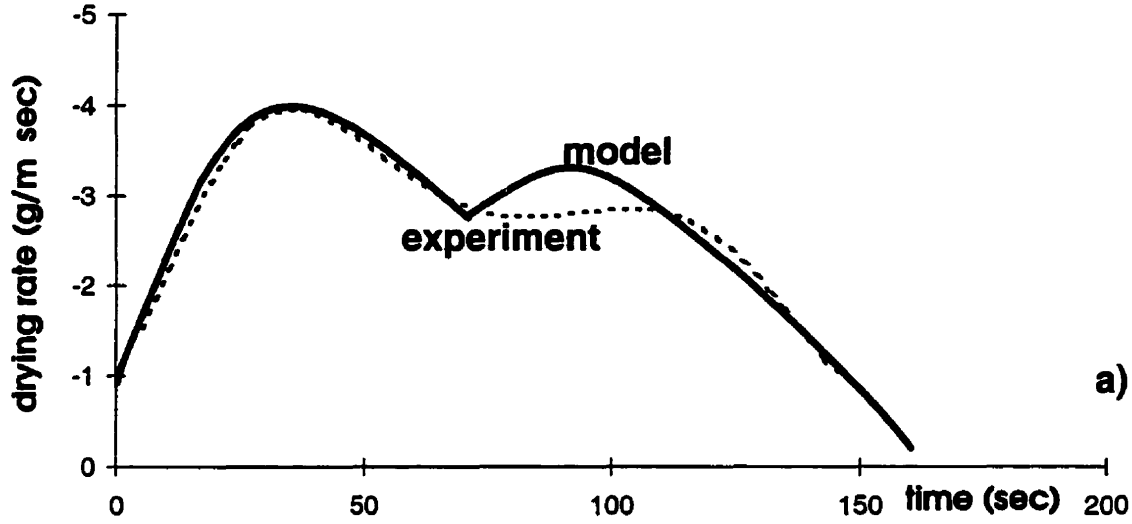


Figure 6.4.3.3.2 a Extended-Model Predictions of: (a) - Experimental Drying-Rate Curve; (b) - Temperature at the Pellet's Center and Surface

CORRELATION BETWEEN EXTENDED MODEL AND EXPERIMENT

AMBIENT TEMPERATURE	300 C
AIR VELOCITY	1.0 m/s
PELLET RADIUS:	5.4 mm
POROSITY:	0.304
BENTONITE	0.6 %
MATERIAL	GRIFFITH MAGNETITE
PARTICLE SIZE	19.9 um
SATURATION	0.84



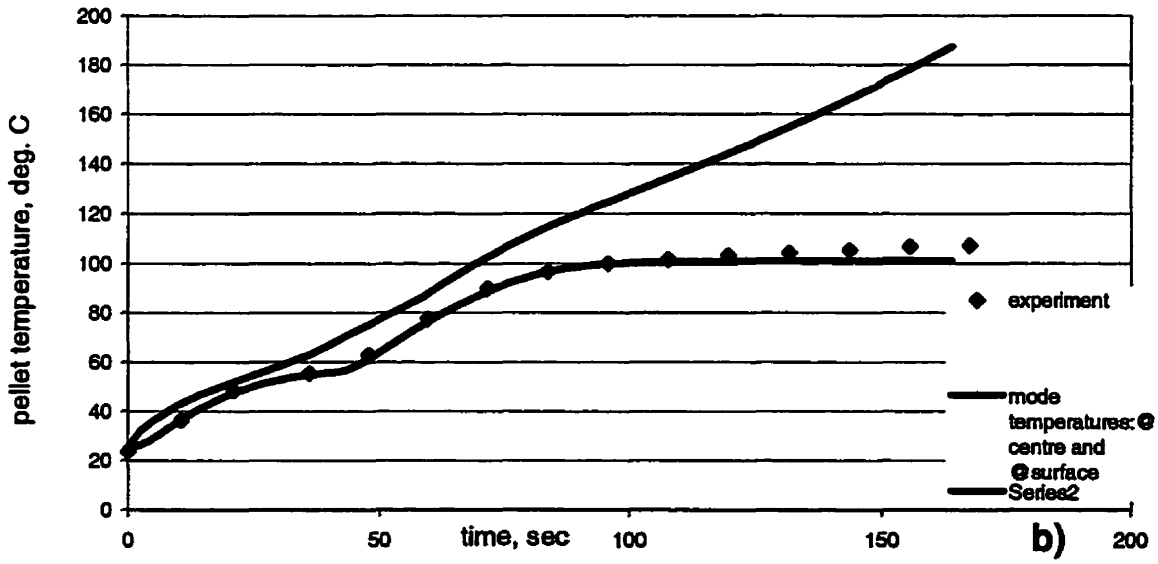
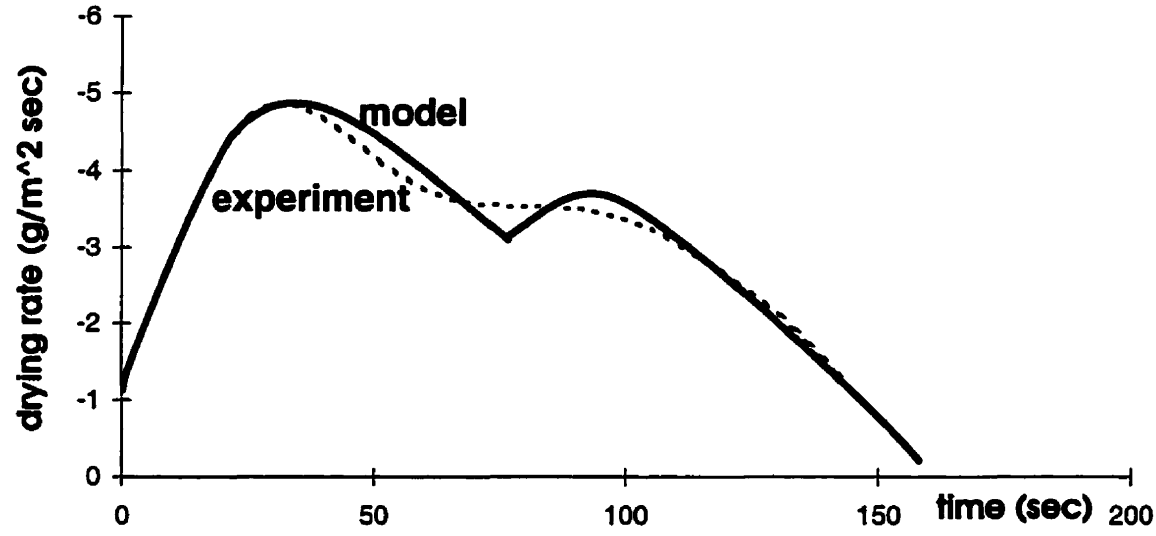


Figure 6.4.3.3.2 b. Extended-Model Predictions of: (a) - Experimental Drying-Rate Curve; (b) - Temperature at the Pellet's Center and Surface

CORRELATION BETWEEN EXTENDED MODEL AND EXPERIMENT

AMBIENT TEMPERATURE	300 C
AIR VELOCITY	1.6 m/s
PELLET RADIUS:	5.3 mm
POROSITY:	0.292
BENTONITE	0.6 %
MATERIAL	GRIFFITH MAGNETITE
PARTICLE SIZE	19.9 um
SATURATION	0.85



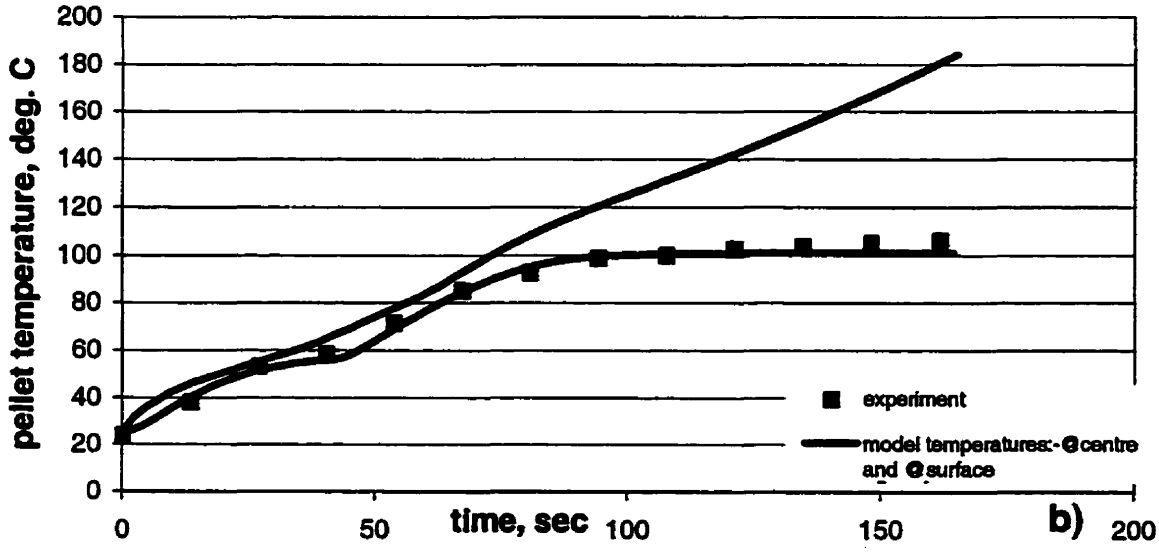
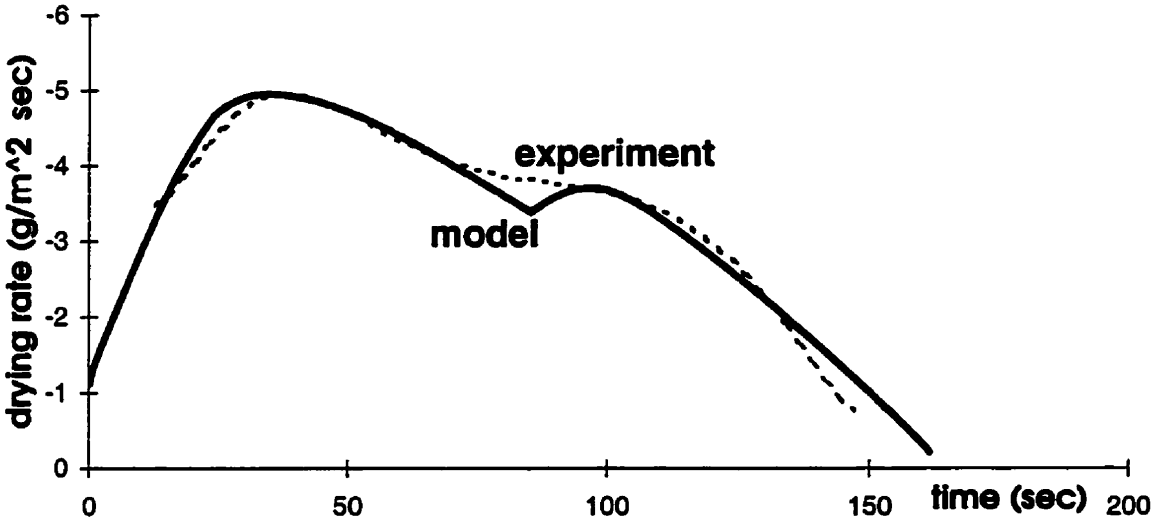


Figure 6.4.3.3.2 c. Extended-Model Predictions of: (a) - Experimental Drying-Rate Curve; (b) - Temperature at the Pellet's Center and Surface

CORRELATION BETWEEN EXTENDED MODEL AND EXPERIMENT

AMBIENT TEMPERATURE	300 C
AIR VELOCITY	1.6 m/s
PELLET RADIUS:	5.5 mm
POROSITY:	0.289
BENTONITE	0.6 %
MATERIAL	Griffith magnetite
PARTICLE SIZE	19.9 um
SATURATION	0.96



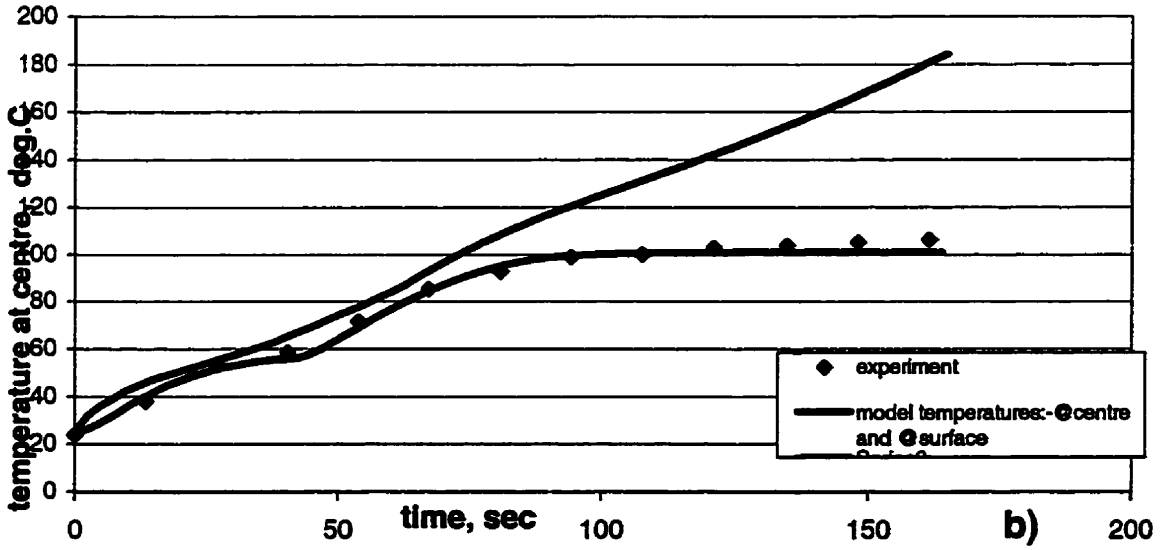
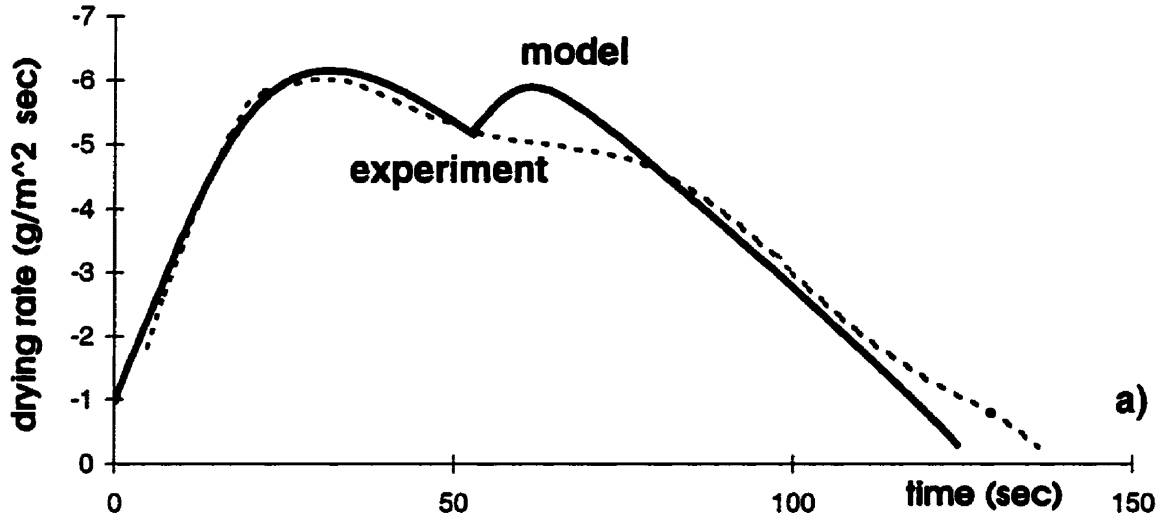


Figure 6.4.3.3.2 d. Extended-Model Predictions of: (a) - Experimental Drying-Rate Curve; (b) - Temperature at the Pellet's Center and Surface

CORRELATION BETWEEN EXTENDED MODEL AND EXPERIMENT

AMBIENT TEMPERATURE	400 C
AIR VELOCITY	1.0 m/s
PELLET RADIUS:	5.3 mm
POROSITY:	0.315
BENTONITE	0.6 %
MATERIAL	GRIFFITH MAGNETITE
PARTICLE SIZE	19.9 um
SATURATION	0.91



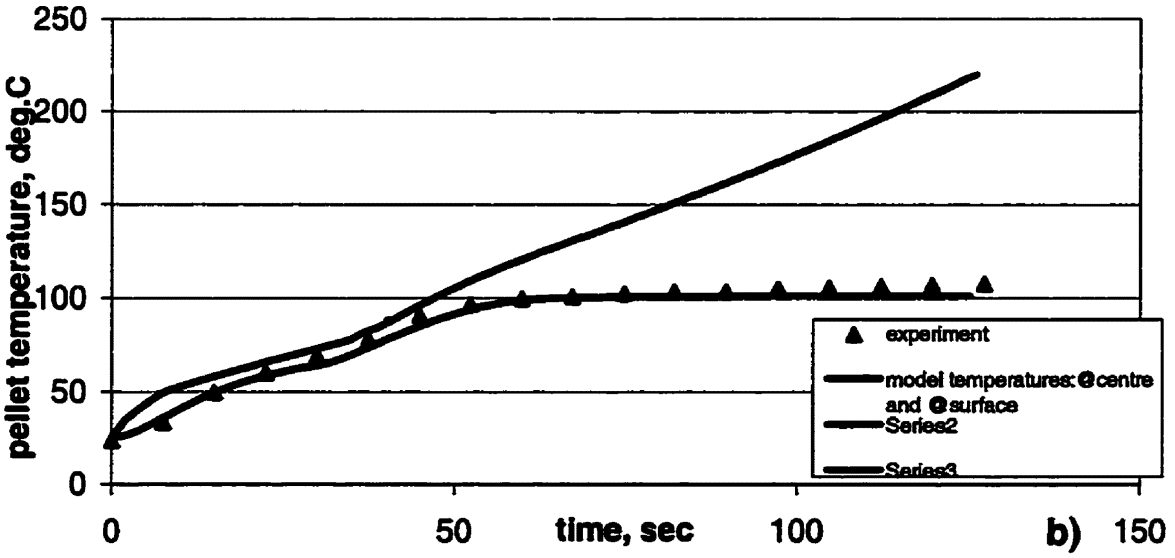
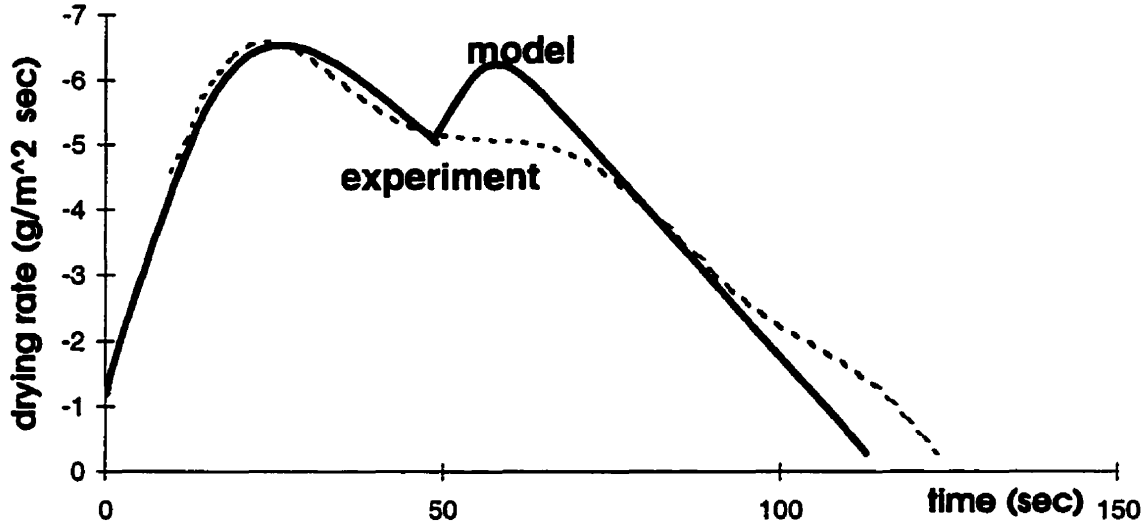


Figure 6.4.3.3.2 e. Extended-Model Predictions of: (a) - Experimental Drying-Rate Curve; (b) - Temperature at the Pellet's Center and Surface

CORRELATION BETWEEN EXTENDED MODEL AND EXPERIMENT

AMBIENT TEMPERATURE	400 C
AIR VELOCITY	1.6 m/s
PELLET RADIUS:	5.6 mm
POROSITY:	0.302
BENTONITE	0.6 %
MATERIAL	GRIFFITH MAGNETITE
PARTICLE SIZE	19.9 um
SATURATION	0.95



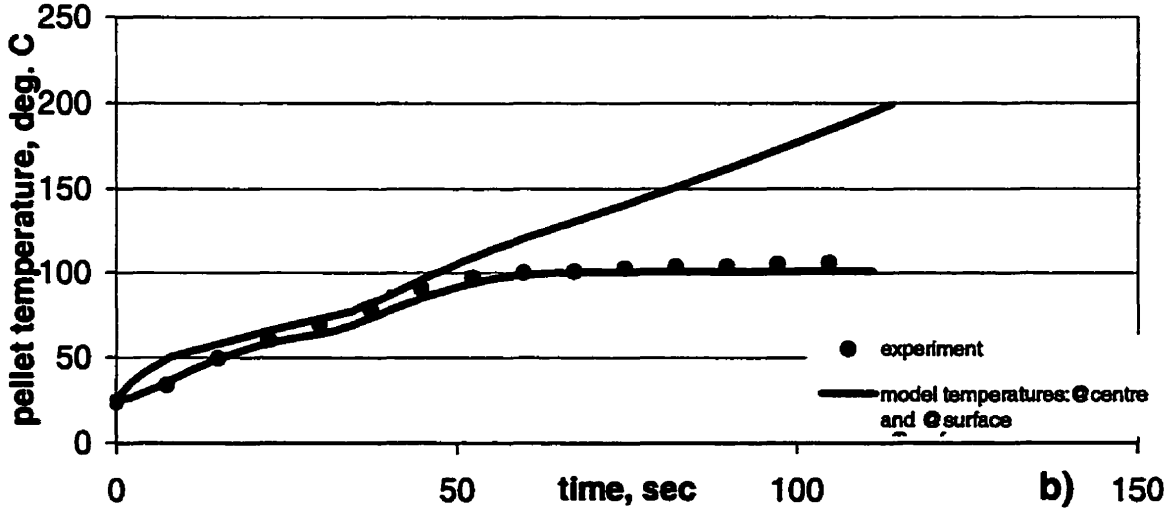
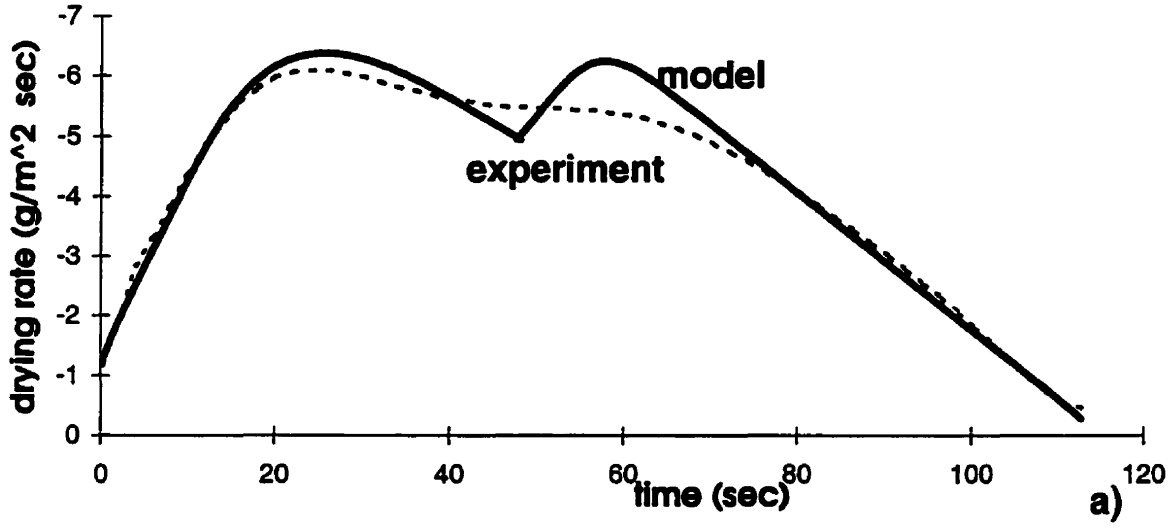


Figure 6.4.3.3.2 f. Extended-Model Predictions of: (a) - Experimental Drying-Rate Curve; (b) - Temperature at the Pellet's Center and Surface

CORRELATION BETWEEN EXTENDED MODEL AND EXPERIMENT

AMBIENT TEMPERATURE	400 C
AIR VELOCITY	1.6 m/s
PELLET RADIUS:	5.4 mm
POROSITY:	0.317
BENTONITE	0.6 %
MATERIAL	GIRFFITH MAGNETITE
PARTICLE SIZE	19.9 um
SATURATION	0.98



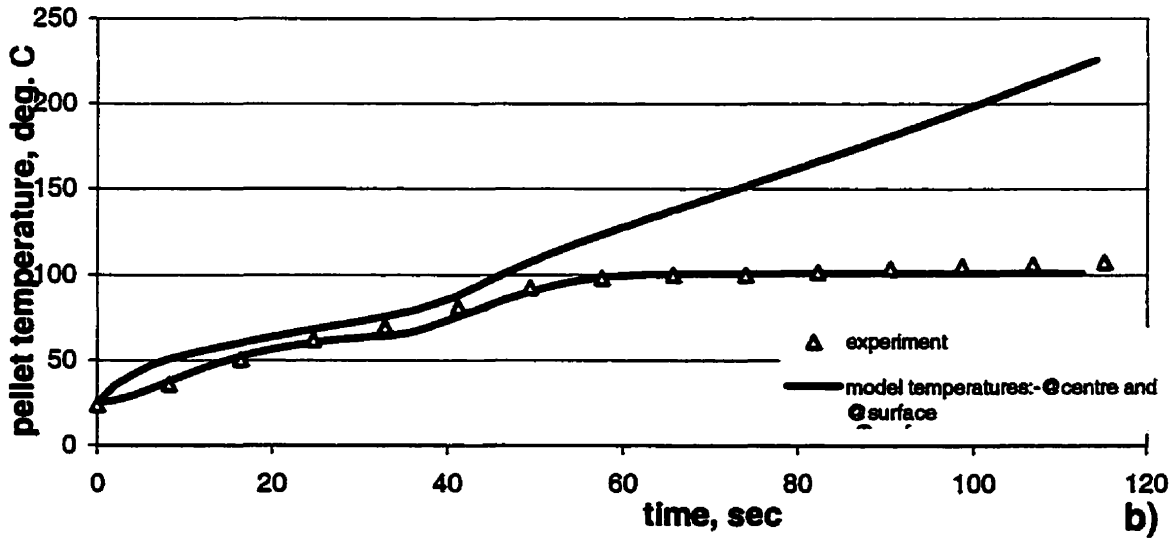
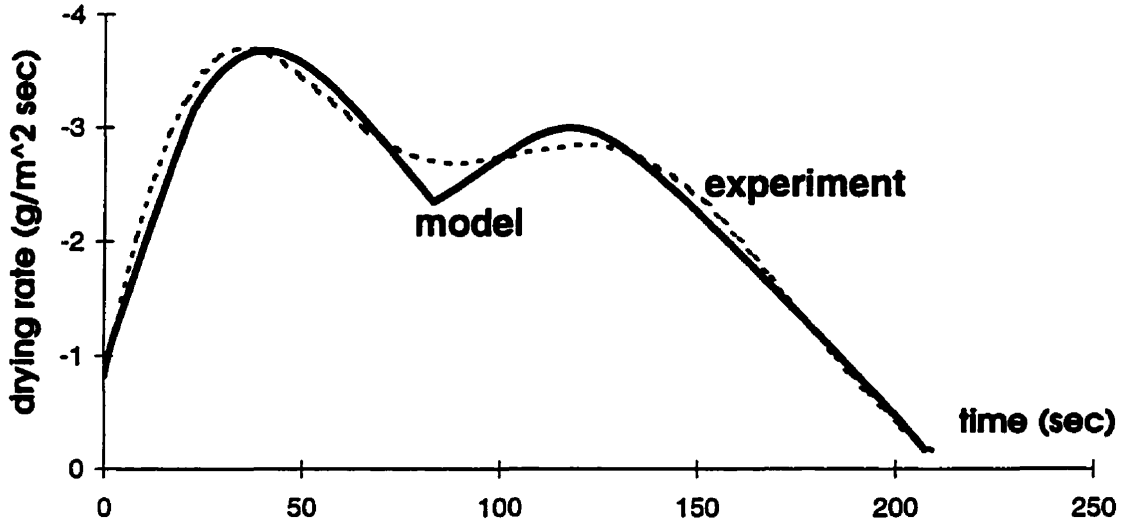


Figure 6.4.3.3.2 g. Extended-Model Predictions of: (a) - Experimental Drying-Rate Curve; (b) - Temperature at the Pellet's Center and Surface

CORRELATION BETWEEN EXTENDED MODEL AND EXPERIMENT

AMBIENT TEMPERATURE	300 C
AIR VELOCITY	1.0 m/s
PELLET RADIUS:	5.2 mm
POROSITY:	0.301
BENTONITE	1.2 %
MATERIAL	GRIFFITH MAGNETITE
PARTICLE SIZE	18.6um
SATURATION	0.82



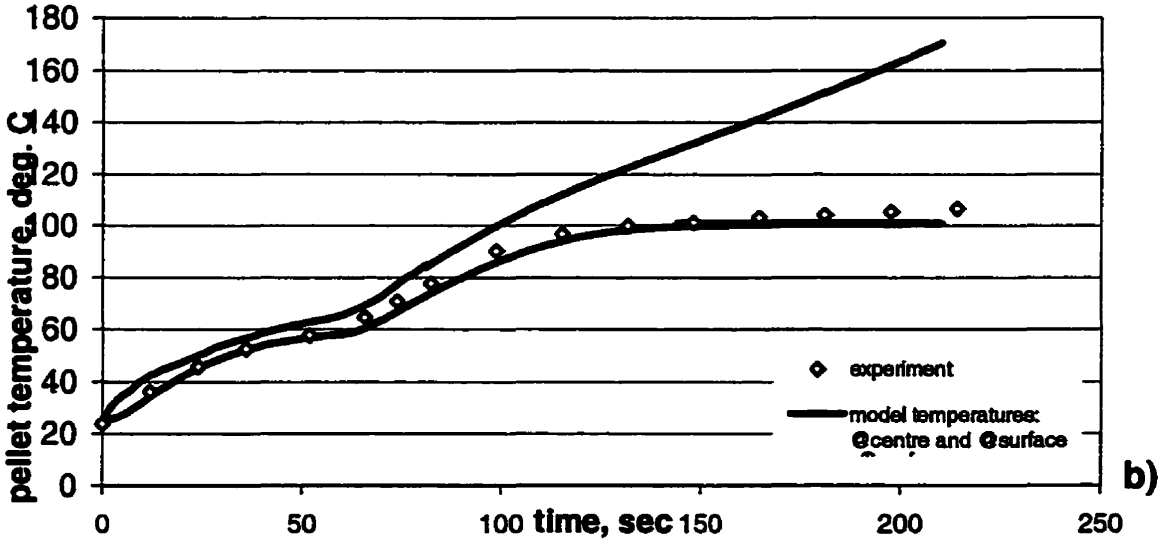
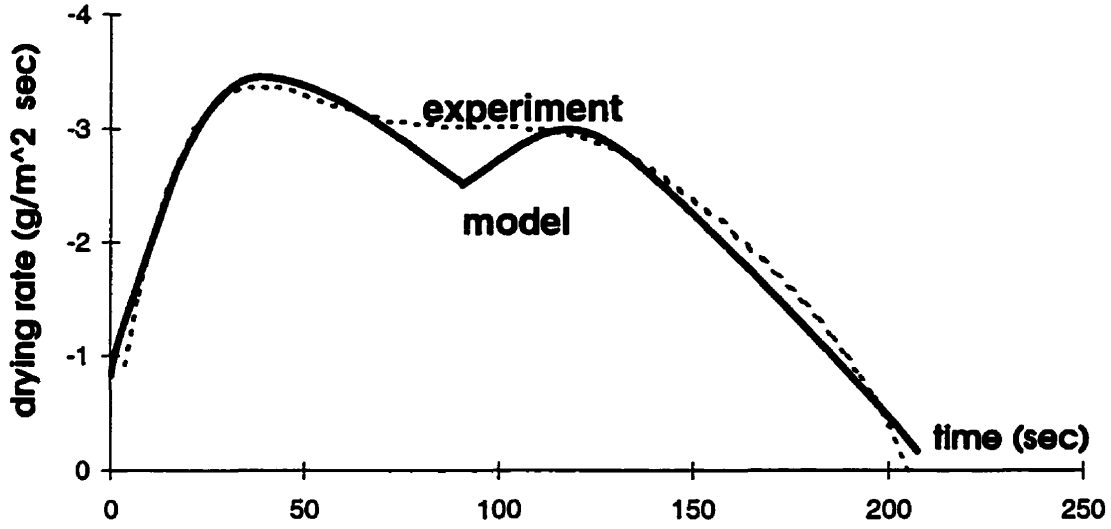


Figure 6.4.3.3.3 a. Extended-Model Predictions of: (a) - Experimental Drying-Rate Curve; (b) - Temperature at the Pellet's Center and Surface

CORRELATION BETWEEN EXTENDED MODEL AND EXPERIMENT

AMBIENT TEMPERATURE	300 C
AIR VELOCITY	1.0 m/s
PELLET RADIUS:	5.1 mm
POROSITY:	0.308
BENTONITE	1.2 %
MATERIAL	GRIFFITH MAGNETITE
PARTICLE SIZE	18.6um
SATURATION	0.84



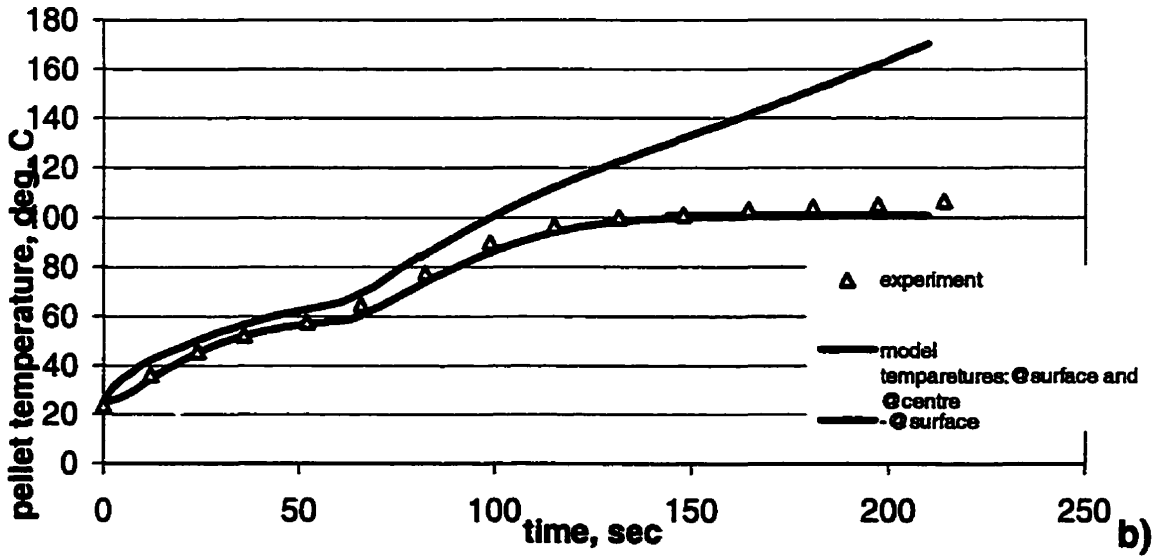
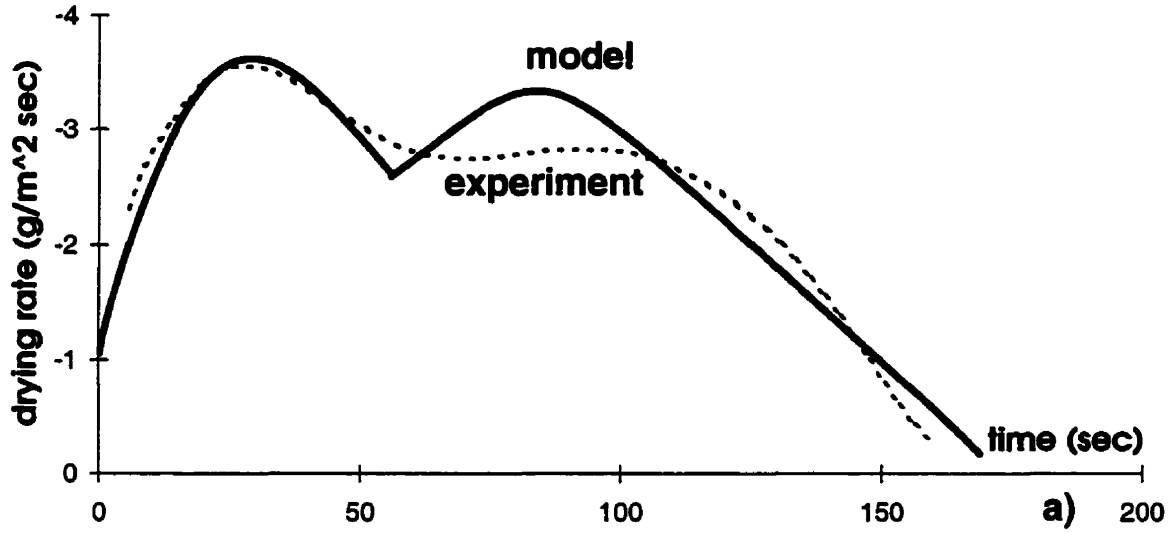


Figure 6.4.3.3.3 b. Extended-Model Predictions of: (a) - Experimental Drying-Rate Curve; (b) - Temperature at the Pellet's Center and Surface

CORRELATION BETWEEN EXTENDED MODEL AND EXPERIMENT

AMBIENT TEMPERATURE	300 C
AIR VELOCITY	1.6 m/s
PELLET RADIUS:	5.3 mm
POROSITY:	0.312
BENTONITE	1.2 %
MATERIAL	GRIFFITH MAGNETITE
PARTICLE SIZE	18.6um
SATURATION	0.88



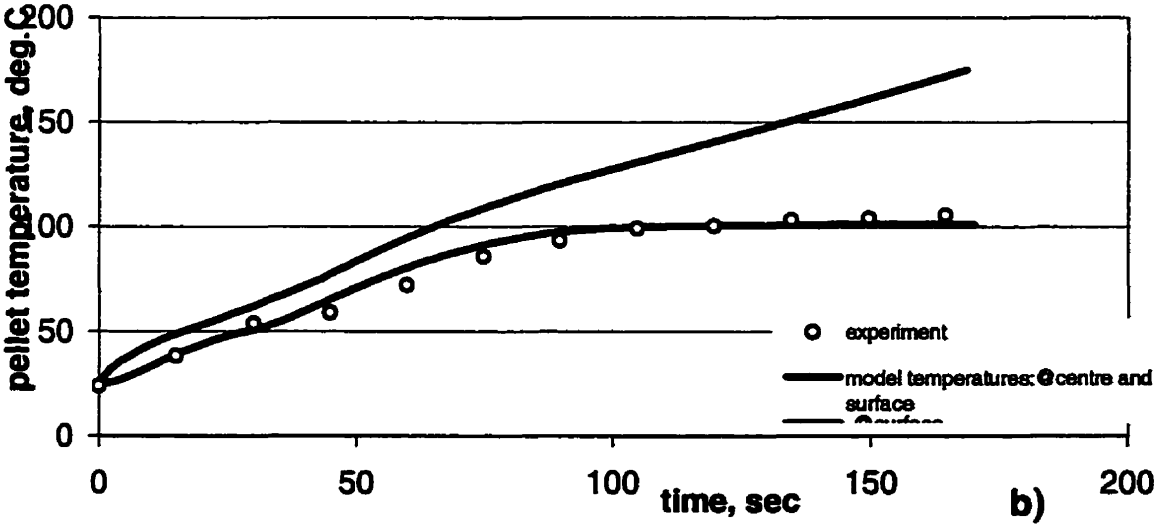
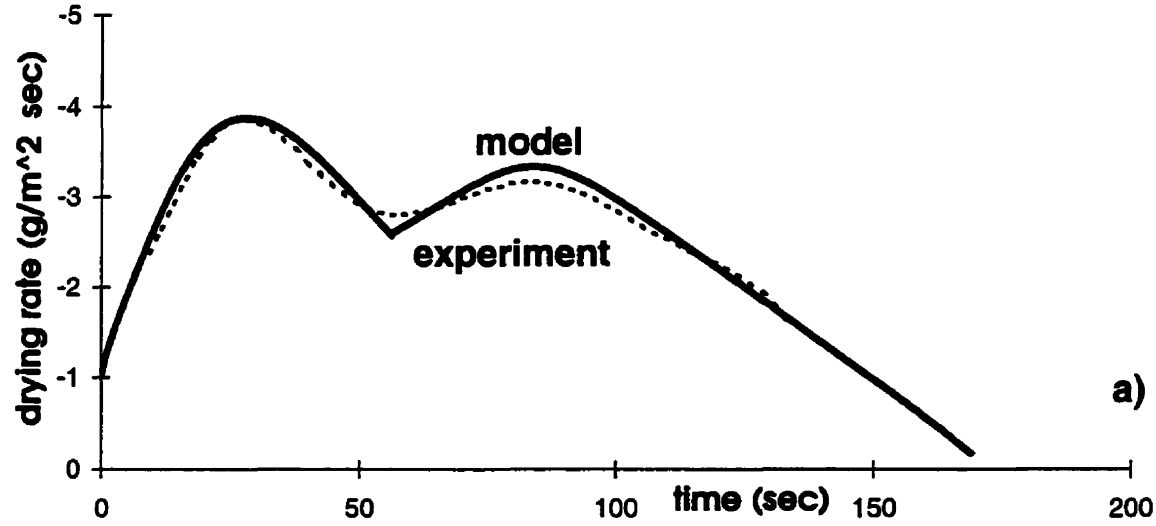


Figure 6.4.3.3.3 c. Extended-Model Predictions of: (a) - Experimental Drying-Rate Curve; (b) - Temperature at the Pellet's Center and Surface

CORRELATION BETWEEN EXTENDED MODEL AND EXPERIMENT

AMBIENT TEMPERATURE	300 C
AIR VELOCITY	1.6 m/s
PELLET RADIUS:	5.15 mm
POROSITY:	0.318
BENTONITE	1.2 %
MATERIAL	GRIFFITH MAGNETITE
PARTICLE SIZE	18.6um
SATURATION	0.86



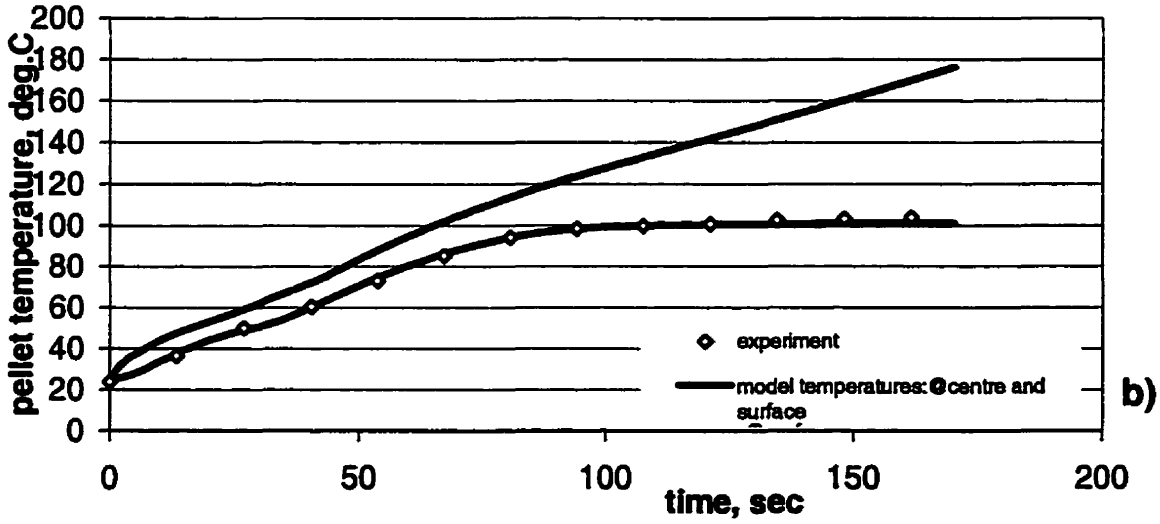
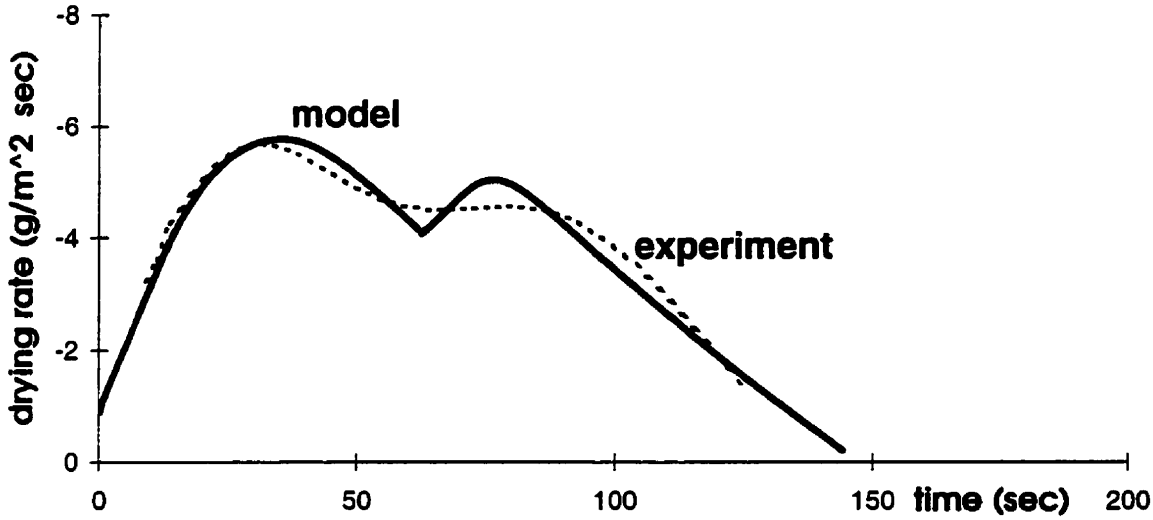


Figure 6.4.3.3.3 d. Extended-Model Predictions of: (a) - Experimental Drying-Rate Curve; (b) - Temperature at the Pellet's Center and Surface

CORRELATION BETWEEN EXTENDED MODEL AND EXPERIMENT

AMBIENT TEMPERATURE	400°C
AIR VELOCITY	1.0 m/s
PELLET RADIUS:	5.15 mm
POROSITY:	0.288
BENTONITE	1.2 %
MATERIAL	GRIFFITH MAGNETITE
PARTICLE SIZE	18.6μm
SATURATION	0.88



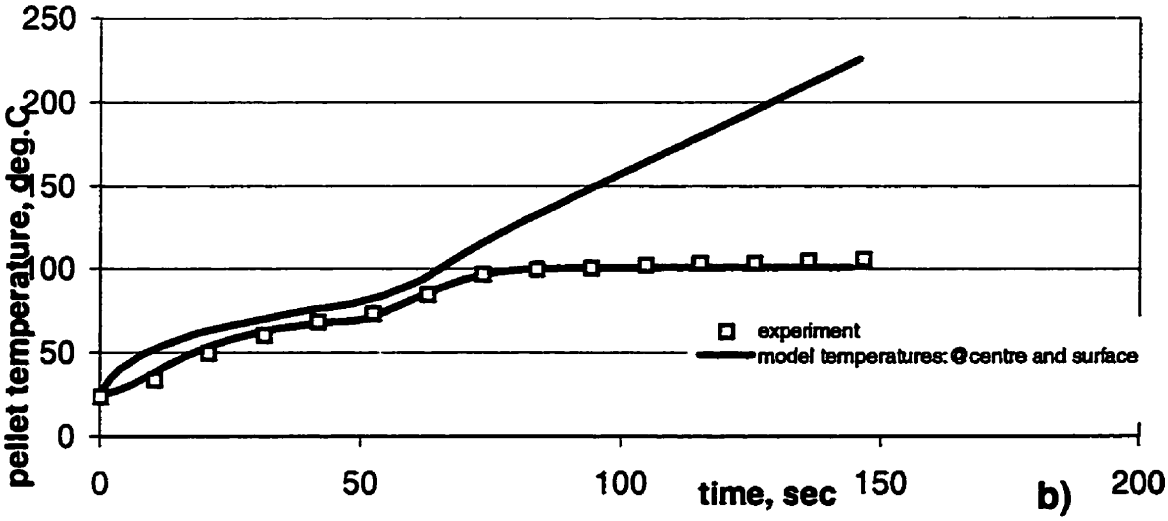
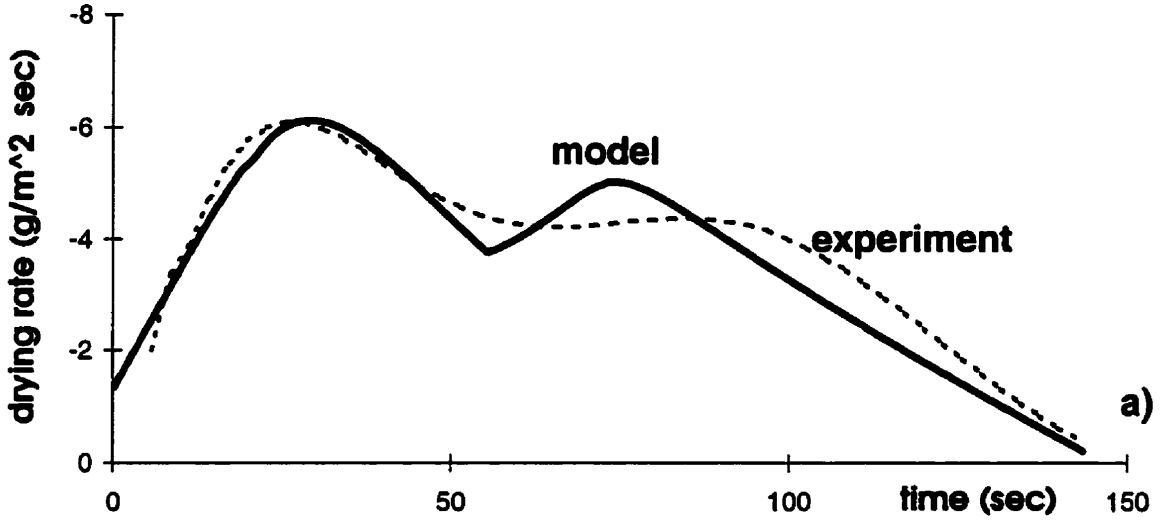


Figure 6.4.3.3.3 e Drying Rate Curves for a Pellet with 1.2 % Bentonite (a); Temperature at the Pellet Centre and Surface (b).

CORRELATION BETWEEN EXTENDED MODEL AND EXPERIMENT

AMBIENT TEMPERATURE	400 C
AIR VELOCITY	1.0 m/s
PELLET RADIUS:	5.3 mm
POROSITY:	0.292
BENTONITE	1.2 %
MATERIAL	GRIFFITH MAGNETITE
PARTICLE SIZE	18.6um
SATURATION	0.88



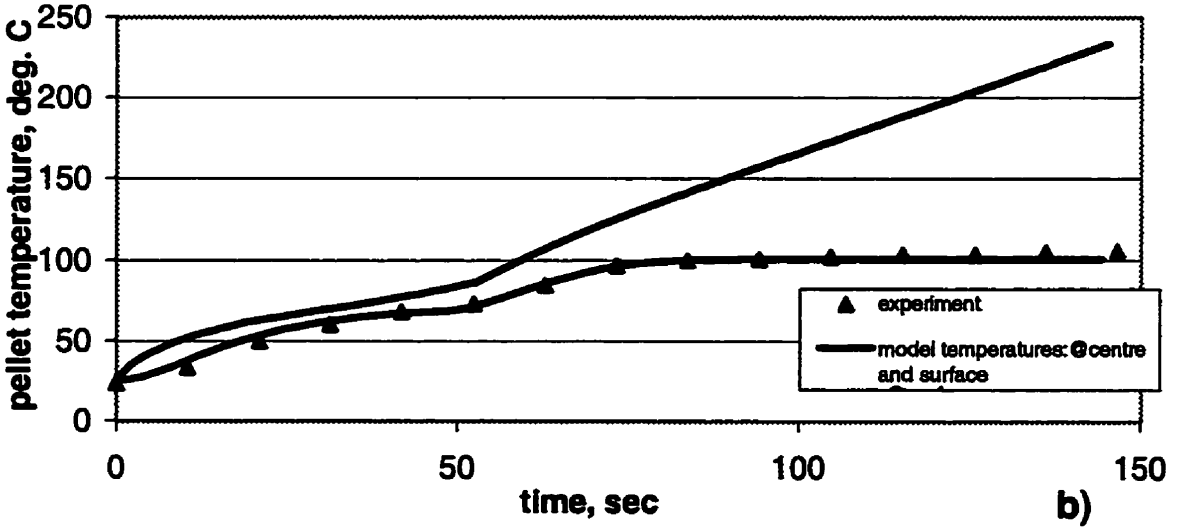
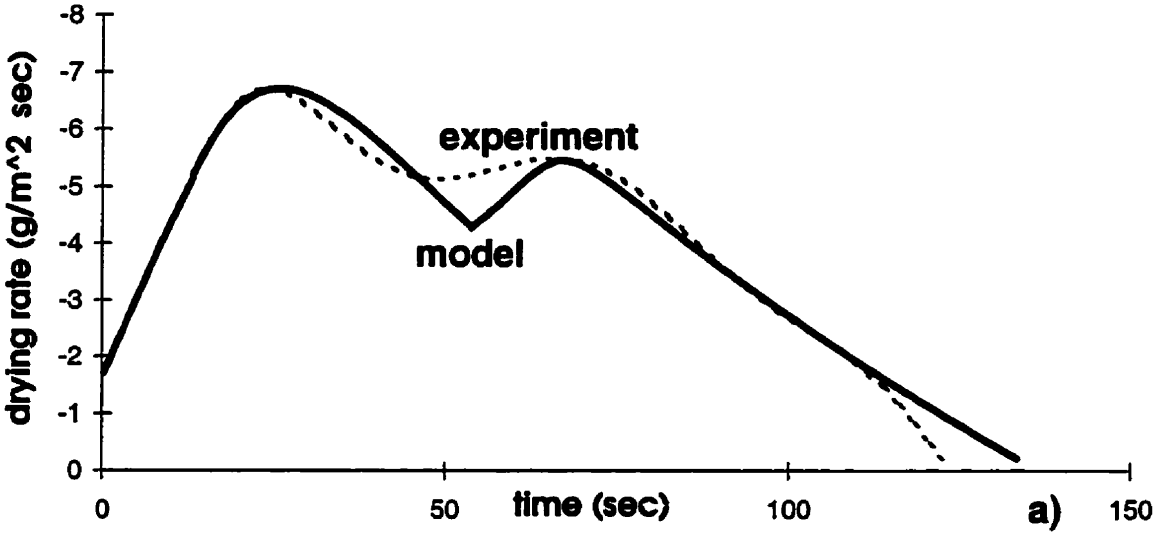


Figure 6.4.3.3.3 f. Extended-Model Predictions of: (a) - Experimental Drying-Rate Curve; (b) - Temperature at the Pellet's Center and Surface

CORRELATION BETWEEN EXTENDED MODEL AND EXPERIMENT

AMBIENT TEMPERATURE	400 C
AIR VELOCITY	1.6 m/s
PELLET RADIUS:	4.9 mm
POROSITY:	0.305
BENTONITE	1.2 %
MATERIAL	GRIFFITH MAGNETITE
PARTICLE SIZE	18.6um
SATURATION	0.84



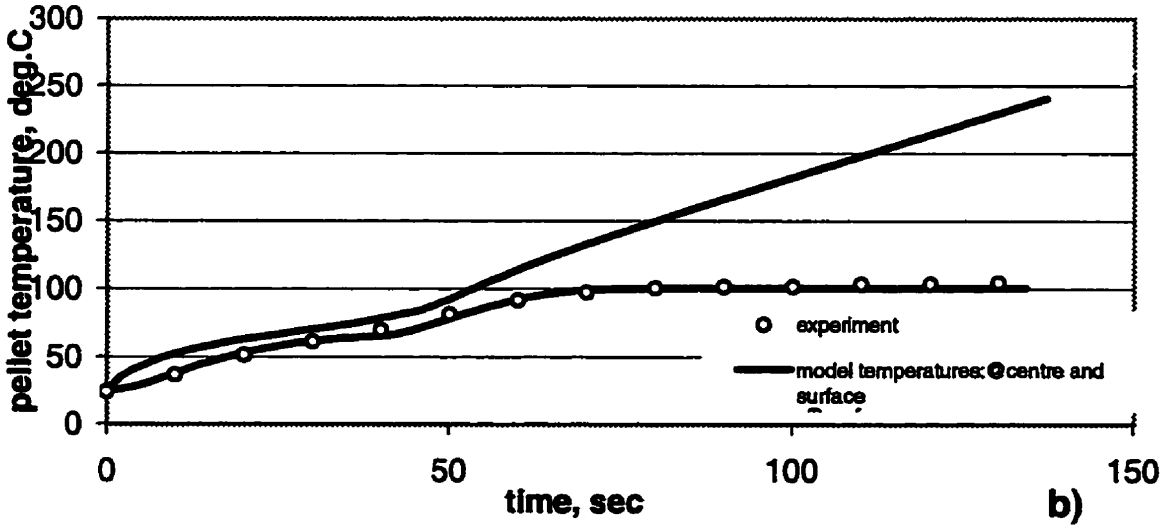
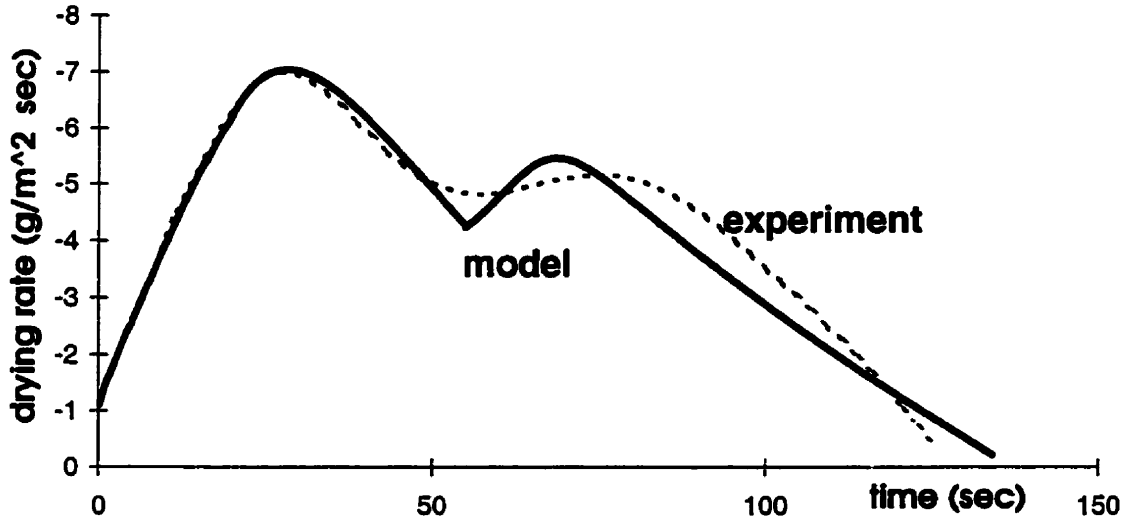


Figure 6.4.3.3.3 g. Extended-Model Predictions of: (a) - Experimental Drying-Rate Curve; (b) - Temperature at the Pellet's Center and Surface

CORRELATION BETWEEN EXTENDED MODEL AND EXPERIMENT

AMBIENT TEMPERATURE	400 C
AIR VELOCITY	1.6 m/s
PELLET RADIUS:	4.85 mm
POROSITY:	0.308
BENTONITE	1.2 %
MATERIAL	GRIFFITH MAGNETITE
PARTICLE SIZE	18.6um
SATURATION	0.88



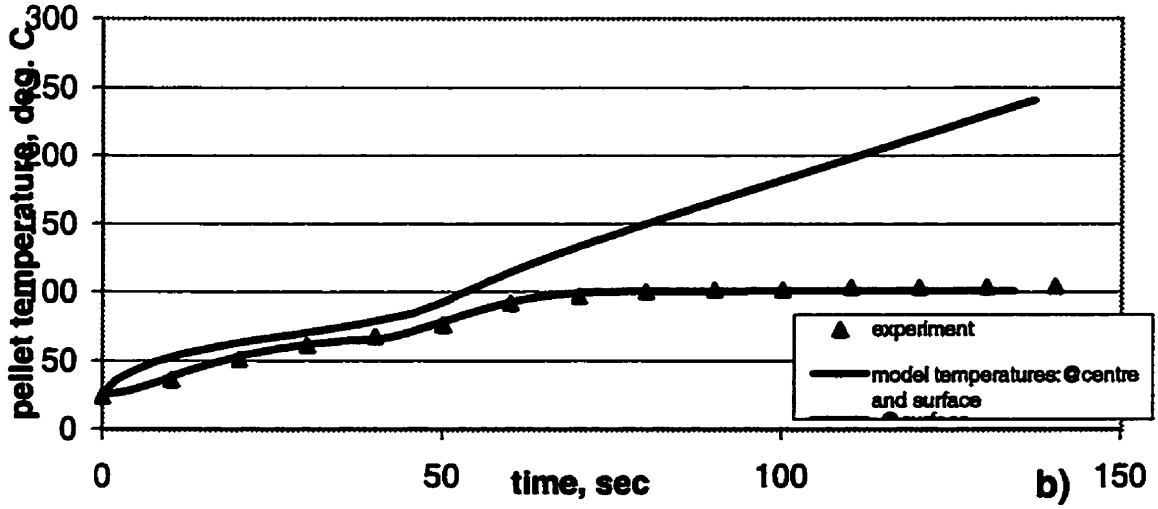


Figure 6.4.3.3.3 h. Extended-Model Predictions of: (a) - Experimental Drying-Rate Curve; (b) - Temperature at the Pellet's Center and Surface

Chapter 7

SUMMARIZING DISCUSSION

The scope of this PhD project is evidently rather broad and multifaceted. There is a strong unifying theme, however, which has formed a basis for the present thesis. This is the interrelationship between the microstructure of the agglomerates with, on the one hand, the mechanical and physical properties of the pellets and their behaviour during drying, on the other.

The work has been both theoretical and experimental. The scope of these investigations will now be summarized under the following headings:

1) Modelling the drying behaviour of the agglomerate spheres during their intensive drying, and experimental validation of the extended drying model;

2) Investigations of the agglomerates' microstructure and its modifications during drying under various drying conditions;

3) Investigations of the binder-additive behaviour during drying and its effect on pellet properties.

7.1. Drying Investigations

The comprehensive mathematical model, developed by D. Zaharchuk, proved to be a

highly effective tool to predict drying behaviour under intense drying conditions. One of the very significant contributions in the development of this model was identification of the loss of capillarity, resulting from the vapour lock, as a critical component of the mechanism of drying. It showed that the absence of the constant-rate period under intense-drying conditions is a natural consequence of the onset of the vapour lock.

One large part of the investigation within the present project was the experimental validation of the Zaharchuk model, on the one hand, and on the other -- the definition of the limitations and inadequacies of this preliminary model. Significant contributions were then made to improve the original model, so as to eliminate these inadequacies.

The Zaharchuk model treats the transition between the surface- and the shrinking-core drying regimes as an instantaneous event. This works adequately for the cases where the pore size is small and where the onset of the vapour lock occurs when the degree of saturation is still very high (even though there is the objectionable sharp maximum, e.g., Fig. 3.1.3). Major inadequacies become evident, however, when the pore size is in excess of about 2.0μm. Also, the original model is inadequate when the agglomerate matrix features a wide pore-size distribution (see Figures 6.1.1.2 - 6.1.1.6).

The extension to the model, developed in the present work, has overcome the major limitation of the original model. The extended model is based on microstructural characteristics of the porous agglomerate, i.e. the pore-size distribution function, as a key parameter of the surface/shrinking core transition. The model includes a *period* of transition between the two drying regimes.

The fundamental difference in the *mechanistic* nature of the surface/shrinking core transition during intense drying, as opposed to during drying under mild conditions has been identified presently. In the mild-drying case, water is being delivered to the surface through the small pores reaching the surface. This is because these small pores have the lower liquid pressure, and thus a greater driving force for Darcy flow of the liquid. Water delivery through the small pores proceeds by the larger pores being drained.

Under conditions of intense drying the vapour lock occurs first in the smallest capillaries reaching the surface. Consequently, these smaller capillaries are the first to become dry. Surface drying can, however, still continue via the system of interconnected larger pores delivering water to the surface. This vapour-lock-driven mechanism is fundamentally different from the conventional, or mild drying case. The model modifications are based on this insight.

When fine-particle pellets are being dried under intense conditions, their center temperature is rising steeply until it reaches 100^{0}C and then stays at this constant level. Significantly, this point coincides in time with the maximum on the drying-rate curves, which, according to our theoretical considerations, is associated with the mechanism change: the vapour transport through the dry shell changes from diffusion to Darcy flow. For pellets made of coarser particles the maximum drying rate is reached at much lower temperatures -- e.g. around 60^{0}C for the pore size investigated in detail presently. (This is similar to the constant-rate cases, e.g. Figure 3.1.2). Afterwards, the drying rate declines while the temperature at the pellet's center continues to rise. Mechanistically, the drying in this period is still at the surface, but the heat demand of the vaporization step there is insufficient to consume all the heat transferred across the boundary layer. (The latter fact is due to the reduced rate of Darcy flow, the smaller pores having been de-

activated). Part of the heat transferred is, therefore, consumed in raising the temperature of the matrix -- which continues to rise, but relatively more slowly (see Figures 6.1.2.2 a-e). The process continues until the rate of liquid-water delivery to the surface by Darcy flow through the 'still active' capillaries becomes less than the potential rate at which water can be evaporated there. At this instant the wet/dry interface shifts into the pellet interior and the shrinking-core drying regime sets in.

The rigorous experimental validation of the improved drying model has been another important contribution of the present work. Two independent and mutually-complementing sets of model-validation experiments were undertaken:

- experimental measurements of the time dependence of the drying rate;
- measurements of the pellet-center temperature.

Both these sets of experiments ultimately validated both the original and the extended model for agglomerates with a wide range of particle size, and dried under wide range of drying conditions. These investigations fully validate the assumptions made in the work and thus establish the vapour lock as a physical 'effect' in drying. They also show that our understanding of the intense-drying process is satisfactory.

7.2. Microstructural Investigations

The microstructural aspects of the agglomerates under study were investigated more specifically in the light of the insights gained from modelling.

An important microstructural characteristic of the agglomerates produced by tumbling is

the existence of large and mid-sized particles in contact with each other, forming the skeletal network structure. Another important characteristic of these agglomerates is the existence of a sizeable fraction of fine particles which are not part of the network structure, i.e. which are "loose" within the skeletal network. An important contribution of this study was the establishing that, depending on the intensity of drying regime, these loose particle can reposition themselves into new locations, thus modifying significantly the physical and mechanical properties of the pellets.

Upon drying under mild conditions there is a significant volume increase. Our research supports the idea that this is caused by the engulfment of loose fine particles with the receding wet/dry interface. The latter occurs at the late stage of mild drying; when the liquid phase recedes into pendular bridges between the skeletal-network particles, thus concentrating the fine particles into the contact areas. The capillary radius in these regions, therefore, is small resulting in a high local capillary suction. The consequent large capillary pressure is, evidently, sufficient to pry apart the skeletal-network structure. The result is the observed increase in porosity.

Next, our results establish firmly that there is no porosity increase in agglomerates dried under intense conditions. This is fully consistent with -- and constitutes a confirmation of -- the mechanistic picture proposed so far. Under intense drying conditions the contact areas between the network-forming particles are the primary sites of the vapour lock. Creation of gas/liquid interfaces in these areas may still result in loose-particle movements by engulfment but any likelihood for engulfment into the network contact areas is eliminated. These results, therefore, enlarge the scope of evidence regarding the interaction of the vapour lock and the engulfment effects.

Finally, agglomerates that do not contain a significant fraction of fine particles, do not expand. This, again, is consistent with the mechanistic picture: the structural features here do not include a network structure nor loose fine particles.

The two groups of pellets, dried under the mild versus intense conditions, feature significant deviations between their respective dry strengths. Microstructural differences between them are, evidently, the cause. The mildly-dried pellets, possessing the higher porosity due to the matrix-expansion phenomenon, have dry strength as much as 17% lower than those dried under intense conditions. Referring back to the Rumpf equation for dry strength (eqn. 2.5.1.1), the product $(1-\varepsilon)\cdot k^0$ in mildly-dried higher-porosity pellets is lower.

Our tumbling-and-drying investigations were theoretical and were limited to modelling. Relevant presently is that tumbling-and-drying involves *matrix densification* and, therefore, evolution of the microstructure, and thus strengthening of the dried pellets. Here, densification takes place with simultaneous removal of a volume-equivalent amount of moisture. The pellet interior is continuously in the fully saturated or capillary (more explicitly, the entry-suction) state. Hence, no particle engulfment processes can take place during this operation. But the significant densification of the pellets' microstructure by tumbling-and-drying must be accompanied by an equivalently-significant rearrangement of the particles within the matrix. This is reflected in lower porosity ε. Significant changes of the particle arrangements almost certainly involve the destruction of the original network structure, of the filling of large pores and thus "adjustments" in the ink-bottle effect. The result must be an increase in the coordination number of interparticle contacts k^0. Both ε and k^0 contribute to the higher dry strength (see again eqn. 2.5.1.1). Future

investigations to more closely define this microstructure evolution are called for.

The reason for inclusion of tumbling-and-drying in the scope of our work were the significant prospective industrial benefits of this operation. The first is, that part of moisture is removed prior to the drying operation, making the latter technological process easier and/or increasing the capacity of the moving-grate machines. The second is a significant degree of strengthening of the pellets due to their densification. The latter fact leads to a significant improvement of the spalling resistance of the pellets and thus again to easier and more flexible process control.

7.3. Binder Additive Behaviour

Pellets with bentonite, when dried under mild drying conditions, experience matrix expansion, similarly to bentonite-free pellets discussed in Section 7.2. The corresponding decrease in dry strength, however, is much less drastic (only 7% against 17% in bentonite-free pellets). Evidently, precipitation of bentonite, which under mild drying conditions occurs mostly in the contacts of skeletal-network structure, reduces the detrimental effect of porosity increase on the dry strength by reinforcing the interparticle bond in these critical contact areas.

Our investigations of the microstructural aspects of bentonite deposits during drying involved different materials and drying conditions. They have added significantly to the data base here. During mild drying, bentonite precipitates mostly in the pendular bridges between particles. Also, there is small but significant degree of efflorescence of bentonite to the surface, consistent with an extended surface-drying regime. This is consistent with literature evidence.

Under intense drying conditions, on the other hand, bentonite precipitates more evenly

throughout the pellet interior. There is no efflorescence. This is consistent with the absence of the constant-rate/surface-drying regime under these conditions. Also, precipitation in the iterparticle contacts is more limited. This is more evidence for the occurrence of the vapour lock and the effect it has on the creation of local gas/liquid interfaces in the contact areas.

On the subject of addition of bentonite to improve spalling resistance, an important contribution made as part of this work was identifying the reason for the existence of an optimal amount of bentonite addition, to maximize the spalling resistance. Another was the quantitative explanation for the existence of this phenomenon. According to our modelling results, at low bentonite concentrations the stress level induced in the pellet matrix by drying is rising at a much slower rate than the pellets' strength. As the 'optimal' concentration of bentonite is approached (0.8% by weight, which happens to be a standard amount used in industry), this trend inverts. The induced-stress curves rise faster than the pellet strength. It is this inversion of slopes that is responsible for leveling-off the spalling resistance near 0.8% bentonite content and its actual decrease at higher bentonite contents.

In iron-ore pelletizing bentonite is added for several reasons (e.g., drop test improvements and water immobilization) in addition to improving spalling resistance (see Section 2.5.2). Bentonite additions beyond the maximum of 0.8%, for the sake of these other reasons, can actually enhance the highly objectionable spalling phenomenon. This fact is not yet recognized widely in the pelletizing industry.

Chapter 8

CONCLUSIONS

(1) The mechanistic mathematical model of drying of porous spheres, developed by D.J. Zaharchuk, and which features the ability to describe drying behaviour of porous spheres under "intense" drying conditions, has been:

a) extended to include the gradual transition from the surface- to the shrinking-core drying regime;

b) validated -- and shown to be a powerful description of the physical process -- by a series of experiments measuring the drying rate and the temperature of the sphere center.

(2) Significant additional evidence has been contributed as part of the present work, to establish that the vapour lock is an omnipresent physical effect, acting during intensive drying. This evidence arises from:

a) the success of the model as per (1) above to predict drying-rate behaviour under a variety of combinations of porous-body properties and drying conditions;

b) ability to satisfactorily explain changes in the porosity of agglomerates resulting from drying and/or re-drying under various degrees of intensity.

(3) Significant additional evidence, both modelling and experimental, has been generated to confirm that the reason for the absence of a constant-rate period under intense-drying conditions is the vapour lock. The latter prevents the maximum drying rate, potentially possible under the given conditions of heat and mass transfer across the boundary layer, from being achieved.

(4) The combination of agglomerate-matrix properties (pore size and porosity) and heat convection/radiation conditions (temperature and Reynolds Number), which result in intense- versus mild- drying behaviour (including the transition between the two) have been defined and are shown in Figures 4.3.2 and 4.3.3.

(5) Agglomerates may experience a significant microstructural evolution during drying. This can lead to different physical and mechanical properties in the dry state. Three findings, contributed in this respect presently, are:

- Pellet matrix expansion occurs under mild drying conditions; leading to lower dry strength of the pellets;
- *No* significant porosity changes occur during intense drying; leading to higher dry strength compared to the previous case;
- Pellet densification achieved by a tumbling-and-drying operation;

leading to significant improvements in dry strength and spalling resistance.

(6) A significant body of new data has been contributed on the subject of drying behaviour and the pattern of drying-rate curves for iron-ore pellets containing bentonite. Satisfactory agreement between model and experiment can be achieved by -- effectively -- using the viscosity and thermal conductivity of the wet matrix as adjustable parameters. This raises several issues regarding Darcy flow of bentonite-containing water within a system of interconnected pores in a porous medium and defines interesting future work.

(7) The character of bentonite precipitation within individual pores and the overall distribution of bentonite precipitates throughout the pellet interior are both affected by the intensity of the drying regime. This fact constitutes additional evidence of the vapour-lock mechanism in the intensive drying. The significant effect on physical and mechanical properties of the dried agglomerates (see Table 6.4.2.1) can be, thus, better understood.

Of significance for the understanding and control of industrial processes:

(8) Densification of pellets by tumbling-and-drying increases significantly the dry strength of the pellets while, in addition, not affecting significantly the circumferential stresses built up during (intensive) drying. Tumbling-and-drying,

therefore, is a promising means to counteract spalling in industrial processes.

(9) The existence of a maximum in the shock temperature vs. bentonite-added curve has been confirmed and its cause identified and explained. The reason is that bentonite increases both the strength of the agglomerate matrix as well as its Young's modulus (and thus the stress buildup upon heating). The maximum is a consequence of first a favorable and then an unfavorable balance in the rates of increase with bentonite content of the stress and the strength (Figure 4.5.2).

Of significance beyond iron-ore pelletizing:

(10) Although this study was focused on a specific industrial process, the pelletizing of iron-ore concentrates, the interrelationship between microstructure and drying behaviour has important implications in understanding the nature of soils, rocks, ceramics, catalyst pellets and processed foods.

Chapter 9
LITERATURE

1. Zaharchuk, D.J.
Ph.D. Thesis, University of Waterloo, (1993).

2. Kudlyk, R.
M.A.Sc. Thesis, University of Waterloo, (1994).

3. Graton, J. and Fraser, P.M.
J.Geology, 43, (8), (1935), p. 785.

4. Gray, W.A.
'The Packing of Solid Particles', *Pub. Chapman Hall,* (1968)).

5. McGeary, R.K.
J.Am. Ceramic.Soc., 44, (10), (1961), p.513.

6. Haughey, D.P. and Beveridge, G.G.
Chem. Eng.Sci., 21, (1966), p.905.

7. Reynolds, O.
Phil. Mag., 20, (1985), p.469.

8. Salsburg, Z.W.
J. Chem. Educ., 43, (7), (1966), p. 353-357.

9. Pietsch, W.
'Size Enlargement by Agglomeration', *Pub. J.Wilye N-Y*, (1990), p.71.

10. Alder, B.J.
J.Chem.Phys., 40, (1964), p. 2724.

11. Fuller, W.B., Thompson, S.E.
'The Laws of Proportioning Concrete', *Trans. Am. Soc. Civ. Engng.*, **LIX**, *67*, (1907).

12. Sherrington, P. and Oliver, R.
'Granulation', *Pub. J.Wiley N-Y,* (1981).

13. Batterham, R. and Oliver, R.
'Agglomeration Fundamentals', *Can.Soc.chem.Eng.,* (1985).

14. Orr, C.
'Particulate Technology', *Pub. Mc.Millan N-Y,* (1966).

15. Ergun, S.
Chem. Eng.Prog., 48, (1952), p. 89.

16. Macrae, J.C. and Gray, W.A.
Brit. J. Appl. Phys. 12, (1960), p.164.

17. Debbas, S. and Rumpf, H.
Chem. Eng. Sci., 21, (1966), p.1271.

18. Bernal, J.D. and Finney, J.L.,
Disc.Faraday Soc., No. 43, (1967), p.62.

19. Fuller, W.B., and Thompson S.E.
'The laws of proportioning concrete', *Trans. Am. Soc. Civ. Engng,* **LIX**, 67, (1907).

20. Waddel, H.
J. Geology, 43, (1935), p. 250.

21. Heywood, M.
J. Imp. Coll.Chem. Eng. Soc. 2, (1946), p. 9.

22. Hoffman, F.
Trans. Am. Foundry Soc., 67, (1959), p. 125.

23. Srinagesh S.
Brit. Foundry Man., 56, (1963), p.411.

24. Furnas, C.C.
Ind. Eng. Chem., 23, (1931), p.1052.

25. Karlsson, K. and Spring, L.
J. Mat. Sci., 5, (1970), p.340.

26. Touloukian, Y.S., Powell, R.W., Ho, C.Y., Clements, P.G., eds.
Thermophysical Properties of Matter, v.2, v.5, v.13, NY, Plenum, (1970).

27. Yeranuzis, S., Cornell, S.W., Wintner, B.
Nature, 207, (1965), p. 835.

28. Richards, J.C.
'Storage of Particulate Material', *Inst. Chem. Eng.*, (1966).

29. Burgreen, D.
Elements of Thermal Stress Analysis, Jamaica, NY.: C.P. Press, (1971).

30. Berg, T.G.O., McDonald, R.L., Traynor, R.J.
Powder Technol., 3, (1969), p.183.

31. Sohn, H.Y. and Moreland, C.
Can. J. Chem. Eng., 46, (1968), p.162.

32. Bo, M.K., Freshwater, D.C., Scarlett, B.
Trans. Inst. Chem. Eng., 43, (1965), p.T228.

33. Sherrington, P.J.
'The granulation of sand as an aid to understanding fertilizer granulation', *The Chem. Engineer*, July/Aug, (1968), pp. CE201-215.

34. Wynnyckyj, J.R.
Proc.of the 6th Int.Symp.on Agglomeration, (1993), pp.143-160.

35. Butensky, M. and Hyman, D.
'Rotary drum granulation. An experimental study affecting granule size', *Ind. Eng. Chem. Fundam., 10, (2)*, (1971), pp.212-219.

36. Treybal, R.E.
'Mass Transfer Operations', 3rd edn., Toronto, *McGraw-Hill Co.*, (1980)

37. Brinker, C.J. and Scherer, G.W.
'Sol-Gel Science', *Academic Press,N-Y*, (1990).

38. Clark, K.N.
Trans. Inst. Min. Met., 90 C, (1981), pp.C66-C72.

39. Chen, S. and Whitaker, S.
Drying'86, *Pub. Hemisphere Co., N-Y*, V.1, (1986), pp.39-48.

40. Schadler, N. and Kast, W,
Int. J. Heat, 30, (1987), p.2031.

41. Goodwin, J.W.
Coll. Sci., ed. Roy.Soc.Chem., (1982).

42. Grebenkin, G.A. and Polyakov, V.M.
Steel in USSR, 11, (98), (1981), pp.200-202.

43. Wei, C.K. and Davis, H.T.
AIChE J., 31, (8), (1985).

43. Chen, P.
Advances in Heat Transfer, 14, Irvine T.F., Hartnett J.P., eds., (1988), pp.1-105.

44. Hadley, G.R.
Int. J. Heat Mass Trans., 25, (10),(1982), pp. 1511-1522.

45. Åberg, B.
J. Geotech. Eng., 118, (9), (1992), pp.1315-1334.

46. Omenyi, S.N., Smith, R.P. and Neumann, A.W.
Powder Tech., 15, (1980), pp.253-260.

47. Zaharchuk, D.J.
M.A.Sc. Thesis, University of Waterloo, (1985).

48. Wynnyckyj, J.R.
How Bentonite Acts to Improve the Dry Strength of Agglomerates. WCPD Report #662-8749, Dept.of Chem.Eng., UW, (1986).

49. Goodwin, J.W.
Coll.Sci., Goodvin J.W., ed., Roy.Soc.of Chem., London, (1982).

50. Lisieczko, D.
Unpublished Research, (1981-1983).

51. Wynnyckyj, J.R.
Can.J.Ch.Eng.,63, (1985); pp.591-597.

52. Craig, A.
'Soil Mechanics', (1974).

53. Saleh, Y.A.
M.A.Sc. Thesis, University of Waterloo, (1985).

54. Geiger, G.H. and Poirier, D.R.
'Transport Phenomena in Metallurgy', *ed. Addison -Wesley Co.*, (1980).

55. Liu, C. and Evett, J.B.
'Soil Properties: Testing, Measurement and Evaluation', *ed. Prentice-Hall, NJ,* (1984).

56. Carlslaw, J.S. and Jaeger, J.C.
'Conduction of Heat in Solids', *Oxford:Carlton Press*, (1959).

57. Popov V.A.
'Stress Analysis', (1985).

58. Lubinski, J.
Proceedings of the US Conf. on Stress Analysis , 53, (1952), pp.1095-1121.

59. Pearse, J.F., Oliver, T.R., Newitt, D.M., *Trans. Instn. Chem. Engnrs., 27*, 1949, pp. 1-8.

60. Oliver, T.R., Newitt, D.M., *Trans. Instn. Chem. Engnrs., 27*, 1949, pp. 9-18.

61. Encyclopaedia of Science and Technology, 8th ed., Toronto, McGraw-Hill Book Company, vol 3, 1997, pp 350-353.

62. Encyclopaedia of Science and Technology, 8th ed., Toronto, McGraw-Hill Book Company, vol 19, 1997, p. 183.

63. Crouse, W.H., and Anglin, D.L.,
Automobile Engines, 1986.

64. Whitaker, S.,
Advances in Heat Transfer, Vol. 13, ed. Harnett, J.P., Irvinr, T.F., 1977, pp.119-200.

65. Ranz, W.E., Marshall, W.R.,
Chem. Eng. Progress, 48 (3), 1952, pp.141-146.

66. Ranz, W.E., Marshall, W.R.,
Chem. Eng. Progress, 48 (4), 1952, pp.173-180.

67. Yuen, M.C., Chen, L.W.,
Int. J. Heat Transfer, 21, 1978, pp.537-542.

68. Krupiczka, R.,
Int. Chem. Eng., 7, No.1, January 1967, pp.122-144.

69. Wonchala, E.P., Wynnyckyj, J,R.,
Can. Jour. Chem. Eng., 62, 1984, pp719-722.

70. Holman, J.P.,
Heat Transfer, 6th edition, Toronto, McGraw-Hill Book Company, 1986.

71. Vargaftik, N.B., ed.,
Tables on the Thermophysical Properties of Liquids and Gases, New York, Hemisphere Publishing Company, 1975.

72. Perry, R.H., Chilton, C.H., eds.,
Chemical Engineering Handbook, 5th edn., Toronto:, McGraw-Hill Book Company, 1973.

73. Wakao, N., Kaguei, S.,
Heat and Mass Transfer in Packed Beds, New York, Gordon and Breach Science Publishers, 1983.

74. Hadley, G.R.,
Int. J. Heat Trans., 1, Irvine Jr., T.F., Harnett, J.P., eds., 1964, pp.123-184.

75. Geiger, G.H., Poirier, D.R.,
Transport Phenomenon in Metallurgy, Don Mills:Addison-Wesley Publishing Co., 1980.

76. Chen, P.,
Mathematical Modelling of Drying and Freezing Processes in the Food Industry, Ph.D. Thesis, University of Waterloo, 1987.

77. Thomson, W.,
Phil. Mag., 42, (1871), p.448.

78. Folman, M., Shereshefsky, J.L.,
J. Phys. Chem., 72, (1950), p.3682.

79. Cross, N.L., Picknett, R.G.,
Trans. Faraday Soc., 59, (1963), p.846.

80. Pashley, R.M.,
J. Colloid Interface Sci., 78, (1980), p.246.

81. Fisher, L.R., Israelachvili, J.N.,
Chem. Phys. Lett., 76(1980), p. 251.

82. Fisher, L.R.,
Adv. Coll. Interface Sci., 16, (1982), pp.117-125.

83. Wonchala, E.P.,
Gas Flow Maldistribution in the Iron-Ore Pelletizing Shaft Furnace, Ph.D. Theis, University of Waterloo, 1988.

84. Hodgkin, N.M. and Murr, L.E.,
Microstructural Science, 2, (1973), pp.129-146.

85. Markievicz, P.C.,
Microscopic Investigations of Particle Agglomerates, M.A.Sc. Theis, University of Waterloo, 1984.

86. M. Tigerschiöld,
Aspects on Pelletizing of Iron Ore Concentrates, *Journal of the Iron Ore and Steel Institute, 05*, (1954), pp.13-20.

87. Capes, C.E.,
Powder Technol., 4, (1970/71), pp.77-82.

88. Pietsch, W.B.,
Can. J. Chem. Eng., 47, (1969), pp. 403-409.

89. Wynnyckyj, J.R., McCurdy, W.A.,
Metallurgical Trans., 5, (1974), pp.2207-2215.

90. Wynnyckyj, J.R., Fahidy, T.Z.,
Metallurgical Trans., 5, (1974), pp. 991-999.

91. Fahidy, T.Z.,
Personal communication, (1998).

92. Washburn, E.W.,
Proc. Natl. Acad. Sci., 7, (1921), p.115.

93. Schultz, N.F., Lex, N.A., Zetterstrom, J.D.,
Trans. AIME, 235, (1966), pp.251-255.

94. Roorda, M.J., Burghardt, O., Kortmann, H.A., Jipping, M.J., Kater, T., *Proceedings: 11th International Mineral Processing Congress, Cagliari,* (1975), pp. 139-180.

95. Nicol, S.K., Adamiak, Z.P., *The Aust. I.M.M. Conference, Western Australia,* (1973), pp. C22-C33.

96. Nicol, S.K., Adamiak, Z.P., *Inst. Min. Met., 82,* (1973), pp.511-519.

97. Rumpf, H., "The Strength of Granules and Agglomerates", in *Agglomeration*, Knepper, W.A., ed., NY: Interscience Publishers, (1962), pp. 379-418.

98. Capes, C.E., *Particle Size Enlargement*, NY: Elsevier Scientific Publishing Company, (1980).

99. Newitt, D.M., Conway-Jones, J.M., *Trans. Instn. Chem. Engnrs., 36,* (1958), pp. 422-441.

100. Haines, W.B., *J. Agric. Sci., 17,* (1927), pp.264-289.

101. Kapur, P.C., and Fuerstenau, D.W., *J. Am. Ceram. Soc., 50,* (1967), pp.14-18.

102. Omenyi, S.N., and Capes, C.E., *Powder Techn., 33,* (1982), pp. 167-174.

103. Tireschiold, M. and Ilmoni, P.A., "Fundamental Factors Influencing the Strength of Green and Burned Pellets Made from Fine Magnetite-Ore Concentrates", *Proc. Blast Furnace, Coke Oven, Raw Materials Conference, 9,* New York,: AIME, 1950, pp.18-45.

104. Ritter, H.L., Drake, L.C., *Ind. Eng. Chem. Anal. Ed., 17,* (1945), pp. 782, 787.

105. Meyer, H.I., *Jour. Appl. Phys., 24,* (1953), pp.510-512.

106. Chatzis, I., Dullien, F.A.L., *Powder Tech., 29,* (1981), pp.117-125.

107. Lai, F.S.Y., et al.,
Jour. Colloid. Inter. Sci., 84, (1988), pp. 362-378.

108. Wynnyckyj, J.R.,
Waterloo Intensive Course on Agglomeration Fundamentals, Waterloo, 1985.

109. Wynnyckyj, J.R., Capes, C.E., Hraste, M.,
Materials of the 3rd International Symposium on Agglomeration, Nürnberg, (1981), pp. A2-A13.

110. Whitaker, S.
Advances in Drying, vol. 1, A.S. Mujumdar, ed., Hemisphere Publ. in coop. with McGraw Hill Int'l, NY, (1980), pp.23-61.

111. Whitaker, S. and Chou, W.T.H.
Drying Technology, 1, (1), (1983-84), pp.3-33.

112. Whitaker, S.
Advances in Drying, vol. 5, A.S. Mujumdar, ed., Hemisphere Publ., NY, (1985), pp.21-32.

Chapter 10

NOMENCLATURE

a	interparticle distance in eqn. 2.1.1 [m]
A	Area [m^2]
A_v	Adhesion force in eqn. 2.1.1. [N]
B_i	Coefficients in Capillary Pressure Curve [Pa] or [-]
B	Concentration of bentonite in agglomerate [$wt.\ \%$]
C	Lattice spacing [μm]
c	Cohesion [Pa]
C_p	Heat capacity [J/K kg]
C_v	Heat capacity [Pa m^3/mol K]
D_{AB}	Diffusion Coefficient for species A in B [m^2/s]
d_p	Particle diameter [m]
D_p	Pellet diameter [m]
D_K	Knudsen diffusion coefficient [m^2/sec]
E	Modulus of elasticity [Pa]
F	Bond force [N]
G	Evaporation rate [kg/sec]

g Gravitational constant [9.8m/s^2]

H Hammaker's constant [J]

h Convective heat transfer coefficient [W/m^{2}K]

h_m Mass transfer coefficient [m/s]

h_r Radiative heat transfer coefficient [W/m^{2}K]

ΔH Heat of vaporization [J/kg H_2O]

J Evaporation rate [mol H_2O/ sec]

k_{gas} Thermal conductivity of gas species [W/m K]

k_{dry} Thermal conductivity of dry media [W/m K]

k^0_{eff} Effective conductivity of porous matrix for gas or liquid without flow or radiation effects [W/m^{2}K]

k_{flow} Contribution of a porous matrix to the thermal conductivity caused by fluid motion [W/m^{2}K]

k_s Thermal conductivity of solid [W/m K]

k_K Knudsen gas thermal conductivity [W/m K]

k_p Permeability [m^2]

k_r Relative permeability [-]

k_{wet} Thermal conductivity of wet porous media [W/m K]

M Size distribution function in eqn. 2.2.2.2.

MC Moisture content [kg H_2O]

P Pressure [Pa]

P^i Interference pressure between wet core and dry shell [Pa]

p_c Capillary pressure [Pa]

p_e Entry suction [Pa]

p_l Liquid pressure [Pa]

p_T Total pressure of gas phase [Pa]

p^0_v Equilibrium vapour pressure [Pa]

r Radius [m]

r_c Capillary radius [m]

R_0 Gas constant [8.3147 Pa m^3/mol K]

R_p Pellet radius [m]

r_p Particle radius [m]

S Pellet saturation [-]

S_W Measured particle surface area [m^2]

S_{th} Theoretical specific external surface area of particle [m^2]

t time [sec]

T Temperature [K]

v superficial velocity through a porous medium [*m/s*]

v_g Velocity of gas [m/s]

V Volume [m^3]

w Pore size fraction [-]

x Particle size in eqns. 2.1.1, 2.2.2.1 and 2.2.2.2

x distance [m]

Greek Letters

α Thermal diffusivity [m^2/s]

α_t Coefficient of thermal expansion [K^{-1}]

γ Surface tension [J/m^2]

η packing density in eqns. 2.2.2.3 and 2.2.2.4.

ε Porosity [-]

ε_R Emissivity

Θ Angle [rad]

μ Viscosity [Pa s]

ν Poisson ratio

Π Location of interface between wet core and dry shell as measured from pellet centre [m]

τ time step [*s*], or tortuosity [-]

ρ_l Density [kg/m^3]

σ_{SB} Stephen-Boltzman constant [$6.99\ 10^{-8}$ W / K^4m^2]

σ Stress [Pa]

σ_C Circumferential stress [Pa]

σ^i Interference stress [Pa]

σ^t Thermal stress [Pa]

σ^p Pressure stress [Pa]

σ_R Radial stress [Pa]

σ_T Tensile strength of agglomerate [Pa]

ϕ_d Volume fraction of suspended solids in a dispersion

Φ_{bin} Packing efficiency of binary system in eqn. 2.2.2.3.

Subscripts and Superscripts

∞ ambient value

bin binary (mixture)

c critical

c capillary

d dispersion

eff effective value - used for porous properties

f failure (stress); also film value

i initial; also interferense (stress)

l liquid phase

max maximum

min minimum

* critical (pore size)

^{0} equilibrium (vapour pressure)

p pellet, particle (size)

s surface; also shell

t thermal

v	vapour phase
wet	wet region

Dimensionless Variables

B	Spalding number	$\left[\frac{C_p \cdot (T_s - T_\infty)}{\Delta H}\right]$
Nu	Nussult number	$\left[\frac{hL}{k}\right]$
Pr	Prandtl number	$\left[\frac{C_{p_f}\mu}{k_f}\right]$
Re	Reynolds number	$\left[\frac{v_\infty D_p}{\upsilon}\right]$
Sc	Schmidt number	$\left[\frac{\upsilon}{D_{AB}}\right]$
Sh	Sherwood number	$\left[\frac{h_m D_p}{D_v}\right]$

Appendix A

DERIVATION AND NUMERICAL SOLUTION OF THE HEAT BALANCE EQUATION

The heat balance equation, equation 2.4.1:

$$\frac{\partial T}{\partial t} = \frac{\alpha_{wet}}{r^2}\left[\frac{\partial}{\partial r}\left(r^2 \frac{\partial T}{\partial r}\right)\right] - \frac{\Delta H \cdot G}{\rho_{wet} C_{pwet} V}\bigg|_{r=R_p} - \left(\frac{\rho_l C_{pl}}{\rho_{wet} C_{pwet}}\right) \cdot v_l \frac{\partial T}{\partial r} \qquad (2.4.1)$$

has been taken directly from the PhD Thesis of D.J. Zarachuk [1]. This equation has formed the basis of the intense-drying model calculations forming part of the Zaharchuk, as well as of the present thesis. An explicit derivation of the above heat balance equation has not, however, been documented in the Zaharchuk's thesis.

The form of the heat balance in equation 2.4.1 is, moreover, somewhat "unorthodox" in that, being an equation which describes the heat balance on an element inside the porous body being heated, it also contains a term restricted to the surface of the body, i.e. the *second* term on the right-hand side.

The purpose of this Appendix, therefore, is to justify the basis for equation 2.4.1, i.e. derive the equation. The approach taken is essentially that of Whitaker [39, 64, 110-112], but adapted to spherical coordinates.

In deriving an overall or comprehensive drying model, the challenge is to suitably describe all of the momentum and mass transport of the water, *and* of the heat transfer, required to enable the former. The above references offer a thorough quantitative definition of the issues involved, and provide a derivation for a one-dimensional system. (The intense-drying or vapour-lock aspect is, of course, not provided for).

The complexity of the problem, moreover, necessitates that the model consist of closely coupled complex second-order differential equations (two for the surface drying stage; i.e. equations 2.4.1 and 2.4.11, and three for the receding-interface stage, i.e. equations 2.4.20, 2.4.21 and 2.4.36). These balance equations contain heat and mass flux terms as well as property parameters, all of which are time, position and temperature dependent. An " unorthodox" equation system is, therefore, unavoidable; the complexity of the system precludes description by an analytically soluble equation system. "Special tricks" are, moreover, required -- and have been used presently -- in the numerical solution of the equation system. Needless to say, the equation system is very stiff and requires time and volume elements or modes which are of variable thickness.

The basis for the derivation of the heat balance equation for the surface drying regime is shown in Figure A.1. The basis is the volume element at the surface.

Complete heat balance, written for the surface volume element, is:

Heat conducted into the vol. element	-	***Heat consumed by water vaporization***	-	***Heat consumed by water heating***	=	***Heat accumulation within the element***	+	***Heat conducted out of the vol. element***
q_{in}	-	$q_{vap.}$	-	q_{wh}	=	q_{acc}	+	q_{out}

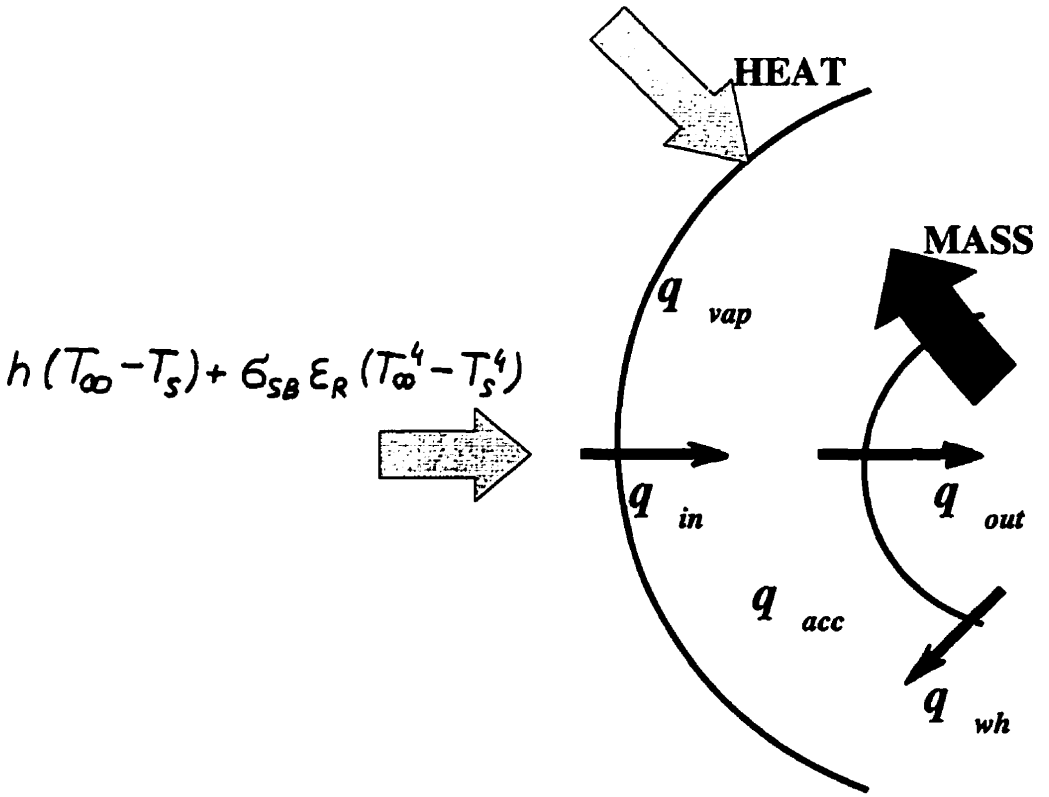


Figure A.1. Schematic Representation of the Surface Volume Element.

In analytical form the above terms can be presented as:

$$-kA\left(\frac{\partial T}{\partial r}\right)\Big|_{r=R_p} - \Delta H \cdot v_l \rho_l A\Big|_{r=R_p} - \rho_l C_{p_l} \cdot v_l A \frac{\partial T}{\partial r} dr =$$

$$\rho_{wet} A C_{p_{wet}} \frac{\partial T}{\partial t} dr - kA\left[\frac{\partial T}{\partial r} + \frac{1}{r^2}\frac{\partial}{\partial r}\left(r^2 \frac{\partial T}{\partial r}\right)dr\right] \qquad \text{(A.1)}$$

The first term on the left-hand side represents heat conducted from the pellet surface towards the

interior of the surface volume element. This term can be otherwise presented as a heat influx at the surface due to convection and radiation. The second term on the left-hand side represents the heat requirement for water vaporization at the surface, and the third term - the heat expenditure on raising the temperature of the water traveling to the surface. Solving for $\partial T/\partial t$, after simplifying ($v_l \cdot \rho_l \cdot A=G$), the heat balance equation for the surface-drying regime is:

$$\rho_{wet} C_{pwet} \frac{\partial T}{\partial t} = \frac{k}{r^2}\left[\frac{\partial}{\partial r}\left(r^2 \frac{\partial T}{\partial r}\right)\right] - \frac{\Delta H \cdot G}{V}\bigg|_{r=R_p} - \rho_l C_{pl} \cdot v_l \frac{\partial T}{\partial r} \qquad \text{(A.2)}$$

Further simplification ($\alpha_{wet}=k/(\rho_{wet} \cdot C_{p\,wet})$) yields equation 2.4.1. It is to be noted that the water evaporation term applies only for the surface volume element. For the volume elements inside the pellet this term is equal to zero, and that requirement is satisfied in the numerical-solution algorithm (see below).

To solve heat balance equation 2.4.1 in our model (given in Appendix C of Reference [1]) the numerical method must include appropriate steps. In the numerical code subscript *j* refers to the volume element, subscript *n* refers to the time step. In general, equation A.2 is represented by:

$$\left[C_{p_s}^{n+1}V_j\cdot(1-\varepsilon)\rho_s + C_{p_{H_2O}}\cdot V_j\varepsilon S^{n+1}\cdot\rho_{H_2O}\right]\frac{T_j^{n+1}-T_j^n}{\Delta t} = k^{n+1}A_{outer}\left(\frac{T_{j-1}^{n+1}-T_j^{n+1}}{\Delta r_{(j-1)-j}}\right)+$$

$$+k^{n+1}A_{inner}\left(\frac{T_{j+1}^{n+1}-T_j^{n+1}}{\Delta r_{j-(j+1)}}\right)+C_{p_{H_2O}}\left(T_j^{n+1}-T_{j+1}^n\right)\left(MC_{j+1}^n-MC_{j+1}^{n+1}\right)+$$

$$+C_{p_{H_2O}}\left[MCIN_j^{n+1}-MC_{j+1}^n-MC_{j+1}^{n+1}\right]\left(T_j^{n+1}-T_{j+1}^{n+1}\right) \qquad \text{(A.3)}$$

where MC_j represents the moisture content of a volume element in kg liquid, *MCIN* represents the mass of water traveling across the volume element boundary.

If the volume element is at the surface, an additional heat sink is included to represent evaporation at the surface. Also, the appropriate boundary condition (eqn. 2.4.3) representing heat flux by convection and radiation is used. Further details are given in Appendix C of Reference [1].